UNIVERSITAT POLITÈCNICA DE CATALUNYA BARCELONATECH

# *Analysis and implementation of a methodology for optimal PMa-SynRM design taking into account performances and reliability*

**by**

**Carlos López Torres**

UNIVERSITAT POLITÈCNICA DE CATALUNYA
BARCELONATECH

# ANALYSIS AND IMPLEMENTATION OF A METHODOLOGY FOR OPTIMAL PMA-SYNRM DESIGN TAKING INTO ACCOUNT PERFORMANCES AND RELIABILITY


By

**Carlos López Torres**


Thesis submitted in partial fulfillment of the requirements of the degree of Doctor of Philosophy in Electrical Engineering



Supervisors:

Dr. Antoni Garcia Espinosa

Dr. José Luis Romeral Martínez

*“Nunca consideres el estudio como una obligación sino como una oportunidad para penetrar en el bello y maravilloso mundo del saber”*

- *Albert Einstein*

# Abstract

Automotive applications focus to develop drive-train technologies with higher energy efficiency and lower environmental impact. Electric and hybrid vehicles are gaining popularity since they fulfill these requirements. The aim of optimal motor design is to achieve high torque and power densities, wider speed range and high efficiency within the area defining the most frequent operating points. This work presents a methodology to optimize electric motors for traction applications considering a multi-physics approach. The magnetic behavior is evaluated using a complex reluctance networks capable to compute the cross-coupling. The results of the magnetic model are the inductances, iron losses, and magnet flux linkage. The thermal behavior is evaluated using a thermal network and it is coupled with the magnetic model. The electric model is feed with the solution of the thermal and magnetic model. The electric model aims to calculate the whole operating area of the motor to allow optimizing the machine considering the most frequent operating zone. Therefore, a fast tool to evaluate different variables within the torque-speed map is convenient for this purpose. In this context, starting from a preliminary motor design, and taking into account motor cross-coupling effects and power losses, this thesis presents a new methodology for optimizing and evaluating the behavior of permanent magnet machines, such as synchronous reluctance machines, and permanent magnet assisted synchronous reluctance machines, in all operational points. Apart from the torque and efficiency, many other electrical variables can be obtained, such as the current space vector angle, power factor or electrical power among others. The proposed methodology also allows optimizing the design of the machine under a pre-established control law, thus obtaining the current set point trajectory in the *dq* frame and allowing a fast and accurate evaluation of motor performance. The results obtained by means of the proposed simulation tool are compared against finite element analysis simulations and experimental data, thus validating the usefulness and accuracy of the proposed methodology.

# Keywords

*Synchronous Reluctance Motor*

*Permanent Magnet Motor*

*Design*

*Optimization*

*Magnetic analysis*

*Thermal analysis*

*Genetic algorithm*

*Electrical analysis*

*Behaviors maps*

*Control parameters*

# Acknowledgement

Ha habido muchas personas cerca de mí durante el desarrollo de este trabajo. En estos tres años he necesitado ayuda para desarrollar, mejorar o implementar las diferentes ideas que forman esta tesis y apoyo para avanzar y no rendirme. Por estos motivos me gustaría dedicar unas palabras a estas personas.

Primero quiero agradecer a mis directores de tesis, Toni Garcia y Luis Romeral, por su guía y ayuda en el desarrollo de la tesis. A Toni, porque que sin conocerme mucho me dio la oportunidad de empezar esta aventura, por los consejos que me ha dado, por el apoyo y por los ánimos. Porque no solo ha sido un director para mí, también ha sido y es un amigo. A Luis, por permitir mi contratación y por confiar en mí y contar conmigo para el desarrollo de proyectos con empresas.

Segundo quiero agradecer a todo el grupo MCIA su amistad y compañía. A Carles, por su ayuda en prácticamente todo lo que tiene que ver con la tesis, por sus charlas y por su amistad. A Alejandro, por su compañía en las largas noches de trabajo, por recordarme que mi trabajo es bueno y por subirme la moral. A Efren, por contagiar su alegría y su seguridad. Los cuatros formamos el eterno despacho 160. A Dani, por siempre estar dispuesto ayudar y por su afecto y cariño hacia mí. A Enric, por las alegrar las comidas. A María, por traer aire fresco al grupo. A Vite, por sus conversaciones y sus excursiones. A Jordi Riba, por su ayuda, esfuerzo y colaboración en los artículos y por motivarme para seguir publicando. Con todos ellos se ha creado una relación que no solo es profesional, se ha creado una amistad.

Tercero quiero agradecer a mi familia y amigos, un conjunto de gente que necesitas a tu alrededor para poder realizar una tesis. A mi padre, Carlos, y mi madre, Dulces, por apoyarme siempre, por su cariño y afecto, por siempre estar cuando se les necesita. A mi hermano, Raúl, porque aunque nos discutamos en el fondo nos queremos, por acompañarme en momentos especiales y por estar siempre cerca. A Joan, Albert, Manel y Lorena, por su visita a Padova y por sus tardes de distracción. A Jordi, Isma, Alejo, Dani y Mire por estas comidas y cenas que permiten desconectar.

Cuarto quiero agradecer al profesor Nicola Bianchi y su grupo, EDLab, y permitirme realizar una estancia con ellos en Padova. A Francesco, Grazia, Virginia, Cristian y Giaccomo, por hacerme sentir como en casa, por enseñarme buenos sitios de Padova para comer y salir y por la rápida amistad que ser formo.

Una tesis de tres años no se puede realizar sin una ayuda económica. Por ello, quiero agradecer a dos instituciones que me han permitido costearme los tres años de trabajo. Por un lado, está AGAUR que me otorgó la beca FI-DGR 2015, que me ha permitido tener un salario estos tres años. Por otro lado, el Col·legi D'Enginyers Industrials de Catalunya y la Fundació Caixa D'Enginyers por su ayuda económica. Fue un orgullo y una satisfacción ser unos de los ganadores de *"beques per a tesis doctoral 2017"*.

Por último pero no menos importante, darle las gracias a la persona con la que comparto mi vida, Sandra. Gracias por aguantar mis días malos, por soportar mis horarios y por el cariño y afecto que me has dado.

# Contents of the document

# Index of figures

# Index of tables

# Acronyms and their definitions

| | |
|---|---|
| **Dy** | Dysprosium |
| **EV** | Electric Vehicle |
| **FEA** | Finite Element Analysis |
| **FEM** | Finite Element Methods |
| **GA** | Genetic Algorithm |
| **HEV** | Hybrid Electric Vehicle |
| **IPMSM** | Interior Permanent Magnet Synchronous Motor |
| **LUT** | Look-Up Table |
| **ME** | Maximum Efficiency |
| **MLC** | Minimum Losses Control |
| **MMF** | Magneto Motive Force |
| **MTPA** | Maximum Torque Per Ampere |
| **MTPV** | Maximum Torque Per Voltage |
| **Nd** | Neodymium |
| **PMa-SynRM** | Permanent Magnet assisted Synchronous Reluctance Motor |
| **PM** | Permanent Magnet |
| **PMSM** | Permanent Magnet Synchronous Motor |
| **RN** | Reluctance Network |
| **SMPMSM** | Surface Mounted Permanent Magnet Synchronous Motor |
| **SynRM** | Synchronous Reluctance Motor |
| **TN** | Thermal Network |
| **WLTP** | Worldwide harmonized Light vehicles Test Procedure |

# Nomenclature

| | |
|---|---|
| $\boldsymbol{A}$ | Linear current density [A] |
| $\boldsymbol{B}$ | Magnetic flux density [T] |
| $\boldsymbol{C_{mec}}$ | Mechanical constant [(kW·s)/m$^3$] |
| $\boldsymbol{D_g}$ | Air gap diameter [m] |
| $\boldsymbol{E}$ | Back EMF [Vrms] |
| $\boldsymbol{g}$ | Air gap length [m] |
| $\boldsymbol{H_c}$ | Coercive force [A/m] |
| $\boldsymbol{I_f}$ | Phase current [Arms] |
| $\boldsymbol{i_{max}}$ | Maximum current vector amplitude (peak value)[A] |
| $\boldsymbol{i_{cd}}$ | *d*-axis core loss current [A] |
| $\boldsymbol{i_d}$ | *d*-axis stator current [A] |
| $\boldsymbol{i_{od}}$ | *d*-axis torque-generating current [A] |
| $\boldsymbol{i_{cq}}$ | *q*-axis core loss current [A] |
| $\boldsymbol{i_q}$ | *q*-axis stator current [A] |
| $\boldsymbol{i_{oq}}$ | *q*-axis torque-generating current [A] |
| $\boldsymbol{l}$ | Length of the magnetic reluctance [m] |
| $\boldsymbol{l_{st}}$ | Stack length [m] |
| $\boldsymbol{L_d}$ | *d*-axis magnetizing inductance [H] |
| $\boldsymbol{L_q}$ | *q*-axis magnetizing inductance [H] |
| $\boldsymbol{m}$ | Phase number |
| $\boldsymbol{N}$ | Number of conductors on each slot |
| $\boldsymbol{p}$ | Pole pairs |
| $\boldsymbol{P_i}$ | Losses in node *i*-th [W] |
| $\boldsymbol{P_{cu}}$ | Copper losses [W] |
| $\boldsymbol{cos\varphi}$ | Power factor |
| $\boldsymbol{P_{Fe}}$ | Iron losses [W] |
| $\boldsymbol{P_h}$ | Hysteresis losses [W] |
| $\boldsymbol{P_e}$ | Eddy current losses [W] |
| $\boldsymbol{R_{ih}}$ | Thermal resistance between nodes [º/W] |
| $\boldsymbol{R_{Fe}}$ | Iron resistance [Ω] |
| $\boldsymbol{R_s}$ | Phase resistance [Ω] |
| $\boldsymbol{S}$ | Cross-section of the magnetic reluctance [m$^2$] |
| $\boldsymbol{u_{max}}$ | Maximum voltage vector amplitude (peak value)[V] |
| $\boldsymbol{u_d}$ | *d*-axis stator voltage [V] |
| $\boldsymbol{u_q}$ | *q*-axis stator voltage [V] |
| $\boldsymbol{V_f}$ | Phase voltage [Vrms] |
| $\boldsymbol{T_{emp}}$ | Temperature (ºC) |
| $\boldsymbol{T}$ | Torque [Nm] |
| $\boldsymbol{\eta}$ | Efficiency |
| $\boldsymbol{\omega_e}$ | Electrical angular speed [rad/s] |
| $\boldsymbol{\psi_{PM,d}}$ | *d*-axis permanent magnet flux linkage [Wb] |
| $\boldsymbol{\psi_{PM,q}}$ | *q*-axis permanent magnet flux linkage [Wb] |
| $\boldsymbol{\mu}$ | Magnetic permeability [H/m] |
| $\boldsymbol{\phi_i}$ | Magnetic flux on each reluctance [Wb] |
| $\boldsymbol{\phi_d}$ | *d*-position magnetic flux linkage [Wb] |
| $\boldsymbol{\phi_q}$ | *q*-position magnetic flux linkage [Wb] |
| $\boldsymbol{\theta_i}$ | Temperature in node *i*-th [ºC] |
| $\mathfrak{R}_{ii}$ | Reluctance [H$^{-1}$] |
| $\boldsymbol{sp}$ | Specific power [kW/kg] |
| $\dot{m}$ | Mass flow rate [kg/s] |
| $\boldsymbol{c_p}$ | Specific heat capacity [J/(kgK)] |

# 1.

# Introduction

The first chapter presents the subject of the proposed work in this thesis. The state of the arte related with this work is summarized on this section. Finally, the introduction, hypothesis and objectives can be found in this chapter.

*CONTENTS:*

# 1. Introduction

## 1.1 Research topic

In the current century, the global warming and resources scarcity have become an important issue to be attended. In terms of preventing global warming and conserving natural resources, vehicles are playing an increasingly critical role [1, 2] since the $CO_2$ emission caused by automobile represents the 90% of the emission by the total amount of transportation [3].

Then, the interest on hybrid vehicles (HV) and electric vehicles (EV) increase, so electric motors for traction applications are a hot topic [4]. Among the most suited electric motor types for traction purposes, rare-earth-based PMSMs (permanent magnet synchronous motors) highlight due to their superior characteristics, including specific power, speed range capability or efficiency [5-7]. Therefore, PMSMs in all their variants have received much interest [8-11]. As an example, the shape of the rotor of Toyota Prius' motor is shown in Figure 1. As can be observed, the depicted motor is an Interior Permanent Magnet Synchronous Motors (IPMSM).

Figure 1. Rotor of Prius (2010) [12]

Figure 2 shows the motor of Insight of Honda; as can be notice the shape of the rotor is not illustrated. However, Insight and Prius have the same rotor distribution, i.e. both of them are a V-shape, and so they are IPMSM. The main different between the both motors is the winding distribution. Prius has a distributed winding meanwhile Insight uses a concentrated winding.

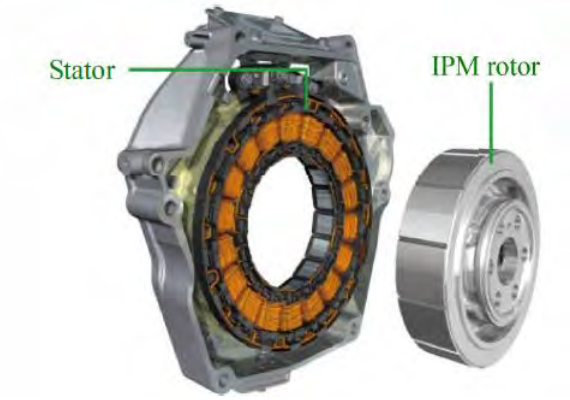


Figure 2. Insight Motor [13]

However, different concerns about rare-earth permanent magnet materials, such as price volatility, scarcity [14] and China's monopoly are pushing the industry to focus on other options. Therefore, electric motor manufacturers are focusing the attention in reducing the amount of rare-earth materials or replacing them by hard ferrites, thus arising the concept of rare-earth-less or rare-earth-free machines, respectively [15, 16]. In this context, SRMs and PMaSynRMs are gaining popularity since they combine the advantages of PMSMs with the low manufacturing costs of induction motors [14].

The use of rare-earth-free motors increases the importance of the optimization. The optimization process of electric motors has been habitually performed based on one or few characteristic operating points [17]. However, motor performance is highly influenced by the driving cycle of the vehicle, which comprises a large number of operating points different than those representing the rated conditions. Therefore, a thorough knowledge and optimization of the behavior of the motor over the whole drive cycle is gaining importance [8, 18, 19]. The classical design based on some operating points under rated conditions must change to a range optimization based on the most frequent operating zone [17, 19, 20], which can be obtained according to a given driving cycle.

There are many works dealing with the topic of design and optimization of electric motors, although many of them deal with FEM (finite element method) models of the machine [8, 18, 19, 21] by applying both single- and multi-objective approaches. However, FEM simulations present a high computational burden [22, 23], thus limiting the number of simulations to be carried out for optimization purposes. Different motor families are object of these studies, including PMSMs [19], SRMs (switched reluctance motors) [18], PMaSynRMs [17] or FSPMMs (flux-switching permanent-magnet motors) [5] among others.

The optimal design of electric machines requires the development of accurate models which are able to reproduce physical effects such as magnetic saturation or power losses among others. One of the challenges is to develop accurate models with an acceptable computational cost [8]. Since the optimization process requires a large number of simulations, especially when analyzing many operating points, accurate machine models with low computational cost are compulsory. Therefore, current approaches try to reduce the use of FEM-based models during the optimal design process [4, 24, 25]. However, these methodologies present some drawbacks, since they tend to avoid a multi-physics analysis, disregard iron losses or perform FEM simulations to determine non-linear variables such as machine inductances. In [26] the predesign stage of the machine is done from analytical equations and the motor characteristics (magnetic, thermal and electrical behaviors) are evaluated by means on FEM simulations. In [27], both FEM simulations and analytical calculations are applied. In [28], FEM simulations are performed to obtain the final design of the machine, although as a first approach, the motor is calculated using a reluctance network, which does not take into account cross-coupling effects or a multi-physics perspective. In [17] a PMaSynRM is designed and optimized by analyzing a selected number of representative operating points which are considered for the global optimization, since this strategy allows reducing the computational burden of the optimization process.

Traditionally, the design process of electric motors has been based mainly on the analysis of a few number of operating points, such as the rated torque at the rated speed or the torque at the maximum speed, respectively [5]. However, this thesis focuses on an accurate multi-domain design optimization

of two machines, a PMaSynRM and a SynRM, which avoids the use of FEM simulations to speed up the optimization process. The accurate approach presented considers magnetic saturation, iron losses and the temperature of the different parts of the machine. These effects are evaluated by using two coupled reluctance and thermal networks representing the analyzed machines. The proposed magnetic model can be represented with de-coupled *dq*-networks or as a unique reluctance network that allows calculating the *d* and *q* inductances, including the cross-coupling saturation effects. Since this reluctance network provides the values of the *d* and *q* currents for all angular positions, as well as the magnetic saturation of all parts of the machine, the magnetic losses are calculated for all rotor positions, thus increasing the accuracy of the solution. The machine parameters calculated by means of the coupled reluctance and thermal networks are introduced into a detailed *dq* electric model, and the different working points are calculated to obtain the torque-speed plane.

To summarize, the proposed work aims to develop a methodology to optimize the machine without the use of FEA. In this context, a multi-physic approach is realized to ensure the correct behavior of the machine in thermal, magnetic, and electrical domains. Analytical equations based on reluctance networks are developed to model the machine and perform the optimization. Moreover, the developed model could be used to run real time accurate control, because it not only represent the real behavior of the machine, but also can be executed and solved faster than any other FEM solver.

## 1.2 Research problem

The implementation of an adaptable methodology for optimal design of Permanent Magnet Synchronous Reluctances Motors is studied in this thesis. A multi-objective optimization is developed to optimize the motors in terms of torque, efficiency, low cost and high power density, among others. Moreover, the optimization according to driving cycles is considered in the proposed work.

In the context of evaluating several working points to include them in the optimization, the creation of a several models to evaluate the multi-physic behavior of the machine is required. These models allow calculating the parameters of machine such as inductances, losses, temperature, among others to evaluate the performances of the it in the whole torque-speed range.

Concluding, the thesis goal is the implementation of a **methodology capable of obtaining an Optimal Design of Permanent Magnet assisted Synchronous Reluctance Motor** taking into account the different requirements of each possible application, including the range optimization, and without using FEM software in the optimization loop.

## 1.3 Hypotheses

In order to address the presented research problems, the following hypotheses have been formulated as a starting point for this research work:

**Regarding motor type design**

- PMa-SynRM with accuracy design will achieve a good power density ratio. The aim of the optimal design of PMa-SynRM is to achieve power density ratio close to those of the PMSM.
- Torque ripple reduction of PMa-SynRM motors can be achieved by considering advance design for the flux barriers, ribs and rotor magnets shape and dimensions in a transversally laminated rotor.
- Torque ripple characteristic of electric machines can be reduced by using multi-phase motor.

**Regarding fault tolerance**

- A large number of phase increase the drives capability of working in fault-tolerant regime, while reducing the current phase.
- An accurate motor design regarding thermal, electrical and magnetic isolation of the phases and limitation of short-circuits fault current by a high phase impedance can limit the risk of total motor failure.

**Regarding Design methodology**

- The implementation of a fast and adaptable methodology for optimal design of Permanent Magnet assisted Synchronous Reluctance Motors can be achieved by using evolutionary algorithms.
- The use of Reluctance Networks to evaluate the magnetic behavior of PMaSynRM allows calculating with high accuracy the inductances taking into account the cross-coupling effect, the iron losses and the magnet flux linkage.
- The implementation of a coupled multi-physics models (magnetic, thermal and electrical) allows calculating the different behavior maps, such as efficiency map, current map, voltage map, among others, to assist the optimization process. The information obtained from these maps helps to optimize the design according to a driven cycle. In addition, if someone wants to implement a control for the motor, the information of all operation points will be needed.

## 1.4 Aim and objectives

The main objective of the thesis is to **develop a methodology capable to optimize a PMaSynRM according to a multi-objective function considering the whole operating area.**

In this context, the development of a several analytical models to determine the different parameters of the machine is mandatory. Then, the aims related to the **calculation of multi-physic behavior** are;

1. Development of a **magnetic model** to
    - Calculate the current dependency of inductances
    - Calculate the magnetic saturation of the machine to determine the iron losses
    - Calculate the magnet flux linkage
2. Development of a **thermal model** to
    - Calculate the temperature of the different part of the machine
    - Calculate the copper losses
3. **Coupling** the magnetic and thermal model
    - Magnetic properties of the magnets varies with the temperature
4. Development of an **electrical model** to
    - Use the different data from the coupled thermal and magnetic model to feed the *dq*-electric circuit
    - Generalize the equations to calculate the different performances for all the combinations of voltage, current, and speed.

Then, the objectives to calculate the whole operating area can be summarized as:

5. Development of a **procedure to calculate** all the **working points**
6. Represent the performances of the calculated working points in a **torque-speed map** or **power-speed map**

Finally, the optimization must use the models to obtain the optimal design according to a cost function without the use of Finite Element Methods (FEM).

## 1.5 Different motor topology

For electrical traction and EV/PHEV IPMs have been well studied and the motor design has achieved optimal improvements [29-31], so this kind of motor can give good performances [32]. By contrast, the cost and the temperature limitation are important drawbacks [14]. The high cost of the IPMs is related with the magnets; the rare-earth magnets cost is more or less the 65% of the total material cost of IPM machine. Moreover, the rare-earth magnets limits the temperature because the neodymium suffer demagnetization about 90ºC [14]. It can be noticed that the new tendency is avoiding the use of rare-earth magnets on motors, so there are two possibilities:

1. The use of different motor topology which avoids the magnets, such as;
   1.1. Switched Reluctance Motors
   1.2. Induction Motors
   1.3. Synchronous Reluctance Motors
2. To design Permanent Magnet assisted Synchronous Reluctance Motors, with the objective of the reduction of the magnets on the motor design. Two possibilities are possibles;
   2.1. Rare-earth magnets
   2.2. Ferrite magnets

### 1.5.1 Rare-earth-less magnets motors

***Switched Reluctance Motors (SRM)***

SRMs are brushless machines [33] that present a doubly salient structure since both rotor and stator have salient-pole structure. The stator has wound field windings similar to the stator windings of DC motors. The rotor has neither windings nor PMs. The rotor tends to shift towards the position of the excited stator winding, in order to maximize the inductance (minimize the reluctance) [34], thus aligning the rotor pole with the closest stator pole. To maintain the rotor in motion, it is required to excite the stator poles in a sequence, which is done by an electronic controller. Conventional inner rotor SRMs have radial flux and doubly saliency, as shown in Figure 3, although axial flux and outer rotor topologies exist.

SRMs can have different phases number, being most frequent 3 or 4 phases. SRMs are usually fed by shifted pulsed DC phase voltages, whereas the phase currents have a near trapezoidal shape. To generate sufficient reluctance torque, SRMs must work under deep saturation conditions; therefore the air gap is usually very small and the magnetic properties of the stator and rotor steel laminations are especially important [34]. Since the power flows through the narrow air gap in the radial direction, important radial forces, vibrations and acoustic noise are generated [35, 36]. SRMs present inherent fault tolerant capability since they have concentrated phase windings which are independent and isolated from each other. Therefore, when a phase fails, the SRM may still operate at reduced power with the remaining healthy phases [37].

SRMs are simple and inexpensive machines because of their simple construction, easy assembly

and therefore easy manufacturing [33, 38, 39], in part due to the absence of windings and PMs in the rotor [37], and offer an extended Constant Power Speed Ratio (CPSR) up to 7 [40], these being very appealing features for gearless EV drives. Since SRMs are PM-free machines, they allow high temperature operation [35, 41]. SRMs also exhibit low rotor inertia and high start-up torque and therefore fast acceleration capability [42]. SRMs have concentrated windings which have good thermal performance and therefore inherent fault tolerant capability. In addition, SRMs are easily cooled since the heat generated by both iron and copper loss is mainly concentrated in the stator [37]. Test results also prove higher power density than IMs [40]. However, SRMs present inherent limitations, including high torque ripple, high vibrations and acoustic noise levels and complex control due to the high nonlinear behavior or higher iron losses compared to IPMSMs because the higher frequency of the flux, thus presenting lower efficiency [38].

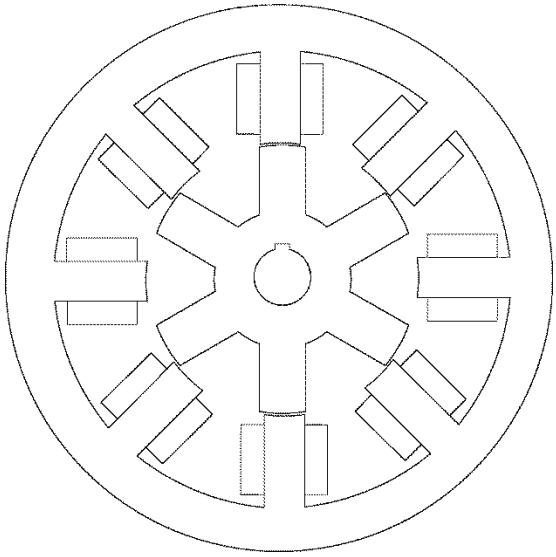

Figure 3. Basic geometry of a four-phase 8/6 SRM

According to [43], to improve torque density and efficiency and the operating area, the number of stator and rotor pols must be increased, extremely low-loss laminations must be used and the continuous current mode of operation must be applied at high speeds.

Some authors are considering the possibility of adding permanent magnets within the stator structure to further increase the torque density and efficiency while minimizing torque ripple [44, 45]. However these motor types are still under research and are not considered in this paper.

### *Induction Motors (IM)*

Squirrel cage IMs (SCIMs) are brushless alternating current (AC) machines fed by sinusoidal voltages-currents, which are widely applied in industrial applications and for electrical propulsion systems [39, 46] since they offer high simplicity, low cost, reliability, robustness, low torque ripple, low maintenance needs and ability to operate in harsh environments. SCIMs are being applied in some commercial FEVs including electric cars, buses and light trucks [36]. Some examples of electric cars driven by SCIMs are the Tesla S-2014, Tazzari Zero, Mercedes-Benz B-Class Electric Drive, Mahindra

e2o [47], Toyota RAV4 [2]. Other examples are the Newton light electric truck from Smith Electric Vehicles that in the first version was equipped with a three-phase SCIM [38] or the Optare Solo EV battery electric bus [48].

SCIMs are asynchronous machines, that is, the speed of the rotating field generated by the stator windings and the rotor speed are different. SCIMs have a simple structure compared with other motor types, which facilitates the design and manufacture [38]. In addition they don't use any type of PM but cheaper materials. Although three-phase SCIMs are the most habitual, motors with higher number of phases are being developed since they allow increasing power density, reducing torque pulsations and the current per phase [48]. The rotor contains a cast aluminum cage in which the rotor currents are induced by the rotating magnetic field generated by the stator windings. The interaction between the rotating magnetic field and the magnetic field generated by the rotor currents produces the electromagnetic torque. Efficiency can be boosted by using rotor bars and end rings of copper instead of aluminum [49, 50]. Figure 4 shows the cross-section of a SCIM.

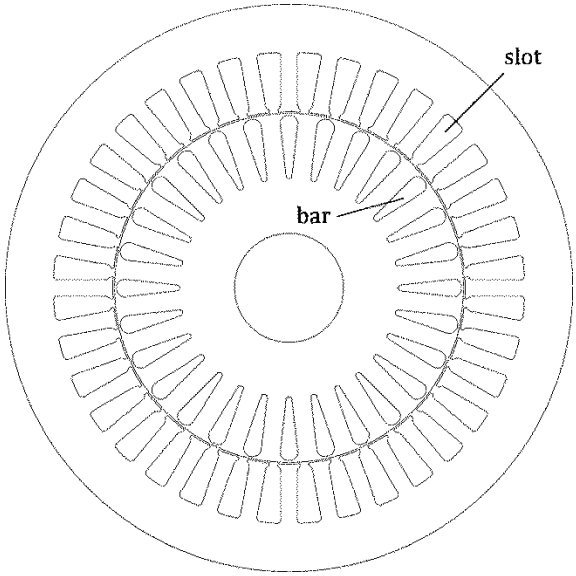


Figure 4. Cross-section of a squirrel cage induction motor (SCIM)

SCIMs present inherent drawbacks, including difficult control at low speed operation, low power factor under light load conditions, high starting currents [42], low efficiency and low inverter usage [39]. The magnetization current, which is absorbed even under no-load conditions, increases copper losses and the rating of the electronic converter [36]. By applying suitable control techniques, the maximum torque can be attained during starting while keeping starting current low. SCIMs can also be applied in in-wheel applications by using an outer cage rotor, thus increasing the air gap diameter and therefore the output torque [51]. It is notorious that SCIMs have lower torque density and less efficiency than other motor types [38]. Therefore, SCIMs are more applied in FEVs than in HEVs or PHEVs due to the space restrictions imposed by the latter two types of vehicles. The maximum speed is usually limited to10000 r/min [37]. By applying flux weakening techniques, the constant power range can be extended up to 4–5 times the base speed, which is a key requirement for EVs [39].

Different speed and torque control techniques are being applied. The simpler of them is the scalar control, which changes the magnitude and the frequency of the phase voltages. However, its

performance under transient conditions is limited. To improve performance during transient conditions, field oriented control (FOC) and direct torque control (DTC) are being applied, and also sensorless control methods, that is, drives without a speed or position sensor, are receiving much attention.

### *Synchronous Reluctance Motors (SynRM)*

As the name indicates, SynRMs are synchronous machines usually supplied by three-phase AC voltages. The ducted rotor of a SynRM is made of magnetic steel laminations with neither current-conducting paths nor windings or PMs. Therefore rotor losses are very low. The only component of the torque in a SynRM is the reluctance torque, therefore SynRMs must present a very high salience ratio Ld/Lq to increase the efficiency, maximum torque, power factor and constant-power speed range (CPSR) [52]. To this end a multi flux barrier structure is applied in the rotor [36], with the flux barriers perpendicular to the flux lines. The flux barriers guide the flux through the desired paths, that is, whereas the q-axis flux is blocked by the flux barriers, the d-axis flux is guided through an iron path [53]. This design strategy, jointly with the use of axially-laminated (ALA) rotors, allows obtaining a reasonably small Lq inductance due to the large air gap path [54]. The salience ratio can be increased by appropriate placement, number and geometry of flux barriers, a challenging design task. The rotor has low inertia because of the air flux barriers [55]. Since the rotor is only made of magnetic steel laminations and the stator is very similar to that of a conventional induction motor, SynRMs are easy to manufacture [14]. However, SynRMs have lower efficiency, torque density and power factor than PMSMs [56] although SynRMs are competitive with induction machines in terms of power factor, inverter kVA requirements, and easy speed control without encoders even at low or zero speed operation [54]. SynRMs are usually controlled by either vector or direct torque control.

Main weaknesses of SynRMs are high torque ripple [57] and low torque density which can be partially overcome by an adequate design of the magnetic configuration of the rotor [14]. Appropriate selection of the number of flux barriers taking care of their geometry [57] and rotor skewing by one stator slot pitch allows drastically dropping the torque ripple while reducing slightly the average torque [54].

### *Permanent Magnet assisted Synchronous Reluctance Motor (PMa-SynRM)*

According to [14], the cost of rare-earth PMs can be about 60% the total costs of materials of an IPMSM machine. Therefore, by replacing the rare-earth PMs by ferrite magnets the material costs can be reduced by 50%.

Torque density and torque production capability in SynRMs can be increased by incorporating magnets in the rotor [58, 59], thus resulting a PMa-SynRM, which is a promising candidate to propel EVs. This motor is similar to an IPMSM. The ferrite magnets are inserted in the rotor flux barriers on the quadrature axis to increase the saliency ratio [36]. PMs' polarity is selected to counteract the magnetic flux in the q-axis to minimize Lq, thus maximizing the Ld/Lq saliency ratio [59], so PMa-

SynRMs increase the reluctance torque, which is much greater than the alignment torque [60]. Due to the cost and supply risk issues associated to rare-earth PMs, PMa-SynRMs based on cost effective ferrite PMs are being developed. PMa-SynRMs combine the features of PM and reluctance machines, thus presenting high efficiency, high density, high power factor and a wide speed range.

The air flux barriers partially protect the PMs against demagnetization [59] although there is a risk of demagnetization when operating at extremely low temperatures [61].

PMa-SynRMs use lower PMs mass than IPMSMs [57], thus inducing lower back-EMF and lower short-circuit currents [55]. In addition they use ferrite instead of NdFeB PMs and the flux-linkages due to PMs are smaller compared to those of conventional IPMSMs [59]. In IPMSMs the main component of the flux comes from the PMs, so the repulsion torque is the main torque component, however PMa-SynRMs maximize the reluctance torque.

The structure of PMa-SynRMs is very similar to that of IPMSMs, but the rotor is designed to raise the magnetic saliency in order to further increase the reluctance torque, thus enhancing flux weakening performance at high speed operation and increasing the power density [62] and the overload capability [57]. To maximize the magnetic saliency and thus the reluctance torque, the rotor has a multi-layered cavity structure with buried ferrite PMs, as displayed in Figure 5.

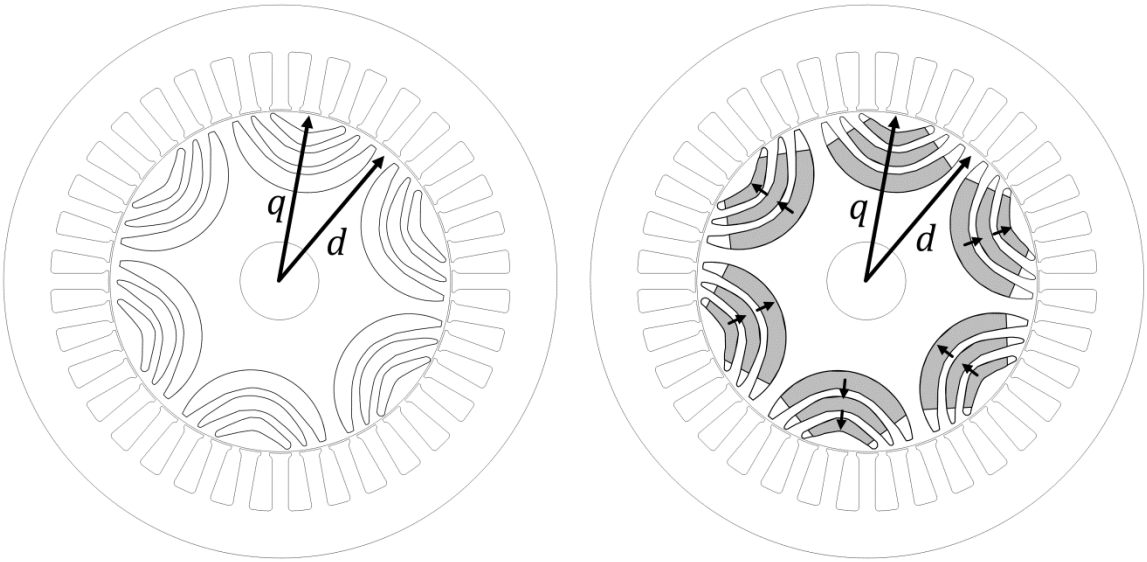


Figure 5. Structures of a SynRM and PMa-SynRM

### 1.5.2 Topology selection

As can be observed, there are different solutions to avoid the use of rare-earth-magnets in motors to EV or HEV. Around the latter concept the ferrite Permanent Magnet assisted Synchronous Reluctance Machines becomes increasingly important since they have the advantage among the mentioned types to combine the low production cost of induction motors with a performance comparable to PMSM [14]. Besides, the magnetic properties of the ferrites are not so temperature dependent as Neodymium is. In this context, the thesis deals with the optimal design of a PMa-SynRM.

## 1.6 SynRM evolution

The Permanent Magnet assisted Reluctance Synchronous Motor suffers an evolution over time [59]. The rotor evolution is noticed on the different topologies, such as multi barrier, axial laminated or in the position of magnets. To contextualize the PMa-SynRM the SynRM evolution is explained. The SynRM starts on the sixties; the Figure 6 shows a typical rotor of that era. The flux barriers are utilized for difference the magnetic flux on the d-axis and q-axis. That difference on the reluctance is called saliency.

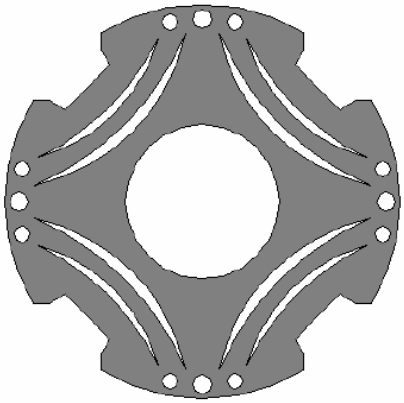

Figure 6. Rotor type of the sixties [59]

In the next decade, the double barrier per pole design appears, it means there is a radial rib in the flux barrier to increase the mechanical integrity of the rotor. In Figure 7 the rotor with double barrier is shown. They had two barriers per pole and were fitted together with a starting cage.

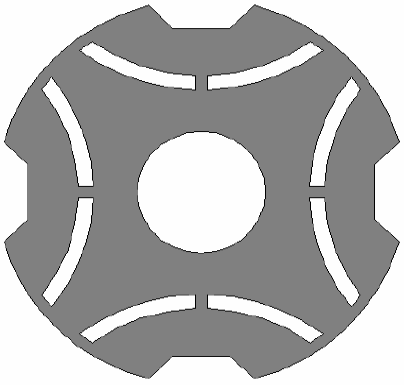

Figure 7. Double barrier rotor [59]

In the final of the sixties the first axially-laminated anisotropic (ALA) rotor was designed by Cruickslank. In the seventies this ALA-SynRM was improved and performed. In the eighties that kind of motor obtains high saliency ratio and high performances, so that electric motor topology was considered a good alternative compared to the other electric machines.

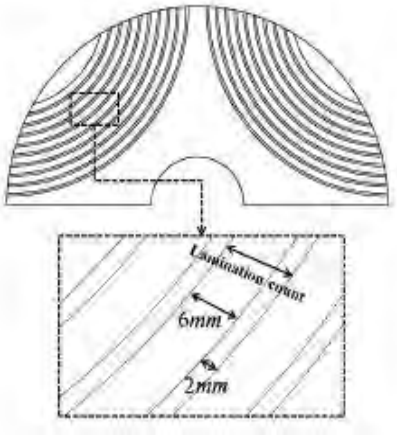


Figure 8. ALA-SynRM rotor [59]

The next generation of the SynRM came when transversally laminated (TLA) rotors were introduced. This SynRM type is easier and cheaper than the ALA-SynRM. However, the performances are lower than the axially type. In spite of this fact, TLA rotor has suitability of rotor skewing and it is easy for mass production. Moreover, TLA rotor can be improved with optimal design of the flux barrier.

Figure 9. TLA-SynRM rotor

Finally, the possibility of introduce permanent magnets into the flux barriers of this kind of motor creates the new topology called Permanent Magnet assisted Synchronous Reluctance Motor. The difference between PMa-SynRM and IPM regards on the rotor type of both. In addition, the major part of the torque on the PMa-SynRM is reluctance torque. By contrast, in IPM the major part of the torque is synchronous torque, i.e. it is realized by the interaction of magnets and stator currents. There are many types of PMa-SynRM, because the number of magnets and the position of them are variable. For example, the magnets can puts in radial direction [63] or perpendiculars to radial direction [64].

In this thesis, the number, shape and position of the flux barriers are variables to optimize since they are very important to the performances of the machine. Furthermore, the quantity of ferrites inside of the barriers is variable depending on the required performances.

# 2.

# Design Methodology

This chapter shows how the methodology proposed works. The different sections of the methodology proposed are presented as well as the aim of each part.

*CONTENTS:*

# 2. Design methodology

## 2.1 Introduction

The interest on electric and hybrids vehicles has increased in the recent years due to the scarcity of fossil fuel resources and the need to reduce greenhouse gases emissions [15]. Permanent magnet synchronous motors (PMSMs) have the best performances, in terms of torque and power density, efficiency or speed range [11, 65]. However, the cost of the magnets significantly affects the final cost. For that reason, and due to the price volatility and concerns about the risk of supply of rare-earth permanent magnets, rare-earth-free motors are being increasingly demanded in automotive applications [16].

In the category of rare-earth-free motors, synchronous reluctance motors (SynRMs) and ferrite PM-assisted synchronous reluctance motors (PMa-SynRMs) are gaining importance. PMa-SynRMs are advantageous over other rare-earth-free motor types, since they combine the low manufacturing costs of induction motors with a performance comparable to that of PMSMs [66].

However, the design process of SynRMs and PMa-SynRMs is complex, fundamentally because of the high magnetic saturation. FEA-based (finite element analysis) approaches are being commonly applied to analyze such machines [22, 67]. The major drawback of using FEA during the optimization process is the high computational time.

Focusing on current trends, including the automotive sector and applications requiring energy restrictions, the design based on the rated working point is changing to the most-frequent operational zone [19, 20, 68]. However, the design process based on FEA is slow and tedious when considering an iterative optimization approach that must consider multiple operating points. Current methodologies focus on reducing the FEA contribution to minimize the computational time [24, 69, 70]. Moreover, some optimization approaches apply a multi-objective approach by minimizing the cogging torque and maximizing the efficiency [71] or increasing the torque and reducing power losses [72]. However, most of these optimization approaches are focused on a single working point, instead of focusing on the most frequent torque-speed range.

Therefore, there is a lack of more flexible and faster optimization technologies for electric motors in EV/PHEV applications considering wider operational zones with multi-objective approaches, including thermal, magnetic, electrical and mechanical ones.

This section summaries a fast methodology to design and optimize PMa-SynRMs and SynRMs by means of coupled magnetic, thermal and electric models. The design is evaluated in different domains, while minimizing the computational cost, since the use of FEA analysis is minimized. Next, the motors are optimized within a specific torque-speed range, which depends on the particular application. Once obtained the optimized design, FEA is applied to validate the mechanical integrity. The mechanical analysis helps to include mechanical solutions (radial ribs) to avoid rotor breakage, the insertion of radial ribs affects the magnetic behavior of the motor, so it affects the performance. Then, the optimization process must be start again including the mechanical solution to obtain the optimal design including mechanical, magnetic, thermal and electrical domains.

## 2.2 Methodology

The proposed methodology in this work aims at avoiding the use of FEA during the optimization stage, whereas extend the optimized operation to a wider operational speed/torque range. Figure 10 summarizes the workflow applied. To restrict the optimization possibilities and to accelerate the optimization process, the first step is the pre-design. The pre-design requires the features desired and the different restrictions, including the electric and thermal constraints, and the coolant characteristics. Pre-design provides a first motor geometry, using the well-known analytical equations and a simplified reluctance network, requiring a low computational burden. The pre-design solution is applied as a seed value during the GA-based optimization stage. Therefore, the optimization creates the range of the variables to optimize considering the obtained solution. The different candidates are generated with the variation of the motor's geometrical parameters, such as width of tooth, height of yoke, stack length, among others. The different motors are evaluated using coupled thermal and reluctance networks. These networks allow calculating the temperature and the magnetic behavior of the different candidates. Then, by evaluating the operating points of the machine considering realistic voltage and current limits, a cost function is evaluated within the operational range under study. After the optimization process, the optimized motor design is analyzed through FEA to validate the optimization process and to evaluate the mechanical integrity of the machine.

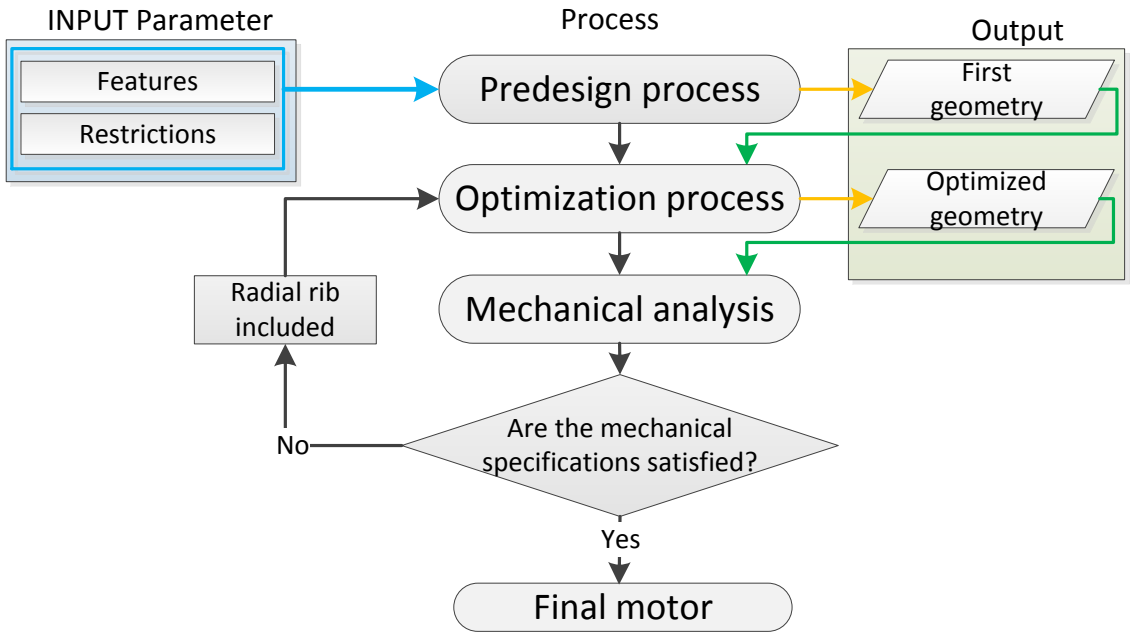


Figure 10. Design methodology workflow

It is worthy of mention that the range study realized in the optimization stage not only give relevant information about efficiency or power factor but also current angle or current module are obtained too. Then, the obtained results in the design process are the geometry of a motor according to several required features and behavior maps to feed a control based on lookup tables.

### 2.2.1 Pre-design

As former, the predesign step consists on an analytical set of equations to determine the first sizing of the machine in a few seconds. The further explanation of the pre-design is developed in *Section 3. Pre-design.* However, the workflow and some concepts are introduced in this sub-section.

The required data to obtain the first approach of the geometry can be classified in three main blocks. The first one is the features regarding the motor application, which can be divided in torque, speed, and power. The second one is the restrictions, which fix some parameters such as outer stator diameter, motor length, and maximum temperature, among others. Finally, the last block is the related to the known parameters generally done by the application, i.e. the bus DC, the number of poles, number of phases, among others. After the collection of all the mentioned information, the pre-design starts with the aim to obtain a first approach of the motor as can be observed in Figure 11.

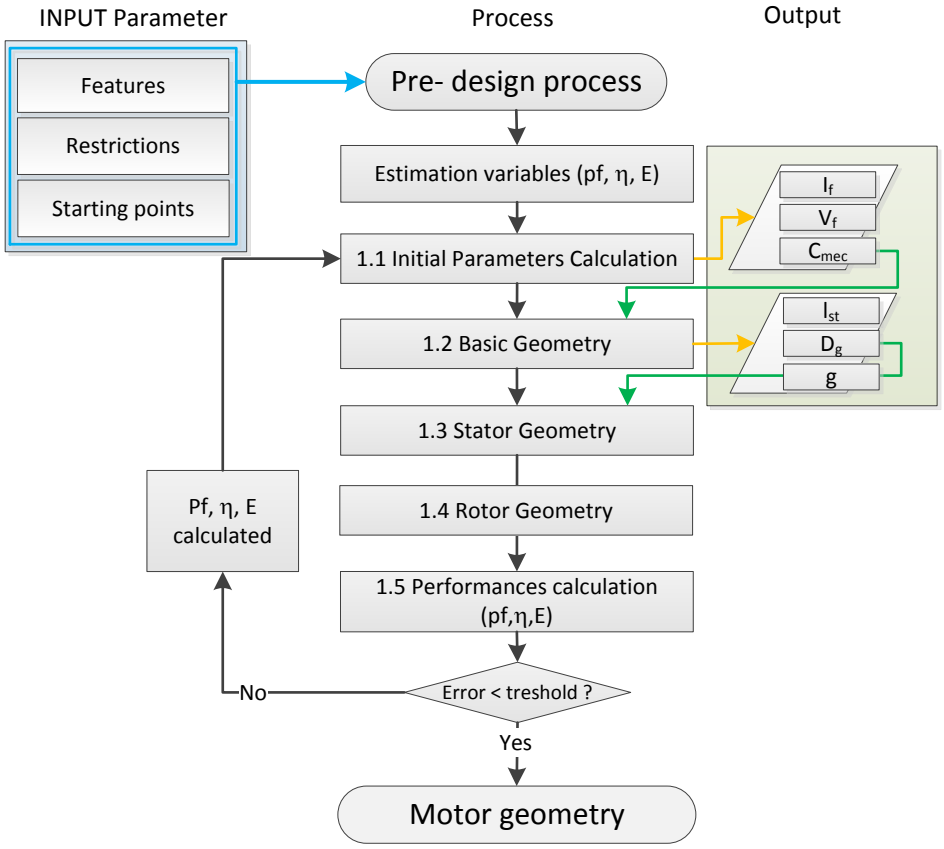


Figure 11. Pre-design workflow

The first step is estimating some parameters, such as power factor, efficiency, back EMF and airgap flux density. These values are estimated according to the experience. For instance, the power factor of the SynRM in the corner speed could be 0.7 or 0.85 in the case of PMa-SynRM. Then, the calculation of main parameters such as phase current and voltage or the mechanical constant (step 1.1 of Figure 11) are mandatory to size the slot size and the rotor volume respectively.

The mechanical constant allows calculating the stack length, and the inner stator diameter. Then using the required power the airgap length is obtained (step 1.2). After that, the stator geometry, which it is composed by the size of the tooth, slot, and yoke are calculated according to the thermal and

magnetic restrictions (step 1.3). Then, the rotor is determined (step 1.4) taking into account the rules to size the flux barriers and segments. It is worthy to mention that in this step several iteration loops are included to determine the inner rotor diameter as can be observed in *Section 3. Pre-design*.

In this point, the whole geometry is defined. However, this first motor approach has been calculated using several estimated parameters so the geometry can be improved. Therefore, a simple magnetic model is created to evaluate the motor performances and increase the accuracy of the estimated parameters (step 1.5). Using the calculated parameters the pre-design process can start again to obtain an accurate design.

### 2.2.2 Optimization

The geometry provided by the pre-design must be optimized according to the different criteria. For example, maximize the torque or power density, reducing the motor mass or maximize the efficiency. Furthermore, some restrictions must be considered such as power factor must be over pre-defined value, maximum temperature has to be lower than the insulator limit or achieve specific torque at different speeds.

Note that, the whole geometry of the machine can be considered as variable. It means, the stack length, inner and outer rotor diameter, inner and outer stator diameter, airgap length, and all the variables of the rotor and stator as can be observed in Figure 12.

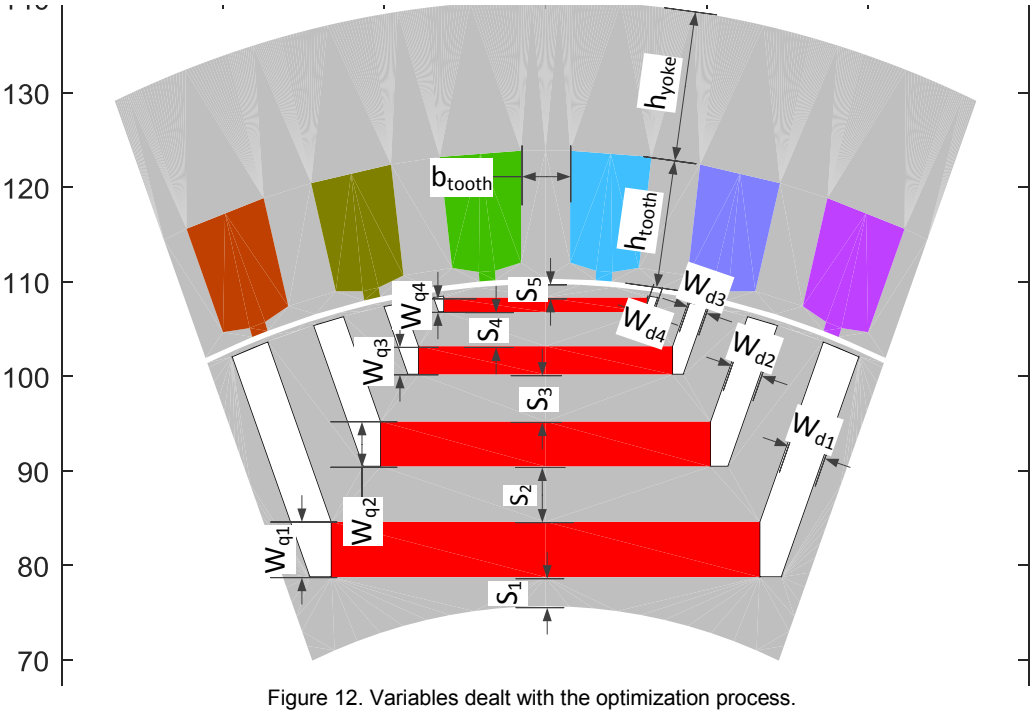


Figure 12. Variables dealt with the optimization process.

Considering the number of variables and multi-objective optimization the deterministic optimization methods can be disregarded since the complexity of the problem makes difficult the use of these optimization methods. In order to solve complex optimization problems involving even non-differentiable, discontinuous, highly nonlinear objective and constraint functions stochastic optimization method are best option [73].

These stochastic optimisation methods base in probabilistic and randomly mechanisms. This characteristic makes probably to obtain different solutions to the same problem. These methods have a big capability to found the global optimum. The major different with deterministic methods is that the stochastic methods do not need the initial point and do not need to know the gradient of the objective function. However, it requires a big number of iterations to obtain the solution.

The Genetic Algorithm (GA) is one of the stochastics methods and it is the used in this thesis to deal with the PMa-SynRM multi-objective optimization. GAs are heuristic search methods which attempt to approximate the mechanics of the natural selection and evolution process, offering powerful robustness and flexibility. They differ from traditional optimization techniques in several aspects, for instance GA allows parallelism in the searching process since multiple solutions can be considered concurrently [74]. GA is used for search problems or for finding optimal designs. For example, in [75] it is used to calculate the optimum phase current of multi-phase induction machine and in [76] GA is used for fault detection in induction machines.

A GA iteratively modifies a population of possible solutions of an optimization problem. The members of the population are often called individuals and they are described by a vector codification called chromosome. Over successive generations of the population, the individuals evolve towards an optimal solution. At each iteration, the algorithm selects individuals from the current population to be parents and uses them to calculate the children in the next generation. This is done using a set of rules named selection, crossover and mutation

The GA starts with an initial randomly generated population of individuals. After the initial population is selected, each individual is evaluated using a fitness function that associates a score to each individual. After that, the algorithm finds the best individual of the population by comparison of their score. If its score meets the stopping criteria, the algorithm halts and that solution is chosen. Else, the algorithm generates new individuals for the next generation, and continues to evaluate populations until the criteria is satisfied, combining parts of good individuals in order to improve the solution. The individuals are created following a selection rule, to select the individuals that will contribute to the next population, a crossover rule, to combine the selected individuals and form children, and a mutation rule, randomly changing the current individuals to generate new ones.

Then, according to the traction applications the optimization considering the whole operation area is required. For instance, the behavior of the motor based on the torque-speed range is evaluated under the conditions defined by a predefined driving cycle. For example, the WLTP driving cycle (worldwide harmonized light vehicles test procedure), a global driving cycle representing the typical usage of a vehicle in Europe. Figure 13 shows the acceleration and speed profiles according to this cycle.

The motor requirements are obtained taking into account different vehicle requirements, such as maximum speed or maximum torque and other vehicle parameters, including mass, gear box ratio, mechanical efficiency or drag coefficient among others .From the acceleration profile of the WLTP cycle and the vehicle characteristics found in [17], the operating points of the electric motor can be calculated. These characteristics are vehicle mass 1500 kg, gearbox ratio 8:1, gearbox efficiency 90%, wheel radius 25 cm, rolling coefficient 0.01, drag coefficient 0.4, and frontal area 1.85m$^2$. Figure

14 shows the torque-speed plane obtained by combining the requirements of the WLTP driving cycle and the vehicle.

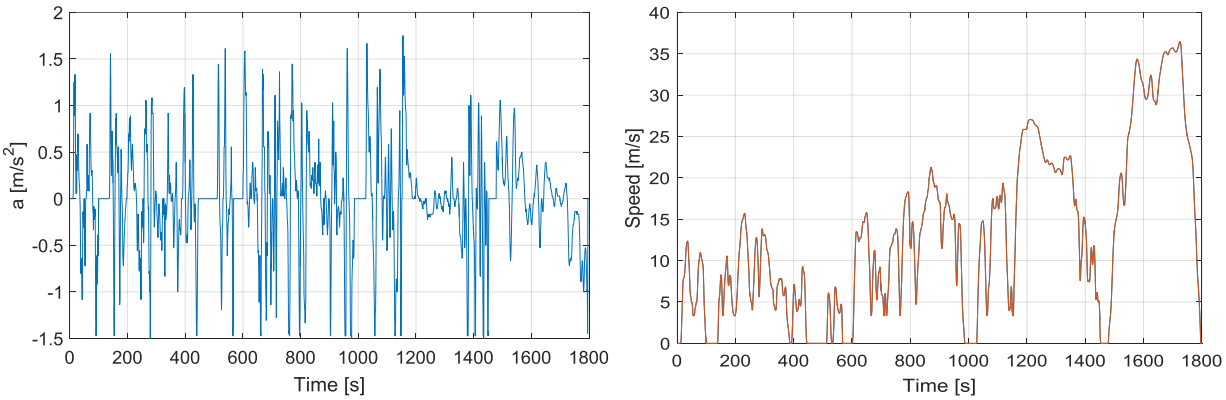


Figure 13. Acceleration and speed profiles of the WLTP driving cycle

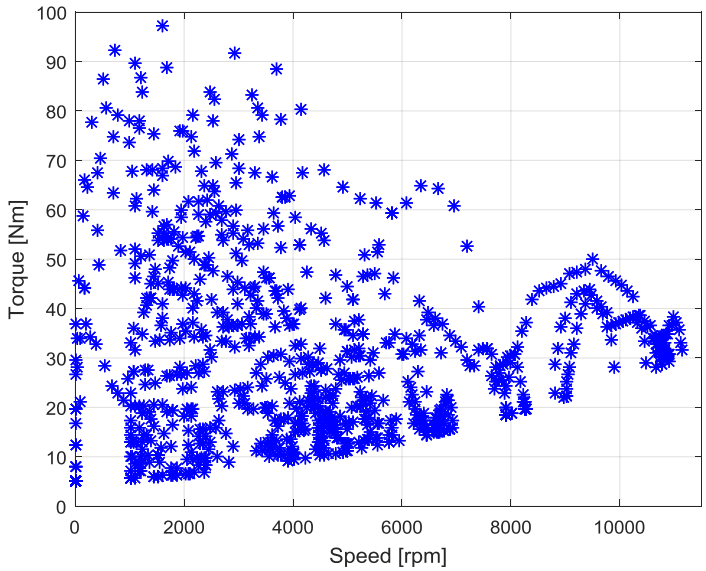


Figure 14. Torque-speed motor plane under the WLTP driving cycle

By analyzing the data represented in Figure 14, the motor features are obtained. The maximum torque at steady state conditions is 100 Nm, the power required is 45 kW and the torque at maximum speed is 37 Nm. Note that, methodology proposed allows evaluating different parameters, including the power factor, output power or the amount of permanent magnet required, among others. In this context, this example calculates the cost function as the arithmetic mean of the average efficiency, power factor and specific power. The average efficiency and power factor are evaluated by averaging the efficiency and power factor of the whole torque-speed plane of the WLTP driving cycle. Some torque restrictions are applied to ensure a correct match with the torque-speed plane shown in Figure 14. The proposed cost function applied to the optimization process is given by,

$$\max\left\{\eta_{avg} + cos\varphi_{avg} + \frac{sp}{sp_{pre-design}}\right\}$$

subject to $T_{max} > 100\ Nm, T_{9.000\,rpm} > 50\ Nm$ and $T_{11.000\,rpm} > 40\ Nm$ .

where "$\eta_{avg}$" is the average efficiency in the whole torque-speed range, "$cos\varphi_{avg}$" is the average power factor in the whole torque-speed range, and "$sp$" is the specific power represented as the ratio power per mass.

It is noted that because of the inherent restrictions of traction applications, electric vehicles require motors with high specific power, efficiency and power factor, this latter being very important to reduce the input current and thus power losses and the size of the inverter. It is worthy to mention, that this cost function is only an example and can be adapted depending on the application.

Then, the proposed methodology aims to optimize the PMa-SynRM considering all the working points, so the use of FEM in the optimization process must be avoided. In this context, several multi-physics models are developed to estimate the behavior of the machine in terms of thermal, magnetic, and electrical domains. The details of the different models and results are detailed in the following sections; *Section 4. Magnetic model, Section 5. Thermal model, and Section 6. Behavior maps calculation.*

The optimization workflow is shown in Figure 15. It should be noted that after the optimization the solution obtained must be evaluated in terms of mechanical analysis.

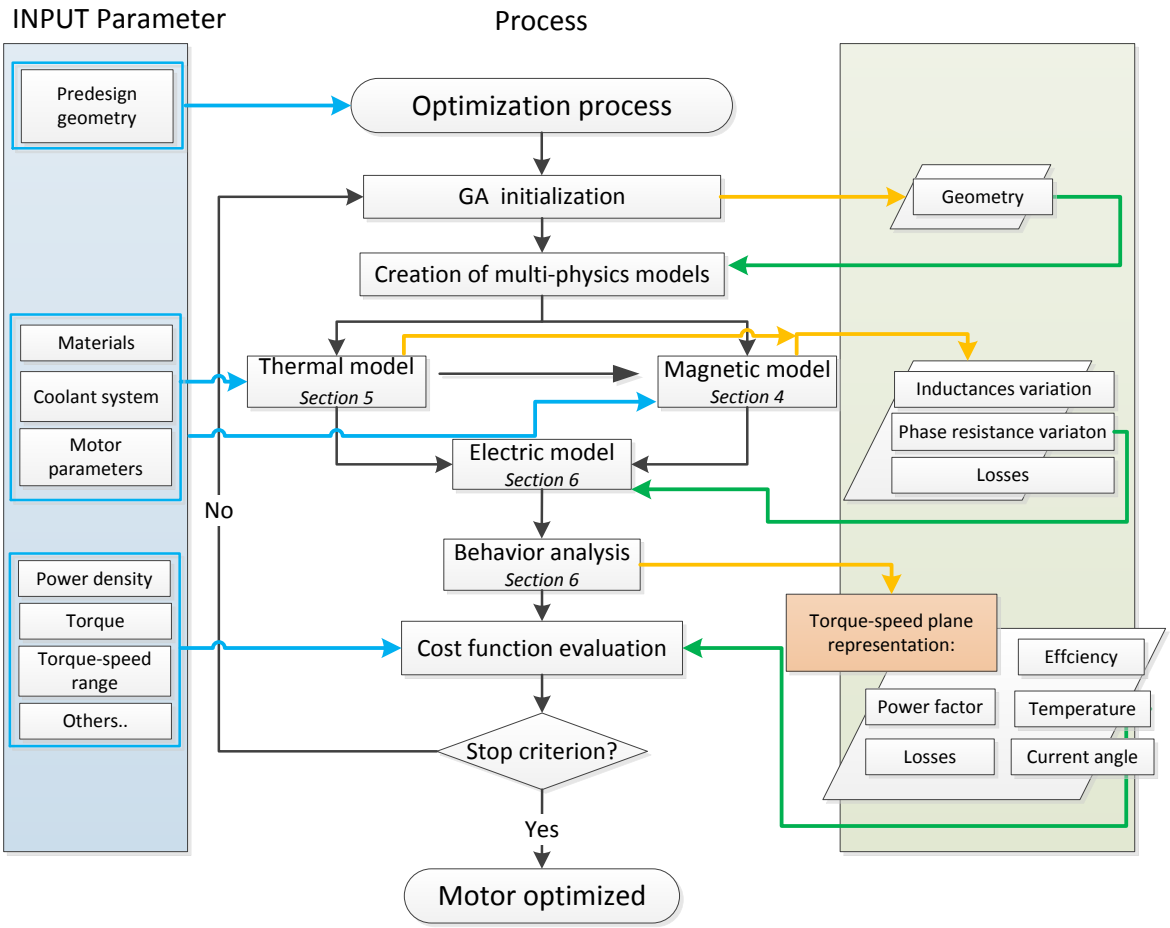


Figure 15. Optimization workflow

### 2.2.3 Mechanical analysis

The mechanical analysis is required to validate the mechanical behavior of the machine. The rotor structure and the magnets make difficult the use of analytical equations to determine the mechanical stress of the machine, so it is calculated by using FEA. This analysis is carried out after the optimization process, to speed up the optimization part of the methodology. If the mechanical stress is greater than the limit of the material, several radials ribs must be included in the geometry to increase the mechanical integrity of the rotor. Since the magnetic behavior of the machine changes when the radial ribs are introduced, new optimization iteration is required to determine the final design. In this new iteration, the calculated radial ribs are constrains, i.e. they cannot change during this optimization iteration.

Figure 16 shows an example of the Von Mises analysis of the rotor of the final design when rotating at maximum speed. The magnets, which are located inside the flux barriers, are represented as distributed mass on the exterior surface of the flux barrier, to simulate the worst case scenario. Due to the symmetry of the problem and to speed up the process, this simulation is applied to only one magnetic pole.

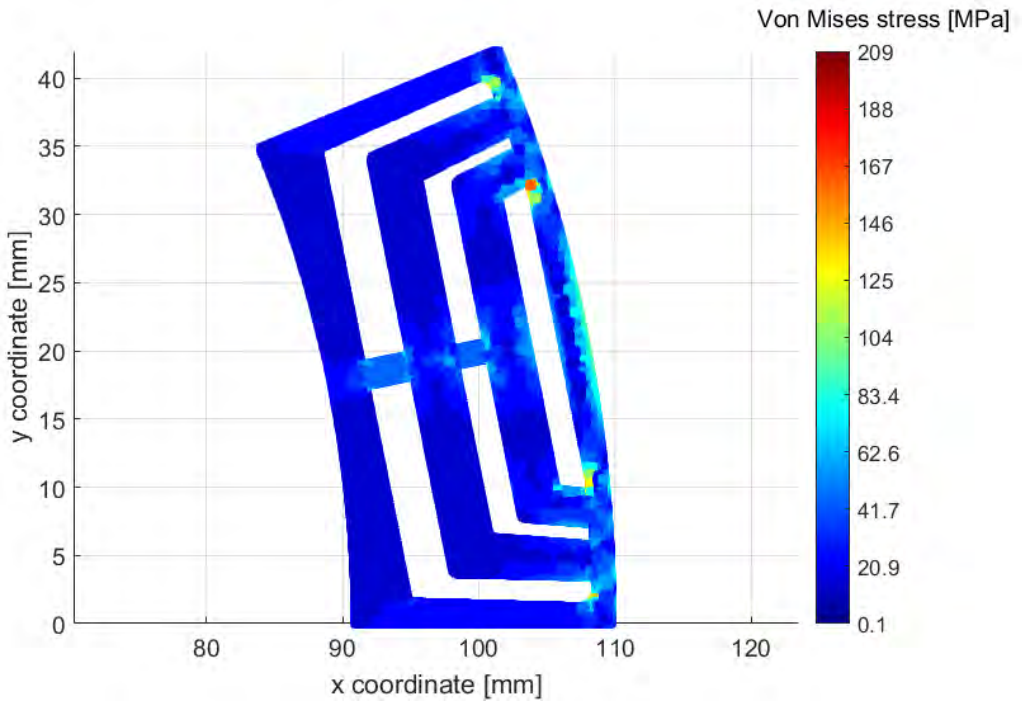


Figure 16. Example of a Von Misses analysis

As can be observed in Figure 16, the maximum stress appears in the corner of the last barriers, which is below 210 MPa. For example, the yield strength of the material M330-35A is 300 MPa, so the security coefficient is 1.4.

# 3.

# Pre-design

This chapter aims to explain the analytic procedure to obtain the electro-magnetic pre-design of PMaSynRM.

*CONTENTS:*

# 3. Pre-design

## 3.1 Introduction

Electrics motors for traction applications have been optimized in terms of power and torque density, efficiency, cost, power factor, and wider speed range. There are different motor topologies to meet the requirements for such application, for instance, permanent magnet synchronous motors (PMSM), induction motors (IM), switched reluctance motors (SRM), and synchronous reluctance motors (SynRM). PMSMs have the best power density ratio and can maintain the power in a wide speed range. However, the material cost due to the rare-earth magnets and concerns about availability and supply of the magnets makes it necessary to use other type of motors. In this context, the concept of rare-earth-free-motors gains attention [15]. Synchronous reluctance motors are good candidates in terms of material and manufacture cost, however the power density and power factor are low. Then, the idea of permanent magnet assisted synchronous reluctance motors (PMa-SynRM) appears, since they improve the performances of SynRMs by using magnets.

The design of a motor usually consists of a multi-physics analysis where the thermal, electric, magnetic, and mechanic domains are analyzed. In the electromagnetic pre-design stage, the geometry of the machine is often calculated based on criteria that take into account different domains. The electromagnetic domain allows calculating the necessary amount of the magnet, the thermal domain settles the size of the slots of the stator, and the mechanical domain settles the size of the radials ribs.

The final geometry of the motor is obtained after an optimization process, where the values of the motor's parameters are variated to determine the best solution. However, the starting point of the design is based on the electro-magnetic pre-design. This work aims at guiding the electro-magnetic pre-design of the PMa-SynRM.

The pre-design is performed with the basic specifications of the machine, such as mechanical power, corner speed, phase current, pole number, or efficiency required, among others. Since FEA is often not applied to speed up the design process, the parameters are calculated must by using analytical equations and several refinement loops are introduced. In this context, the whole process, which is summarized in Algorithm 1, is a combination of analytical equations with iterative loops to refine the estimated parameters, which are required to start the electro-magnetic pre-design.

The starting point consist on estimating some parameters, such as efficiency, power factor, airgap flux density or back EMF, in order to determine the required phase current, electrical power or number of turns per phase, among others. These estimated values depend on the machine type, for instance in the SynRM the power factor can be selected around 0.7, and the efficiency around 95%, and they are normally based on experience and rules-of-thumb.

## 3.2 Calculation of Electrical parameters

The pre-design starts calculating some electrical parameters, such as the electrical power required (1), phase current (2), or number of turns (3).

The initial set of equations is given by;

$$P_e = \frac{P_{mec}}{\eta} \quad (1)$$

Where, "$P_{mec}$" is the output mechanical power, which is one of the inputs of the electro-magnetic pre-design, "$\eta$" is the estimated efficiency, and "$P_e$" is the required electrical power. Using the electrical power calculated in (1), the phase current is given by;

$$I_f = \frac{P_e}{mU_f \cos(\varphi)} \quad (2)$$

Being, "$m$" and "$U_f$" are the number of phases and the RMS phase voltage, respectively, which are inputs, and "$\cos(\varphi)$" is the estimated power factor.

To finalize with the electrical part of the design, the number of turns per phase can be calculated according to (3).

$$N_s = \frac{\sqrt{2}E}{\omega_e k_{w1} l_{eff} \tau_p \frac{D_{is}}{2} \alpha_i \hat{B}_g} \quad (3)$$

Where, "$E$" is the back EMF, which is estimated according to 0.97 of the phase RMS voltage [77], "$\omega_e$" is the mechanical speed in electrical rad/s of the base point, "$l_{eff}$" is the effective length of the machine, "$\hat{B}_g$" is the peak flux density in airgap, which is an estimated value, "$k_{w1}$" is the winding factor of the fundamental component, which is fixed by the winding distribution, "$\alpha_i$" is the coefficient to obtain the arithmetical average of the flux density, "$D_{is}$" is the inner stator diameter, and "$\tau_p$" is the slot pitch.

Considering a sinusoidal flux density, the value of "$\alpha_i$" is 0.64 ($2/\pi$). However, "$\alpha_i$" is related in [77] with the saturation factor the machine ($k_{sat}$). The saturation factor is obtained taking into account the magnetic saturation of the rotor and stator, so the first value is estimated. The saturation factor is given by;

$$k_{sat} = \frac{U_s + U_r}{U_g} \quad (4)$$

Being, "$U_s$", "$U_r$", and "$U_g$" the magnetic potential of the stator, rotor, and airgap respectively.

Note that the effective length and the pole pitch cannot be determined since the airgap volume is unknown. The mains dimensions must be calculated before the number of turns per phase.

## 3.3 Main dimensions

The first step to calculate the motor geometry is the determination of the main dimensions of the motor. These parameters are the outer and inner diameter of the rotor, the outer and inner diameter of the stator, and the stack length. It is worthy to mention that depending on the restrictions of the application, the outer dimensions can be fixed. Figure 17 shows several motor's parameters, such as inner and outer rotor radius ($R_{ir}$ and $R_{or}$, respectively), inner and outer stator radius ($R_{is}$ and $R_{os}$, respectively), air gap length ($g$), slot pitch ($\tau_s$), and pole pitch ($\tau_p$). The stack length ($L_{stk}$) is the length of the active part, i.e. the end winding length is not considered.

The calculation of the motor's geometry starts determining the air gap volume/surface or the outer volume/surface of the machine. In this context, different approaches can be found in the literature to calculate the motor geometry using the data obtained from the specifications. On the one hand, [78] and [79] calculate the exterior geometry, which is represented by the outer stator diameter and the stack length. The first one uses a relation between the torque generated and the volume ($K_v$) meanwhile the second one relates the losses generated with the outer surface ($K_j$). According to [78] the $K_v$ for these kind of machines is around 10 Nm/L. However, these values can change depending on the value of the torque. In the second approach the thermal loading depends on the coolant system, so it is required to determine the outer motor geometry. If the outer geometry is fixed, the thermal loading determines the coolant system required [80]. On the other hand, the electrical loading ($A$) is used to calculate the geometry of the airgap [81]. In this case, the allowed electrical loading is also determined by the coolant system. Another interesting approach relates the mechanical power of the machine with the airgap volume.

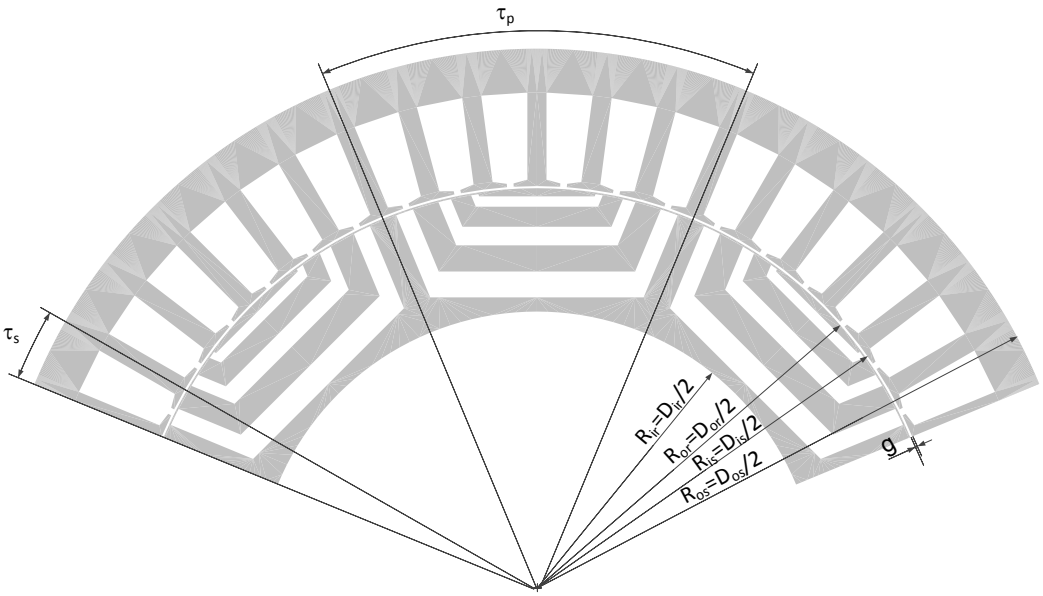


Figure 17. Motor basic geometry

This approach is based on the mechanical constant [77, 82], which is given by;

$$C_{mec} = \frac{P_{mec}}{D_{is}^2 l_{eff} n_{syn}} \quad (5)$$

Where, "$n_{syn}$" is the rated electrical frequency.

The proposed pre-design starts with the mechanical constant, so a further explanation of the different values of such constant is required. The value of the mechanical constant is obtained analyzing several motor of the same typology and coolant systems. Figure 18, extracted from [15], shows the relation between the mechanical constant and efficiency for different motor types. The shown motor types are Wounded Field Flux Switching Machines (WFFSM), Switched Reluctance Machines (SRM), Permanent Magnet assisted Synchronous Maachines (PMa-SynRM), Ferrite Permanent Magnet Flux Switching Maachines (Ferrite PMFSM), Permanent Magnet Synchronous Machine (PMSM), and Squierrel Cage Inudction Machine (SCIM).

Note that, the same motor families tend to be grouped in the same region of the plane. However, there are divergences, which can be due to the coolant system or the number of poles. The mechanical constant is not only grouped by motor typologies and coolants but also by the number of poles as can be observed in Figure 3 [77].

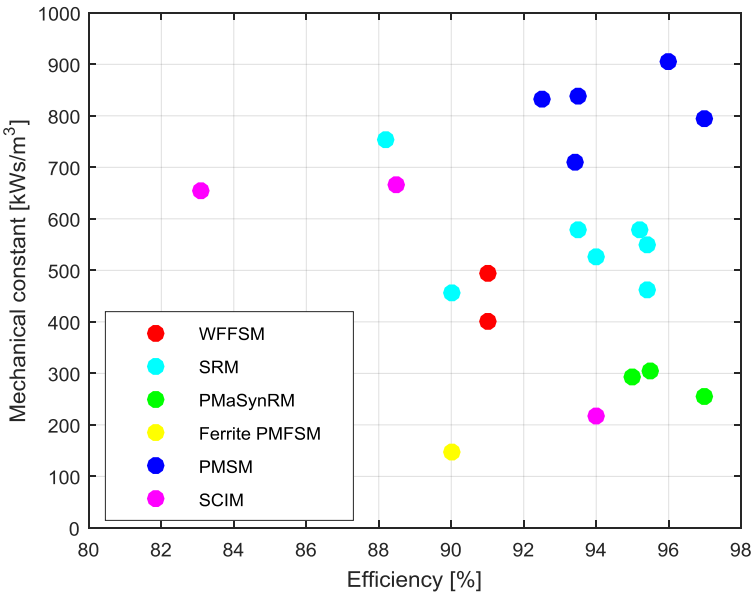


Figure 18. Machines comparison based on the maximum efficiency point and machine constant of mechanical power. Data presented have been collected from [38, 41, 43, 56, 61, 83-94].

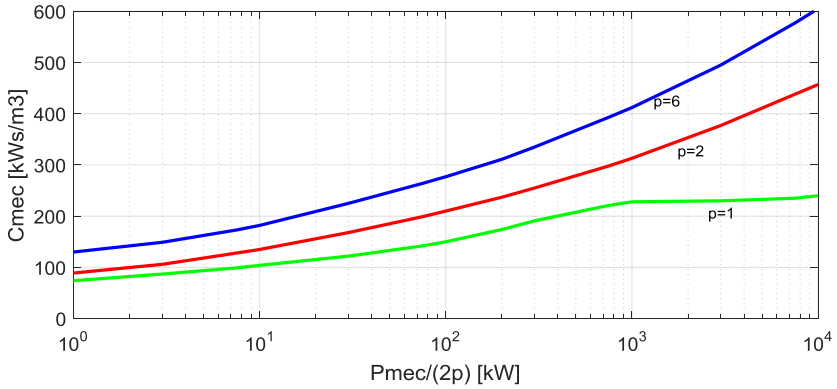


Figure 19. Curve of the mechanical constant of totally enclosed induction motors with the mechanical power per pole.

Nevertheless, when using the electrical loading, mechanical constant, or other parameters to obtain the volume or surface of the airgap, the relation between diameter and length is required. The form factor "$X$" is given by;

$$X \approx \frac{\pi}{4\sqrt{p}} \quad (6)$$

"$p$" being the number of pole pairs.

Using (5) and (6) the effective length $l_{eff}$ and the bore diameter $D_{is}$ can be calculated. The stack length is obtained according to;

$$L_{stk} = l_{eff} - 2g \quad (7)$$

In order to maximize the saliency ratio, the airgap thickness must be as low as possible [78]. According to [77], the airgap should be smaller compared to induction machines. The airgap in induction machines is given by;

$$g = \frac{0.18 + 0.006P_{mec}^{0.4}}{1000} \quad (8)$$

Where, "$P_{mec}$" is given in watts.

## 3.4 Stator geometry

The stator geometry is completed when the size of the slot, teeth, and yoke are determined. The width of the teeth ($b_t$) and slots ($b_s$) can be constant or radial as can be observed in Figure 20A. However, some simplifications can be realized in order to determine the size of these parts. Figure 20B shows the geometry of the teeth and slots using the smaller dimension, which it is the most restrictive width. The yoke height ($h_y$) is the space between the outer stator radius and the end of the slots. The slot opening ($S_o$) is dimensioned to be higher than the diameter of the conductors. The height of the slot ($h_s$) is shown in Figure 20B. Finally, the height of tooth tip ($h_{tip}$) is not important in this stage of the design, although it can be fixed at 1 mm, depending on the machine. In the same way, the "Δ" is not important in the pre-design and can be fixed at 0.5mm depending on the machine.

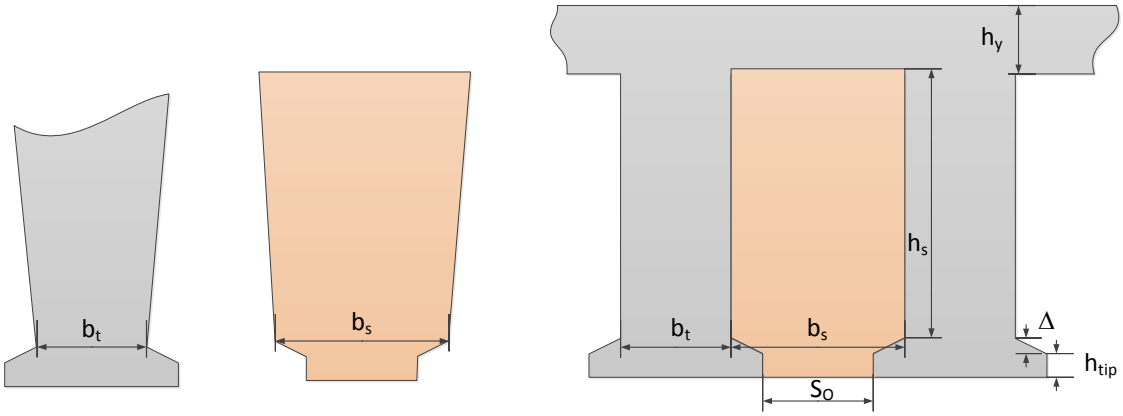


Figure 20. A) Tooth and slot radial geometry. B) Approximate geometry using the most restricted dimensions

In order to calculate the size of the slots, the number of conductors in each slot and the tooth size are required. Then, (3) can be solved since the pole pitch is known. When the number of turns in series per phase is calculated, the number of conductors in each slot ($z_q$) can be determined as follows;

$$z_q \approx \frac{2mN_{ph}}{Q_s} \quad (9)$$

Being, "$m$" is the number of phases and "$a$" is the number of parallel paths.

Note that, "$z_q$"must be an integer, so the result obtained needs to be round to obtain the final number of conductors in each slot. Then, the number of turns in series per phase must be updated as,

$$N_{ph\_new} = \frac{z_q Q_s}{2m} \quad (10)$$

In this point, the estimated flux density within the airgap changes, so it is calculated as;

$$\hat{B}_{g\_new} = \frac{\sqrt{2}E}{\omega_e k_{w1} l_{eff} \tau_p \frac{D_{is}}{2} \alpha_i N_{ph\_new}} \quad (11)$$

Considering a sinusoidal magnetic flux distribution within the airgap and how this magnetic flux distributes through the stator, the size of the teeth and yoke are calculated to obtain a magnetic saturation below a pre-defined value.

The teeth have to be sized to withstand the magnetic flux that comes from the airgap. The magnetic flux will enter in the teeth instead of the slots, so the magnetic flux in the pole is divided in the different teeth. However, the teeth are dimensioned considering the worse scenario. Figure 21 shows the magnetic fluxes lines of air gap entering in the teeth. The sinusoidal magnetic flux density is superimposed to understand the different quantity or density of magnetic flux (blue arrows) in both teeth. Then, the width of teeth is calculated considering the teeth with higher magnetic flux.

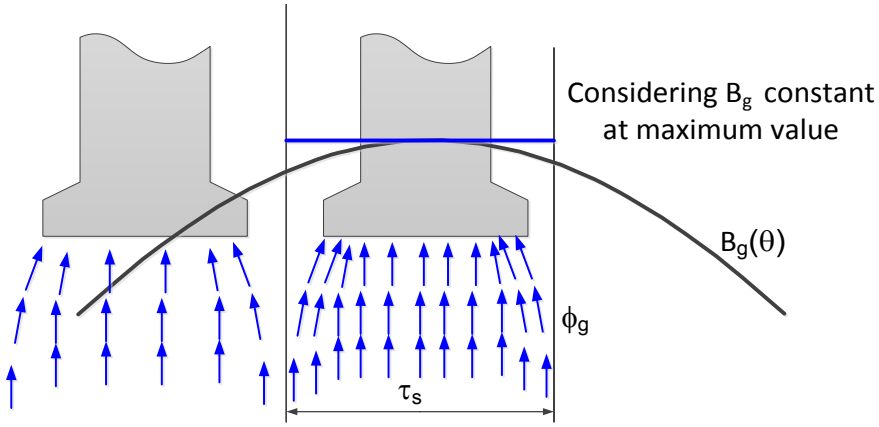


Figure 21. Detail of the magnetic flux in the airgap entering in the tooth

Furthermore, in order to oversize the teeth, the magnetic flux density is considered constant at the maximum value as can be observed in Figure 21 (blue line in the teeth). Therefore, the estimated magnetic flux in this tooth is given by;

$$\phi_t = \hat{B}_{g\_new} l_{eff} \tau_s \frac{D_{is}}{2} \quad (12)$$

Where, "$\tau_s$" is the slot pitch, which is given by;

$$\tau_s = \frac{2\pi}{Q_s} \quad (13)$$

"$Q_s$" being the number of slots.

In order to obtain a correct size of teeth, the maximum allowed magnetic flux density on this motor part is fixed between 1.5-1.8 T, which depends on the magnetic material of the shape. Therefore;

$$b_t = \frac{\phi_t}{k_{sf} \hat{B}_t L_{stk}} \quad (14)$$

Where, "$\hat{B}_t$" is the maximum allowed magnetic flux density and " $k_{sf}$" is the stacking factor.

On the other hand, the yoke's width must be calculated to drive half of the airgap's magnetic flux on one magnetic pole as can be observed in Figure 22.

Then, the magnetic flux in the airgap is calculated as follows;

$$\phi_g = \frac{2}{\pi} \hat{B}_{g\_new} l_{eff} \tau_p \frac{D_{is}}{2} \quad (15)$$

Where, the term "$2\hat{B}_g/\pi$" is to obtain the average value of a sinusoidal waveform, and "$\tau_p$" is the pole pitch, which are calculated as follows;

$$B_{g\,av} = \frac{1}{\pi}\int_0^{\pi} \hat{B}_{g\_new}\sin(\theta)d\theta = \frac{1}{\pi}\hat{B}_{g\_new}(-\cos(\pi)+\cos(0)) = \frac{2}{\pi}\hat{B}_g \quad (16)$$

$$\tau_p = \frac{2\pi}{2p} \quad (17)$$

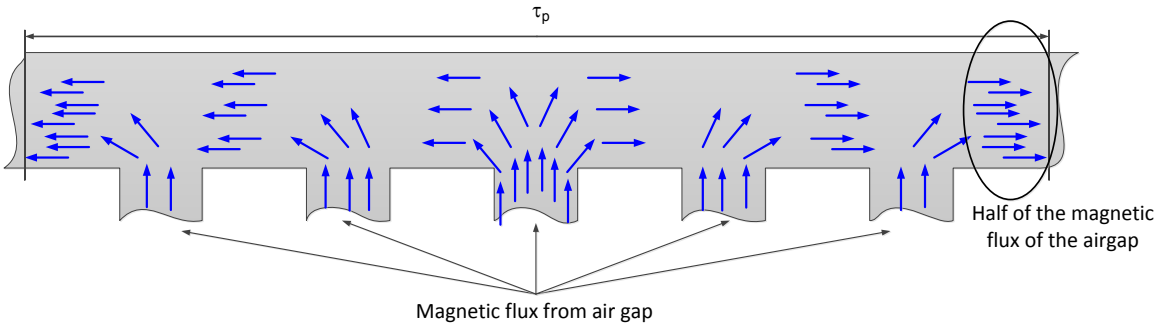


Figure 22. Detail of the magnetic flux in the yoke

Then, the width of the yoke is;

$$h_y = \frac{\phi_g}{2k_{sf}\hat{B}_y L_{stk}} \quad (18)$$

Where, "$\hat{B}_y$" is the maximum allowed magnetic flux density in yoke, which is fixed between 1.4-1.6 T.

According to Figure 20B, when the width of the teeth is kwon, the slot's width can be determined as;

$$b_s = \tau_s \frac{D_{is}}{2} - b_t \quad (19)$$

Then, height of the slot is determined by;

$$S_{slot} = b_s h_s = \frac{z_q I_{ph}}{J k_u} \rightarrow h_s = \frac{z_q I_{ph}}{J k_u b_s} \quad (20)$$

Where, "$J$" is the current density [A/m$^2$] and variates with the coolant system [77, 81] and "$k_u$" is the winding factor, which can be fixed at 0.40.

The height of the teeth is given by;

$$h_t = h_s + h_{tip} + \Delta \quad (21)$$

where $h_{tip}$ has been selected beforehand.

Then, the outer stator diameter is obtained as;

$$D_{os} = D_{is} + 2h_t + 2h_y \quad (22)$$

## 3.5 Rotor geometry

The rotor of the SynRMs is punched to create the anisotropy in TLA design. The insulation, which is the air cavity created in the rotor's perforation, is called flux barrier. The magnetic steel material between flux barriers is called segment or flux carrier. The rotor structure is completed by ribs; there are two different ribs. The first one is the tangential rib, which connects the segments. The other type is the radial rib, which increase the mechanical integrity of the machine. The mentioned parts are depicted in Figure 23.

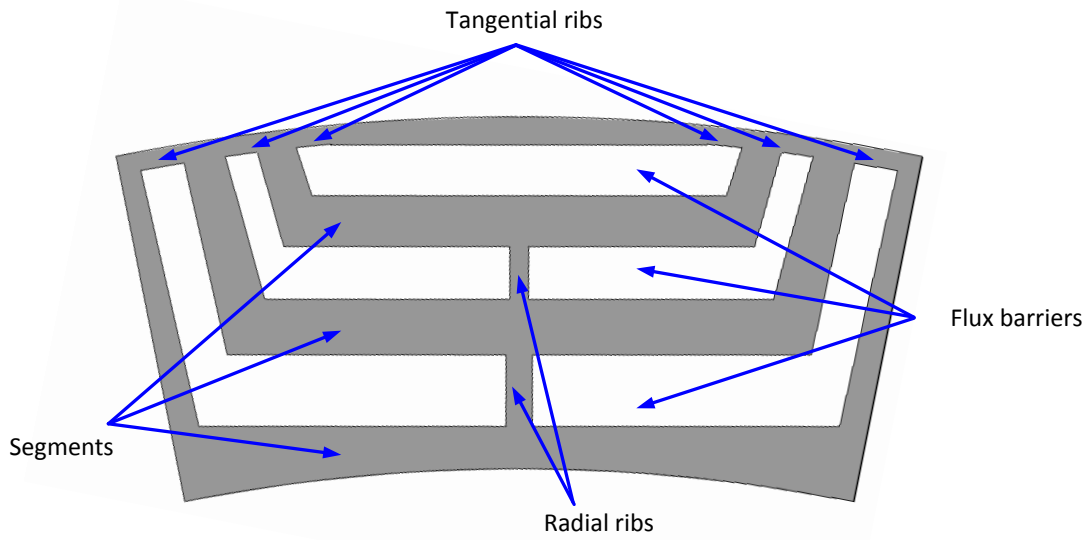


Figure 23. Basic geometry of the rotor of SynRM

A good saliency ratio can be enhanced by a correct design of the rotor [95]. It starts choosing the proper number of flux barriers [59, 78, 96, 97], which is given by;

$$k = \frac{Q_s}{2p} \pm 2 \qquad (23)$$

Note that according to (23) there are two possibilities for *k*. The choice depends on the application or the rotor size.

Then, the positioning of the barriers is realized to obtain a good distribution of the magnetic flux, i.e. a reduction of the torque ripple. The ripple reduction is obtained by means of an optimization process, where the angle of the barriers is changed to find the best solution [98-100]. However, during the pre-design stage, the angle between the end points of the barriers is fixed according to [97, 101];

$$\alpha_i = \frac{\pi/p}{k+1} \qquad (24)$$

Note that (24) calculates the angle between barriers. The angle between the last barrier and the pole center is $3\alpha_m/2$ as can be observed in Figure 24.

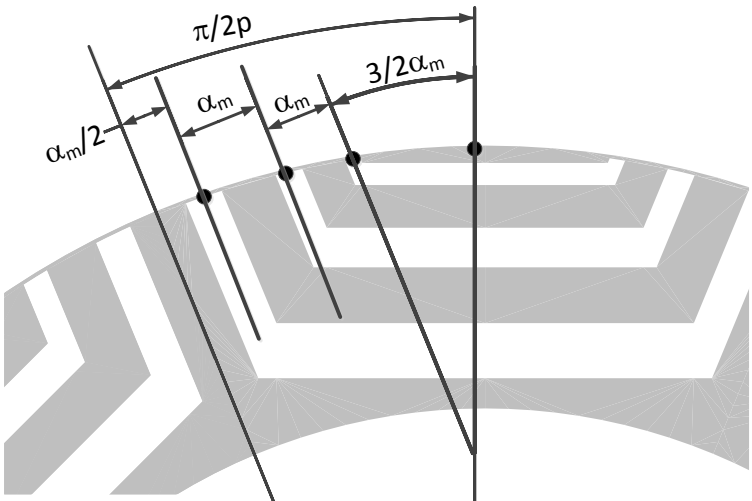


Figure 24. Barriers positioning during the pre-design

The magnetic flux flows through the segments, so a correct sizing is mandatory. Note that the low reluctance of the magnetic steel is related to the magnetic saturation of the segments. Then, the calculation of the width of the flux carriers considers the rotor position with the highest magnetic flux. In this position, which it is called direct axis (d-axis), the maximum magneto-motive force (MMF) in the stator is located between the magnetic poles, meanwhile the zero MMF is in the middle of the magnetic pole, as can be observed in Figure 25. It is worthy to mention that the MMF is considered sinusoidal in order to simplify the calculation of the rotor's geometry.

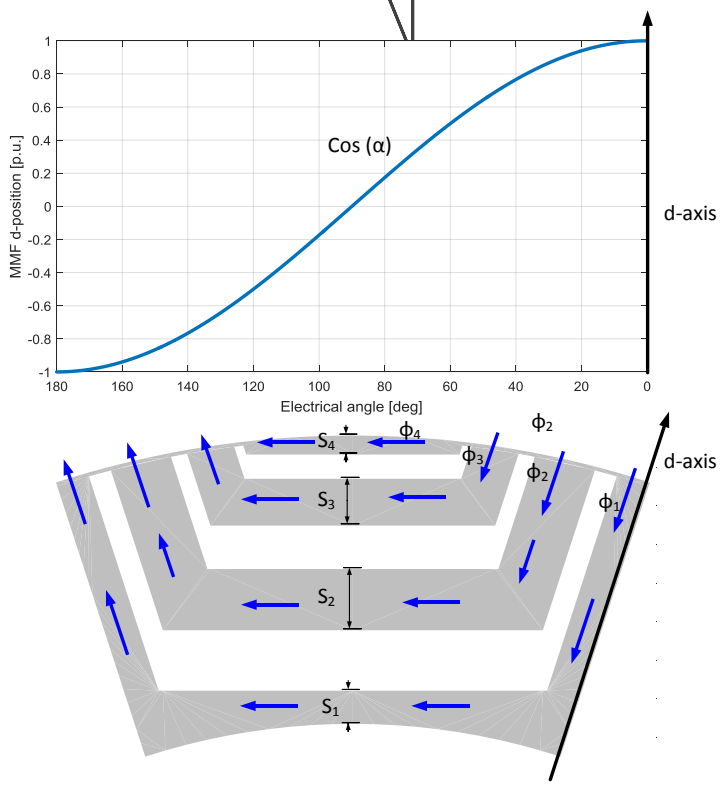


Figure 25. MMF distribution in the d-position. The blue arrows represent the magnetic flux in the rotor.

The widths of the different the segments ($S_i$) are dimensioned to obtain the same magnetic saturation in each segment. In order to estimate the magnetic saturation, the magnetic flux (φ) must be calculated. Considering the geometry shown in Figure 25, an equivalent magnetic circuit can be built to determine the relation between the magnetic fluxes, as depicted in Figure 26. Only one half of the pole is represented due to the magnetic symmetry.

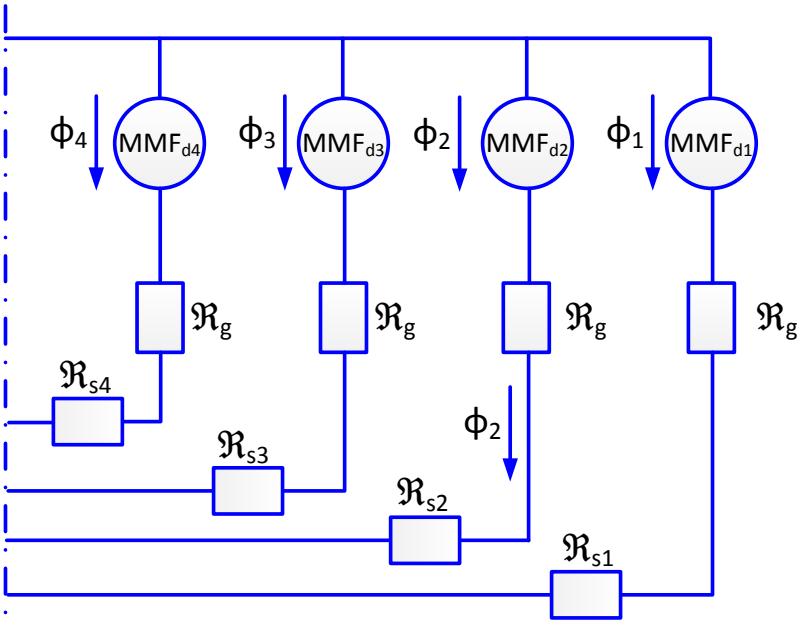


Figure 26. d-axis equivalent magnetic circuit used to determine the width of the segments

Note that the reluctance of the airgap is much bigger than the segments' reluctances, so the latter can be disregarded. Then, the magnetic fluxes are given by;

$$\phi_i = \frac{MMF_{di}}{\Re_g} \tag{25}$$

Therefore, the value of fluxes depends on the MMF. The MMF of each segment is represented by stairs function where the value is the average value of the MMF distribution shown in Figure 25. Since all position angles of the barriers have been fixed, the average MMF of each segment can be calculated as follows;

$$MMF_{di} = \frac{\int_{\frac{2i-3}{2}p\alpha_i}^{\frac{2i-1}{2}p\alpha_i} \cos(\alpha)\, d\alpha}{p\alpha_i} = \frac{\sin\left(\frac{2i-1}{2}p\alpha_i\right) - \sin\left(\frac{2i-3}{2}p\alpha_i\right)}{p\alpha_i}$$
$$MMF_{dn_b+1} = \frac{\int_{\frac{2n_b-3}{2}p\alpha_i}^{\frac{\pi}{2}} \cos(\alpha)\, d\alpha}{p\frac{3}{2}\alpha_i} = \frac{1 - \sin\left(\frac{2n_b-3}{2}p\alpha_i\right)}{p\frac{3}{2}\alpha_i} \tag{26}$$

Then, taking into account (25), where the flux is proportional to the MMF, and the condition of obtaining an equal magnetic saturation on each segment, the relation of segment's width is given by;

$$\frac{S_i}{S_{i+1}} = \frac{MMF_i}{MMF_{i+1}} \tag{27}$$

The magnetic saturation is calculated using the magnetic flux and the cross section, so (28) is deducted as follows;

$$B_i = \frac{\phi_i}{S_i L_{stk}} \rightarrow B_i = B_{i+1} \rightarrow \frac{\phi_i}{S_i L_{stk}} = \frac{\phi_{i+1}}{S_{i+1} L_{stk}} \rightarrow \frac{\frac{MMF_{di}}{\Re_g}}{S_i L_{stk}} = \frac{\frac{MMF_{di+1}}{\Re_g}}{S_{i+1} L_{stk}} \quad (28)$$

In addition, is worthy to mention that (27) must be adapted in segment 1, since the magnetic flux is divided in the two magnetic poles, so the final equation to determine the relationship between $S_1$ and $S_2$ is given by;

$$\frac{2S_1}{S_2} = \frac{MMF_1}{MMF_2} \quad (29)$$

Finally, there are one more unknowns that equations, so one more equation is required to find out the width of the segments. Since the width of all the segments is equal to the total iron length in the rotor, the last equation results in;

$$L_s = \sum_{i=1}^{i=nb+1} S_i = \frac{h_{rotor}}{1 + k_{insq}} \quad (30)$$

Where, "$h_{rotor}$" is calculated as $h_{rotor} = (D_{or} - D_{ir})/2$, and "$k_{insq}$" is the insulation ratio in the q-axis. Note that "$k_{insq}$" , which has values around 1 [77], is defined by;

$$k_{insq} = \frac{L_a}{L_s} \quad (31)$$

"$L_a$" being the total length of width of air in the rotor given in (38) in the q-axis and "$L_s$" is the t width of all the segments of magnetic steel along the q-axis.

On the other hand, the flux barriers must be designed to offer a large magnetic resistance to the flow of the magnetic flux. In this context, the sizing of the flux barriers is carried out when the magnetic flux is positioned in the quadrature position, as can be observed in Figure 27.

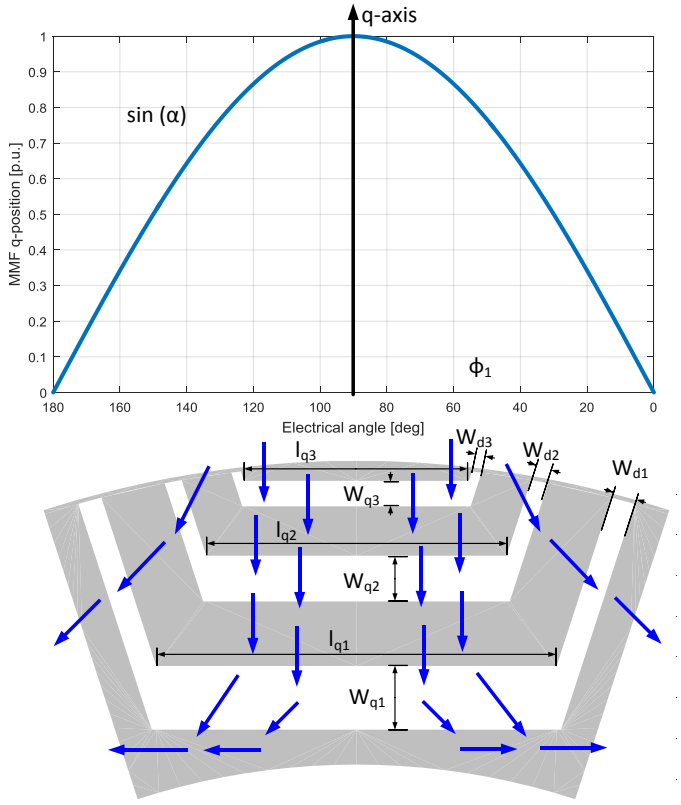


Figure 27. MMF distribution in the q-position. The blue arrows represent the magnetic flux in the rotor.

The correct sizing of the flux barriers is necessary to obtain a high anisotropy, to improve the performances of the machine. As can be observed in Figure 27, not the same number of magnetic blue arrows crosses the different barriers. Then, the size of the barriers varies according to the MMF drop in each barrier.

The MMF distribution in the q-position is calculated as in the d-position, i.e. using the average value of the MMF considering a sinusoidal distribution, as shown in Figure 27. In this case the MMF is given by;

$$MMF_{qi} = \frac{\int_{\frac{2i-3}{2}p\alpha_i}^{\frac{2i-1}{2}p\alpha_i} \sin(\alpha)\, d\alpha}{p\alpha_i} = \frac{-\cos\left(\frac{2i-1}{2}p\alpha_i\right) + \cos\left(\frac{2i-3}{2}p\alpha_i\right)}{p\alpha_i}$$
$$MMF_{qn_b+1} = \frac{\int_{\frac{2n_b-3}{2}p\alpha_i}^{\frac{\pi}{2}} \cos(\alpha)\, d\alpha}{p\frac{3}{2}\alpha_i} = \frac{\cos\left(\frac{2n_b-3}{2}p\alpha_i\right)}{p\frac{3}{2}\alpha_i} \quad (32)$$

Figure 28 depicts the equivalent magnetic circuit in the q-position to calculate the size of the different flux barriers.

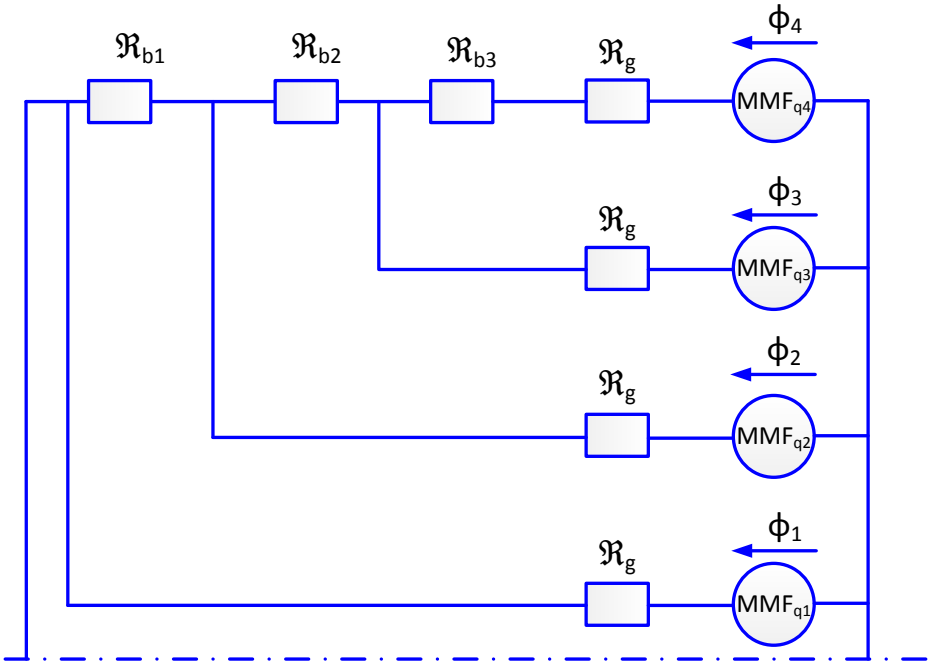


Figure 28. q-axis equivalent magnetic circuit to determine the width of flux barriers

Note that the $MMF_{q1}$ is zero, so the path of flux 1 can be removed. As can be observed, the magnetic flux in the q-axis is given by the addition of fluxes 1 to 4. Then, the purpose of the barriers' sizing is to minimize the q-flux. Then, the relation between the widths of each barrier is given by;

$$\frac{W_{qi}}{W_{qi+1}} = \frac{MMF_{i+1} - MMF_i}{MMF_{i+2} - MMF_{i+1}} = \frac{\Delta MMF_i}{\Delta MMF_{i+1}} \quad (33)$$

A demonstration of the procedure to obtain (33) is further developed. However, the following example is realized with two barriers for the shake of simplification. Figure 29 shows a rotor with two flux barriers, the magnetomotive force in each segment, which have been calculated with (32), and the variable to optimize, which is the size of the first barrier.

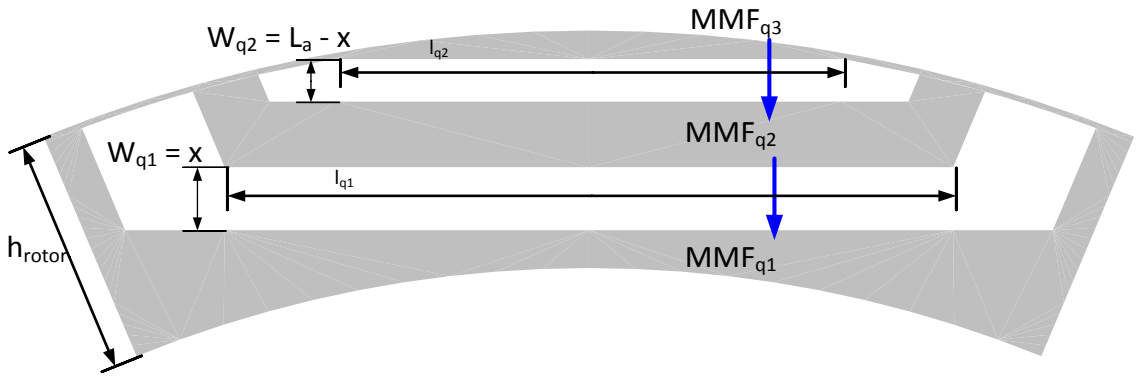


Figure 29. Example of two barriers to determine the relation between the widths of the barriers

As mentioned before, the sizing of the barriers aims to reduce the total flux in the q-axis (blue arrows). Then, the flux in each barrier is given by;

$$\phi_1 = \frac{MMF_{q2} - MMF_{q1}}{\Re_{b1}} = \frac{\Delta MMF_1}{\Re_{b1}}$$
$$\phi_2 = \frac{MMF_{q3} - MMF_{q2}}{\Re_{b2}} = \frac{\Delta MMF_2}{\Re_{b2}} \quad (34)$$

The reluctance of the barriers is given by;

$$\Re_{b1} = \frac{W_{q1}}{\mu_o l_{q1} L_{stk}}$$
$$\Re_{b2} = \frac{W_{q2}}{\mu_o l_{q2} L_{stk}} \quad (35)$$

Therefore, the total flux is given by;

$$\phi = \frac{\Delta MMF_1}{W_{q1}} \mu_o l_{q1} L_{stk} + \frac{\Delta MMF_2}{W_{q2}} \mu_o l_{q2} L_{stk} \quad (36)$$

Note that the total flux is a function of the reluctances of the flux barriers, i.e. the total flux is a function of the variable “x” (see Figure 29). Hence,

$$\phi(x) = \frac{\Delta MMF_1}{x} \mu_o l_{q1} L_{stk} + \frac{\Delta MMF_2}{L_a - x} \mu_o l_{q2} L_{stk} \quad (37)$$

Where, the total width of air in the rotor is given by;

$$L_a = \sum_{i=1}^{i=nb} W_{qi} = \frac{h_{rotor}}{1 + \frac{1}{k_{insq}}} \quad (38)$$

Then, the minimization of the flux is obtained as follows

$$\frac{d\phi(x)}{dt} = -\frac{\Delta MMF_1}{x^2} \mu_o l_{q1} L_{stk} + \frac{\Delta MMF_2}{(L_a - x)^2} \mu_o l_{q2} L_{stk} = 0 \quad (39)$$

Then, the final result is;

$$\frac{\Delta MMF_1}{x^2} l_{q1} = \frac{\Delta MMF_2}{(L_a - x)^2} l_{q2} \rightarrow \frac{\Delta MMF_1}{W_{q1}^2} l_{q1} = \frac{\Delta MMF_2}{W_{q2}^2} l_{q2} \quad (40)$$

Finally, the permeance of each barrier can be assumed constant in order to obtain a better distribution of the flux in the airgap.

$$\frac{l_{q1}}{W_{q1}} = \frac{l_{q2}}{W_{q2}} \quad (41)$$

Finally, by introducing (41) in (40), (33) appears.

It is worthy to mention that there is another approach [96, 97], which relates the size of the barriers as follows;

$$\frac{W_{qi}}{W_{qi+1}} = \frac{\Delta MMF_i^{\,2}}{\Delta MMF_{i+1}^{\,2}} \quad (42)$$

As can be observed in Figure 27, there is another variable to define, which it is the width of the flux barrier in the lateral location ($W_{di}$). The relation between the widths of the barriers in the q-axis with the thickness in the d-axis is given by [97];

$$\frac{W_{di}}{W_{di+1}} = \frac{W_{qi}}{W_{qi+1}} \quad (43)$$

Note that one more equation is required to solve the sizing of the barriers. The total length of the barriers can be determined by using the insulation ratio in the d-axis.

$$L_{ad} = \sum_{i=1}^{i=nb} W_{di} = \frac{L_s}{k_{insd}} \quad (44)$$

"$k_{insd}$" being the insulation ratio in the d-axis, which is applied to determine the width of the barriers according to the mechanical angle defined in Figure 24. "$L_s$" is the total thickness of the segments, which it is constant in the whole segment.

In this point, the sizing of the rotor is explained. However, there are several uncertain points. These undefined variables are the inner rotor diameter and the insulation ratios ($k_{insd}$ and $k_{insq}$).

On the one hand, the inner rotor diameter ($D_{ir}$) determines the total space in the rotor since the outer rotor diameter is known;

$$D_{or} = D_{is} - 2g \quad (45)$$

Then, the inner rotor diameter is defined as;

$$D_{ir} = D_{or} - 2h_{rotor} \quad (46)$$

"$h_{rotor}$" is required to calculate the width of the barriers and segments, as can be observed in (30) and (38). Then, an iterative system to determine the correct size of the rotor is proposed as can be observed in Figure 30. Depending on the design restrictions, this part must be adapted. For instance, the use of magnets makes necessary to size the barriers with thickness greater than a certain value, which depends on the magnet's manufacturer (around 3mm), or to increase the rotor size to obtain a desired saliency ratio, or to introduce the necessary quantity of magnet to improve the motor performances in terms of constant power ratio. In this context, Figure 30 shows the iterative design procedure. Furthermore, an example of the differences is depicted. In the first iteration (i=1), the width of the last barriers is 0.5mm, however the specifications only allow values higher than 3mm. Then, after the iterative procedure (i=n) the solution is obtained according to the restrictions imposed. Note that the inner diameter of the rotor in the first case is 90mm meanwhile in the final solution is 75mm. The insulation ratio in the q-axis is defined by the designer, and probably the best option is obtained after an optimization. However, values around 1 are good solutions.

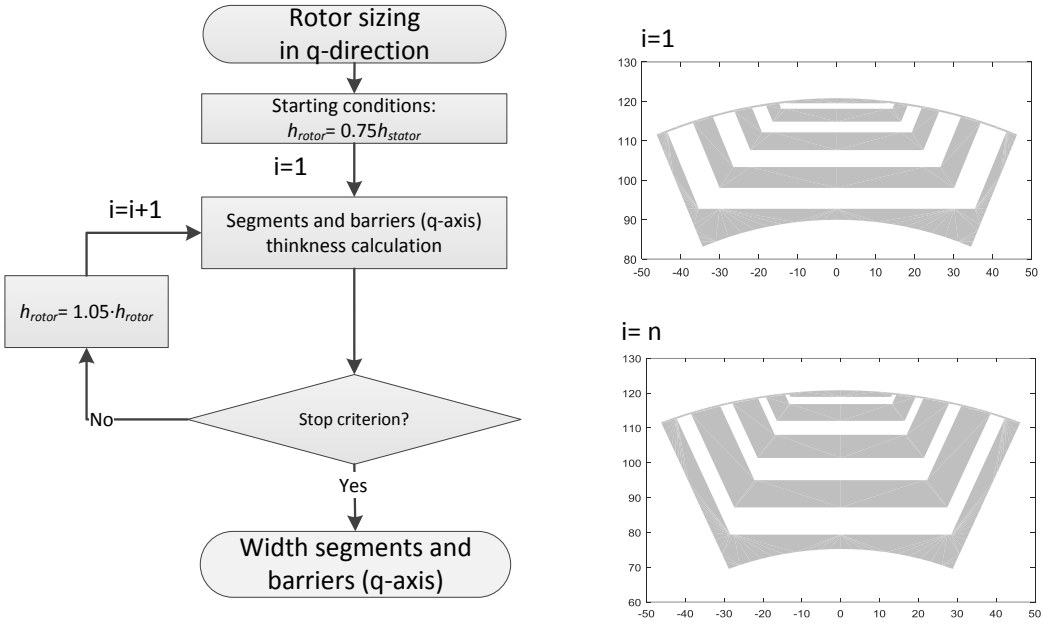


Figure 30. Iterative loop to size the rotor segments and barriers in the q-position

On the other hand, the d-axis insulation ratio is not defined. As explained before, this insulation ratio is determined to locate the barriers according to Figure 24. Then, the value of this variable is swept to obtain the final design. In this case the criterion to halt the iterative process is the correct position of the last barrier (the angle is $3/2\alpha_m$). Figure 31 shows the iterative procedure and the solutions of two different iterations.

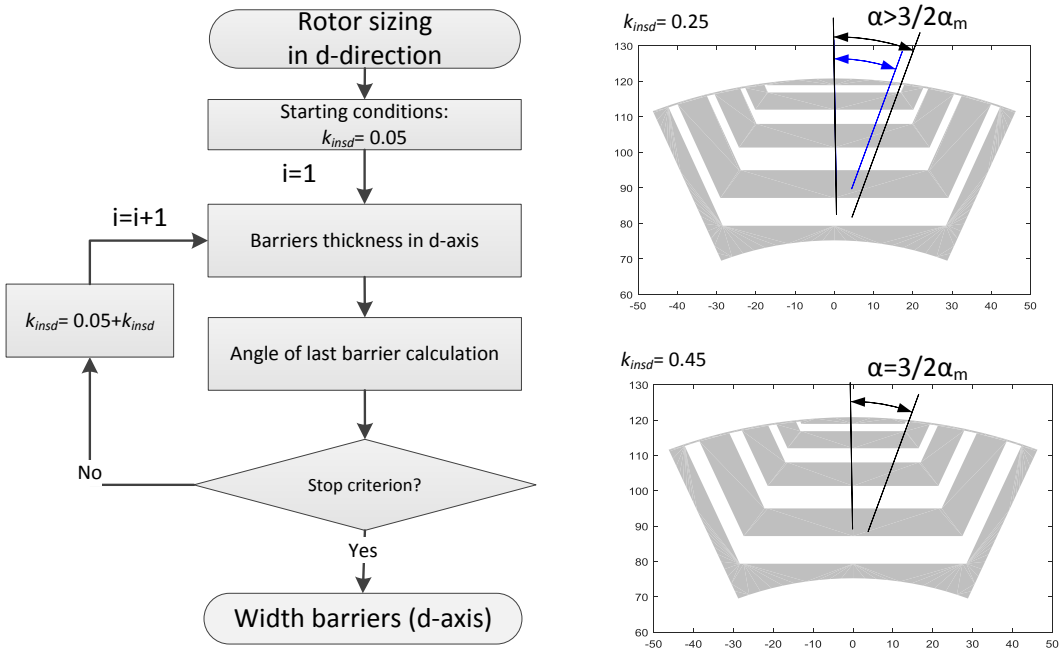


Figure 31. Rotor iterative loop to size the segments and barriers in d-position

After the calculation of the rotor size, the magnet quantity must be determined in order to obtain a suitable behavior of the machine during the operation. The north of the magnet is located in the negative direction of the q-axis (see Figure 32) in order to improve the motor capabilities, such as torque, base speed, and angle between voltage and current (see Figure 32B).

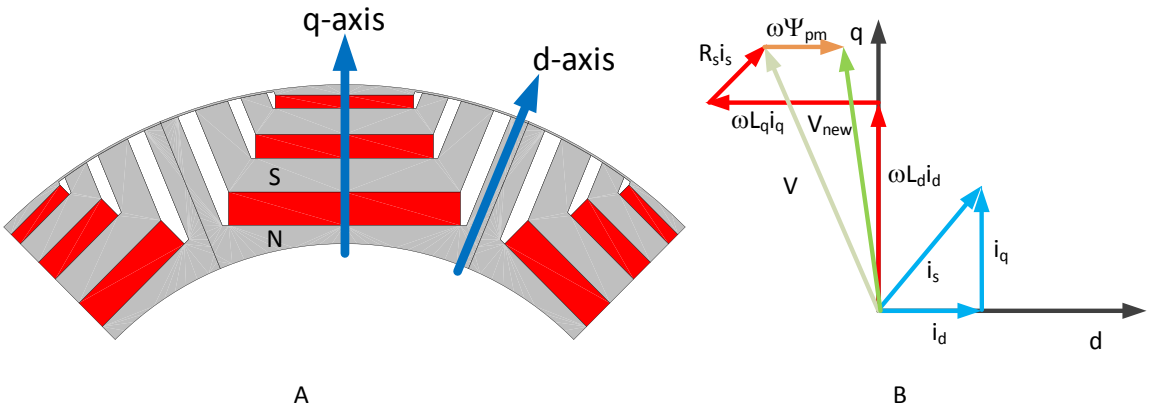


Figure 32. A) Magnet orientation in the rotor. B) Phasor diagram with and without magnets.

The motor capability within the flux weakening region is related with the magnet contribution [102, 103]. It means that the magnets can be or not be inserted in all the barriers, depending on the requirements. In the case of not inserting magnets in all barriers, it is recommended to put the magnets in the innermost barrier, since the outset barriers are more magnetically stressed, so the magnet can suffer demagnetization [78, 104].

Three different conditions can be determined. When the magnet flux linkage ($\lambda_{pmq}$) is smaller than the stator q-flux ($\lambda_{pmq} < L_q i_q$), which is determined by the q-inductances ($L_q$) and q-current ($i_q$), the machine works in under compensation situation. In this point, the power never drops to zero, so it is an infinite speed machine, however the power decreases with the speed. When, the magnet flux linkage is equal to the stator q-flux ($\lambda_{pmq} = L_q i_q$), the machine works in a natural compensation situation. In this case, the power remains almost constant with the speed. Finally, when the magnet flux linkage is greater than the q-flux ($\lambda_{pmq} > L_q i_q$) , the machine works in over compensated situation. In this case, the power factor and torque generation are improved. However, the machine obtained has finite speed, so the power will be zero at high speed. Furthermore, the ratio of constant power is almost null.

In order to ensure the correct behavior of the motor and prevent the demagnetization is better to avoid the under compensation situation. Then, the other two situations can be used depending on the requirements of the application (high speed or high torque density). To compute the inductances and the magnet flux linkage a fast and simple magnetic model is introduced. Is important to mention, that a complex magnetic model is required in the optimization stage [68, 105], however in the electro-magnetic pre-design the proposed magnetic model is good enough to calculate the magnet and improve the accuracy of the geometry.

The magnetic model based on two reluctance networks not only calculates the magnetic flux linkage but also estimates the *dq*-inductances, so the motor performances can be calculated. Using this magnetic model, the back EMF, power factor, efficiency, saturation factor, and airgap flux density

can be defined with more accuracy and the electro-magnetic pre-design can be improved (see Algorithm 1).

There are two reluctance networks to analyze the d- and q-axis. The q-reluctance network (RN) allows calculating the q-inductances and the magnet flux linkage. Figure 33 shows an equivalent magnetic model to determine the mentioned parameters of the machine.

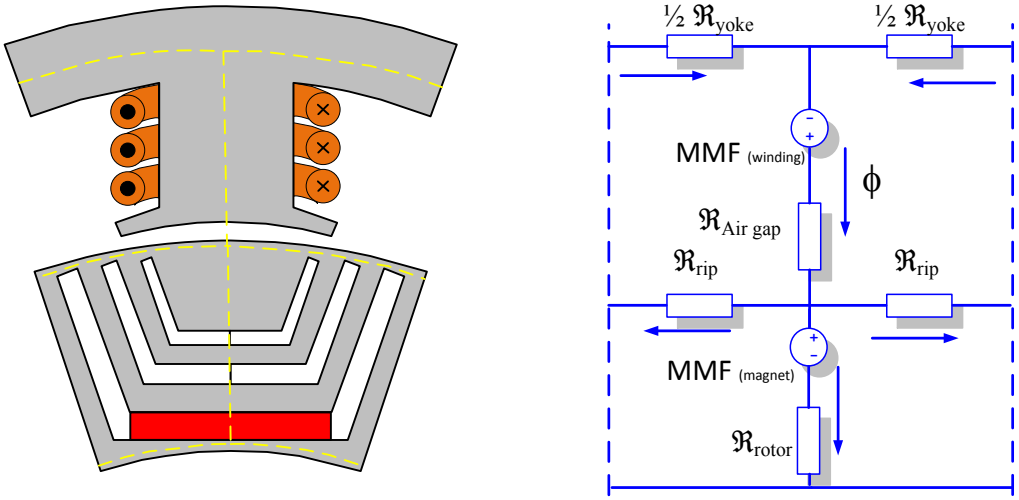


Figure 33. Simple reluctance network in q-axis

Note that, the magnet is only located in the innermost barrier, however it can be removed or more magnets can be introduced in the remaining barriers. The RN is formed by MMF generators and reluctances. The first one is created by the coils and magnets.

$$MMF_{winding} = \sum NI \quad (47)$$

"$N$" being the number of conductors in the coil and "$I$" the current in each phase (in this select the rated current).

It is worthy to be mentioned, that this magnetic model is not complete. The winding MMF generator is only represented in one tooth, so the whole contribution of the different teeth has to be added. In [106] there is more information to calculate the $MMF_{winding}$ according a given winding distribution

$$MMF_{magnet} = H_c W_{qi} \quad (48)$$

Where, "$H_c$" is the coercive force and "$W_{qi}$" is the width of the magnet, which is the same width as that of the flux barriers. Then, the reluctances are calculated as follows;

$$\Re = \frac{l}{\mu_o \mu_r S} \quad (49)$$

Where, "$l$" is the length of the magnetic reluctance, "$S$" is the cross-section of the magnetic reluctance, "$\mu_o$" is the magnetic permeability of the vacuum, and "$\mu_r$" is the relative magnetic permeability, which in the air is equal to 1 meanwhile in the magnetic steel varies with the saturation. Note that, the magnetic steel is not saturated along the q-axis. Finally, the airgap reluctance must be multiplied by Carter's coefficient to reflect the effect of the slot opening.

On the other hand, the d-axis RN is shown in Figure 34. In this case the magnet is not reflected since it only influences the q-axis. The magnetic saturation of the magnetic steel must be considered.

The magnetic saturation in the teeth and yoke can be fixed at the value chosen in the design stage (14) and (18), and in in the rotor can be fixed at 1 T.

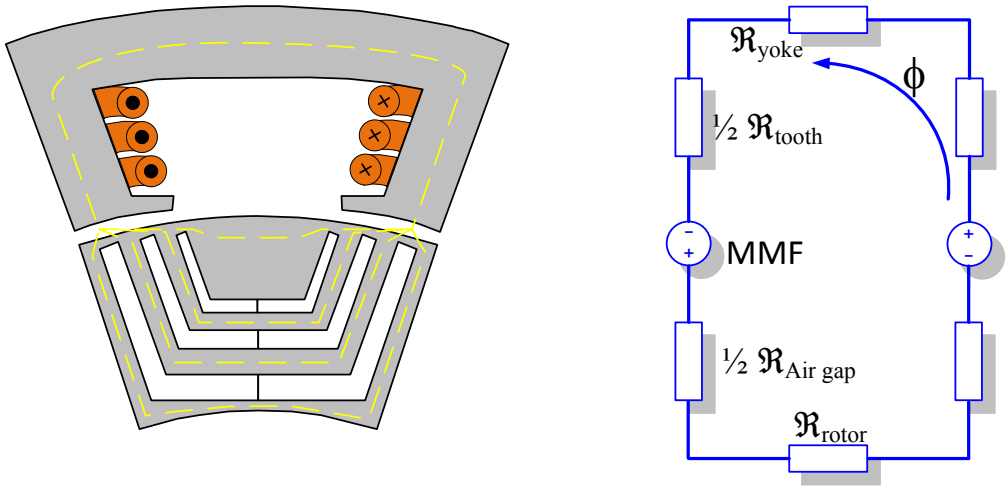


Figure 34. Simple reluctance network in d-axis

The unknown magnetic flux is calculated using two different equations. The first one (50) relates the MMF obtained in a closed path with the reluctances and the magnetic flux in this path.

$$MMF = \sum \Re\phi \tag{50}$$

The second one relates the total magnetic fluxes in a node (see Figure 33).

$$\sum \phi = 0 \tag{51}$$

The q-axis is solved twice; the first one only considers the MMF generated by the magnets in order to calculate the magnet flux linkage ( $\Psi_{mpq}$), meanwhile the second one takes into account both MMF generators. The inductances and flux magnet linkage are calculated as follows;

$$L_d = 2pN\frac{\phi_d}{I}; L_q = \frac{2pN\phi_q - \Psi_{mpq}}{I};\ \Psi_{mpq} = 2pN\phi_q \ where\ I_q = 0 \tag{52}$$

By using these values, the motor performances can be deducted, so the process could be re-started with these new values. The back EMF is calculated as follows;

$$E_d = -\omega_e L_q i_q - \omega_e \Psi_{mpq};\ E_q = \omega_e L_d i_d \tag{53}$$

The current angle is given according to the MTPA rule, so the d- and q-currents are known. Then, the power factor can be deducted by calculating the phase shift between the current and voltage. Finally, the torque and output power can be calculated.

$$T = \frac{m}{2}p\left(\left(L_d - L_q\right)i_d i_q - \Psi_{mpq} i_d\right) \tag{54}$$

$$P_{out} = \omega_e T \tag{55}$$

Then, the losses, which are composed by copper and iron losses, are given by;

$$P_{cu} = mR_s I_{rms}^2 \tag{56}$$

$$P_{fe} = k_h \frac{\omega_e}{2}\hat{B}^{n_i} + k_e\left(\frac{\omega_e}{2}\hat{B}\right)^2 \tag{57}$$

"$R_s$" being the phase resistance calculated with the geometry obtained during the calculation of the stator geometry, "$m$" the number of phases, and "$I_{rms}$" the rated current in rms value. On the other

hand, the iron losses are composed by hysteresis and eddy current components. The hysteresis and eddy current coefficients ($k_h$, $k_e$, $n_i$) are obtained by using the material specific losses obtained from the manufacturer's datasheets. The iron loses are per unit of mass, so the final value must be multiplied by the mass of the different parts. The computed parts can be the yoke, teeth, and rotor since these three parts have different magnetic saturation. Then, the efficiency is given by;

$$\eta = \frac{P_{out}}{P_{out} + P_{cu} + P_{fe}} \quad (58)$$

In this point, the thermal behavior of the machine has been considered in the sizing of the slot. The magnetic behavior is analyzed by using the proposed simple magnetic model. Then, the oversize of the slots and the magnet compensated situation ensure the reliability of the motor in terms of magnetic and thermal behaviors. However, the mechanical stress has to be considered to ensure the correct behavior of the machine, since the rotor structure reduces the mechanical integrity.

The mechanical problems are solved by the correct sizing of the radial ribs. Several authors deal with this problem [107-109]. The centrifugal force is given according to;

$$F_c = M\omega_m^2 R_G \quad (59)$$

Being, "$M$" the mass that the calculated radial rib has to support (see the scratched area in Figure 35), "$R_G$" is the radius of the gravity center of the mass, and "$\omega_m$" is the mechanical speed.

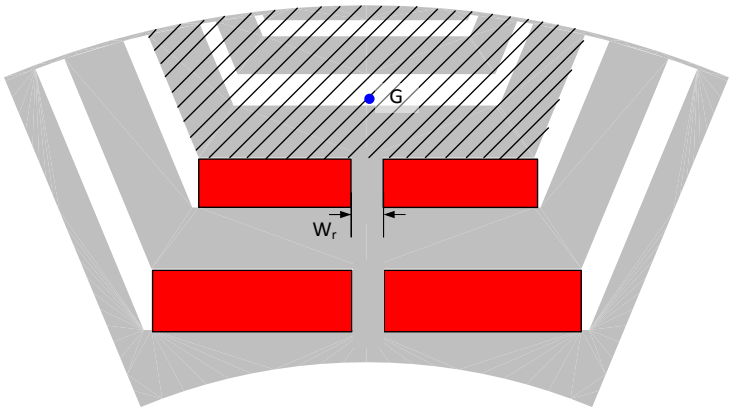


Figure 35. Scheme of the thickness of the radial ribs

Then, the width of the radial ribs ($W_r$) is given as;

$$W_r = \frac{k_s F_c}{\sigma_r L_{stk}} \quad (60)$$

Where, "$k_s$" is the safety factor, which is chosen over 2 and "$\sigma_r$" is the tensile strength of the lamination.

## 3.6 Summary of the design procedure

In this point, the whole process to obtain the electro-magnetic pre-design according to the given requirements is realized. A summary detailing the parameters and equations required in each step is shown in Algorithm 1.

1: Introduce the desired performances (power, rated speed)
2: Introduce the fixed parameters (pole pairs, phase number, slots, Bus DC)
***Start electro-magnetic pre-design process***
3: Estimate parameters (efficiency, power factor, back EMF, saturation factor)
4: **while** stop criterion is not achieved **do**
5: Basic parameters calculation: Electric power (1), phase current (2)
6: Estimate $C_{mec}$ according to Figure 18
7: Calculate $D_{is}$ and $l_{eff}$ using (5) and (6). Compute the $g$ (8) and $L_{stk}$ (7)
8: Estimate number of turns in series $N_{ph}$ (3)
9: Calculates the number of conductors in slot (9)
10: Calculates the number of turns in series $N_{ph}$ new (10) and the $B_g$ (11)
11: Calculates the stator geometry (teeth, yoke, and slots dimensions) (12-22)
12: Chose the number of flux barriers (23)
13: Calculates the position of the barriers (24)
***Calculation of rotor in q-axis (Figure 30)***
14: **while** stop criterion is not achieved **do**
15: Define $h_{rotor}$
16: Calculates the width of the segments and barriers (26-31) and (32-33)
17: Evaluates stop criterion
18: **end**
***Calculation of rotor in d-axis (Figure 31)***
19: **while** stop criterion is not achieved **do**
20: Define $k_{insd}$
21: Calculates the width of the and barriers in d-axis(43-44)
22: Evaluates stop criterion
23: **end**
24: ***Solve Magnetic model (Figure 33 and Figure 34)***
25: Calculates Inductances, magnetic flux linkage (52)
26: Calculates losses (56-57)
27: Calculates motor performances: Torque (54), output power (55)
28: Calculates the estimated values: Back EMF (53), efficiency (58), power factor, saturation factor (4), peak airgap flux density (using the d-flux from magnetic model).
29: Evaluates stop criterion (error of estimated parameters)
30:**end**
31: Calculates the thinkness of the radial ribs (59-60)

Algorithm 1. Electro-magnetic pre-design procedure

# 4.

# Magnetic model

This chapters presents the contributions of this thesis to analysis of magnetic model. In this regard, the procedure to calculate the inductances, magnetic saturation, and torque ripple is detailed. The chapter is divided in two main parts, single-saturation and cross-coupling saturation.

*CONTENTS:*

# 4. Magnetic model

## 4.1 Introduction

As mention before, the proposed work tries to eliminate the use of FEA in the optimization process, so different models are required in order to calculate the multi-physics behavior of the machine. One of them is the magnetic behavior. The magnetic saturation is closely related with the motor performances, so an accurate calculation of the magnetic behavior of the machine is required to obtain a good design. Specifically, the design of PMaSynRM is a very complex process [60, 110] because of its high magnetic saturation, resulting in a very dependent on FEA computation [111], since effects of the rotor saturation on the machine performance have not been properly studied [23] and there is still no analytical method to accurately predict the performance of the machine due to non-linearity created by local saturation [112]. Others effects such as the interaction between the spatial harmonics of electrical loading and the rotor anisotropy, causes torque ripple, [113], whose mitigation or suppression is currently under investigation, since it is an undesirable effect depending upon the application [114]. There are several design approaches in order to address this problem, which present a suitable number combination of flux barriers and stator slots [111, 115], or designing the flux barriers in such a way that the outer edges do not correspond to the position of stator teeth [116]. Nowadays the reluctance networks appear as a strong candidate tool to cope with electromagnetic motor design, due to its advantages in terms of computation burden [117, 118] and accuracy.

In this framework, a further explanation of the magnetic model based on reluctance network is realized in this section. The reluctance network (RN) can be defined as the magnetic circuit of each motor. The RN is obtained from the motor's geometry. It is formed from reluctances and magneto-motive forces. The magnetic model allows calculating the motor inductances, the magnet flux linkage, the magnetic saturation of the different motor parts, which can be used to calculate the iron losses, and the demagnetization of the magnets.

Two different approaches are detailed, the first one consists at calculate the *dq*-inductances using two reluctance networks, so neglecting the cross-coupling saturation. By this way, the magnetic model is easy to develop and the solution can be calculated in a few seconds. On the other hand, the second approaches works with a unique reluctance network in order to determine the effect of cross-coupling saturation. In this case, the use of multi-physics domain software is necessary to solve the complex magnetic model proposed.

The single and complex reluctance networks are solved in Simscape (MATLAB). The use of Simscape allows not only calculating the cross-saturation but also increasing the detail of the reluctance networks. In fact, this new level of detail is used to calculate the torque ripple. In addition, the magnetic model is more adaptable using Simscape, because an object-oriented programing can be developed using this tool. The principal drawback of usisng the second method is the time required. In this case, the time could be 10 times more than the previous one due to the complexity of the reluctance network.

## 4.2 Single-saturation

Decoupling the *dq*-axes allows reducing the complexity of the RN, so the number of unknowns is lesser than considering the cross-coupling saturation. With this solution, two RNs are required to evaluate the magnetic behavior in both magnetic axes.

This section aims to explain how to build the RN for SynRM and PMaSynRM, how to compute the inductances, and how to obtain other useful results. In this context, this section is divided in magneto motive forces (MMF) and reluctance calculation, *q*-axis RN, *d*-axis RN, inductance calculation, and FEA validation.

### 4.2.1 Magneto motive force and Reluctance calculation

This sub-section aims to explain the MMF and reluctances calculation. Both are the main parameters in the RNs, so it is important to understand how to calculate it.

On the one hand, the MMF is given by the current and magnets. The first one is located on the stator teeth. Depending on the coil distribution and the number of slots per pole and phase the MMF waveform varies. The MMF values are calculated by;

$$MFF_{1,2,3\ldots k} = \sum_{i=1}^{m} n_c I_i \qquad (61)$$

where the sub-index *"$k$"* in the MFF means each tooth in the RN, *"$i$"* represents the different phases, *"$m$"* is the phase number, *"$n_c$"* the number of conductor of each phase which contributes to create MMF in $k$-tooth, and *"$I$"* is the value of the current.

Note that, the sign (positive or negative) of each phase's MMF depend on the winding distribution, and then the well-known right hand rule is used to determine it. Therefore, the go-return matrix is required since the direction of the winding is necessary to know the sign of the MMF as shown in Figure 36. In this figure, an example of winding distribution for a 3-phases machine is shown. The go-return is depicted as black dots and crosses respectively.

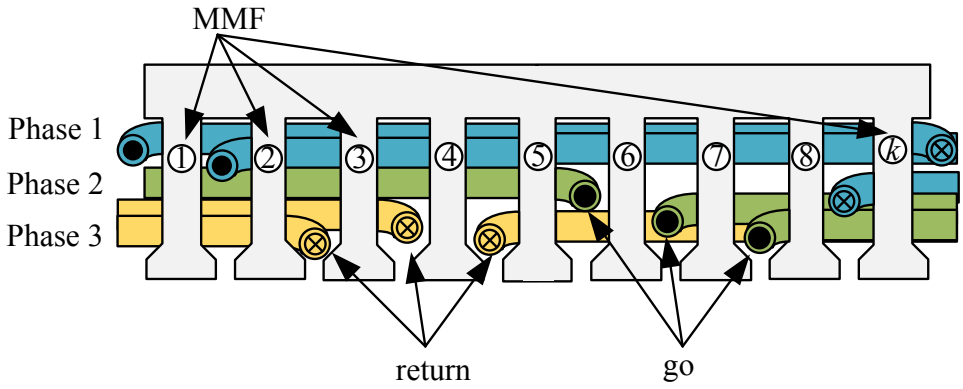


Figure 36. Sing of MMF determination

For instance, the coil of phase 1, which comprise the teeth from 1 to k, has the center in tooth 5, so the MMF created in tooth 1 is positive (top direction). Note that, the final value of the MMF depends on the current value since the current can be positive or negative. Therefore, according to the sign criteria defined and (61), the MMF on teeth 1, 2 and 3 are;

$$MMF_1 = n_c(I_1 - I_2 + 2I_3)$$
$$MMF_2 = n_c(2I_1 - I_2 + 2I_3) \quad (62)$$
$$MMF_3 = n_c(2I_1 - I_2 + I_3)$$

The second MFF is located on magnets. The magnet is represented as MMF and reluctance. The value of the MMF depends on the magnetic properties and the geometry of the magnets. The MMF is calculated as;

$$MMF_{magnet} = H_c W_{qi} \quad (63)$$

where, the *"$H_c$"* is the coercive force of the magnet and *"$W_{qi}$"* represents the width of each magnet (sub-index *"$i$"* represent the different magnets on the RN) as shown in Figure 37

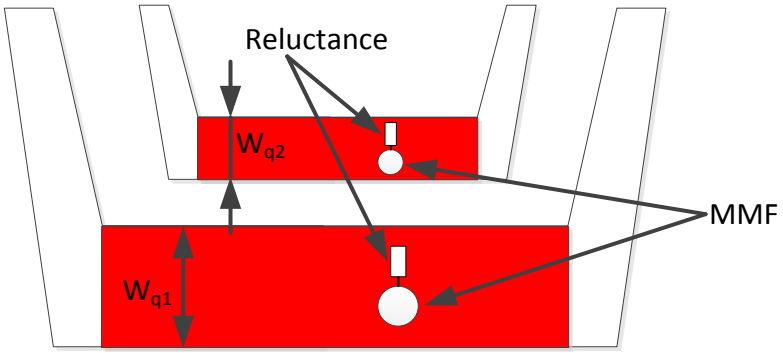


Figure 37. Example of flux barriers with magnets (red). The MMF and Reluctance are detailed.

On the other hand, the reluctance ($\Re$) can be defined as the opposing of the passing of the magnetic flux ($\phi$) lines, equal to the ratio of MMF to the magnetic flux.

$$\Re = \frac{MMF}{\phi} \quad (64)$$

The reluctance also is determinated by the permeability of the materials and arrangement of the geometry of the magnetic circuit. Therefore, the reluctance is given by;

$$\Re = \frac{l}{\mu(B)\, S} \quad (65)$$

Where "$l$" is the length of magnetic reluctance (m), "S" is is the cross section of the magnetic reluctance ($m^2$) as shown in Figure 38.

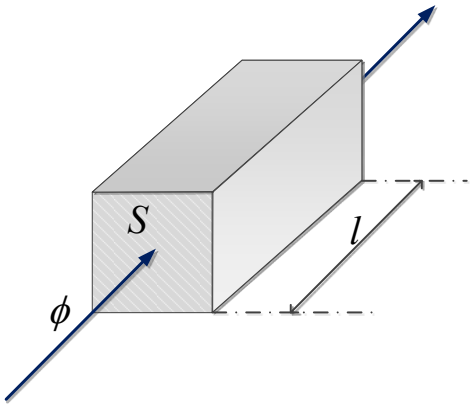


Figure 38. Detail of the geometry of reluctances

Then, "$\mu$" is the magnetic permeability, which is calculated as $\mu = \mu_o \mu_r$. The "$\mu_o$" is the permeability of the vaccumm and the "$\mu_r$" is the relative permeability, which depends on the material. The relative permeability of magnetic materials varies with the magnetic flux density (B). Figure 39 shows the permeability curve of magnetic sheet M330-35A in function of magnetic flux density.

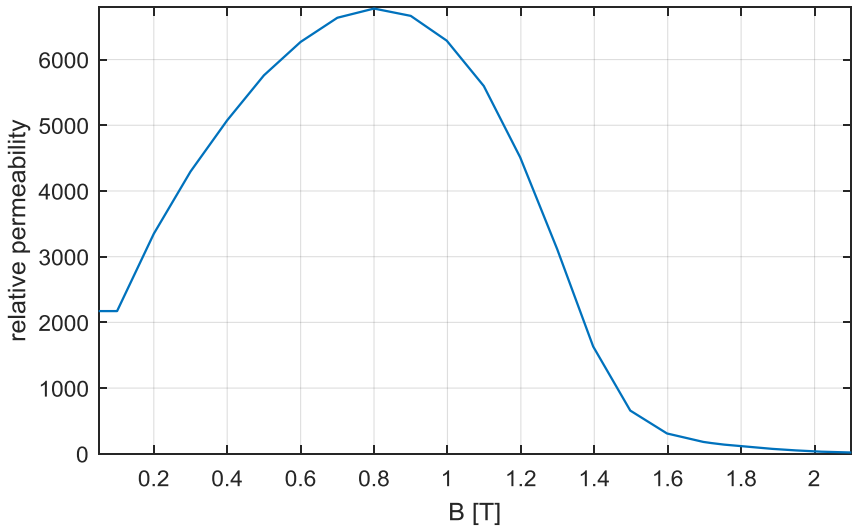


Figure 39. The relative permeability curve in function of magnetic saturation

It is worthy to mention that the relative permeability of air is constant and it is practically one, so the reluctances of the air's parts are easy to compute. However, the reluctances of the airgap require a coefficient to takes into account the opening slot effect. The airgap's reluctances have to be multiplied by Carter's coefficient [81]. Then, the airgap's reluctances are given by;

$$\Re_g = \frac{g}{\mu_o S} K_c \qquad (66)$$

where, "*g*" is the airgap length and "$K_c$" is the Carter coefficient;

$$K_c = \frac{5+s}{5+s-\frac{s^2}{\lambda}} \qquad (67)$$

Where, "*s*" is the ratio *(slot opening)/g* and "$\lambda$" is the ratio *(slot pitch)/g*.

### 4.2.2 Inductance calculation

This sub-section aims to explain how to calculate the inductances. Is worthy to mention that the magnetic model depends on the motor geometry, such as the number of phases, number of slots per pole, number of flux barriers, among others. However, the proses to compute the inductances are the same, i.e. the magnetic model have to be solved. Then, the value of magnetic fluxes is obtained.

The magnetic flux, which is generated by the current and magnets, form closed magnetic path in the motor geometry. The RN represents the magnetic circuits in order to calculate the magnetic fluxes for each current value. When the magnetic flux crosses the loops of the coils is called flux-linkage. Then, the inductances can be defined as flux-linkage per ampere. Figure 40 illustrates the definition of the flux-linkages. The stator of one magnetic pole and the magnetic flux lines can be observed.

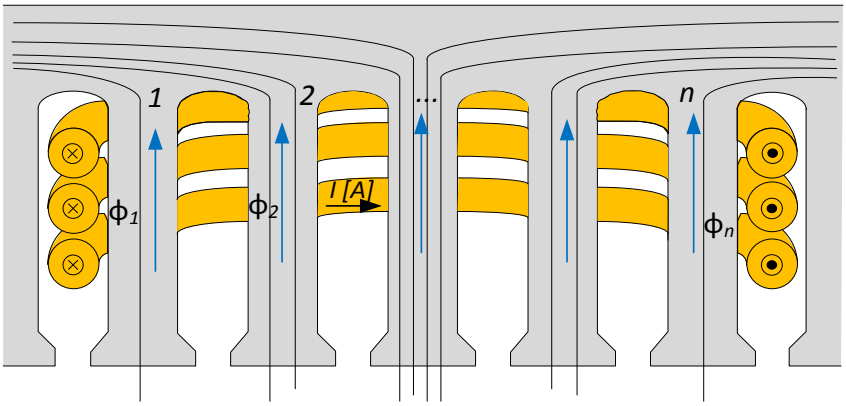


Figure 40. Illustration of inductance definition. Example of stator of one magnetic pole.

Considering the example proposed on Figure 40. The inductance is given by;

$$L = 2p\,N\frac{\sum_1^n \phi_i}{I} \qquad (68)$$

where, "*p*" is the poles pair, so the term "*2p*" is used to compute the total motor inductances, "*N*" is the number of turns, "*I*" is the current, and "$\phi$" is the magnetic flux of each tooth. Is worthy to mention, that the magnetic flux-linkage used to calculate the inductances are created by the coils, so the magnetic flux-linkage provided by the magnet has to be disregard to compute the inductances.

As mention before, the magnetic flux-linkage is obtained solving the RN. The equation system is formed by two type of equations. The first one represents the closed magnetic path (69). It relates the total MMF in a closed path with the sum of the product of the reluctances and magnetic fluxes.

$$MMF = \sum \Re\phi \qquad (69)$$

The second one is applied to the nodes (70). The total magnetic flux in one node must be zero.

$$\sum \phi = 0 \qquad (70)$$

Figure 41 shows an example of the application of (69-70). The rotor is not represented, so the example is only to understand the equations system.

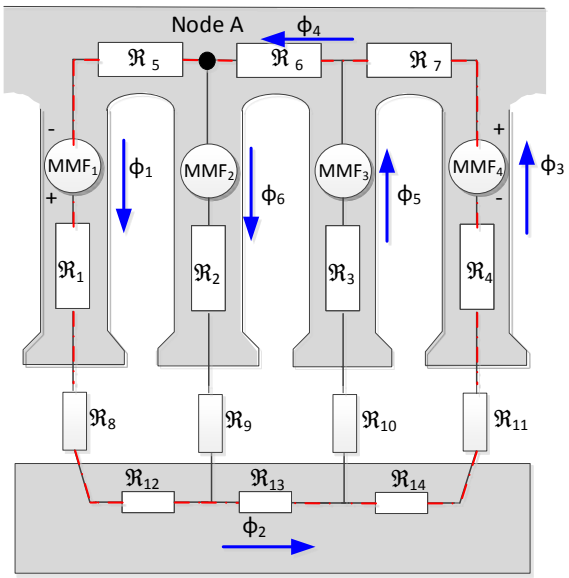


Figure 41. Example of RN

In this example, there are six magnetic fluxes, which are the unknowns of the system. Then, six equations are required. For instance, an example of (69) is given by the red closed path;

$$MMF_1 + MMF_4 = (\Re_1 + \Re_5 + \Re_8 + \Re_{12})\phi_1 + \Re_{13}\phi_2 + \Re_6\phi_4 + (\Re_4 + \Re_7 + \Re_{11} + \Re_{14})\phi_3$$

An example of (70) is given by the node A;

$$\phi_1 - \phi_4 - \phi_6 = 0$$

Is worthy to be mentioned that the value of some reluctances varies with the value of the magnetic flux density. Concretely, the reluctances of the magnetic material, which are represented as white boxes in the grey parts, are affected by the magnetic flux density. Therefore, an iterative system is required in order to solve the RN. The iterative system starts with a seed value for the magnetic fluxes, then using this seed value the magnetic flux density can be calculated (dividing by surface of the cross section). Then, the reluctances can be calculated since the relative permeability is obtained, and the equation system can be solved. Finally, the results are compared with the seed value and the error can be computed. If the error is higher than a threshold, the results are used as the new seed value, and the process starts again.

Finally, the inductances must be calculated for each current, so the iterative process has to be repeated for each current. Figure 42 shows the process to obtain the inductance in function of the current.

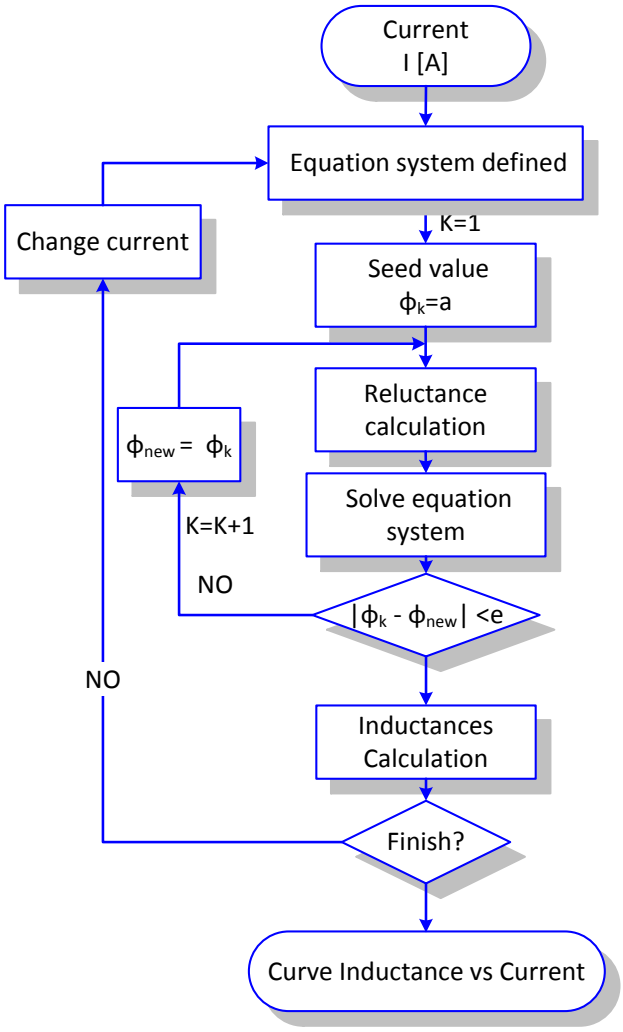


Figure 42. Workflow of inductance calculation.

### 4.2.3 *q*-axis reluctance network

As mention before, the quadrature position of the machine is the position with less magnetic flux, i.e. the position with the higher reluctances. Considering the motor topology of this work (SynRM and PMaSynRM), the maximum reluctances appear when the magnetic flux crosses the flux barriers or magnets. The maximum winding MMF has to be in the middle of the magnetic pole to force the magnetic flux to cross the flux barriers.

In this context, the position of the rotor depends on the winding distribution and the current state. The proposed singular state of the electric loading for a 3-phases machine is;

$$\begin{aligned} i_a &= \hat{I} \\ i_b = i_c &= -\frac{\hat{I}}{2} \end{aligned} \qquad (71)$$

Where, "$i_a, i_b$ and $i_c$" represents the current of phase a, b and c, respectively in a specific time instant, and "$\hat{I}$" represents the peak value of the current. Note that, the current phase must complies

$$i_a + i_b + i_c = 0 \qquad (72)$$

These values can be observed in Figure 43, when the blue curve is at the maximum 1, the two curves are -0.5.

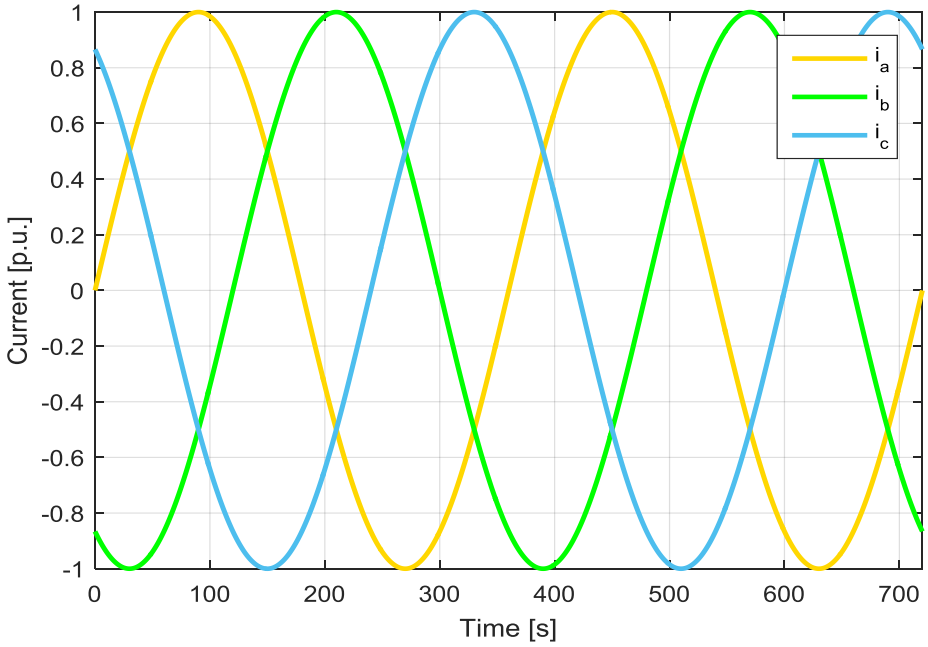


Figure 43. Three phases' current signal

Figure 44 shows the RN of the quadrature position. In this figure, the motor geometry of one magnetic pole and the winding distribution can be observed. The dashed red lines represent the symmetry of the machine. The winding distribution is represented as one conductor per phase and the value of the MMF in each tooth is summarized in Table 1. The MMF of each phase is detailed and the total MFF is calculated according to (61).

Table 1. Calculation of MMF in each tooth

| Teeth | 1 | 2 | 3 | 4 | 5 | 6 | 7 |
|---|---|---|---|---|---|---|---|
| Phase A | 0 | $N\hat{I}$ | $N\hat{I}$ | $N\hat{I}$ | $N\hat{I}$ | $N\hat{I}$ | 0 |
| Phase B | $-0.5N\hat{I}$ | $-0.5N\hat{I}$ | 0 | $0.5N\hat{I}$ | $0.5N\hat{I}$ | $0.5N\hat{I}$ | $0.5N\hat{I}$ |
| Phase C | $0.5N\hat{I}$ | $0.5N\hat{I}$ | $0.5N\hat{I}$ | $0.5N\hat{I}$ | 0 | $-0.5N\hat{I}$ | $-0.5N\hat{I}$ |
| MMF | 0 | $N\hat{I}$ | $1.5N\hat{I}$ | $2N\hat{I}$ | $1.5N\hat{I}$ | $N\hat{I}$ | 0 |

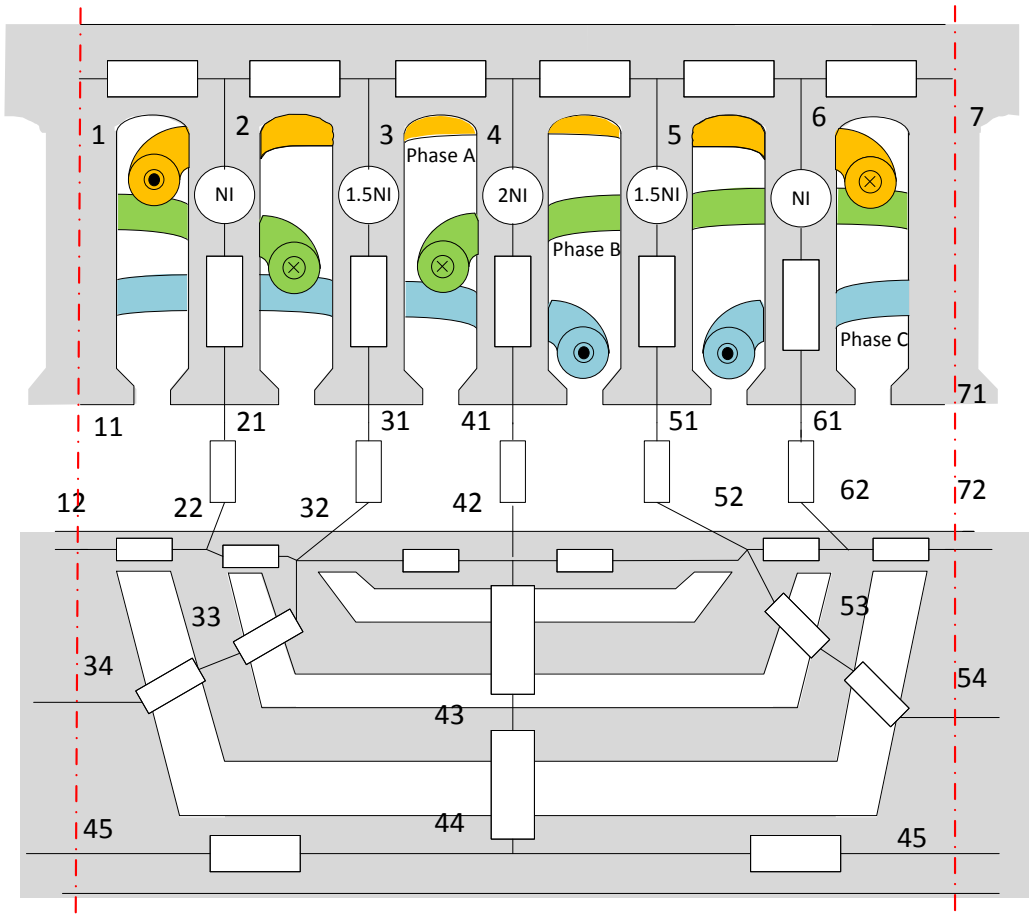


Figure 44. Example of a RN of quadrature position

Note that, there are reluctances on the ribs. Some magnetic models simplify this part because the ribs normally are saturated, so the reluctance can be changed by a magnetic flux source. However, when the current value is low or the size of the rib is big, the ribs are not saturated. Then, the models without these reluctances cannot calculate correctly the value of the inductances in these conditions.

Considering the magnetic symmetry of the machine, the RN proposed can be divided in a half magnetic pole to simply the equation system. The final RN is shown in Figure 45. The different unknown magnetic fluxes are represented and the reluctances are numbered taking into account the nodes position. For example, the reluctance between nodes 1 and 2 is called $\Re_{1\text{-}2}$. Several reluctances on the rotor, such as $\Re_{33\text{-}34}$ and $\Re_{43\text{-}44}$, are composed by the reluctance of the flux barrier and the reluctance of segments as can be observed in Figure 45.

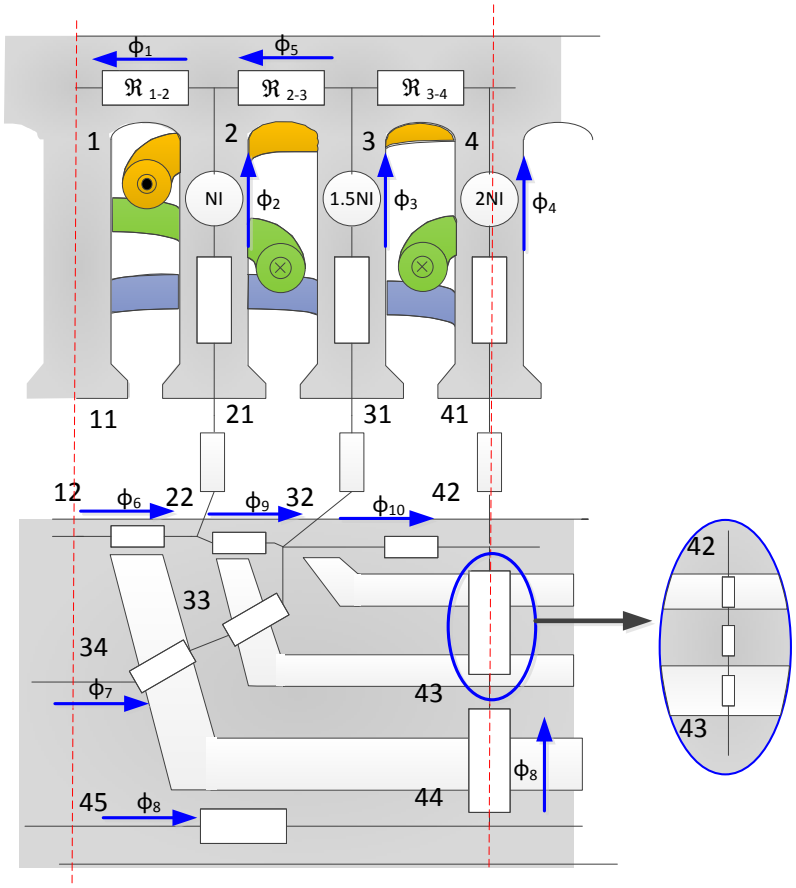


Figure 45. Final reluctance network. The blue arrows represents the unknown values

A system formed by ten equations is required. As mention before, the equation system is formed by (69-70). The final equation system for this example is given by;

$$\begin{bmatrix} MMF_2 \\ MMF_3 \\ MMF_3 \\ MMF_4 \\ MMF_4 \\ 0 \\ 0 \\ 0 \\ 0 \\ 0 \end{bmatrix} = \begin{bmatrix} \Re_{1-2} & \Re_{2T} & 0 & 0 & 0 & \Re_{12-22} & 0 & 0 & 0 & 0 \\ \Re_{1-2} & 0 & \Re_{3T} & 0 & \Re_{2-3} & \Re_{12-22} & 0 & 0 & \Re_{22-32} & 0 \\ \Re_{1-2} & 0 & \Re_{3T} & 0 & \Re_{2-3} & 0 & \Re_{7T} & 0 & 0 & 0 \\ \Re_{1-2} & 0 & 0 & \Re_{4T} & \Re_{2-3} & 0 & 0 & \Re_{8T} & 0 & 0 \\ \Re_{1-2} & 0 & 0 & \Re_{4T} & \Re_{2-3} & \Re_{12-22} & 0 & 0 & \Re_{22-32} & \Re_{32-42} \\ 1 & 0 & 0 & 1 & 0 & -1 & 0 & 0 & 0 & 0 \\ -1 & 1 & 0 & 0 & 1 & 0 & 0 & 0 & 0 & 0 \\ 0 & 0 & 1 & 0 & -1 & 0 & 0 & 1 & 0 & 0 \\ 0 & 0 & 0 & -1 & 0 & 0 & 0 & 1 & 0 & 1 \\ 0 & 0 & 1 & 0 & 0 & 0 & -1 & 0 & -1 & 1 \end{bmatrix} \begin{bmatrix} \phi_1 \\ \phi_2 \\ \phi_3 \\ \phi_4 \\ \phi_5 \\ \phi_6 \\ \phi_7 \\ \phi_8 \\ \phi_9 \\ \phi_{10} \end{bmatrix}$$

where;

$$\Re_{2T} = \Re_{2-21} + \Re_{21-22}$$
$$\Re_{3T} = \Re_{3-31} + \Re_{31-32}$$
$$\Re_{4T} = \Re_{4-41} + \Re_{41-42} + \Re_{3-4}$$
$$\Re_{7T} = \Re_{32-33} + \Re_{33-34}$$
$$\Re_{8T} = \Re_{42-43} + \Re_{43-44}$$

Then, the workflow shown in Figure 42 starts with a small current, which this current represents the phase peak current, so the MMF on each tooth can be calculated. After that, the magnetic fluxes are estimated with a seed value (in the first iteration the magnetic fluxes are zero), so the reluctances can be obtained. Now, the equation system can be solved and the real magnetic fluxes are calculated. If the difference between estimated and calculated magnetic fluxes is bigger than a threshold, the reluctances will be calculated again using the obtained magnetic fluxes. When the solution is achieved, the quadrature inductances can be calculated for the first current using (68). In this case the quadrature inductance is given by;

$$L_q = 2p\,N\frac{(\phi_2+\phi_3+\phi_4)}{I_q}2$$

where "$I_q$" is the quadrature current, which it is the phase peak current in each loop, the last "2" is necessary to takes into account the total magnetic pole (the RN only represents the half of a magnetic pole).

Then, the process starts again with a new current. In order to speed up the process, the new seed value is the final solution of the previous current. The final result of the whole process is the current dependency of the quadrature inductances, i.e. the curve $L_q(I_q)$.

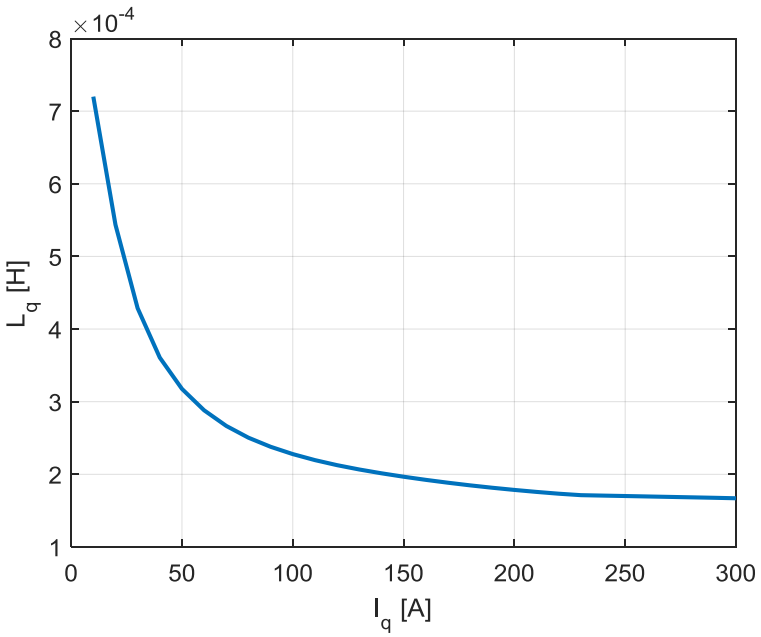


Figure 46. Quadrature inductance curve in function of quadrature current obtained by means of proposed RN

The same geometry is analyzed in FEA to show the accuracy of the model. The magnetic flux lines are depicted in Figure 47. Figure 47 illustrates one magnetic pole of the machine in the quadrature position, so the magnetic flux crosses the flux barriers.

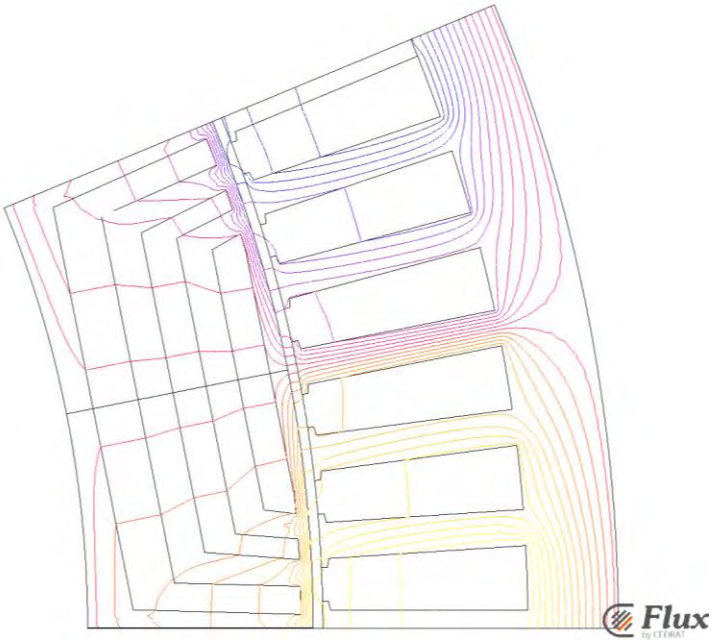


Figure 47. Magnetic flux lines of quadrature position of one magnetic pole

The *q*-inductance calculated by means of FEA is compared with the estimated by means of the proposed RN. Figure 48 displays the comparison between the *q*-inductances calculated in FEA and the estimated by means of the RN. The average error is 1.67% and the variance is 0.41%.

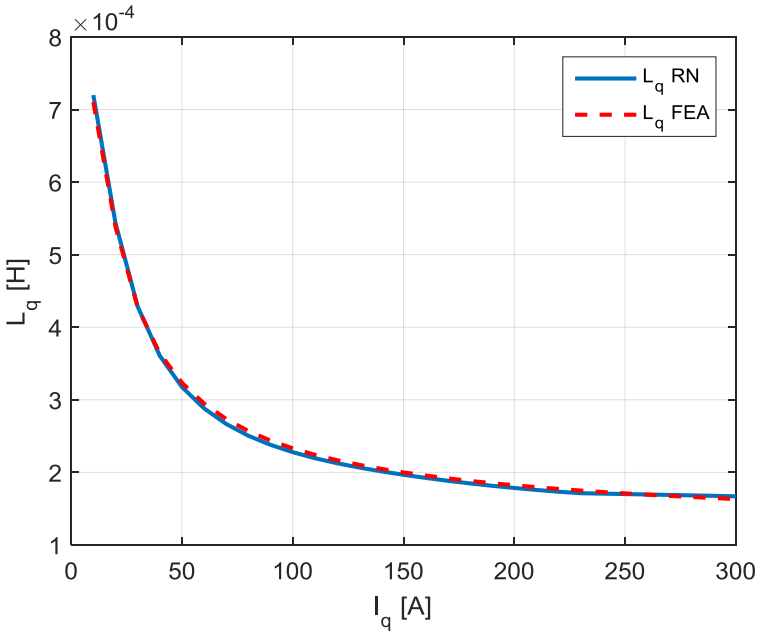


Figure 48. Comparison of *q*-inductances obtained by FEA with the estimated by the proposed RN

The introduction of magnets in the flux barriers can increase the complexity of the inductance calculation. The magnets have to be included in the magnetic model and the equation to calculate the inductances changes a bit.

$$L = 2p\,N\frac{\sum_1^n \phi_i - \Psi_{pm}}{I} \qquad (73)$$

Where, the "$\Psi_{pm}$" is the crossing magnetic flux provided by the magnets, so it is calculated when the MMF of the coils is 0.

Therefore, the RN with magnets allows calculating the magnet flux linkage.

$$\Psi_{PM,q} = 2p\, N\phi_{pm} \quad (74)$$

The same example of Figure 44 with magnets can be observed in Figure 49. Note that, the MMF on teeth is zero, so the current is null. Then, the magnetic flux, which is represented as blue arrows, is generated by the magnets. As can be observed, the direction of the arrows is contrary to the created by the coils (see Figure 45). Remember that the magnet is located against the quadrature axis to increase the motor capabilities.

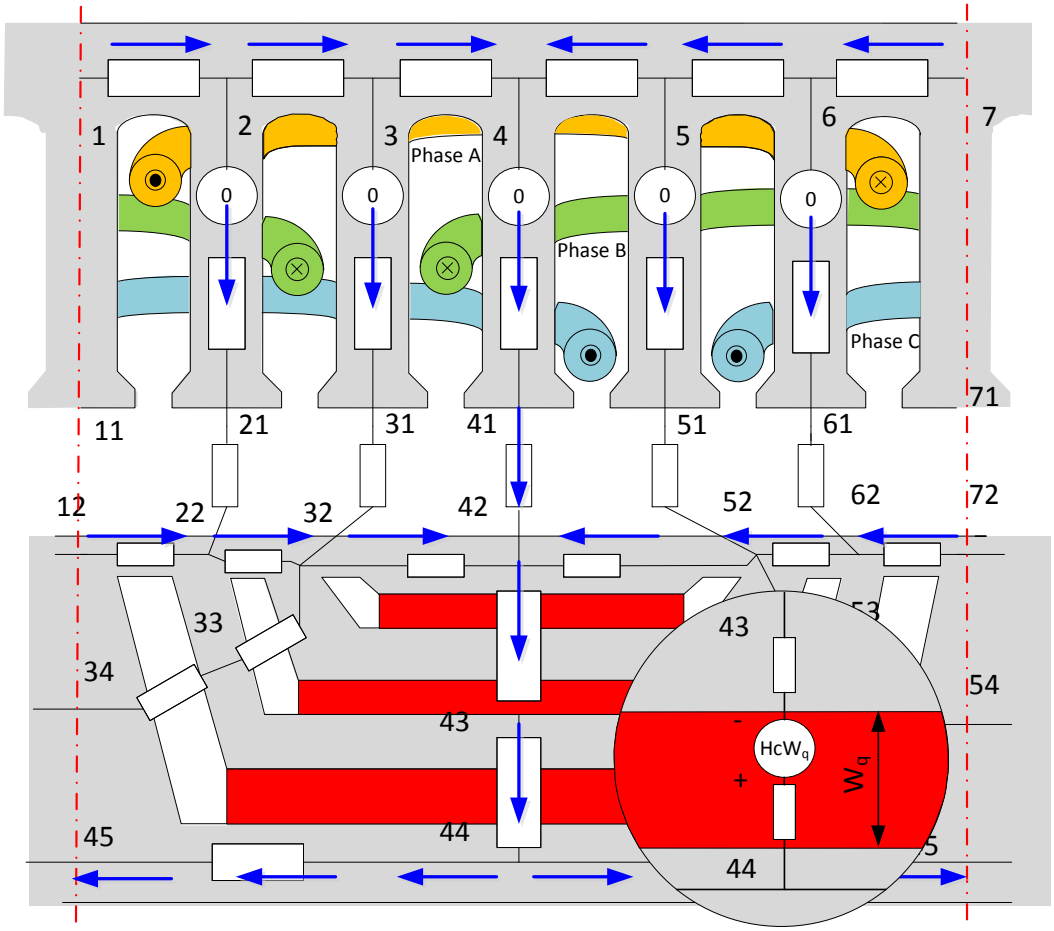


Figure 49. Example of RN for a PMaSynRM

## 4.2.4 *d*-axis reluctance network

On the other hand, the direct position is the position with the major flux. Then, the reluctance of the machine in *d*-position has to be the smallest, so the magnetic flux crosses the flux carriers or segments. The relative position between rotor and stator change to force the magnetic flux to cross the magnetic material in the rotor. Then, keeping constant the electric loading of the *q*-position (71) and turn the rotor 90º electrical degree. Figure 50 shows the RN of the same example, but the rotor is located in direct position.

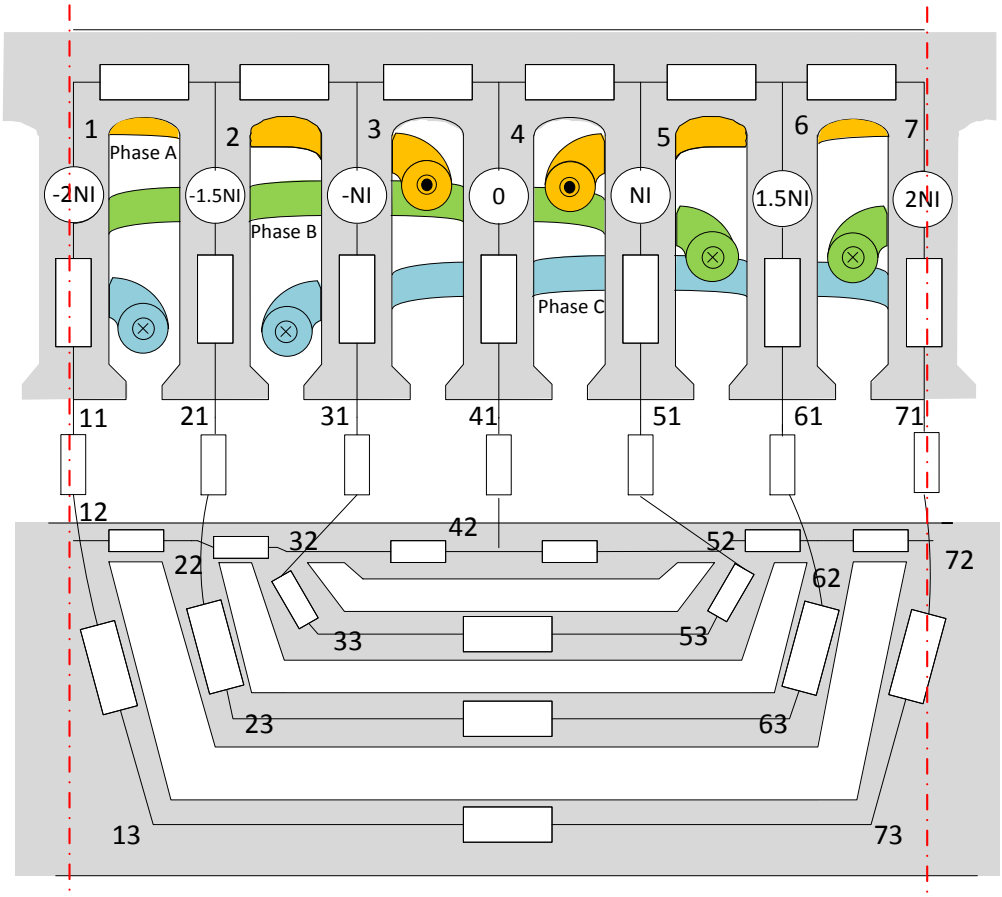


Figure 50. Example of a RN of direct position

It can be observed that the maximum MMF is located in the extremes of the pole and the zero in the middle. Then, the magnetic flux is forced to cross the flux carriers as shown in Figure 50. The MMF distribution is calculated according to (61) and it is detailed in Table 2.

Table 2. MMF distribution for *d*-position

| Teeth | 1 | 2 | 3 | 4 | 5 | 6 | 7 |
|---|---|---|---|---|---|---|---|
| Phase A | $-N\hat{I}$ | $-N\hat{I}$ | $-N\hat{I}$ | 0 | $N\hat{I}$ | $N\hat{I}$ | $N\hat{I}$ |
| Phase B | $-0.5N\hat{I}$ | $-0.5N\hat{I}$ | $-0.5N\hat{I}$ | $-0.5N\hat{I}$ | $-0.5N\hat{I}$ | 0 | $0.5N\hat{I}$ |
| Phase C | $-0.5N\hat{I}$ | 0 | $0.5N\hat{I}$ | $0.5N\hat{I}$ | $0.5N\hat{I}0$ | $0.5N\hat{I}$ | $0.5N\hat{I}$ |
| MMF | $-2N\hat{I}$ | $-1.5N\hat{I}$ | $-N\hat{I}$ | 0 | $N\hat{I}$ | $1.5N\hat{I}$ | $2N\hat{I}$ |

Taking into account the magnetic symmetry, the final RN represents a half of magnetic pole as in the *q*-position. Figure 51 shows the RN of direct position. The blue arrows represent the unknown magnetic fluxes. The magnetic flux in rotor follows the magnetic steel, so the reluctance in this position is smaller than the quadrature position. However, the inductance is strongly related with the magnetic saturation since practically all the reluctances vary with it.

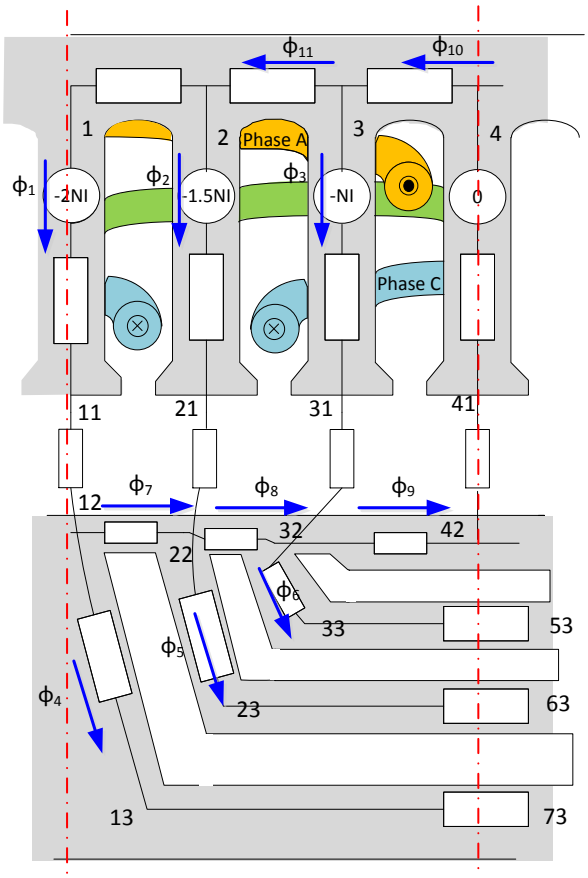


Figure 51. Final *d*-RN of the chosen example

Note that, in this case the number of unknown values is eleven, so a system formed by eleven equations is required. The equation system is formed by (69-70) as in *q*-position. The final equation system for this example is given by;

$$\begin{bmatrix} MMF_1 \\ MMF_1 \\ MMF_2 \\ MMF_2 \\ MMF_3 \\ MMF_3 \\ 0 \\ 0 \\ 0 \\ 0 \\ 0 \end{bmatrix} = \begin{bmatrix} \Re_{1T} & 0 & 0 & \Re_{4T} & 0 & 0 & 0 & 0 & 0 & \Re_{3-4} & \Re_{2-3} \\ \Re_{1T} & 0 & 0 & 0 & \Re_{5T} & 0 & \Re_{12-22} & 0 & 0 & \Re_{3-4} & \Re_{2-3} \\ 0 & \Re_{2T} & 0 & 0 & \Re_{5T} & 0 & 0 & 0 & 0 & \Re_{3-4} & \Re_{2-3} \\ 0 & \Re_{2T} & 0 & 0 & 0 & \Re_{6T} & 0 & \Re_{22-32} & 0 & \Re_{3-4} & \Re_{2-3} \\ 0 & 0 & \Re_{3T} & 0 & 0 & \Re_{6T} & 0 & 0 & 0 & \Re_{3-4} & 0 \\ 0 & 0 & \Re_{3T} & 0 & 0 & 0 & 0 & 0 & \Re_{32-42} & \Re_{3-4} & 0 \\ 0 & 0 & -1 & 0 & 0 & 1 & 0 & -1 & 1 & 0 & 0 \\ -1 & 0 & 0 & 1 & 0 & 0 & 1 & 0 & 0 & 0 & 0 \\ 0 & -1 & 0 & 0 & 1 & 0 & -1 & 1 & 0 & 0 & 0 \\ 0 & 0 & 1 & 0 & 0 & 0 & 0 & 0 & 0 & -1 & 1 \\ 1 & 1 & 0 & 0 & 0 & 0 & 0 & 0 & 0 & 0 & -1 \end{bmatrix} \begin{bmatrix} \phi_1 \\ \phi_2 \\ \phi_3 \\ \phi_4 \\ \phi_5 \\ \phi_6 \\ \phi_7 \\ \phi_8 \\ \phi_9 \\ \phi_{10} \\ \phi_{11} \end{bmatrix}$$

where;

$$\Re_{1T} = \Re_{1-2} + \Re_{1-11} + \Re_{11-12}$$
$$\Re_{2T} = \Re_{2-21} + \Re_{21-22}$$
$$\Re_{3T} = \Re_{3-31} + \Re_{31-32}$$
$$\Re_{4T} = \Re_{12-13} + 0.5\Re_{13-73}$$
$$\Re_{5T} = \Re_{22-23} + 0.5\Re_{23-63}$$
$$\Re_{6T} = \Re_{32-33} + 0.5\Re_{33-53}$$

The same process used to calculate the *q*-inductance is used to obtain the *d*-inductance. Then, the proposed iterative system shown in Figure 42 is used to solve the *d*-RN. In this example, the *d*-inductance is given by;

$$L_d = 2p\,N\frac{(\phi_1+\phi_2+\phi_3)}{I_d}2$$

where "$I_d$" is the direct current, which it is the phase peak current in each loop, the last "2" is necessary to takes into account the total magnetic pole (the RN only represents the half of a magnetic pole).

Then, solving the *d*-RN for all the currents the current dependency of the direct inductances is obtained, i.e. the curve $L_d(I_d)$ is calculated. At last, the same example is solved in FEA to obtain a comparison between both models. Figure 52 shows the flux lines of a one magnetic pole in direct position.

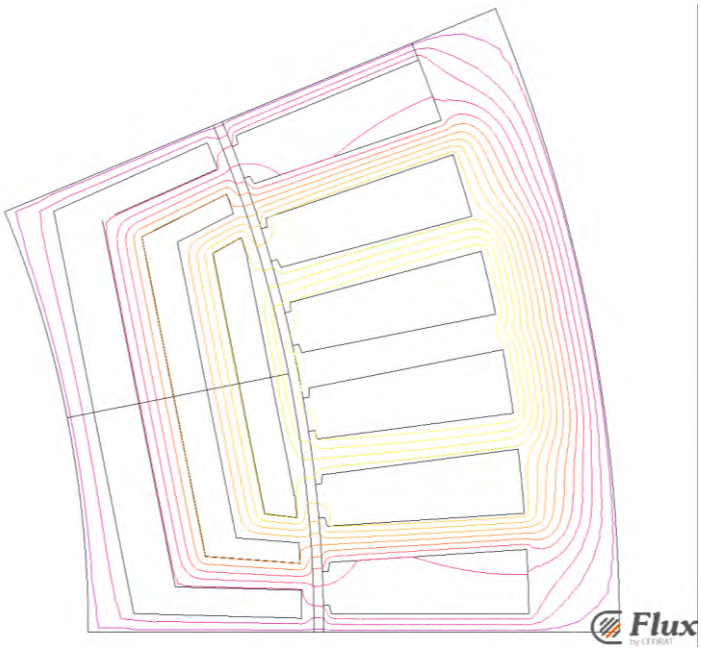


Figure 52. Magnetic flux lines of direct position of one magnetic pole

The comparison between both direct inductances is shown in Figure 53. It can be observed the strong relation between magnetic saturation and inductances in the *d*-position since the value of the inductance decrease when the *d*-current increase. Note that, the proposed RN is less accurate in the zone with high saturation. In fact, the error in the maximum current (300A) is 5.71% meanwhile the average error is 2.84% and the variance is 6.01%. The proposed model can be improved using a better discretization in the rotor. The RN only uses one reluctance in the innermost segment ($\Re_{13-74}$) as can be observed in Figure 50. The cross section of this reluctance is not constant, so if this reluctance is divided in three or more reluctances the accuracy of the example can increase.

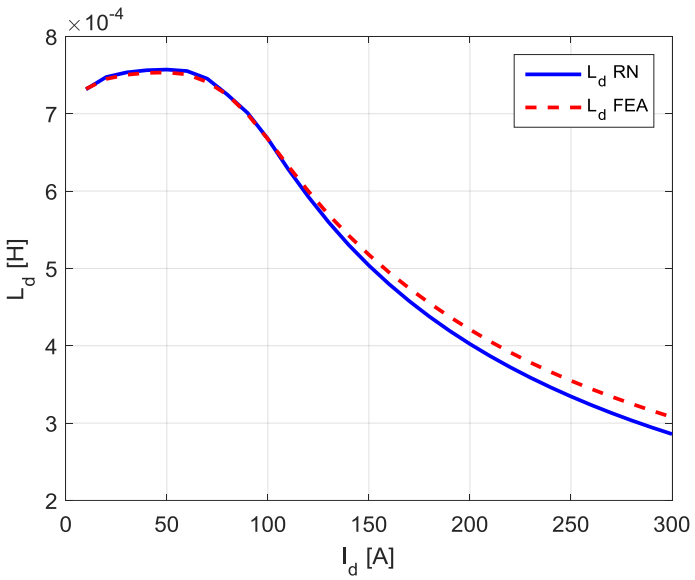


Figure 53. Comparison of the *d*-inductances

The use of magnets in the direct position does not make any change in the direct inductance calculation. In this position, the magnet flux linkage is zero as can be observed in the Figure 54. The fluxes of teeth 1, 2, and 3 are canceled with the fluxes of 5, 6, and 7 meanwhile flux of tooth 4 does not cross the phase A.

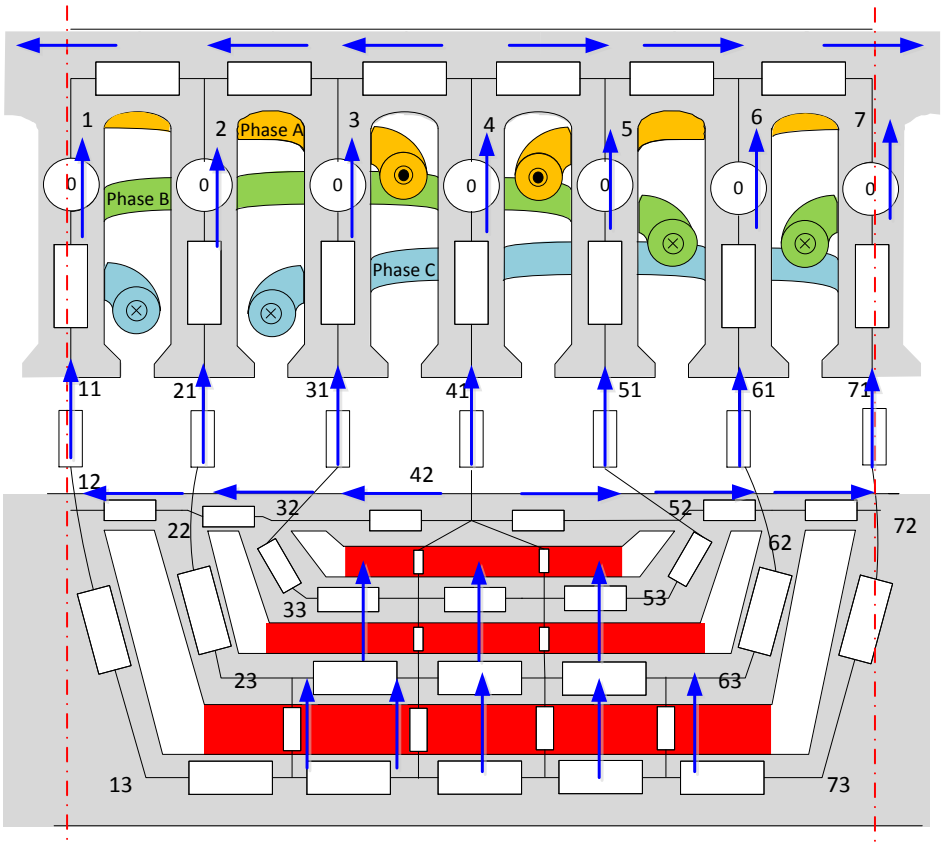


Figure 54. Magnet flux linkage in *d*-position for a PMaSynRM

Although the null effect of magnet in the direct inductance calculation, the RN must be solved including it. The modification of the RN is due to the direct inductances is hardly affected by the magnetic saturation, so the magnet affects the motor magnetic saturation. Concluding, in the case of PMaSynRM the direct inductance calculation is determined as the SynRM, but the RN must be modified due to the direction of magnetic flux provided by the magnets is different that the provided by the coils.

Note that, the magnetic symmetry is lost, so the complete RN is required. The asymmetry not only comes from the magnetic but also comes from the use of radials ribs as mention in chapter 2. Figure 55 shows the magnetic asymmetry. It can be observed the different magnetic behavior of both parts. For instance, in the case of radial rib the left part has less flux lines (blue lines) than the right part. Therefore, the left part is higher saturated than the right part.

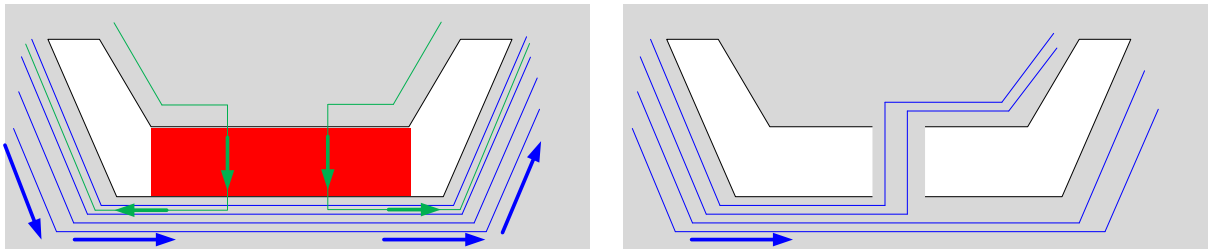

Figure 55. Illustration of the magnetic asymmetry.

## 4.3 Cross-coupling saturation

In the previous section, the process to calculate the self-current dependency of the *dq*-inductances is developed. However, the cross-coupling saturation is neglected due to the presented RN are decoupled, i.e. the *q*-RN is solved considering *d*-current zero and the other way round. The cross-coupling saturation appears when the current is not fixed in one magnetic axis, i.e. when the magnetic material is saturated by the both currents. Although the cross-coupling saturation exists in all the topologies, it has a big impact in SynRM and PMaSynRM.

The direct inductance decreases a lot with the magnetic saturation, so the inductance considering the cross-coupling saturation must be calculated to obtain a better estimation of the motor performances. Furthermore, these kinds of machines use current angles near to 45º, so in the normal use of the machines the current won't be in one axis. Then, determining the variation of the inductances considering the *dq*-currents is necessary.

In this section, the proposed magnetic model to calculate the cross-coupling saturation is explained. This model allows calculating the magnetic saturation for each current angle, so the estimation of the iron losses is improved. In addition, the calculation of the torque using the proposed RN is shown, and a multi-static magnetic model is developed in order to estimate the torque ripple.

### 4.3.1 Inductance calculation

The calculation of inductance considering the cross-coupling saturation requires the use of a complex magnetic model. This new model aims to combine the RN of *dq*-axes to obtain a new magnetic model capable to analyze not only the both inductances but also all the *dq*-current combinations. Figure 56 shows the proposed RN for the same example.

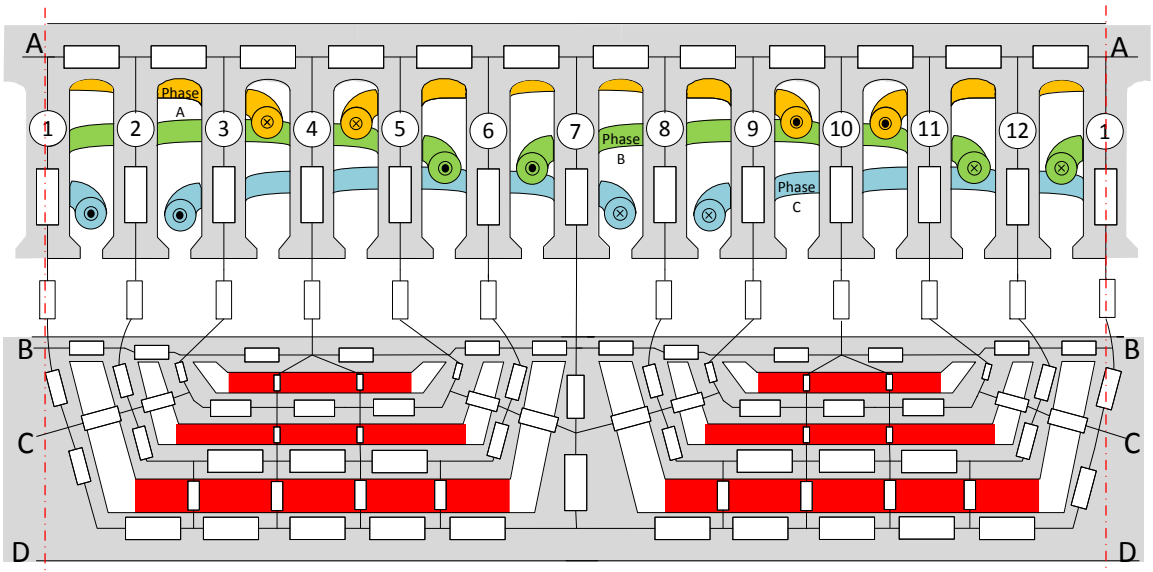


Figure 56. Complete magnetic model

Note that, the red lines represent the same points, i.e. the RN is connected in the points A, B, C, and D. When the maximum MMF stays in tooth 1 and the minimum in 7, the direct position appears.

However, when the maximum position is located in tooth 4 and the minimum in 10, the magnetic position is quadrature. Then, combining other MMF wave's form other magnetic position appears.

The MMF distribution is calculated according to (61) and is shown in Table 3.

Table 3. MMF distribution of complete RN

| Teeth | 1 | 2 | 3 | 4 | 5 | 6 | 7 | 8 | 9 | 10 | 11 | 12 |
|---|---|---|---|---|---|---|---|---|---|---|---|---|
| Phase A | $Ni_a$ | $Ni_a$ | $Ni_a$ | 0 | $-Ni_a$ | $-Ni_a$ | $-Ni_a$ | $-Ni_a$ | $-Ni_a$ | 0 | $Ni_a$ | $Ni_a$ |
| Phase B | $-Ni_b$ | $-Ni_b$ | $-Ni_b$ | $-Ni_b$ | $-Ni_b$ | 0 | $Ni_b$ | $Ni_b$ | $Ni_b$ | $Ni_b$ | $Ni_b$ | 0 |
| Phase C | $-Ni_c$ | 0 | $Ni_c$ | $Ni_c$ | $Ni_c$ | $Ni_c$ | $Ni_c$ | 0 | $-Ni_c$ | $-Ni_c$ | $-Ni_c$ | $-Ni_c$ |

Then the MMF on each tooth depends on the current of each phase ($i_a, i_b,$ and $i_c$). Using the well-known Park's ant-transformation the *dq*-current combination is transformed to the three phases current.

$$\begin{bmatrix} i_a \\ i_b \\ i_c \end{bmatrix} = \begin{bmatrix} \cos(\theta_m) & -\sin(\theta_m) \\ \cos\left(\theta_m - \frac{2\pi}{3}\right) & -\sin\left(\theta_m - \frac{2\pi}{3}\right) \\ \cos\left(\theta_m + \frac{2\pi}{3}\right) & -\sin\left(\theta_m + \frac{2\pi}{3}\right) \end{bmatrix} \begin{bmatrix} I_d \\ I_q \end{bmatrix} \quad (75)$$

Where, "$\theta_m$" represents the mechanical position of the rotor. Then, aligning the direct position ($\theta_m$ is zero) with the phase A the transformation is:

$$\begin{bmatrix} i_a \\ i_b \\ i_c \end{bmatrix} = \begin{bmatrix} 1 & 0 \\ -\frac{1}{2} & \frac{\sqrt{3}}{2} \\ -\frac{1}{2} & -\frac{\sqrt{3}}{2} \end{bmatrix} \begin{bmatrix} I_d \\ I_q \end{bmatrix} \quad (76)$$

In this point, the MMFs provided by the coils are function of *dq*-currents. Then, the RN is solved using (69-70), but the equation system if formed by a huge number of equations since the proposed RN cannot be simplify due to the magnetic symmetry is lost. Then, the complete RN (see Figure 56) must be solved to obtain the current dependency of the *dq*-inductances.

When the RN is solved, the magnetic flux of the different phases is required to calculate the *dq*-magnetic flux. Considering the example of Figure 56 the flux of different phases is given by;

$$\begin{aligned} \phi_a &= pN\left(\phi_1 + \phi_2 + \phi_3 + \phi_{11} + \phi_{12} - (\phi_5 + \phi_6 + \phi_7 + \phi_8 + \phi_9)\right) \\ \phi_b &= pN\left(\phi_7 + \phi_8 + \phi_9 + \phi_{10} + \phi_{11} - (\phi_1 + \phi_2 + \phi_3 + \phi_4 + \phi_5)\right) \\ \phi_c &= pN\left(\phi_9 + \phi_{10} + \phi_{11} + \phi_{12} + \phi_1 - (\phi_3 + \phi_4 + \phi_5 + \phi_6 + \phi_7)\right) \end{aligned} \quad (77)$$

Then, using the Park's transformation the *abc*-magnetic fluxes are transformed to the *dq*-magnetic fluxes.

$$\begin{bmatrix} \phi_d \\ \phi_q \end{bmatrix} = \frac{2}{3} \begin{bmatrix} \cos(\theta_m) & \cos\left(\theta_m - \frac{2\pi}{3}\right) & \cos\left(\theta_m + \frac{2\pi}{3}\right) \\ -\sin(\theta_m) & -\sin\left(\theta_m - \frac{2\pi}{3}\right) & -\sin\left(\theta_m + \frac{2\pi}{3}\right) \end{bmatrix} \begin{bmatrix} \phi_a \\ \phi_b \\ \phi_c \end{bmatrix} \quad (78)$$

When according to the mechanical position chosen ($\theta_m = 0$), the final transformation is;

$$\begin{bmatrix} \phi_d \\ \phi_q \end{bmatrix} = \frac{2}{3} \begin{bmatrix} 1 & -\frac{1}{2} & -\frac{1}{2} \\ 0 & \frac{\sqrt{3}}{2} & -\frac{\sqrt{3}}{2} \end{bmatrix} \begin{bmatrix} \phi_a \\ \phi_b \\ \phi_c \end{bmatrix} \quad (79)$$

Finally, for each combination of *dq*-current, both inductances can be calculated, so the cross-coupling saturation is considered.

$$L_d = \frac{\phi_d}{I_d}$$
$$L_q = \frac{\phi_{q-}\Psi_{pm}}{I_q} \quad (80)$$

Remember that the magnet flux linkage must be eliminated in the inductance calculation and the "$\phi_{pm}$" is calculated when the "$I_q$" is 0. The algorithm to calculate the current dependency of the inductances is detailed below;

1: Set the *dq*-currents steps
2: **for** $I_d = 0$ to $I_d = I_{max}$ **do**
3: **for** $I_q = 0$ to $I_q = I_{max}$ **do**
4: Use the park's anti-transformation to calculate the phase currents (75)
5: Calculate the MMF of each tooth (61)
6: Solve the magnetic model
7: Calculate the fluxes of all phases. Example (77)
8: Use the park's transformation to calculate the *dq*-fluxes
9: **if** $I_q == 0$
10: $\Psi_{pm}(I_d) = \phi_q$
11: **else**
12: Use (70) to calculate the *dq*-inductances
13: **end**
14: save data: $\Psi_{pm}(I_d); L_d(I_d, I_q); L_q(I_q, I_d)$
15: **end**
16: **end**
17:**end**

Algorithm 2. *dq*-inductances calculation considering cross-coupling

It is worthy to mention that the line 6 of Algorithm 2 aims to solve the magnetic model which is based on (69-70). Moreover, the reluctances of the magnetic parts are function of the magnetic saturation, so the solving procedure has to be an iterative process as explain before (the innermost loop of Figure 42).

However, the large number of equation in this case makes difficult the creation the equation system. Then, the use of software capable to solve different physics domains is required to help in the process to create the equation system. In this context, the complete magnetic model is solved using SimScape (MATLAB®). SimsCape is multi-physics software to calculate the behavior of models, which in this case the models represents electric motors, in different domains, such as thermic, electric, mechanical or magnetic domains. Furthermore, it is software based on oriented object programming. It means that the models can be created from elements (objects), i.e. objects, which represent the different parts of the machine, such as yoke, tooth, magnets, and so forth, create the models, which represent the motor under study.

Therefore, the use of SimsCape not only helps to solve the equation system but also increase the adaptability of the proposed magnetic model. One of the problems of solving the RN using equations is the flexibility when the equation system changes with the motor geometry. For example, the number of flux barriers changes the magnetic path in the rotor and increases the number of

necessaries equations, or the number of teeth change the connections between stator and rotor, so the magnetic path are different.

Figure 57 shows the equivalency of the RN used before in SimsCape. Note that, the structure of the model is equivalent to the RN. There are reluctances and MMF in both models.

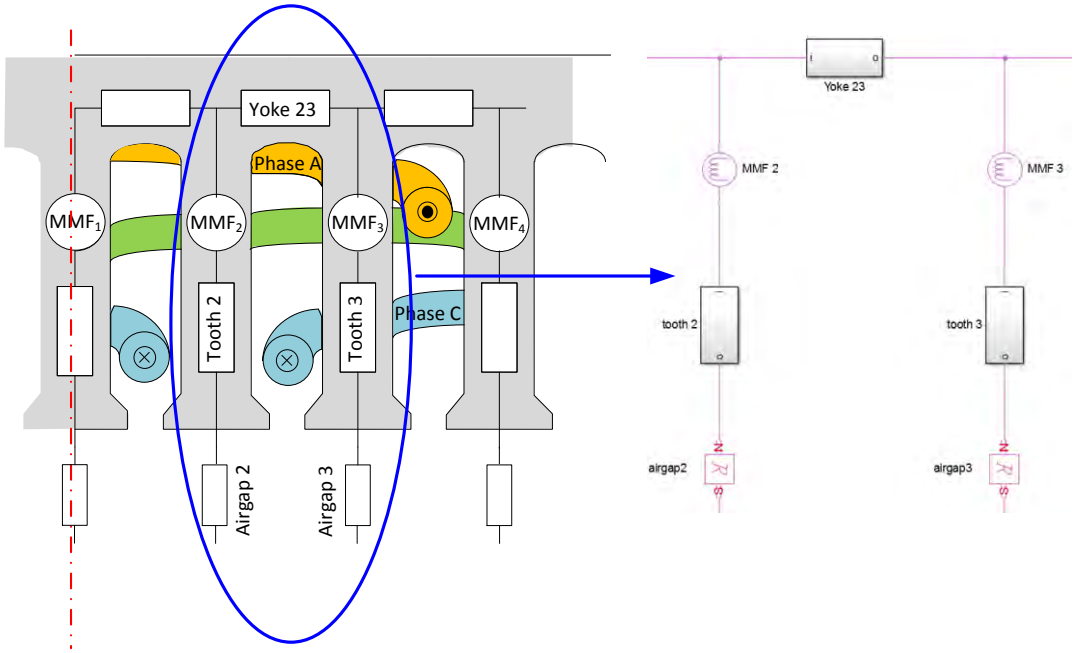


Figure 57. Example of a magnetic model in SimsCape

It can be note that the reluctance of magnetic parts and the reluctances of airgap are different. The airgap reluctances are constant since the relative permeability of the air is constant meanwhile the reluctance of the magnetic parts are variable. The detail of the variable reluctance is shown in Figure 58. Figure 58 depicts the interior of reluctance called *"tooth 3"*. The block "tooth 3" is formed by a variable reluctances, which is calculated according to (65), flux sensor, which read the magnetic flux, a gain, which divides the flux by the cross section, and a lookup table (LUT), which is formed by the curve B-$\mu_r$. In addition, there are two extra blocks, which are called *"PS-Simulink converter"* and *"To Workspace"*. These blocks are necessary to read the information obtained in SimsCape. Then, the magnetic flux of each tooth is required to calculate the inductances (77-80).

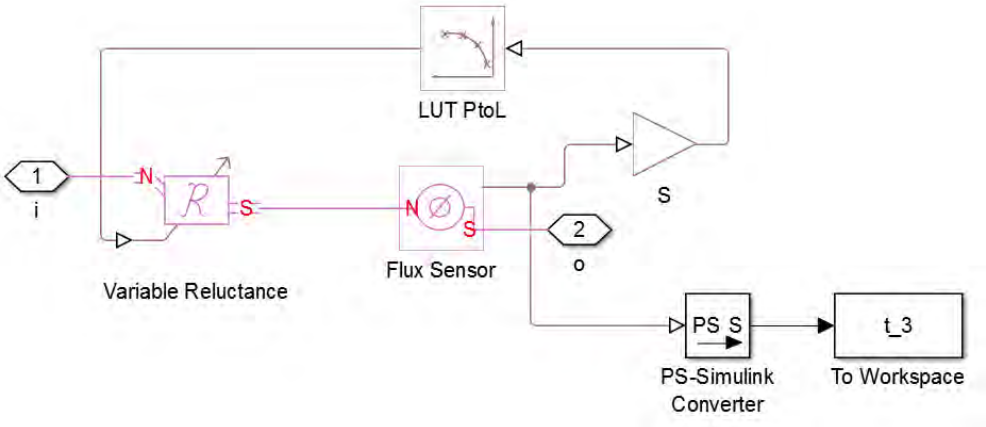


Figure 58. Details of the reluctance "tooth 3"

Moreover, the use of SimsCape allows increasing the level of the detail in the RN, for instance the tooth can be more discretized or the reluctances in the slot opening can be introduced as shown in Figure 59.

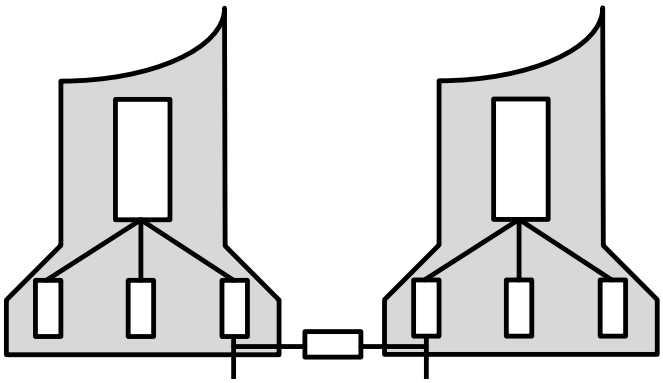

Figure 59. Improving of the magnetic model

Finally, the calculated *dq*-inductances using the complete magnetic model are depicted in Figure 60. The method is compared against FEA, and the average error of *q*-inductances is 5.3% and the variance is 8.6% meanwhile the average error of *d*-inductance is 2.9% and the variance is 2.6%.

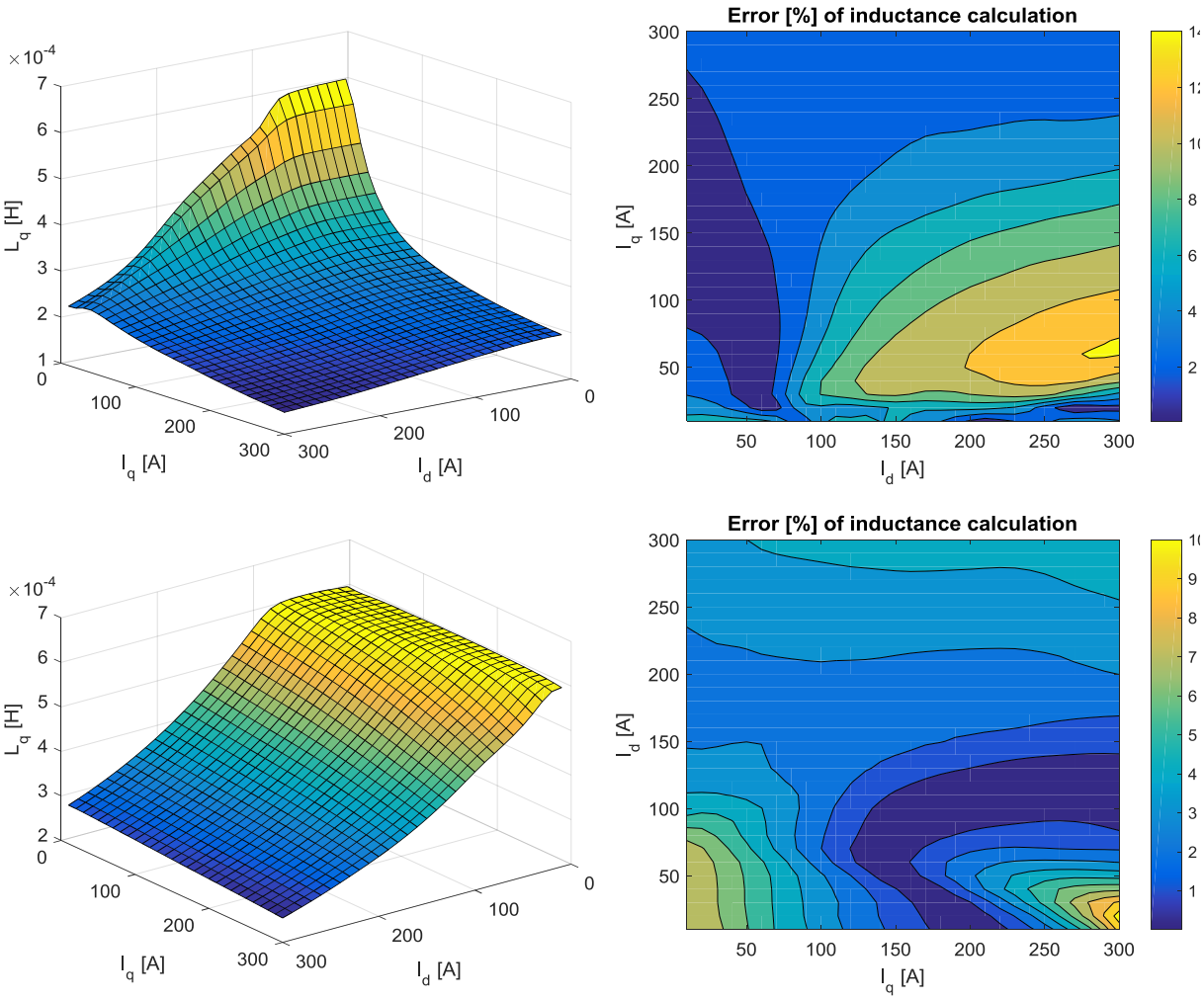


Figure 60. Inductances and error considering cross-coupling saturation

### 4.3.2 Multi-static magnetic model

Taking advantage of the benefits of SimsCape, the complexity of magnetic model increases in order to develop a multi-static magnetic model. The multi-static model allows calculating the torque ripple. Torque ripple is one of the major drawbacks of these machines, so it could be good performance to optimize. Using this multi-static magnetic model the torque ripple can be calculated without the use of FEA. Therefore, it can be included in the cost function of the proposed methodology.

Figure 61 shows how the multi-static reluctance network changes the connections between rotor and stator to evaluate the motor properties in the different motor positions. The different connections simulate the multi-static positions or steps. The rotor turns with an imposed mechanical speed (□m), and thus, the relative position between the rotor and stator changes at each step. Figure 61 shows step 1, in which the teeth and segments are aligned. In next step (step 2), the rotor is in the subsequent position, so the stator-rotor connections are different.

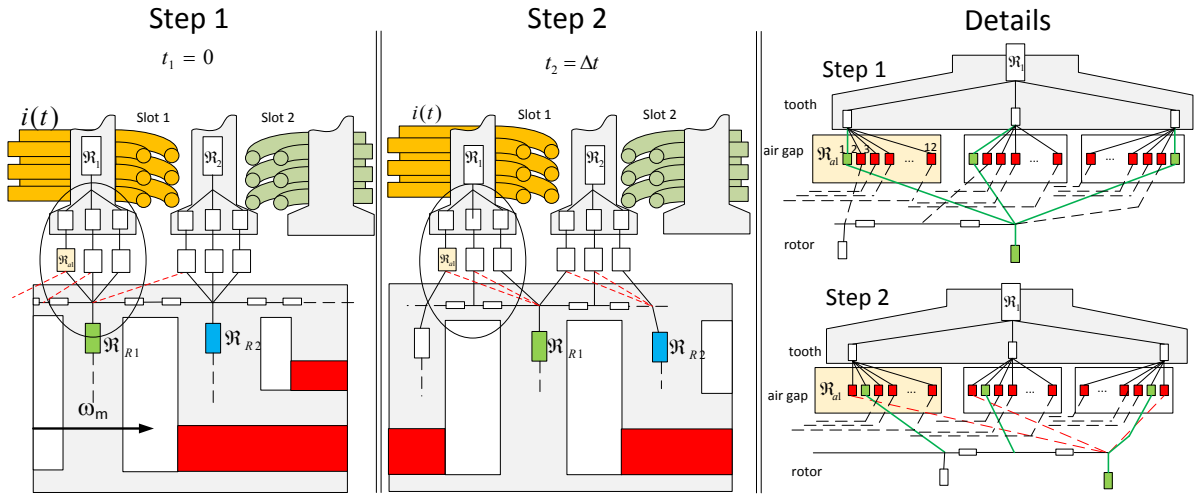


Figure 61. Air gap connection of multi-static reluctance network. Two steps of the magnetic model are shown. Details of the air gap connection

To calculate the torque ripple, the reluctance network considers all possible relative positions of the rotor and stator. First, the current space-vector angle is calculated. The torque is calculated for each current angle, to calculate the current leading to the maximum torque per ampere. The torque is calculated from the Maxwell's stress tensor. It deals with the concept of tangential stress, which is calculated from the magnetic flux density in the airgap $B_g$, and the linear current density $A$ as,

$$\sigma_{Ftan} = B_g(x,t) \cdot A(x,t) \qquad (81)$$

Both, $B_g$ and $A$ depend on the position and time. The proposed RN allows calculating the airgap flux density. The linear current density is calculated as the current sum of the conductors within a slot divided by the slot pitch.

Figure 62 shows the magnetic flux density distribution along one pole pair, calculated with the proposed RN, and the current in the different slots. It is worthy to mention that the RN calculates the magnetic flux density in the discretized parts, so the effect of the slots openings cannot be observed.

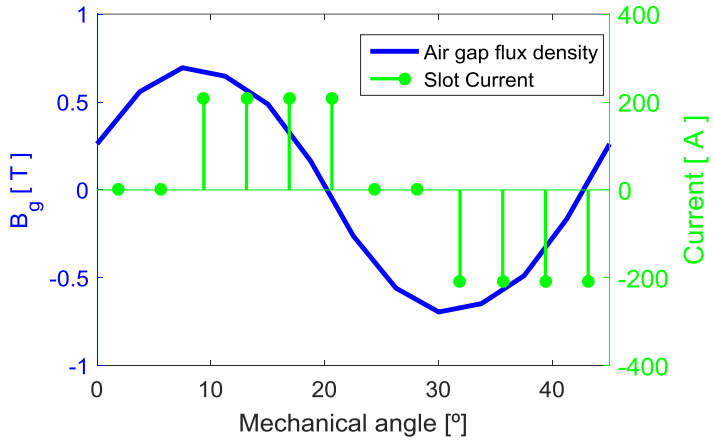


Figure 62. Magnetic flux density and current distribution along one pole pair with 12 slots

Then, the torque is obtained by combining the tangential stress calculated by (81) with the airgap surface. Therefore, the torque can be simplified according to (82),

To calculate the torque ripple, the reluctance network considers all possible relative positions of the rotor and stator. First, the current space-vector angle is calculated. The torque is calculated for each current angle, to calculate the current leading to the maximum torque per ampere. It is calculated using the interaction between the current in the conductors and the magnetic flux density as,

$$T = \frac{D_g}{2} l_{eff} p N \sum_i (BI)_i \qquad (82)$$

Where the sum is for each slot in one magnetic pole pair, so the coefficient i = 1,2,…,12 for the case analyzed. The "$I$" represents the instant current in each conductor in i-slot meanwhile the "$B$" is the magnetic flux density of the airgap under the conductors. "$N$" represents the number of conductors in each slot, "$D_g$" is the airgap diameter, "$l_{eff}$" is the effective length, and "$p$" is the pole pairs.

Then, according to (82) the magnetic model is solved for the whole current space vector to obtain the relation between torque and current angle.

Figure 63 shows the torque of the machine as function of the current angle. As shown, the error with respect to FEA at the maximum torque is below 2.5%.

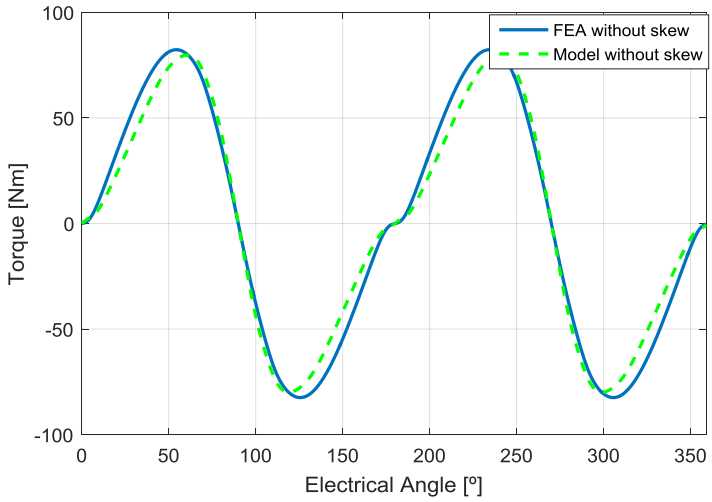


Figure 63. Torque curve depending on current angle (α)

Next, considering the rotor position at the maximum torque, which in this case corresponds to a current angle $\alpha$= 55º (although this value varies with the magnetic saturation), the torque ripple in each discrete rotor position is calculated from (82) by turning the rotor two pole pitches. The rotor angular position step is settled to half of the slot pitch to obtain a sufficient resolution with the minimum number of calculations. The current state varies with the steps as,

$$\begin{aligned} i_a &= \hat{I}\sin(\omega_m \cdot p \cdot t + \alpha) \\ i_b &= \hat{I}\sin\left(\omega_m \cdot p \cdot t + \alpha - \frac{2\pi}{3}\right) \\ i_c &= \hat{I}\sin\left(\omega_m \cdot p \cdot t + \alpha + \frac{2\pi}{3}\right) \end{aligned} \qquad (83)$$

where *"$\hat{I}$"* is the peak phase current [A], "$\omega_m$" is the mechanical angular speed [rad/s], "$\alpha$" is the current angle obtained in Figure 63 (55º in this case) and "$t$" is the time [s]. The time increase according to;

$$t = \frac{1}{2}\frac{\tau_s}{\omega_m}k\,; \quad k = 0,1,2,3,\ldots. \qquad (84)$$

where "$\tau_s$" is the slot pitch [m] and *k* is the step number.

Figure 64 compares the torque ripple obtained from the model proposed in this example with that from FEA. Since the torque ripple is quite important, rotor skew will be included in the design. Rotor skew is preferred over stator skew due to the increase of copper weight and cost of the last option.

A skew angle of one slot pitch has been chosen. To take into account the skew effects, the motor is divided into three sections, each one consisting of the same reluctance network as in Figure 61 but with different rotor positions and *dq* currents.

The current angle in (83) must be different in each section. In the first section of the skewed model, the current angle is $\alpha$, which in this case is 55º, whereas in the two remaining sections, it must be $\alpha$ ± skew_angle/2, respectively. The total torque considering the skew is obtained by adding the torque components of the three sections, which is shown in Figure 64.

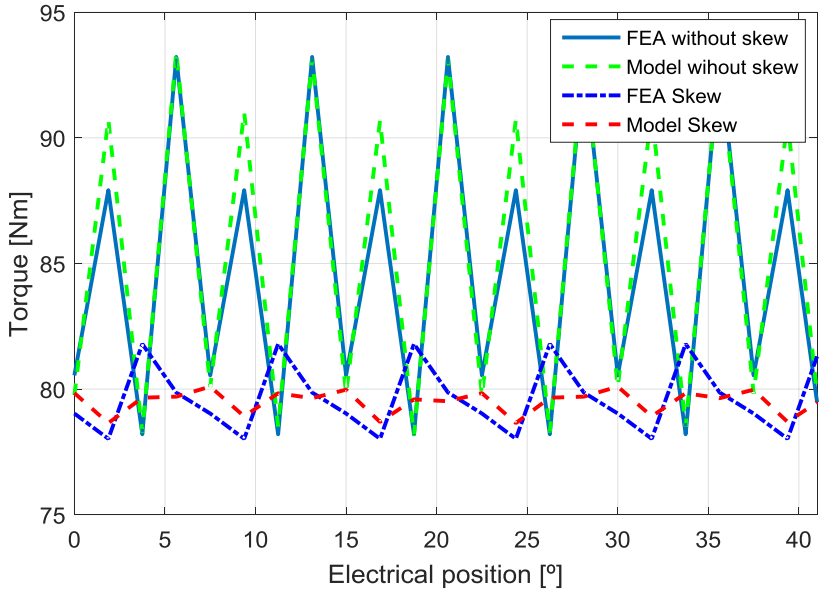


Figure 64. Torque ripple versus electrical position

## 4.4 Conclusions

The presented chapter deals with the contributions on magnetic model calculation. Some conclusions can be extracted,

- The use of magnets or radials ribs creates magnetic asymmetries in the model, so the RN of the total pole is required.
- The cross-coupling saturation can be calculated using a complex RN, which it can be solved using SimsCape instead of traditional equation system.
- The use of SimsCape allows improving the detail of the RN. Then, the magnetic saturation of each motor part can be calculated for all the possible combinations of *dq*-currents.
- The multi-static magnetic model allows calculating the torque ripple, so it can be included in the cost function without the use of FEA.

# 5.

# Thermal model

This chapters presents the contributions of this thesis to analysis of thermal model. In this regard, the procedure to calculate the thermal resistances, losses, and temperatures is presented.

*CONTENTS:*

# 5. Thermal model

## 5.1 Introduction

One of the main handicaps in the motor design is the thermal behavior since the temperature is one of the limits of the machine. The winding temperature is limited by the insulators meanwhile the magnetic properties of the magnets decrease with the temperature. Then, the thermal evaluation during the design process is mandatory to obtain a good design.

On the other hand, the optimization of the machines in terms of power density increases the risk of exceeding the thermal limit of the machine. Therefore, thermal behavior and constraints must be included in the optimization procedure.

Therefore, the calculation of the thermal behavior of the machine in each iteration of the optimization is required for two reasons. The first one is to discard the motors which overpass the thermal limits. The second one is to calculate the correct value of the motor's parameters to improve the performances of the machine.

The thermal behavior can be evaluated using different methods [119], such as using analytical thermal network, using FEA, and computed fluid dynamic (CFD) methods, among others. The proposed work calculates the temperature using a thermal network (TN) because it allows a fast and low-computational thermal analysis. The thermal network is based on lumped parameters, were the motor geometry is represented as thermal resistances. The TN is one of the most used methods to calculate the thermal behaviors. However, the accuracy of TN is hardly related with the calculation of the heat-transfer coefficients. In the current section, the explanation of the thermal network used in the proposed optimization methodology is developed.

## 5.2 Heat transfer calculation

The thermal resistance calculation depends on the heat transfer between two objects. Depending of the contact between surfaces the heat transfers can be by conduction, convection or radiation, the last is not included in the proposed work. This section aims to explain the thermal resistances of the different parts of the motor.

### 5.2.1 Conduction

Thermal conduction describes the transfer of heat by collisions of particles in an object. The heat transfer in conduction is given by the Fourier's' Law. The Fourier's law relates the heat transfer with the gradient of temperature.

$$P = -\lambda S \frac{\partial \theta}{\partial x} \quad (85)$$

Where, "$P$" is the heat transfer, "$\lambda$" is the thermal conductivity of the material, "$S$" is the cross section, and "$\frac{\partial \theta}{\partial x}$" represents the variation of the temperature in the direction of the heat transfer.

According to (85), the heat resistance varies depending on the coordinates of the heat transfer. On the one hand, Figure 65 shows the heat transfer in one direction.

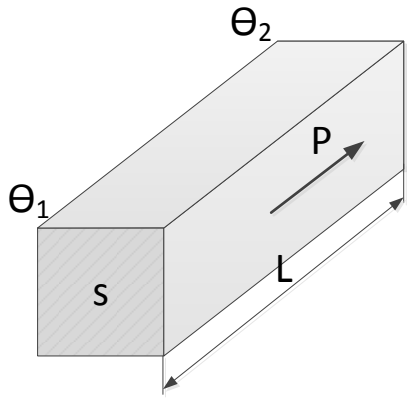


Figure 65. Heat transfer in one dimension

The thermal resistance in this case is given by;

$$R_{th} = \frac{L}{\lambda S} \quad (86)$$

On the other hand, Figure 66 shows the heat transfer in cylindrical coordinates.

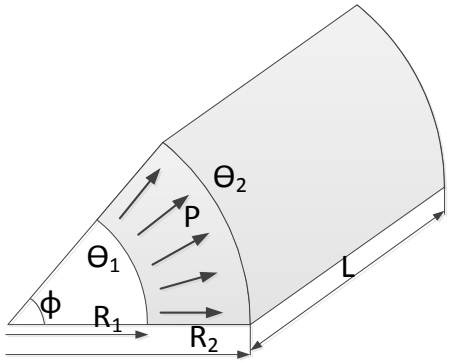


Figure 66. Heat transfer in cylindrical coordinates

The thermal resistance in this case is given by;

$$R_{th} = \frac{\ln\left(\frac{R_2}{R_1}\right)}{\lambda \phi L} \quad (87)$$

### 5.2.2 Convection

When the heat transfer of a body is dissipated by means of a fluid is called convection. Convection occurs between a surface and fluid when there is a temperature gradient. There are two kinds of convection, the free and the forced. The first one occurs when the fluid around the body is not being moved by an external forced meanwhile in forced convection there is an external force applied in the fluid. The convection heat resistance is given by;

$$R_{th} = \frac{1}{hA} \quad (88)$$

Where "$h$" is the heat transfer coefficient, and "$A$" is the contact surface between body and fluid. The value of "$h$" is given by;

$$h = \frac{N_U \lambda_f}{x} \quad (89)$$

Where, "$N_U$" is the Nusselt number, which is a dimensionless number related to the heat transfer, "$\lambda_f$" is the thermal conductivity of the fluid, and "$x$" is the characteristic length.

The Nusselt number is calculated as function of the Reynolds number and the Prandtl number. However, it is calculated using empirical formulas.

### 5.2.3 Thermal resistance calculation

There is a lot of information in the literature to calculate the thermal resistance of the machines. Many authors had developed several equations to calculate the different heat transfers on the electric motors.

In a machine, the convection heat transfers are located in the space between the motor and the frame and in the airgap. Furthermore, the heat transfer between the frame to the exterior is a natural convection.

The interior air thermal resistances can be divided in interior air to frame (90), interior air to rotor (93), and interior air to end-winding (96). According to different authors [120, 121] the heat transfer coefficient "$h$" in (88) is known, so the different interior heat transfers are given by,

$$R_{interior1} = \frac{1}{h_1 A_1} \quad (90)$$

Where; the heat transfer is given by;

$$h_1 = 15 + (6.75 \omega_m R_{or})^{0.65} \quad (91)$$

Where, "$\omega_m$" is the mechanical speed in rad/s, "$R_{or}$" represents the rotor outer radius, and the 15 and 0.65 factors are obtained from literature.

Remember that "$A_1$" is the contact area between the interior air with the frame, i.e. the area of the two end-caps and the cylindrical area of the frame in contact with the air. Hence, the "$A_1$" is calculated as follows;

$$A_1 = 2\pi R_{os}^2 + 2\pi R_{os}(L - L_{stk}) \quad (92)$$

Where "$R_{os}$" is the outer stator radius, "$L$" is the total length of the machine, and "$L_{stk}$" is the stack length of the machine.

$$R_{interior2} = \frac{1}{h_2 A_2} \quad (93)$$

Where, "$h_2$" is given by;

$$h_2 = (16.4\omega_m R_{or})^{0.65} \quad (94)$$

As before, the 16.4 and 0.65 factors are obtained from literature. And the "$A_2$" is the contact area between interior air and rotor, so it is given by;

$$A_2 = 2\pi(R_{or} - R_{ir})^2 \quad (95)$$

Where "$R_{ir}$" is the inner rotor radius.

$$R_{interior3} = \frac{1}{h_3 A_3} \quad (96)$$

Where "$h_3$" is calculated as the same principle as above, so it is given by;

$$h_3 = 6.5 + (5.25\omega_m R_{or})^{0.6} \quad (97)$$

And the "$A_3$" is the contact area between the interior air and the end-winding, so it is approximated as follows;

$$A_3 = A_{slot}\, 2\pi \left(R_{is} + \frac{h_s}{2}\right) \quad (98)$$

Where "$A_{slot}$" is the equivalent slot area, which is considered as circular, "$R_{is}$" is the inner stator radius, and "$h_s$" is the height of the slot.

Then, the heat transfer of airgap is calculated according to (88);

$$R_{ig} = \frac{1}{h_g A_g} \quad (99)$$

Where "$A_g$" is given by;

$$A_g = 2\pi R_g L_{stk} \quad (100)$$

Where "$R_g$" is the airgap radius.

The "$h_g$" is obtained using the Nusselt number (101). The characteristic length is two times the airgap length "$g$" meanwhile the Nusselt number is given by;

$$N_u = 0.409 T_a^{0.241} - 137 T_a^{-0.75} \quad (101)$$

Where "$T_a$" is the Taylor number, which it is calculated as follows;

$$T_a = \frac{\omega_m^2 R_g\, g^3}{v^2} \quad (102)$$

Where "$v$" is the kinetic viscosity of the fluid. It is given by;

$$v = \frac{\mu}{\rho} \quad (103)$$

Where "$\mu$" is the dynamic viscosity and "$\rho$" is the density of the air. Both values vary with the temperature and are given by;

$$\mu = \mu_o \frac{\theta + C}{\theta_O + C}\left(\frac{\theta}{\theta_O}\right);\ \rho = \frac{p_0}{TR_s} \quad (104)$$

Where, "$C$" is the Sutherland's constant for gases, which is equal to $120\ K$, "$\mu_o$" is the dynamic viscosity of the air at the reference temperature "$\theta_O$". The corresponding values are $18.27 \cdot 10^{-6}\ P_a s$ and $291.15\ K$, respectively. "$R_s$" is the specific gas constant and "$p_o$" is the absolute pressure. The value of these variables for dry air is $287.058\ J/kgK$and $101325 N/m^2$ respectively.

The convection between the housing and the exterior can be considered as natural convection. Then, according to [122] the Nusselts is given by;

$$N_u = a(G_r P_r)^b \quad (105)$$

Where, the different coefficients can be extracted from [122]. The value of these variables depends on the position of the motor and the type of flow (turbulent or laminar). Note that, equation (105) works with normal type of housing.

On the other hand, the conduction heat transfers are located in yoke, teeth, rotor, or slots. These thermal resistances are calculated using (86) or (87) depending on the geometrical characteristics.

The heat transfer of the yoke is given by;

$$R_{yoke} = \frac{\ln\left(\frac{R_{os}}{R_{is} + h_t}\right)}{2\pi\lambda_{steel} L_{stk}} \quad (106)$$

The thermal resistance of the tooth is calculated considering two different resistances in series. The tooth is considered square, so the first one is located on the bottom of the tooth meanwhile the second one is located in the rest of the tooth.

$$R_{tooth} = \frac{y}{\lambda_{steel} L_{stk} x} + \frac{h_t - y}{\lambda_{steel} L_{stk} b_t} \quad (107)$$

Furthermore, in the thermal behavior, the different teeth are distributed in a parallel position, so the final heat transfer is;

$$R_t = \frac{R_{tooth}}{Q_s} \quad (108)$$

Where, "$Q_s$" is the number of slots. The different geometric parameters of (86) and (87) are detailed in Fig

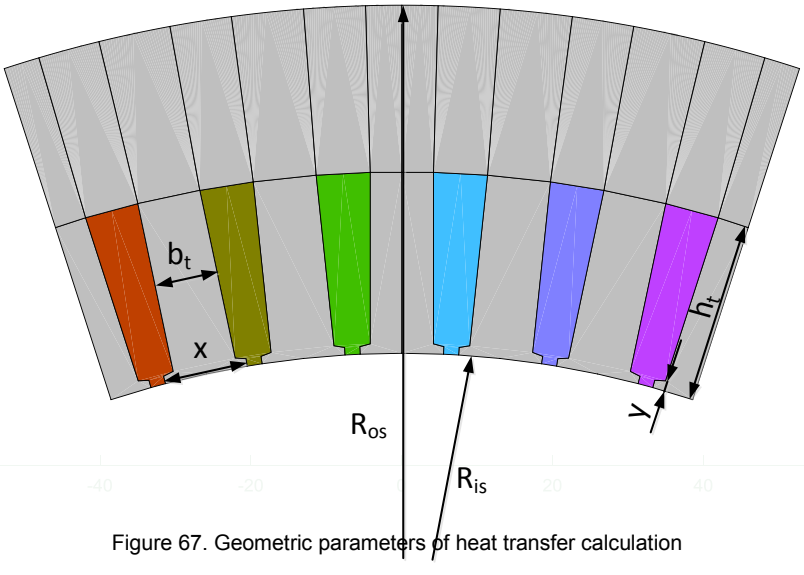


Figure 67. Geometric parameters of heat transfer calculation

Then, the heat transfer of the slots is calculated considering the equivalent thermal conductivity, because the slot is totally full of conductors and impregnation. The equivalent thermal conductivity, which is called the "Hashin and Shtrikman expression" [123] is calculated as follows;

$$\lambda_e = \lambda_{impr}\frac{(1+f_{cu})\lambda_{cu}+(1-f_{cu})\lambda_{impr}}{(1-f_{cu})\lambda_{cu}+(1+f_{cu})\lambda_{impr}} \quad (109)$$

Where, "$f_{cu}$" represents the volume ratio of the cupper in the slot.

Note that, equation (109) only considers two different materials, so the following simplification is required: the conductor insulation has the same thermal conductivity as the impregnation.

The equivalent thermal conductivity can be calculated using other approach, for instance [119].

$$\lambda_e = 0.2749\left((1-k_f)A_{slot}L_{stk}\right)^{-0.4471} \quad (110)$$

Where, "$k_f$" is the filling factor and "$A_{slot}$" is the surface of the slot.

Then, the heat transfer is calculated according to (86) and considering the parallel distribution as the teeth heat transfer.

$$R_w = \frac{L_{stk}}{Q_s\lambda_e A_{slot}} \quad (111)$$

It is worthy to mention that the (86) is the heat transfer in axial direction, so the thermal behavior in the interior of the slot is unknown. In order to evaluate the thermal distribution in the each conductor the use of FEA software or a special thermal network in winding is required [124].

The heat transfer of the end-winding is calculated considering the heat transfer in axial direction as in the winding. In this context, the end-winding heat transfer is given by;

$$R_{ew} = \frac{L_{ew}}{Q_s\lambda_{cu}A_{cu}} \quad (112)$$

Where, "$L_{ew}$" is the length of the copper in end-winding, which can be different in the forward (drive) and rear (non-drive) parts and "$A_{cu}$" is the surface of copper in each slot.

The heat transfer of rotor is calculated depending on the geometry [121, 125]. Then, the thermal representation of the rotor geometry is required.

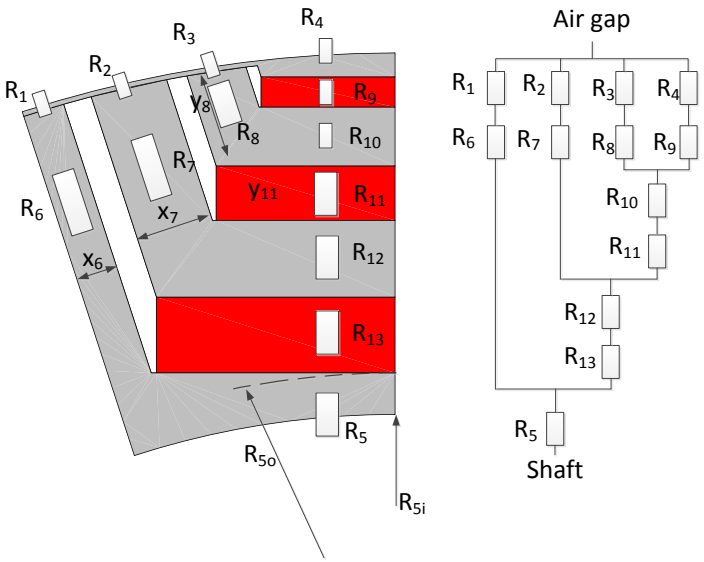


Figure 68. Thermal representation of rotor

Figure 68 shows the equivalent thermal circuit of the rotor. The different heat transfers are calculated using the equations of conduction. In the proposed example of Figure 68, from $R_1$ to $R_5$ the heat transfer is calculated using (87) meanwhile from $R_6$ to $R_{13}$ the equation used is (86). The geometrical details to compute these thermal resistances are obtained from the geometry of the rotor as shown. Note that, there are several data necessaries to compute thermal resistances such as $x_6$, $x_7$, $y_8$ and radius of $R_5$.

Then, the equivalent thermal resistance of the proposed example is given by;

$$R_{eq} = \left(\left(\left(\left((R_3 + R_8)||(R_4 + R_9)\right) + R_{10} + R_{11}\right)||(R_2 + R_7)\right) + R_{12} + R_{13}\right)||(R_1 + R_6)\Big) + R_5 \qquad (113)$$

Then, the final rotor heat transfer is obtained considering the entire rotor, so it is calculated as follows;

$$R_r = \frac{R_{eq}}{2P} \qquad (114)$$

Where "$P$" is the number of poles.

Then, the heat transfer in shaft is assumed in the axial direction, so it is given by;

$$R_{sh} = \frac{l_{sh}}{\pi R_{sh}^2 \lambda_{sh}} \qquad (115)$$

Where "$l_{sh}$" is the length of the shaft

The heat transfer on frame is divided in parts. The first one is located in the region in contact with the stator, the second one is the end-caps and the last is the region between the first and the second as can be observed in Figure 69.

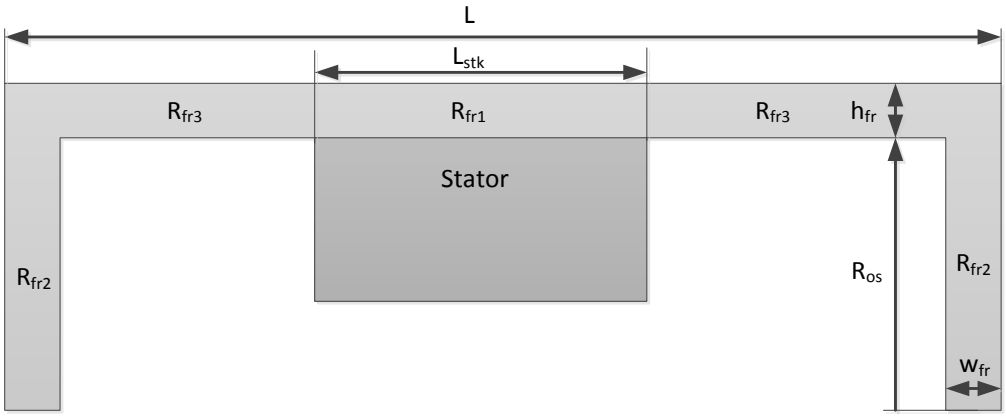


Figure 69. Frame representation.

According to the Figure 69 the frame heat transfer are given by;

$$R_{fr1} = \frac{\ln\left(\frac{(R_{os} + h_{fr})}{R_{os}}\right)}{2\pi L_{stk}\lambda_{fr}}$$

$$R_{fr2} = \frac{w_{fr}}{\pi R_{os}^2 \lambda_{fr}} \qquad (116)$$

$$R_{fr3} = \frac{L - L_{stk}}{2\pi\left(\left(R_{os} + h_{fr}\right)^2 - R_{os}^2\right)\lambda_{fr}}$$

Finally, the thermal resistance of bearings are computed according to the literature [120] and is given by;

$$R_{br} = k_1(0.12 - k_2 d_b)(33 - k_3 \omega_m d_b) \quad (117)$$

Where, the three constants are function of the size and speed of the bearings, "$d_b$" represents the average diameter of the bearing, and "$\omega_m$" is the mechanical speed in rad/s.

## 5.3 Losses calculation

This sections aims to calculate the different losses in the electrical machine. The losses can be divided in joule losses, iron losses, and friction losses. In addition, the coolant system, which dissipates the heat, is discussed.

### 5.3.1 Iron losses

The iron losses ($P_{fe}$) model has two components, hysteresis and eddy current losses. Hysteresis losses ($P_h$) take into account the *B-H* magnetization curve, whereas eddy current () losses include the currents induced by the electromotive force generated in the stator core.

$$P_{fe} = P_h + P_e = k_h \hat{B}^{n_i} f_e + k_e \left(\hat{B} f_e\right)^2 \quad (118)$$

The presence of field harmonics and stresses created within the material during the manufacturing process causes the iron losses to be higher than the results calculated in (18-19), so an empirical correction coefficient ($k_{fe}$) is introduced [126],

$$P_{fe} = k_{fe}\left(k_h \hat{B}^{n_i} f_e + k_e \left(\hat{B} f_e\right)^2\right) \quad (119)$$

The hysteresis and eddy current coefficients are evaluated for a particular core material by using the specific core loss in W/kg obtained from the manufacturer's datasheet. The data necessary to calculate the three iron losses coefficients can be observed in Table 4, which is extracted from the Cogent's catalog [127].

Table 4. Example of manufacturer's datasheet.

| Material | $P_{fe1}\ \left[\frac{W}{kg}\right];$ $f_{e1} = 50Hz, \hat{B}_1 = 1T$ | $P_{fe2}\ \left[\frac{W}{kg}\right];$ $f_{e_2} = 50Hz, \hat{B}_2 = 1.5T$ | $P_{fe3}\ \left[\frac{W}{kg}\right];$ $f_{e3} = 60Hz, \hat{B}_3 = 1.5T$ |
|---|---|---|---|
| M270-35A | 1,10 | 2,70 | 3,36 |
| M300-35A | 1,20 | 3,00 | 3,74 |
| M330-35A | 1,30 | 3,30 | 4,12 |
| M250-50A | 1,05 | 2,50 | 3,21 |

Then, the hysteresis coefficient ($k_h$), the hysteresis exponent ($n_i$) and the eddy current coefficient ($k_e$) are obtained as follows,

$$n_i = \frac{\log_{10}\left(\dfrac{\left(\dfrac{f_{e3}^2}{f_{e2}^2} f_{e1}\hat{B}_3^2\left(P_{fe2} - P_{fe1}\hat{B}_2^2\right)\right)}{P_{fe3} - \dfrac{f_{e3}^2}{f_{e2}^2}\hat{B}_3^2 P_{fe1}} - f_{e1}\hat{B}_2^2}{\dfrac{f_{e3}\left(P_{fe2} - P_{fe1}\hat{B}_3^2\right)}{P_{fe3} - \dfrac{f_{e3}^2}{f_{e2}^2}\hat{B}_2^2 P_{fe1}} - f_{e1}}\right)}{\log_{10}\hat{B}_3} \quad (120)$$

$$k_h = \frac{P_{fe2} - P_{fe1}\hat{B}_2^2}{\hat{B}_2^{n_i} f_{e2} - f_{e1}\hat{B}_2^2} \quad (121)$$

$$k_e = \frac{P_{fe1} - k_h f_{e1}}{f_{e1}^2} \quad (122)$$

Therefore, the iron losses obtained in (119) have to be multiplied by motor mass since the losses coefficients are obtained per unit of mass. The accuracy of the iron losses calculation is strongly connected with the number of parts chosen, i.e. the iron losses can be calculated using the maximum magnetic saturation ($\hat{B}$) on the motor and the motor mass or with the sum of the iron losses of the each tooth, the yoke, and the rotor parts, which are calculated using the magnetic saturation and mass of those parts. Therefore, the magnetic model, which has been explained in section 4, helps to improve the iron losses calculation. The magnetic saturation of yoke, teeth and rotor can be obtained from the magnetic model.

### 5.3.2 Copper losses

Copper losses have been evaluated by neglecting both skin and proximity effects. The phase resistance can be updated according to the operating temperature if the dependence function is known or a thermal model is coupled to the electrical model. The losses by Joule effect are given by,

$$P_{cu} = \frac{mR_S i^2}{2} \quad (123)$$

Where "$i$" is the value of the current in each loop, "$m$" is the number of phases, and "$R_s$" is the phase resistance.

The phase resistance increase with the temperature. The dependency of the phase resistance with the temperature is given by;

$$R_S = R_0\big(1 + \alpha(\theta - \theta_0)\big) \quad (124)$$

Where, "$R_0$" represents the phase resistance at the temperature "$\theta_0$", "$\alpha$" is the coefficient's temperature of the material, and "$\theta$" is the current temperature.

Finally, the resistance is calculated as follows;

$$R_0 = \frac{l_{cu}}{S_{cu}\rho_{cu}} \quad (125)$$

Where, "$l_{cu}$" is the total length of the cooper, "$S_{cu}$" is the cross-section of the copper, and "$\rho_{cu}$" is the resistivity of the copper at $\theta_0$.

### 5.3.3 Friction losses

The friction losses are caused by the movement of rotation. It is located in bearings. The friction losses vary with the speed and the type of bearings. According to SKF [128] the friction losses are given by;

$$P_{fr} = 1.05 \cdot 10^{-4} M n \quad (126)$$

Where, "$M$" is the frictional moment and "$n$" is the mechanical speed.

The frictional moment is given by;

$$M = M_{rr} + M_{sl} + M_{seal} + M_{drag} \quad (127)$$

Where, "$M_{rr}$" is the rolling friction moment, "$M_{sl}$" is the sliding frictional moment, "$M_{seal}$" is the frictional moment of the seals, and "$M_{drag}$" is the frictional moment of drag losses, churning, splashing, among others.

Note that, the different friction moments are calculated using specific variables. These variables depend on the bearing type, the bearing diameter, radial load or axial load. Furthermore, the different friction moment varies with the speed, so the friction losses are not linear with the mechanical speed.

For instance, in [121] the friction losses are measured and approximated as follows;

$$P_{fr} = k_c + k_f \omega_m^3 \quad (128)$$

Where, "$k_c$" and "$k_f$" are coefficient, which had been calculated by experimental approach, and "$\omega_m$" is the mechanical speed in rad/s

### 5.3.4 Coolant system

A coolant dissipates the heat of the machine, so in the equation system the value of the coolant's heat is negative. The heat of the coolant is given by;

$$P_{coolant} = \dot{m} c_p \Delta\theta \quad (129)$$

Where, "$\dot{m}$" is the mass flow rate, "$c_p$" is the specific heat, and "$\Delta\theta$" is the difference between the inlet and the outlet temperature of the coolant.

## 5.4 Thermal Network

The thermal network, which represents the geometry of the machine, allows calculating the temperature of different parts of the motor. Several authors had worked in the creation of TN for several topologies of motors, such as IM [129] or PMaSynRM [121, 125, 130]. According to the literature, the proposed TN is shown in Figure 70.

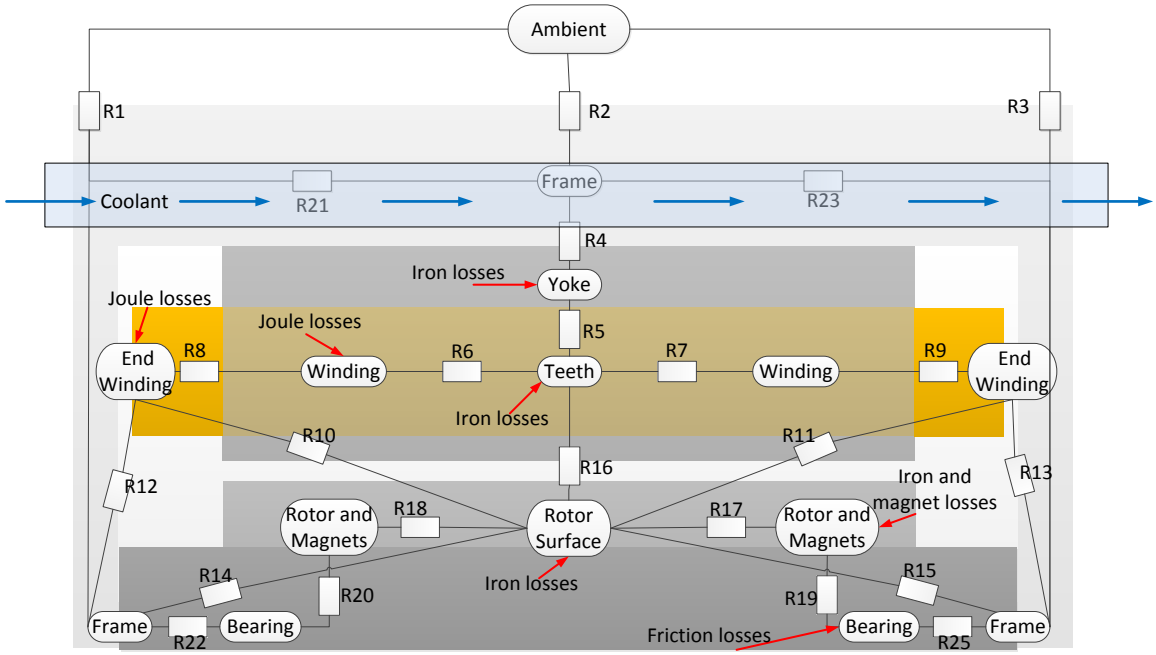


Figure 70. Thermal network

The different motor parts are connected with the heat transfers, which had been explained in the previous sections. These heat transfers are represented as white boxes. The connected parts are the thermal nodes. The name of each node is indicated, such as teeth, yoke, winding, among others. It can be observed that there are fourteen nodes to compute the temperature, i.e. fourteen equations are required. Finally, the different losses are represented as red arrows and the coolant system is represented with blue arrows.

The equation system required to solve the thermal model obtained solving the heat flow in a node. Figure 71 shows a node of the thermal network applied to evaluate the thermal behavior of the machine.

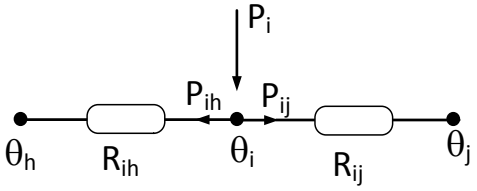


Figure 71. Thermal node

According to Figure 71, the thermal equation in the *i*-th node can be written as,

$$P_i = P_{ij} + P_{ih} \quad (130)$$

Where, $P_i$ represents the losses associates to the node *i*-th, for instance the iron or copper losses, meanwhile $P_{ij}$ and $P_{ih}$ are the heat flow rate between nodes *i-j* and nodes *i-h* respectively. The heat flow rate is calculated by;

$$P_{ih} = \frac{\theta_h - \theta_i}{R_{ih}} \quad (131)$$

Where, $R_{ih}$ is the thermal resistance (heat-transfer) between nodes *i-h* and $\theta$ is the temperature of the different nodes.

Then, developing the (130-131) for each node, the equation system is formed by;

$$\begin{bmatrix} \theta_1 \\ \vdots \\ \theta_n \end{bmatrix} = \begin{bmatrix} G_{11} & \dots & G_{1n} \\ \vdots & \ddots & \vdots \\ G_{n1} & \dots & G_{nn} \end{bmatrix}^{-1} \begin{bmatrix} P_1 \\ \vdots \\ P_n \end{bmatrix} \quad (132)$$

$G_{ij} = 1/R_{ij}$ being the thermal conductance between nodes *i* and *j*. The temperature $\theta_i$ in any node of the thermal network can be calculated for all current and speed values by applying an iterative process, thus allowing to calculate the change of the phase resistance of all elements of the thermal network.

Then, the temperature is calculated using an iterative process like the one used in the magnetic model. First, the temperature of each node is assumed (seed value) in order to obtain the value of different thermal resistances and losses in nodes. For example, the value of copper losses varies with the temperature, or the temperature of the coolant is required to calculate the dissipated heat. After that, the equation system is solved and the real temperature of each node is calculated. If the seed values are closed to the calculated temperature, the systems will finish. However, if the error is higher than a threshold, the calculated temperature will be the new seed values and the process starts again. Figure 72 shows the iterative system to calculate the motor temperature. Note that, the current module and current angle are needed to compute the losses. As former before, the iron losses depends on the magnetic saturation and magnetic saturation is function of the current module and the current angle.

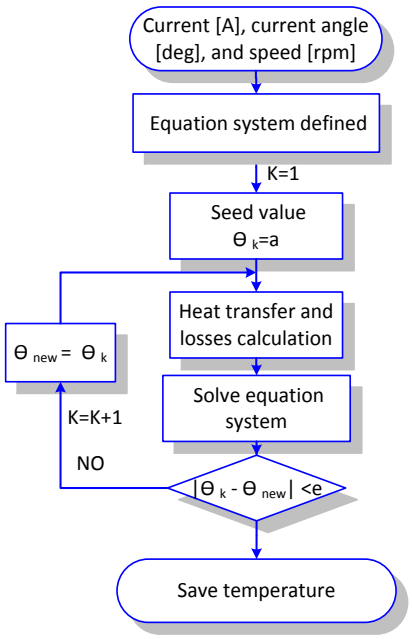


Figure 72. Iterative system to calculate the temperature of the motor's parts

The equation system proposed is defined considering the fourteen nodes. According to Figure 70, the number of the nodes are as follows; the different frames are the nodes 1 (left), 2 (middle), and 3 (right), the yoke is the node 4, the teeth is the node 5, the nodes winding are the nodes 6 (left) and 7 (right), the nodes end-winding are the nodes 8 (left) and 9 (right), the nodes called rotor are nodes 10 (left) and 11 (right), the node called rotor surface is the node 12, and the nodes called bearings are the nodes 13 (left) and 14 (right).

In this context, the equation system is given by;

$$P_1 = \frac{\theta_1-\theta_2}{R_{21}}+\frac{\theta_1-\theta_0}{R_1}+\frac{\theta_1-\theta_8}{R_{12}}+\frac{\theta_1-\theta_{14}}{R_{22}}+\frac{\theta_1-\theta_{12}}{R_{14}}$$

$$P_2 = \frac{\theta_2-\theta_1}{R_{21}}+\frac{\theta_2-\theta_0}{R_2}+\frac{\theta_2-\theta_3}{R_{23}}+\frac{\theta_2-\theta_4}{R_4}$$

$$P_3 = \frac{\theta_3-\theta_2}{R_{23}}+\frac{\theta_3-\theta_0}{R_3}+\frac{\theta_3-\theta_9}{R_{13}}+\frac{\theta_3-\theta_{13}}{R_{25}}+\frac{\theta_3-\theta_{12}}{R_{15}}$$

$$P_4 = \frac{\theta_4-\theta_2}{R_4}+\frac{\theta_4-\theta_5}{R_5}$$

$$P_5 = \frac{\theta_5-\theta_6}{R_6}+\frac{\theta_5-\theta_4}{R_5}+\frac{\theta_5-\theta_7}{R_7}+\frac{\theta_5-\theta_{12}}{R_{16}}$$

$$P_6 = \frac{\theta_6-\theta_5}{R_6}+\frac{\theta_6-\theta_8}{R_8}$$

$$P_7 = \frac{\theta_7-\theta_5}{R_7}+\frac{\theta_7-\theta_9}{R_9}$$

$$P_8 = \frac{\theta_8-\theta_6}{R_8}+\frac{\theta_8-\theta_{12}}{R_{10}}+\frac{\theta_8-\theta_1}{R_{12}}$$

$$P_9 = \frac{\theta_9-\theta_7}{R_9}+\frac{\theta_9-\theta_{12}}{R_{11}}+\frac{\theta_9-\theta_3}{R_{13}}$$

$$P_{10} = \frac{\theta_{10}-\theta_{12}}{R_{18}}+\frac{\theta_{10}-\theta_{14}}{R_{20}}$$

$$P_{11} = \frac{\theta_{11}-\theta_{12}}{R_{17}}+\frac{\theta_{11}-\theta_{13}}{R_{19}}$$

$$P_{12} = \frac{\theta_{12}-\theta_5}{R_{16}}+\frac{\theta_{12}-\theta_1}{R_{14}}+\frac{\theta_{12}-\theta_{10}}{R_{18}}+\frac{\theta_{12}-\theta_8}{R_{10}}+\frac{\theta_{12}-\theta_9}{R_{11}}+\frac{\theta_{12}-\theta_{11}}{R_{17}}+\frac{\theta_{12}-\theta_3}{R_{15}}$$

$$P_{13} = \frac{\theta_{13}-\theta_3}{R_{25}}+\frac{\theta_{13}-\theta_{11}}{R_{19}}$$

$$P_{14} = \frac{\theta_{14}-\theta_1}{R_{22}}+\frac{\theta_{14}-\theta_{10}}{R_{20}}$$

where, the $\theta_0$ represents the exterior temperature of the motor, so it is known. The losses in each node are given by copper losses (123) in nodes 6, 7, 8 and 9, iron losses (119) in nodes 4, 5, 10, 11, and 12, friction losses (128) in nodes 13 and 14, and coolant system (129) in node 2. The losses in node 1 and 3 are equal to zero.

The copper resistances to compute the copper losses of different nodes are adapted taking into account the equivalent length of the copper in each node. For example, the "$l_{cu}$" (125) of node 6 is equal to the half of stack length meanwhile in node 8 is equivalent to the half of the end winding length.

Remember that the iron losses are in per unit of mass, so in each node the iron losses must be multiplied by the representative mass. For instance, in node 5 the iron losses are times the total mass of teeth or in node 4 the iron losses are multiplied by the mass of yoke. Finally, the hysteresis losses in rotor are zero, so only the term of eddy currents is required.

At last, the thermal resistances are obtained combining the heat transfer calculated before. Then, the thermal resistance shown in the proposed equation system are given by;

$$R_1 = \frac{1}{2}R_{fr2} + R_{fr1-amb}$$

$$R_2 = \frac{1}{2}R_{fr1} + R_{fr2-amb}$$

$$R_3 = \frac{1}{2}R_{fr2} + R_{fr3-amb}$$

$$R_4 = \frac{1}{2}R_{fr2} + \frac{1}{2}R_{yoke}$$

$$R_5 = \frac{1}{2}R_{yoke} + \frac{1}{2}R_t$$

$$R_6 = R_7 = \frac{1}{2}R_w$$

$$R_8 = R_9 = \frac{1}{2}R_{ew}$$

$$R_{16} = \frac{1}{2}R_g$$

$$R_{17} = R_{18} = \frac{1}{4}R_r$$

$$R_{19} = R_{20} = \frac{1}{4}R_b + \frac{1}{2}R_{sh} + \frac{1}{4}R_r$$

$$R_{21} = R_{23} = R_{fr3}$$

$$R_{22} = R_{25} = \frac{1}{4}R_b$$

Finally, the resistances 10 to 15 are calculated using the well-known start triangle transformation using the heat-transfer of the internal air. Figure 73 shows the configuration of start-triangle resistances.

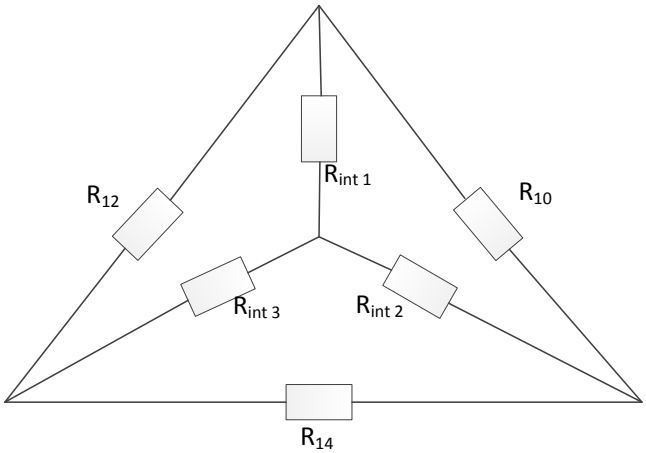


Figure 73. Star-triangle configuration of thermal resistances

The value of resistances is given by;

$$R_{10} = \frac{R_{int1}R_{int2} + R_{int2}R_{int3} + R_{int3}R_{int1}}{R_{int3}} \rightarrow R_{10} = R_{11}$$

$$R_{12} = \frac{R_{int1}R_{int2} + R_{int2}R_{int3} + R_{int3}R_{int1}}{R_{int2}} \rightarrow R_{12} = R_{13}$$

$$R_{14} = \frac{R_{int1}R_{int2} + R_{int2}R_{int3} + R_{int3}R_{int1}}{R_{int1}} \rightarrow R_{14} = R_{15}$$

Now the whole equation system and the thermal resistance are defined, so the thermal behavior of the machine can be evaluated according to the proposed thermal network. Remember that the process is an iterative system (Figure 72) since some resistances and losses vary with the temperature of the nodes.

## 5.5 Conclusions

The presented chapter deals with the thermal model. Some conclusions can be extracted,

- The thermal behavior is mandatory to calculate the motor performances with high accuracy.
- The motor is a multi-physics problem since the iron losses are computed in magnetic model and the magnetic properties of the magnets varies with the temperature as well as the phase resistance.
- The implementation of a fast, accurate, and adaptable thermal network is possible considering one motor topology.

# 6.

# Behavior maps calculation

The contribution in the field of range optimization is due to the fast and accurate calculation of the behavior maps. The developed equation system and proposed procedure are presented in this chapter. Several results are depicted too.

*CONTENTS:*

# 6. Behavior maps calculation

## 6.1 Introduction

In a single or multi-objective optimization case, e.g. torque maximization, the different variations on motor geometry may improve maximum torque, although those variations can negatively affect motor behavior in most frequent operational zones. In these cases, the use of behavior maps during the optimization process is well suited for design assessment in motors either for energy restrictions applications [131] or for traction applications, to calculate the energy consumption for a specific driving cycle [20, 132] or to check the behavior around the corner speed. The efficiency maps are obtained mostly through finite elements analysis (FEA) or experimental analysis [133], whereas power losses are evaluated following specific control strategies such as MTPA (maximum torque per ampere) trajectory, MTPV (maximum torque per voltage) [134], or ME (maximum efficiency) [135]. However, an accurate computation of the iron losses at every single operation point from FEA is very computationally intensive, thus resulting in a process that can last several days depending on the accuracy required.

This chapter presents a tool based on behavior maps for evaluating drive operational boundaries and optimization assessments of PMaSynRMs and SynRMs, which avoids an intensive use of FEM (finite element method) or other expensive software. Behavior maps are understood as a multi-dimensional representation of datasets of different motor variables.

The generation of behavior maps is introduced as a technique capable of analyzing motor operation conditions, design characteristics, optimization and control [136] in a broad spectrum of operational points instead of the rated value or a single point [27]. By computing hundreds of thousands of operation points of a detailed *dq*-model in a few seconds, this technique is able to provide not only the so-called efficiency map but also any other conditioned map such as the minimum losses map. In addition, MTPA or MPTV, unity power factor, maximum efficiency, constant stator flux linkage, and constant power loss trajectories in the *dq*-current axis can be extracted for LUT (lookup table) control drives [137]. This approach stores data in such a way that the motor designer can choose any computed variable and compare it to others by using custom target functions. Because of its ease of implementation and parallel computation capabilities, it is a perfect link for automated optimization workflows. Seed values and input data for the behavior maps process can be obtained from machine equations, reluctance network or FEA approaches [138]. The operation points can be used to feed the optimization cost functions directly or can be interpreted by means of intermediate software to calculate average values in desired working areas of a map instead of the classical target working point. Furthermore, the data transformed into the *dq*-current space allows visualizing not only the interaction of different control laws under the operating limits imposed by drive constraints as well as beyond. Optimization of non-steady state operation or fault condition can be performed by evaluating a motor's performance even beyond the drive limits.

This section aims at developing a fast and accurate tool to assist the optimization procedure of PMSMS and SynRMs by considering different control laws. For each specific control law, the developed tool provides relevant operating data of the machine such as the developed torque-speed

and efficiency maps, power factor, current and voltage angles in the *dq* reference taking into account non-linearity, i.e. saturation effects or power losses

## 6.2 Graphic explanation

In this subsection, the concept of behavior maps is developed in order to facilitate the understanding of this chapter. Several options of behavior maps are presented. Also, the representations of different motors in the *dq*-currents plane are shown as a starting point for the explanation of how the behavior maps are obtained.

### 6.2.1 Behavior maps

As mention before, the behavior maps are understood as a representation of the different motor characteristics in a specific plane. The use of these maps can be focused to assist the design procedure since the cost function can include the average efficiency or the power factor, which is used to determine the size of the inverter. Moreover, they can be used to feed the control based on look up tables since for each torque-speed point the *dq*-current are calculated considering iron losses, cross-coupling saturation, and copper losses.

Furthermore, the different data are calculated according to a control law, for example minimum losses, maximum torque per ampere or maximum torque per voltage. Then, using these maps the control can be developed including the flux weakening region.

For instance, the efficiency in the torque-speed plane as can be observed in Figure 74.

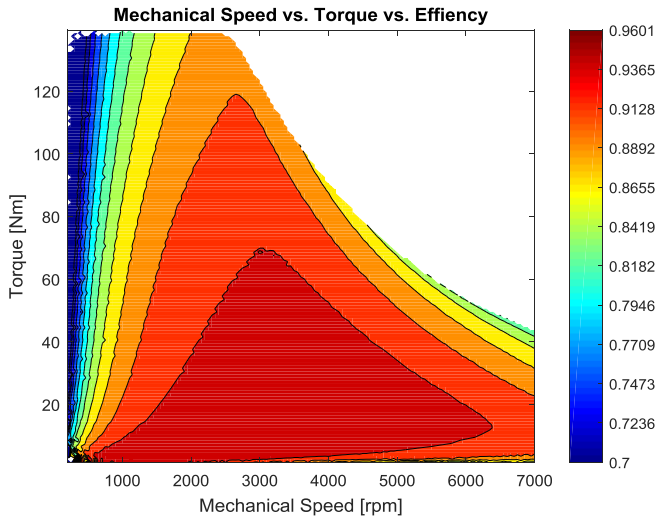


Figure 74. Example of a behavior map. Efficiency representation on torque-speed plane

Other parameters of the machine can be depicted in the same plane, such as power factor, current module, and current angle, among others. Figure 75 shows the current angle of the machine in the whole operating area considering saturation and losses. Moreover, the map is calculated according to the MTPA trajectory until the maximum voltage is achieved, then the MTPV solution is used.

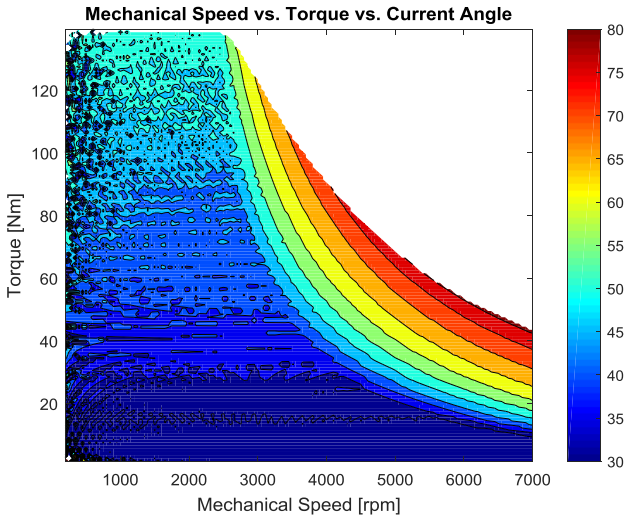


Figure 75. Example of a behavior map. Current angle representation on torque-speed plane

Depending on the necessary information, the plane to represent the parameters of the machine can be power-speed plane or dq-currents plane. For example, Figure 76 shows the power factor of the same machine as previous figures in the power-speed plane.

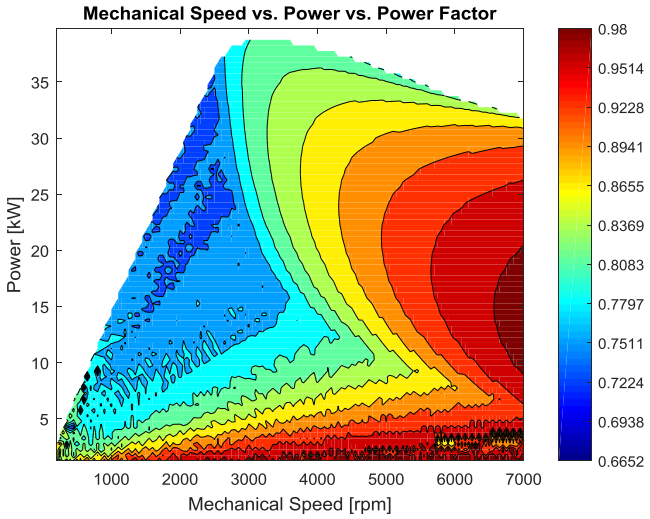


Figure 76. Example of a behavior map. Power factor representation on power-speed plane

More example of behavior maps and using different levels of detail are shown in the *Section 6.3.4. Results.*

## 6.2.2 Motor representation (Blondel diagram)

The behavior maps are obtained from the representation of several working points in the selected plane. The calculation of these working points can be understood as the intersection of two curves in the *dq*-currents plane. The first one is the related with the current limit of the inverter, which is represented as a circle where the radius is the current module. Meanwhile, the second one involves the relation of voltage and speed. The shape of the second curve can be represented as circle or ellipse depending on the typology of the motor. Figure 77 shows the mentioned limits. This representation is called Blondel's diagram.

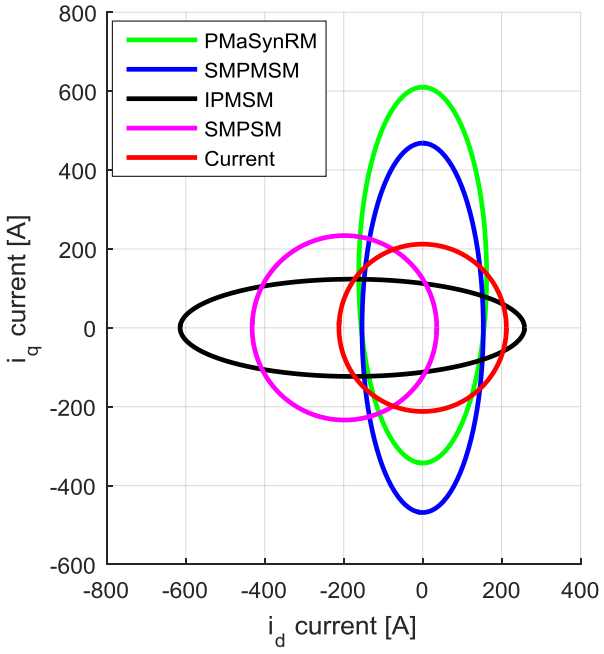


Figure 77. Representation of current limit and voltage/speed ratio limit of different machines in the dq-currents plane

Blondel diagrams are used to ensure feasible results (only voltage and current locus intersections in suitable sectors are computed) and a fast solution, as this method minimizes the number of iterations required. Blondel diagrams allow visualizing the interaction of the machine's voltage, current, and torque in a single chart [139]. Figure 78 shows the several current modules (red circles) and the ellipses of PMa-SynRM when the voltage is constant while the speed increase. Then, several working points, which are defined as the intersection between circle and ellipse, are highlighted (blue points).

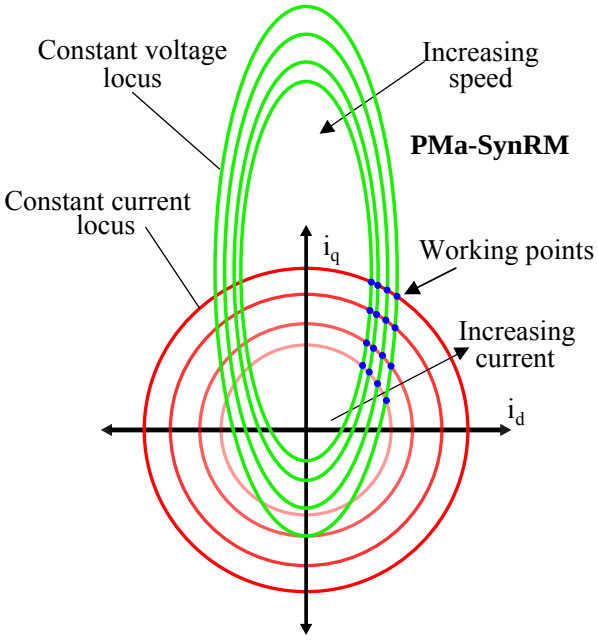


Figure 78. An example of intersection between current limit with voltage/speed limit

The working points are used to compute the parameters of the machine such as, torque, power, efficiency, power factor, among others. Note that, there are three variables to calculate all the working points; Current, voltage, and Speed. For example, the torque-speed curve obtained from one current, one voltage and all the speed is shown in Figure 79. Several working points are emphasized to see the equivalency between the Blondel diagram with the torque-speed plane.

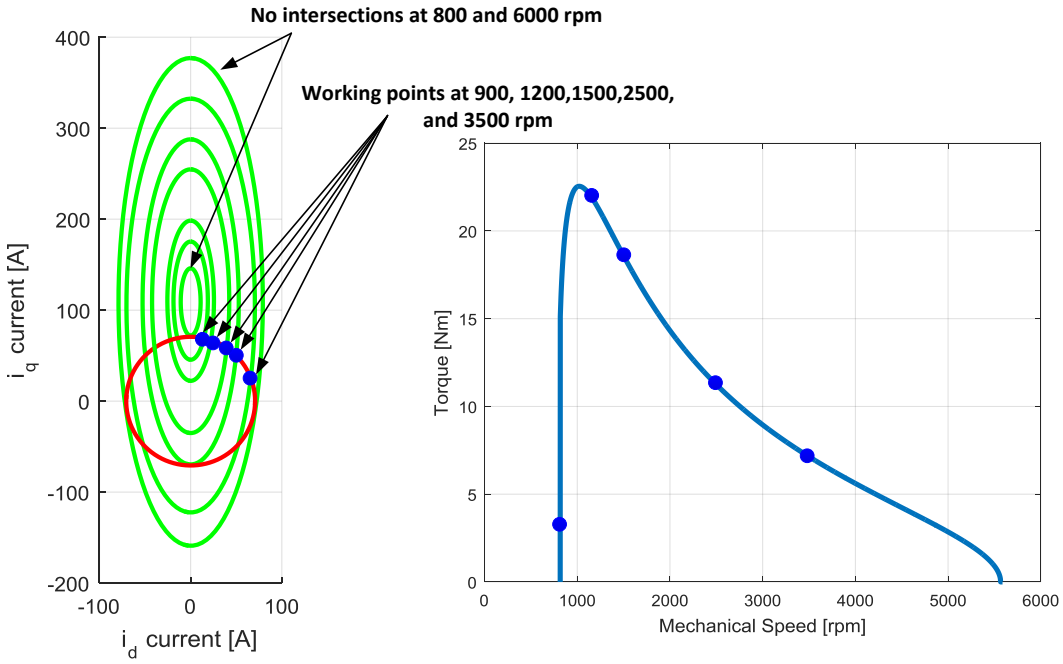


Figure 79. Torque-speed curve for one current, one voltage and all the speed.

Then, calculating all possible intersection, which are obtained from combining all the currents, voltages and speed, and selecting the correct points, the former behavior maps can be obtained. The procedure to calculate and select all the points is explained in the section *6.3.2. Solving procedure.*

Until now, the shown ellipses are calculated neglecting the iron losses and the phase resistance. These variables have big effect in the intersection points since the rotation and positioning of the ellipse varies. Figure 80 shows the effects of considering the iron and copper losses. Note that, the iron losses (A) affects more in higher speed meanwhile the effects of phase resistance are bigger in the smaller speeds meanwhile the copper losses have bigger effect in lower speeds (B).

Therefore, the variation on the shape, position, and orientation of the ellipse including the phase resistance and iron losses makes mandatory the use of them in the behavior maps calculation. Remember that, the behavior maps are calculated using the intersection between ellipses and circles, which it varies when the losses are included. The quantitative effect of neglecting these parameters in the behavior maps calculation is discussed in the *Section 7. Sensitive analysis.*

The concept of Blondel's diagram has been explained, so the analytical calculation to obtain the ellipses must be explained in this chapter. The aim of the next section (*Section 6.3. Electrical model*) is to explain the mathematical development of the ellipses' shape.

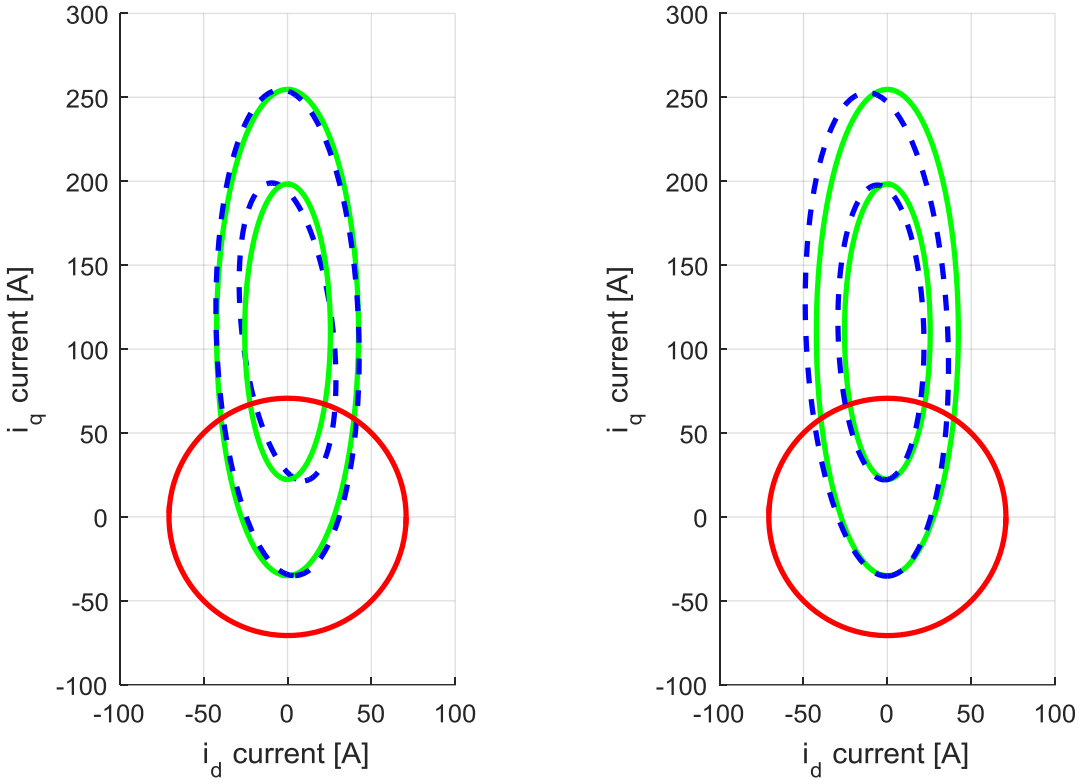


Figure 80. In the Blondel A, the ellipses ideal ellipse are compared with the ellipses with iron losses meanwhile in the Blondel B, the ideal ellipses are compared with the ellipses with phase resistance.

Depending on the motor type, the shape of the ellipse changes as can be observed in Figure 77, so the proposed equation must be adaptable. Furthermore, the iron losses and phase resistance have to be included in the mathematical development.

## 6.3 Electrical model

### 6.3.1 *dq*-circuit

The calculation of behavior maps starts solving the electrical model without simplifications, so the magnetic saturation including the cross-coupling effect, thermal variations, and iron losses are considered in the equivalent electric circuit of the motor, which it is shown in Figure 81. The steady state equations that define the machine behavior in the *dq* rotor flux reference frame are as follows;

$$u_d = R_S i_d - \omega_e L_q i_{oq} - \omega_e \Psi_{PM,q} \quad (133)$$

$$u_q = R_S i_q + \omega_e L_d i_{od} + \omega_e \Psi_{PM,d} \quad (134)$$

$$T = \frac{3}{2} p \left( (L_d - L_q) i_{od} i_{oq} - \Psi_{PM,q} i_{od} + \Psi_{PM,d} i_{oq} \right) \quad (135)$$

Note that, the presented equations can be adapted for different motor topologies. Depending on the permanent magnet flux component and inductances ratio, different machine models can be obtained from (133-135) [140]. Table 5 summarizes the different motor topologies:

Table 5.Detail of machine's parameters depending on the topology

| Motor type | Saliency | $\psi_{pmd}$ | $\psi_{pmq}$ |
|---|---|---|---|
| SynRM | $L_d > L_q$ | $\psi_{pmd} = 0$ | $\psi_{pmq} = 0$ |
| PMaSynRM | $L_d > L_q$ | $\psi_{pmd} = 0$ | $\psi_{pmq} < 0$ |
| IPMSM | $L_d < L_q$ | $\psi_{pmd} > 0$ | $\psi_{pmq} = 0$ |
| SPMSM | $L_d = L_q$ | $\psi_{pmd} > 0$ | $\psi_{pmq} = 0$ |

The general equivalent circuit for all the above mentioned electrical machines is depicted in Figure 81. The time variation of leakage inductances has been disregarded since the proposed method works in steady state conditions.

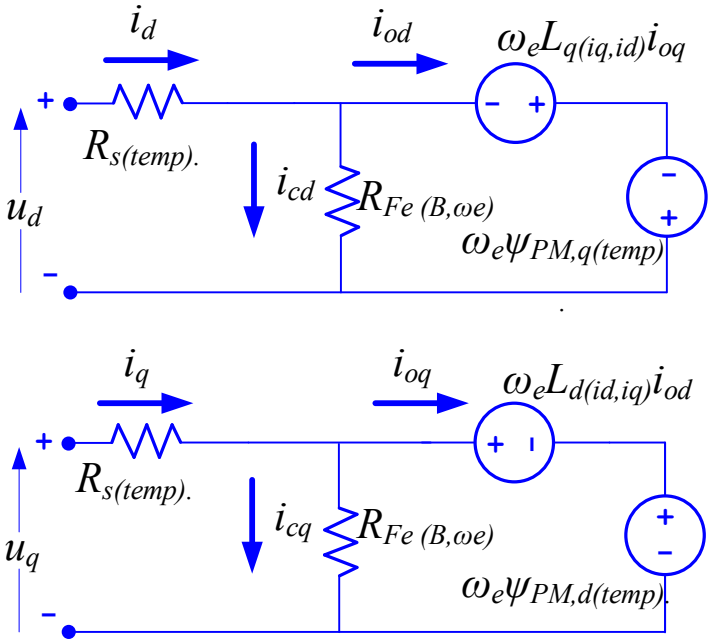


Figure 81. d and q axes steady state model in the rotor flux reference frame for different machine topologies

Where the iron losses are considered since the iron resistance ($R_{fe}$) appears in the electric model. The thermal variations can be observed in the value of phase resistance ($R_S$) and magnet flux linkage ($\Psi_{PM,d}$ and $\Psi_{PM,q}$) due to both of them are affected by the temperature. The magnetic saturation appears in the value of iron resistance and inductances ($L_d$ *and* $L_q$). Based on the circuit shown in Figure 81 and applying Kirchhoff's laws, the following equations are deducted,

$$i_d = i_{od} + i_{cd} \quad (136)$$

$$i_q = i_{oq} + i_{cq} \quad (137)$$

$$i_{cd} = \frac{-\omega_e L_q i_{oq} - \omega_e \Psi_{PM,q}}{R_{fe}} \quad (138)$$

$$i_{cq} = \frac{\omega_e L_d i_{od} + \omega_e \Psi_{PM,d}}{R_{fe}} \quad (139)$$

It is mandatory insolating the *dq*-axes torque-generating currents ($i_{od}$ and $i_{oq}$) in order to simplify the resolution of the final system. Then, the equations (138-139) are introduced in (136-137) and the following equations are obtained,

$$i_{od} = i_d + \frac{\omega_e L_q i_{oq} + \omega_e \Psi_{PM,q}}{R_{fe}} \quad (140)$$

$$i_{oq} = i_q - \frac{\omega_e L_d i_{od} + \omega_e \Psi_{PM,d}}{R_{fe}} \quad (141)$$

Introducing (141) in (140),

$$i_{od} = i_d + \frac{\omega_e L_q}{R_{fe}}\left(i_q - \frac{\omega_e L_d i_{od} + \omega_e \Psi_{PM,d}}{R_{fe}}\right) + \frac{\omega_e \Psi_{PM,q}}{R_{fe}} \quad (142)$$

Then, insolating the d-axis torque-generating current the following equation emerge,

$$i_{od} = \frac{i_d + \frac{\omega_e L_q}{R_{fe}} i_q - \frac{\omega_e^2 L_q \Psi_{PM,d}}{R_{fe}^2} + \frac{\omega_e \Psi_{PM,q}}{R_{fe}}}{\left(1 + \frac{\omega_e^2 L_q L_d}{R_{fe}^2}\right)} \quad (143)$$

Finally, introducing (143) in (141), the q-axis torque-generating current is achieved,

$$i_{oq} = i_q - \frac{\omega_e \Psi_{PM,d}}{R_{fe}} - \frac{\omega_e L_d i_d}{R_{fe}\left(1 + \frac{\omega_e^2 L_q L_d}{R_{fe}^2}\right)} - \frac{\omega_e^2 L_d L_q i_q}{R_{fe}^2\left(1 + \frac{\omega_e^2 L_q L_d}{R_{fe}^2}\right)} + \frac{\omega_e^3 L_d L_q \Psi_{PM,d}}{R_{fe}^3\left(1 + \frac{\omega_e^2 L_q L_d}{R_{fe}^2}\right)} - \frac{\omega_e^2 L_d \Psi_{PM,q}}{R_{fe}^2\left(1 + \frac{\omega_e^2 L_q L_d}{R_{fe}^2}\right)} \quad (144)$$

In this point, the limits of the motor operation must be introduced. The motor behavior is characterized by all possible operating points, which comprise voltage, current and frequency combinations as shown in the previous sub-section. The limit values for those variables are settled by the converter, although they can be exceeded when analyzing the motor behavior beyond rated conditions, for example, to explore its fault-tolerant capability. In this context, (133), (134), (136) and (137) must fulfill,

$$u_d^2 + u_q^2 < u_{max}^2 \quad (145)$$

$$i_d^2 + i_q^2 < i_{max}^2 \quad (146)$$

In this context, combining the explained equation system and the concept of Blondel diagram the behavior maps are extracted in the proposed work. First, the analytical representation of the constant voltage locus is required. Therefore, the voltage equation must be developed in order to obtain a *dq*-current dependent equation, so it can be represented in a *dq*-current plane as in Figure 78. The equations (143-144) are introduced in equations (133-134).

$$u_d = R_S i_d - \omega_e L_q \left( i_q - \frac{\omega_e \Psi_{PM,d}}{R_{fe}} - \frac{\omega_e L_d i_d}{R_{fe}\left(1+\frac{\omega_e^2 L_q L_d}{R_{fe}^2}\right)} - \frac{\omega_e^2 L_d L_q i_q}{R_{fe}^2\left(1+\frac{\omega_e^2 L_q L_d}{R_{fe}^2}\right)} + \frac{\omega_e^3 L_d L_q \Psi_{PM,d}}{R_{fe}^3\left(1+\frac{\omega_e^2 L_q L_d}{R_{fe}^2}\right)} - \frac{\omega_e^2 L_d \Psi_{PM,q}}{R_{fe}^2\left(1+\frac{\omega_e^2 L_q L_d}{R_{fe}^2}\right)} \right) - \omega_e \Psi_{PM,q} \quad (147)$$

$$u_q = R_S i_q + \omega_e L_d \left( \frac{i_d + \frac{\omega_e L_q}{R_{fe}} i_q - \frac{\omega_e^2 L_q \Psi_{PM,d}}{R_{fe}^2} + \frac{\omega_e \Psi_{PM,q}}{R_{fe}}}{\left(1+\frac{\omega_e^2 L_q L_d}{R_{fe}^2}\right)} \right) + \omega_e \Psi_{PM,d} \quad (148)$$

In order to simplify the following calculation, the parameters in equations (147-148) are divided as follows,

$$u_d = k_1 i_d + k_2 i_q + k_3 \quad (149)$$

$$u_q = k_4 i_q + k_5 i_d + k_6 \quad (150)$$

Where,

$$k_1 = R_S + \frac{\omega_e^2 L_d L_q}{R_{fe}\left(1+\frac{\omega_e^2 L_q L_d}{R_{fe}^2}\right)}$$

$$k_2 = -\omega_e L_q + \frac{\omega_e^3 L_d L_q^2}{R_{fe}^2\left(1+\frac{\omega_e^2 L_q L_d}{R_{fe}^2}\right)}$$

$$k_3 = \frac{\omega_e^2 L_q \Psi_{PM,d}}{R_{fe}} - \omega_e \Psi_{PM,q} + \frac{\omega_e^3 L_q L_d \Psi_{PM,q}}{R_{fe}^2\left(1+\frac{\omega_e^2 L_q L_d}{R_{fe}^2}\right)} - \frac{\omega_e^4 L_d L_q^2 \Psi_{PM,d}}{R_{fe}^3\left(1+\frac{\omega_e^2 L_q L_d}{R_{fe}^2}\right)}$$

$$k_4 = R_S + \frac{\omega_e^2 L_d L_q}{R_{fe}\left(1+\frac{\omega_e^2 L_q L_d}{R_{fe}^2}\right)}$$

$$k_5 = \frac{\omega_e L_d}{\left(1+\frac{\omega_e^2 L_q L_d}{R_{fe}^2}\right)}$$

$$k_6 = \omega_e \Psi_{PM,d} - \frac{\omega_e^3 L_q L_d \Psi_{PM,d}}{R_{fe}^2\left(1+\frac{\omega_e^2 L_q L_d}{R_{fe}^2}\right)} + \frac{\omega_e^2 L_d \Psi_{PM,q}}{R_{fe}\left(1+\frac{\omega_e^2 L_q L_d}{R_{fe}^2}\right)}$$

Then, combining the equations (149-150) in equation (145) the following results can be obtained,

$$k_1^2 i_d^2 + k_2^2 i_q^2 + k_3^2 + 2k_2k_3i_q + 2k_1k_2i_di_q + 2k_1k_3i_d + k_4^2 i_q + k_5^2 i_d + k_6^2 + 2k_4k_5i_di_q + 2k_4k_6i_q + 2k_5k_6i_d = u_{max}^2 \quad (151)$$

Grouping the terms, the final equation emerges. The geometrical representation of (151) is shown in Figure 77 and Figure 78. The difference represented ellipses are obtained increasing the electric speed ($\omega_e$) and keeping constant the value of voltage ($u_{max}$).

$$Ai_d^2 + Bi_di_q + Ci_q^2 + Di_d + Ei_q + F = 0 \quad (152)$$

Where,

$$A = k_1^2 + k_5^2 \qquad D = 2(k_1k_3 + k_6k_5)$$
$$B = 2(k_1k_2 + k_4k_5) \qquad E = 2(k_2k_3 + k_3k_6)$$
$$C = k_2^2 + k_4^2 \qquad F = k_3^2 + k_6^2 - u_{max}^2$$

Equation (152) allows calculating all the possibilities mentioned before, i.e. the different motor topologies are obtained according to Table 5. The iron losses and copper losses are computed since the iron resistance ($R_{fe}$) and phase resistance ($R_s$) are included in the equation. However, these effects can be neglected if the values of them are not known. The copper losses are neglected if the phase resistance is zero meanwhile the iron losses are not considered if the iron resistance is infinite, both in the coefficients of (152). Then,

$$k_1 = 0 \qquad k_4 = 0$$
$$k_2 = -\omega_e L_q \qquad k_5 = \omega_e L_d$$
$$k_3 = -\omega_e \Psi_{PM,q} \qquad k_6 = \omega_e \Psi_{PM,d}$$

Then,

$$A = (\omega_e L_d)^2 \qquad D = 2\left(\omega_e^2 L_d \Psi_{PM,d}\right)$$
$$B = 0 \qquad E = 2(\omega_e^2 L_q \Psi_{PM,q} - \omega_e^2 \Psi_{PM,q}\Psi_{PM,d})$$
$$C = \left(-\omega_e L_q\right)^2 \qquad F = \left(\omega_e \Psi_{PM,q}\right)^2 + \left(\omega_e \Psi_{PM,d}\right)^2 - u_{max}^2$$

For example, if a SMPSM must be analyzed, the *dq*-inductance will be equal and the q-axis flux linkage magnet will be zero. Therefore, the result of equation (152) is;

$$(\omega_e L)^2 i_d^2 + (\omega_e L)^2 i_q^2 + 2\left(\omega_e^2 L \Psi_{PM,d}\right) i_d + \left(\omega_e \Psi_{PM,d}\right)^2 - u_{max}^2 = 0$$

As can be observed, the result obtained is a circle as expected (see Figure 77). Figure 82 shows the results of applying (152) in a SMPSMS. Three different curves are shown with different speed but with the same voltage.

The example chosen is the easiest since the losses are neglected and there is no saliency. However, the analytical equation can be used to compute from this easiest example to the most difficult scenario, which it is the ellipses of a PMaSynRM considering the losses as shown in Figure 80.

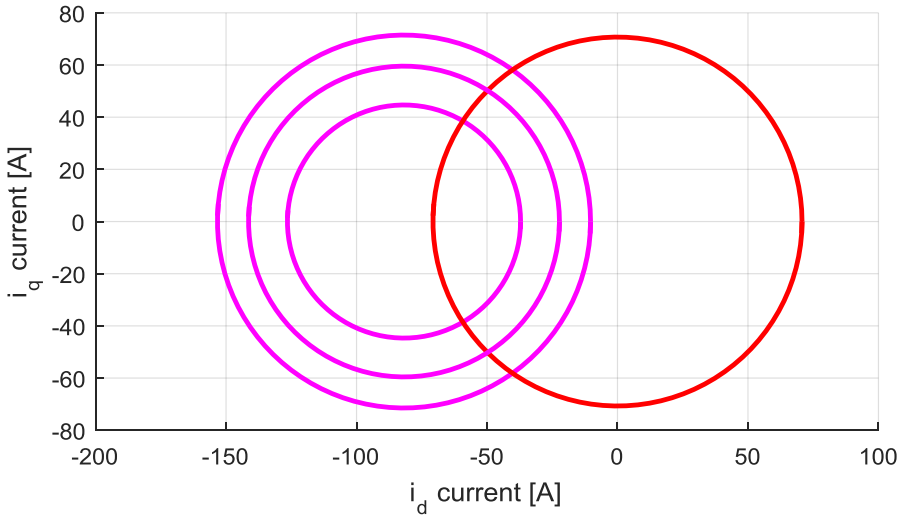


Figure 82. Example of equation (20). The motor chosen is a SMPMSM and the iron and copper losses are neglected

## 6.4 Procedure explanation

To generate the maps characterizing the motor (detailed ensemble of working points), the control parameters are swept within the feasible operating limits. The current is limited by the maximum allowable temperature, the voltage by the insulation requirements and the speed by the mechanical constraints. Note that, the different solutions of equations (146 and 152) are the intersection points between ellipse and circle in Figure 79. The amplitude of circle is related with the current meanwhile the shape of ellipse changes with the voltage and speed, so those variables (voltage, current and speed) define the three main loops of the proposed procedure, which is detailed in Figure 86 and Algorithm 3.

Figure 83 shows the effect of the sweep applied to a PMa-SynRM, visualizing both the current and speed in the two usual working planes, the *dq* and torque-speed planes. The sweep detail depends on the purpose of the maps. A coarse map (100 rpm, 10 A, and 25 V steps) for a 3000 rpm, 50 A, 300 V machine would be useful to study thermal limits. For the same motor, 10 rpm, 1 A, and 5 V steps would be more useful for torque angle data acquisition for control purposes. It is important to save, for each working point, all related variables such as voltage, current, speed, torque, resistance, power losses or flux linkage. It allows a further post-processing stage, by selecting the points matching with a target solution, e.g. maximum efficiency or maximum torque.

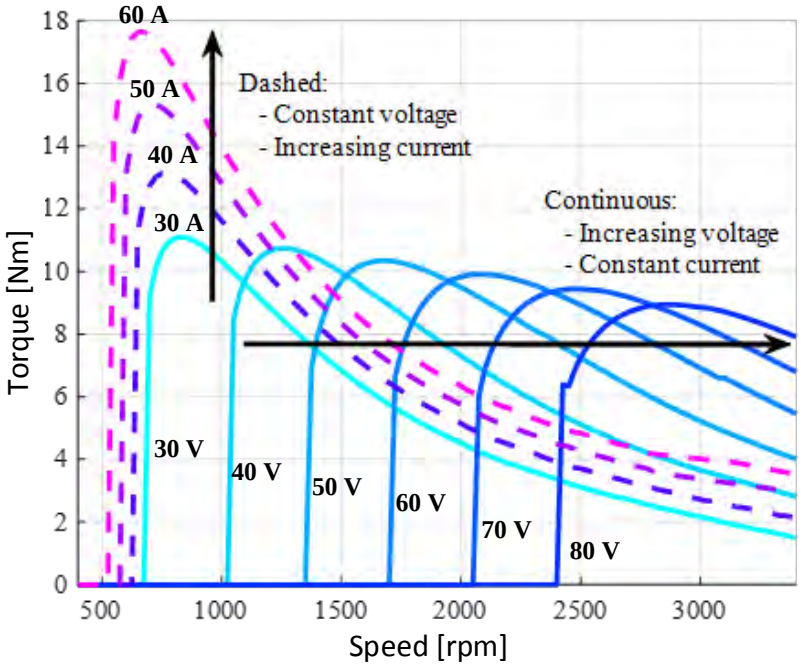


Figure 83. Solving procedure in the torque-speed plane, showing all voltage-current intersection points for a fixed voltage or current.

After analyzing all feasible voltage, current and frequency combinations, the machine operating points are acquired. There are many different torque-speed curves (Figure 83), which represent a different combination of current and voltage. Therefore, the same working point (same torque and speed) can be obtained using different combinations. Next, by manipulating the data included in all operating points, different behavior maps can be obtained.

To delimit the number of points in the different behavior maps, a mesh grid is created. In each interval, the different working points are evaluated according to a pre-established control law, and the best one is chosen.

Figure 84 shows a small area of Figure 83, which includes the different calculated working points and the properties of each one. In this detail, a torque-speed interval is analyzed to choose the best working point. The selected working point represents the full interval in the behavior map. For instance, when applying the MTPA control law, the chosen operating point would be *d*, since this point has the best torque per ampere ratio in the interval analyzed (30 V, 30 A curve).

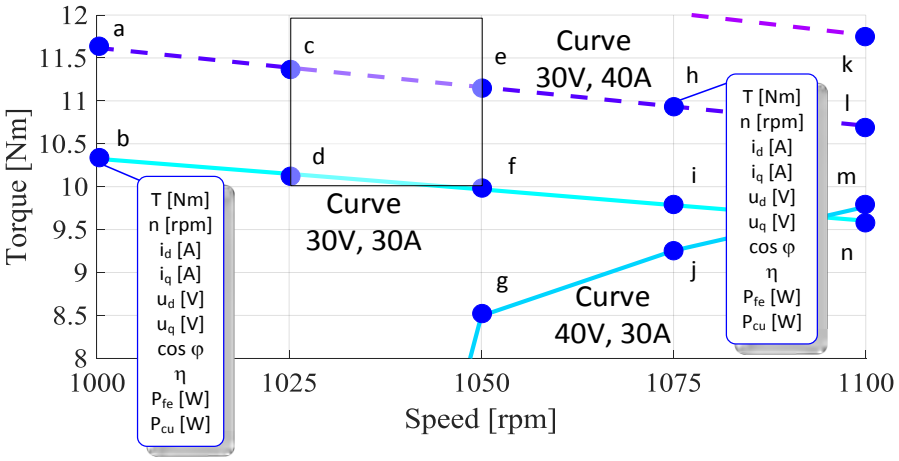


Figure 84. Detail of the torque-speed points selection depending on designer consideration. All points contain the information listed in *b* or *h*. The square represents a discrete $\Delta T - \Delta\omega$ 2D-interval

The size of the mesh grid in the torque-speed plane is strongly connected to the number of working points obtained in the process. The higher the resolution desired, the lesser the voltage, current and speed step size required, which affects the number of points in a torque-speed interval.

In this point, the proposed procedure to obtain the final behavior maps can be explained. Then, Algorithm 3 details the steps and the mains loops mentioned.

There are some terms or equations without description and some steps need a further explanation. On the one hand, there are two inner loops, which are necessaries to the determination of the correct solution of the proposed equation system. The innermost loop allows calculating the iron resistance. It can be observed in the equations of this section that the iron resistance appears in practically all of them. First, the iron losses (119), which had been explained in section 5, are necessary to obtain the iron resistance.

When the iron losses are known, the iron resistance can be defined. The iron resistance is given by,

$$R_{fe} = \frac{m}{2P_{fe}}\left(\left(-\omega_e L_q i_{oq} - \omega_e \Psi_{PM,q}\right)^2 + \left(\omega_e L_d i_{od} + \omega_e \Psi_{PM,d}\right)^2\right) \quad (153)$$

Is worthy to note that it is an iterative system since the iron resistance is necessary to solve the system and the solution of the system allows calculating the correct value of the iron resistance. Then, a seed value of the iron resistance is required (line 11). This value is given by;

$$R_{fe,estimated} = \frac{m}{2P_{fe}}u^2 \quad (154)$$

Where *"$u$"* is the value of the voltage in each loop of the Algorithm 3.

The innermost loop finishes when the iron resistance is correctly calculated. The error between the iron resistance estimation and calculation must be lesser than a predefined threshold.

```
1: Set the voltage, current and speed steps
2: for u = 0 to u = u_max do
3:     One term of F, equation (152), is obtained: F = k_3^2 + k_6^2 − u^2
4:     for i = 0 to i = i_max do
5:         copper losses (123) and circle calculation
6:         for ω_e = 0 to ω_e = ω_max do
7:             set current angle estimation, α_estimated
8:             while error α_estimated < threshold do
9:                 from LUT obtain L_d, L_q, Ψ_PM,d and Ψ_PM,q
10:                calculate iron losses P_fe (119)
11:                estimate iron resistance, using equation (154)
12:                while error of R_fe < threshold do
13:                    ellipse determination
14:                    intersection calculation (i_d, i_q) using (146 and 152)
15:                        determination of i_od (143), i_oq (144), u_d (133),
                           u_q(134), R_fe(153), α_i (157), α_v(158), T(135),
                           PF(159) and η(160).
16:                    calculation of iron resistance error
17:                end
18:                calculation of current angle error
19:            end
20:            save data
21:        end
22:    end
23:end
```

Algorithm 3. Solving procedure to obtain the behaviors maps

The second inner loop focuses to determine the current angle. The developed equation system needs the value of the inductances to obtain the ellipse, i.e. inductances are needed to calculate the solution in each loop. The values of them vary with *dq*-currents, so not only the current module is required but also the current angle. Consequently, an iterative system is required again since the inductances are necessaries to solve the system and the solution is required to obtain the final value of them. Therefore, a seed value of the current angle is defined in line 7 of Algorithm 3. The value of the inductances is obtained using the LUT calculated in the magnetic model. The value of this current angle estimated is different depending on the motor topology. For instance, in the SynRM topology, the seed value could be 45º or in the IPMSMS, the seed value could be 100º. This second loop finishes when the difference between the estimated and calculated current angle is below a defined threshold.

On the other hand, the intersection between current and voltage (line 14 of Algorithm 3) is done algebraically by applying a change of variables to decouple the $i_d$ and $i_q$ currents. The proposed change of variables is given by,

$$i_d = i\left(\frac{1-t^2}{1+t^2}\right) \quad (155)$$

$$i_q = i\left(\frac{2t}{1+t^2}\right) \quad (156)$$

Where "$t$" is the new variable. Is worthy to mention that the solutions obtained will be two or four, if there are solutions. Each solution belongs to different *dq*-currents quadrants, so depending on the motor topology the solution have to be in a specific quadrant. For example, in PMaSynRM the solution must be in the first quadrant ($i_q > 0$ and $i_d > 0$).

When the solution is achieved, for each combination of voltage, current, and speed, several parameters such as power factor ($PF$), current angle ($\alpha_i$), voltage angle ($\alpha_v$), efficiency ($\eta$), among others are obtained. These values are calculated as follows,

$$\alpha_i = \operatorname{atan}\left(\frac{i_q}{i_d}\right) \quad (157)$$

$$\alpha_v = \operatorname{atan}\left(\frac{u_q}{u_d}\right) \quad (158)$$

$$PF = \cos(\alpha_v - \alpha_i) \quad (159)$$

$$\eta = \frac{T\omega}{T\omega + P_{cu} + P_{fe}} \quad (160)$$

Finally, the calculated data in each iteration must be saved to allow obtaining the different behavior maps. In this context, for every combination of voltage, current and speed the properties of this operational point must be saved on a row with different columns (one for each parameter). For instance, the following parameters can be saved: Current module, d-current, q-current, current angle, iron losses, copper losses, speed, torque, efficiency, power factor, voltage module, q-voltage, d-voltage and power. Therefore, the matrix has fourteen columns, but the number of variables can variate. On the other hand, the innermost loop, i.e. the speed loop, increases the number of rows.

Once this loop is finished, the inner loop of current increases the size of third axis of the matrix. Finally, the outer one loop, which changes the voltage magnitude, creates a new package with the same properties that the explained before. An example of this 3D-matrix can be observed on Figure 85. Then, all the combinations are saved on this group of 3D-matrix, so the information necessary to select the best points according to a control law is presented.

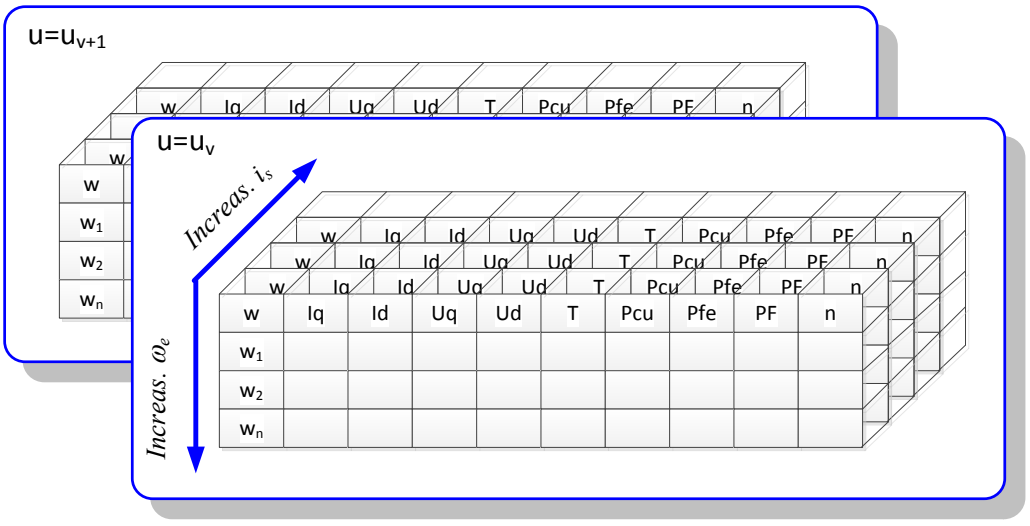


Figure 85. Packaging data description

In this section, the procedure to obtain different working points of the machine (see Figure 83) has been prefesented as well as the different calculated and saved performances of each working points.

The details of the algorithm are shown in Figure 86, which displays the inputs required and outputs obtained.

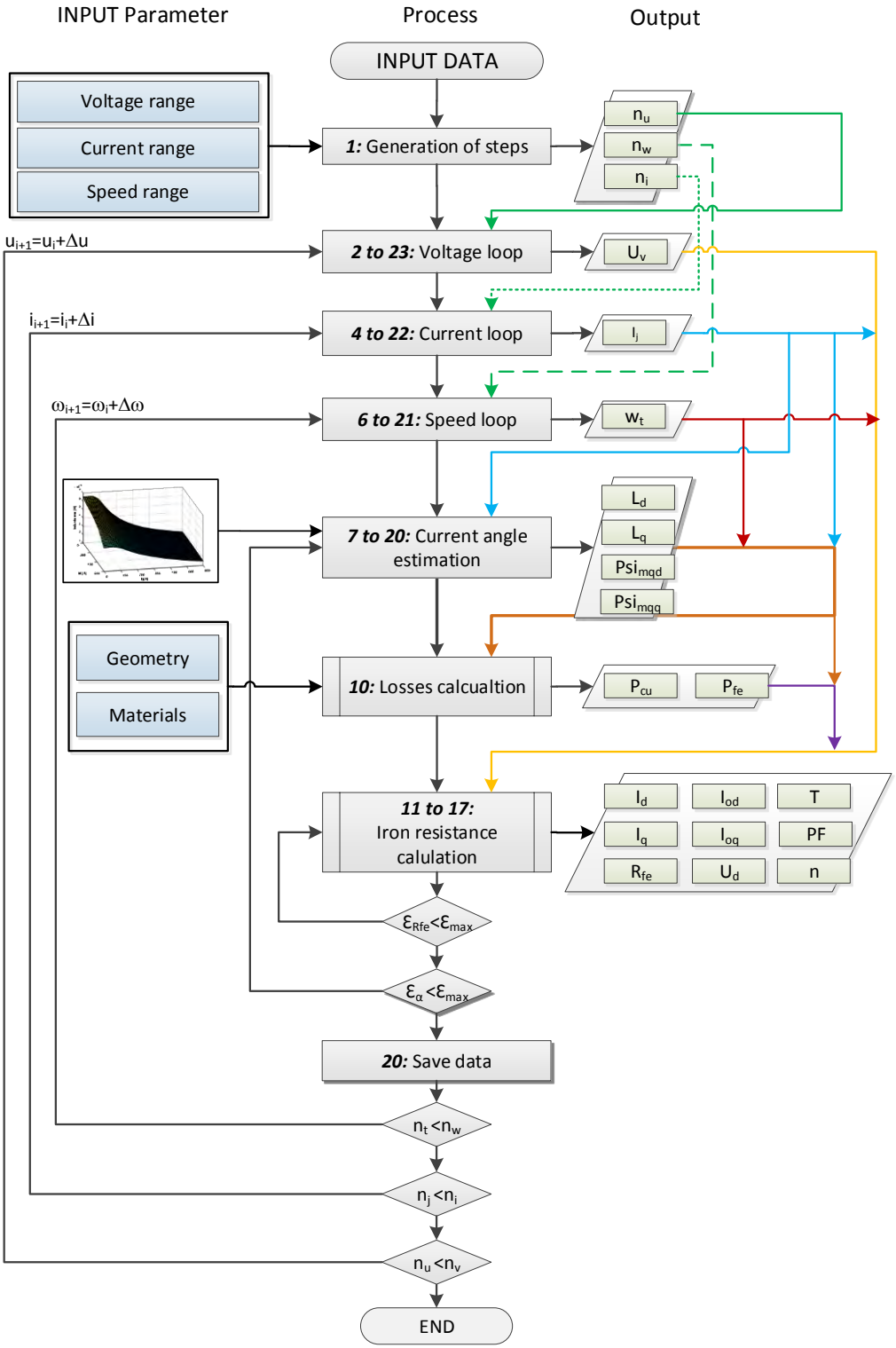


Figure 86. Flow chart of the process to generate the behavior maps

## 6.5 Results

The last part of this Section consists of obtaining the results. As mentioned before, there are several calculated working points with the same torque-speed coordinates (see Figure 84), so the correct one must be selected according to a defined criteria. For instance, the MTPA or MLC can be used to obtain the final behavior maps. Figure 87 shows two efficiency maps, which are represented in a torque-speed plane, obtained according to different control lows. Some differences can be noted in the efficiency contour. The main divergence appears in the speeds over 4500 rpm and torques below 20Nm. Furthermore, the values of several working points are depicted to reveal the exact value of the efficiencies. As expected, the efficiency in the MLC is higher than the extracted from MTPA.

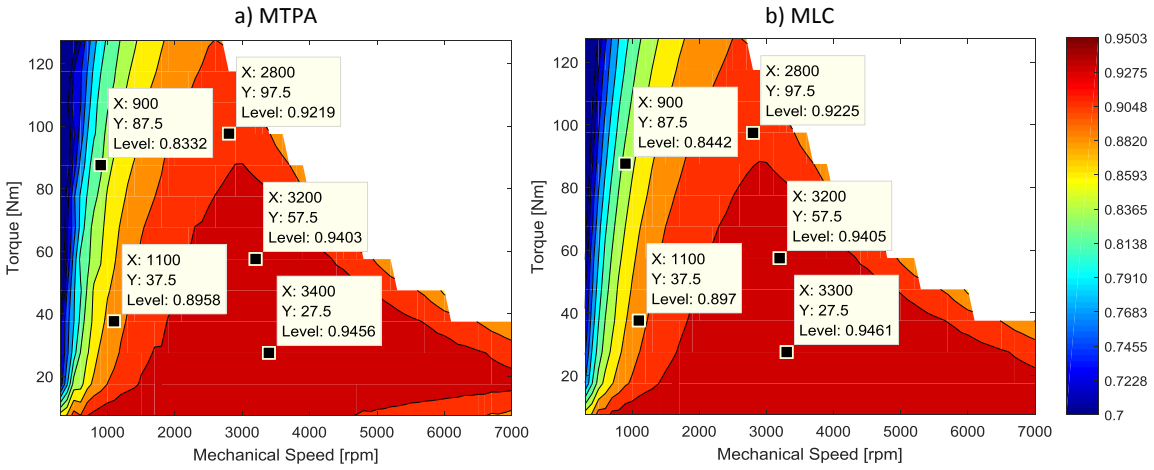


Figure 87. Efficiency map [p.u.] obtained with two different criteria. a) Maximum torque per ampere. b) Minimum losses control.

The differences between these two control laws appear in the rest of motor performances. For example, the current module required in each working point must be lesser in the MTPA map. Figure 88 displays the current module. The values of the same working points are pointed out.

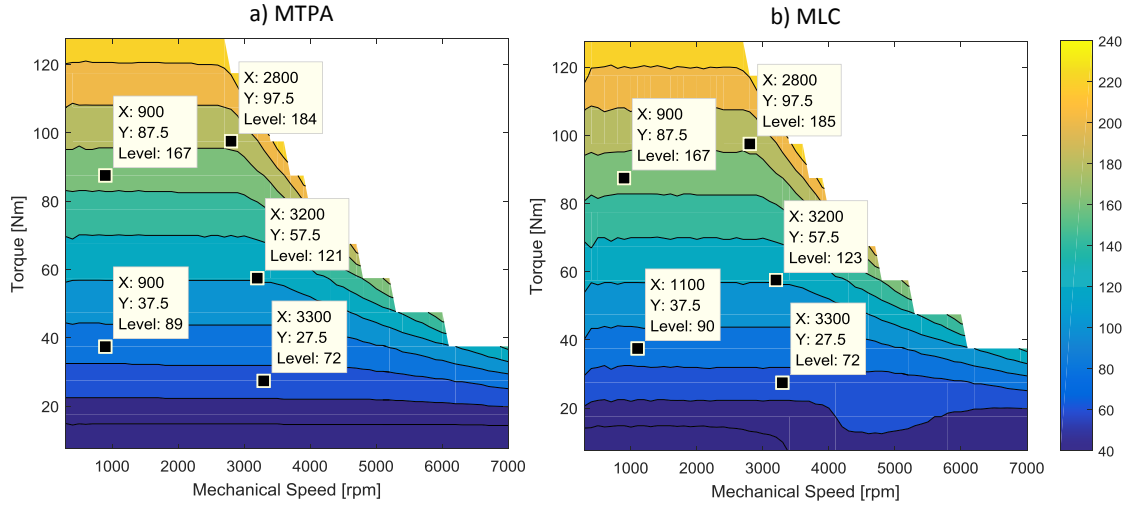


Figure 88. Phase current module [A] map obtained with two different criteria. a) Maximum torque per ampere. b) Minimum losses control

The previous maps are calculated with a low level of accuracy, so the number of steps of voltage, current and speed can be small. Although the proposed method is capable to calculate the different behavior maps in a few seconds, the computation time is strongly related to the number of analyzed points. Then, the use of these maps in an optimization process, which evaluates many motors, makes necessary adapting the steps size. In this context, the behaviors maps are shown in Figure 87 and Figure 88 can be improved. Then, a further comparison between different levels of accuracy is carried out in order to determine the correct use of the proposed tool. Figure 89 shows the efficiency maps under MTPA law of the same motor (Figure 87) with different density of points, i.e. the size of the mesh grid vary in each map ($\Delta T$-$\Delta\omega$).

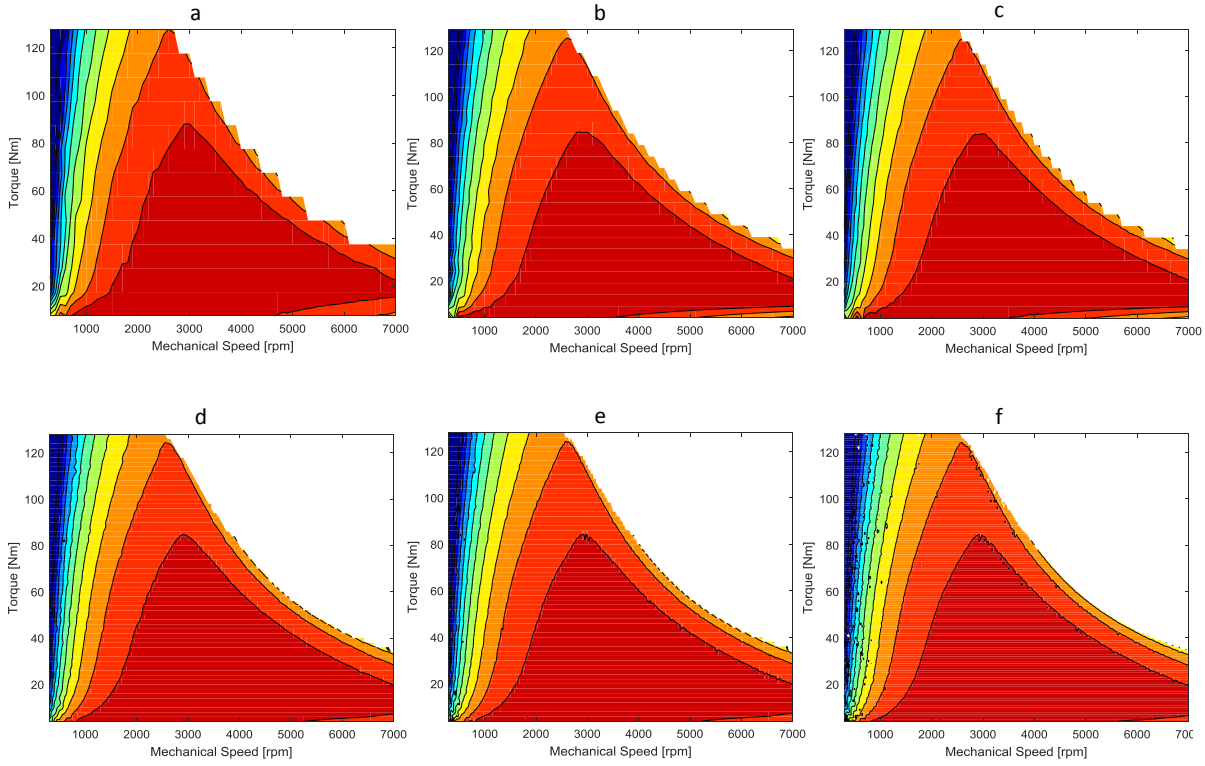


Figure 89. Efficiency [p.u.] maps in torque-speed plane with different resolution ($\Delta T$-$\Delta\omega$). a) $\Delta T$=10Nm, $\Delta\omega$ =100rpm. b) $\Delta T$=5Nm, $\Delta\omega$ =100rpm. c) $\Delta T$=5Nm, $\Delta\omega$ =50rpm. d) $\Delta T$=2Nm, $\Delta\omega$=50rpm. d) $\Delta T$=2Nm, $\Delta\omega$=25rpm f) $\Delta T$=1Nm, $\Delta\omega$=25rpm

As can be observed, the delineation of the torque-speed boundaries improves when the size of the mesh grid decreases. However, the number of calculated points increase exponentially as well as the time required to obtain this level of detail. A study of the time consuming is realized and summarized in Table 6. The steps' size of the three mains loops of the proposed tool (Figure 86, Algorithm 3) are detailed (voltage, current and speed). The number of the total computed points and the time required to calculate them are shown. Note that, the motor represented has a rated phase voltage of $150V_{peak}$, a phase current of $240A_{peak}$ and 7000 rpm as maximum speed. The initial value of the three loops is fixed at $1V_{peak}$ for voltage, $1A_{peak}$ for current and 50rpm for angular speed.

The time consuming is calculated using an Intel® Xeon® E5-1620 processor with 32 GB RAM. Despite the proposed method allows parallelization, the different tests are realized without it.

Table 6. Comparison of number of points and time consuming for each map in Figure 89

| Map | ΔU [V] | ΔI [A] | Δω [rpm] | Computed points | Time consuming |
|---|---|---|---|---|---|
| a | 6 | 6 | 100 | 70.000 | 259 s |
| b | 5 | 5 | 100 | 100.800 | 330 s |
| c | 5 | 5 | 50 | 201.600 | 470 s |
| d | 4 | 4 | 50 | 319.200 | 890 s |
| e | 4 | 4 | 25 | 638.400 | 1875 s |
| a | 4 | 3 | 25 | 861.840 | 3650 s |

The number of computed points considers all the intersection between different currents locus (circles) and voltage locus (ellipses), which are a combination of voltage and speed. Is worthy to mention that not only the efficiency is computed but also several performances are calculated in each point such as torque, speed, current module, current angle, *dq*-torque-generating currents copper losses, voltage module, voltage angle, iron losses, efficiency, power and power factor. Then, a part of the efficiency maps shown, there are other useful behavior maps.

The *dq*-current components can be used to develop a control based on lookup table since these values are computed considering losses, thermal effects, and cross-coupling saturation. Therefore, for each working point, the real values of *dq*-currents are obtained without the use of PIDs. Figure 90 shows the values of *dq*-currents on the whole torque-speed plane.

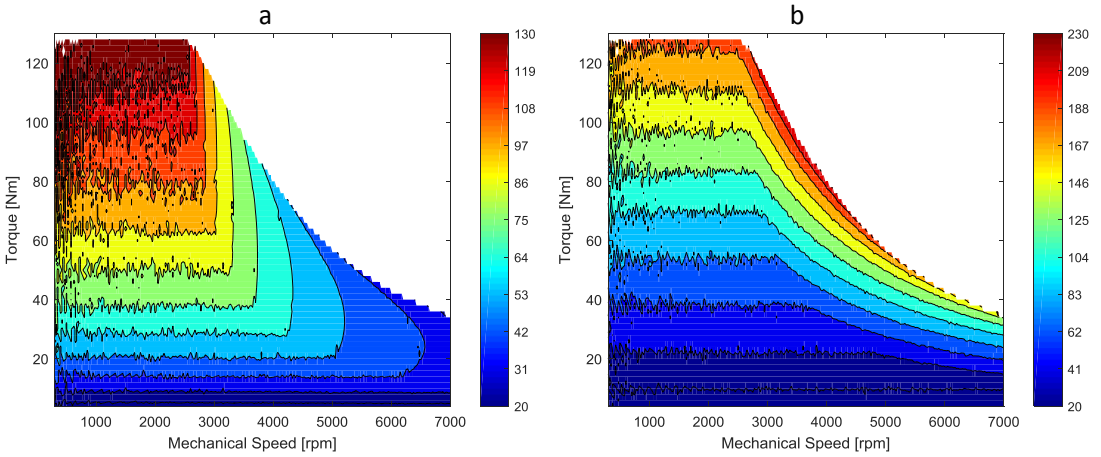


Figure 90. *dq*-currents in torque speed plane. Maps focus on control purposes. a) *d*-current component [A]. b) q-current component [A].

Let new considering an automotive application with the control based on LUTs. The voltage representation in the torque-speed plane can be used to adapt the motor capabilities according to the level of battery's charge. In addition, the voltage map can be used in the design process since the study of the different value of voltage can be carried out.

Furthermore, more maps can assist to design process. For instances, iron losses map helps in the design process too. Using the equations (120-122) and the database of magnetic materials, the iron losses can be calculated depending on the steel chosen, so the effect on the efficiency and the material's cost can be studied. Power factor map is another example of the maps to assist the design. The power factor is one the main drawbacks of the SynRM motors. The use of ferrites in the SynRM helps to improve the motor performances, which one of them is the power factor. However, the material and manufacturer cost increase as well as the total weight of the machine. Then, a good

balance between magnet quantity and improvements is mandatory, so the use of power factor maps can help to choose the correct magnet quantity. Figure 91 shows the mentioned behaviors maps; voltage, iron losses and power factor maps.

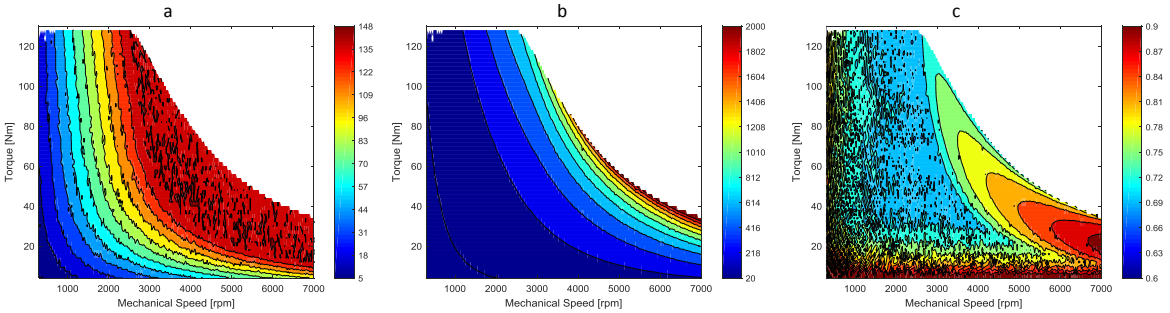


Figure 91. Several behaviors maps to assist the design process. a) Phase voltage [$V_{peak}$] representation on the torque-speed plane. b) Iron losses [W] representation in the torque-speed plane. c) Power factor [p.u.] representation in the torque-speed plane.

As mention before, behavior maps have more representation apart of the torque-speed plane. For example, representing the efficiency or the power factor in the power-speed plane give relevant information about the energy requirement. The torque representation in the power-speed plane reveals the fact of the maximum power is not achieved in the corner speed. Figure 92 shows the described maps, which are power factor, efficiency and torque.

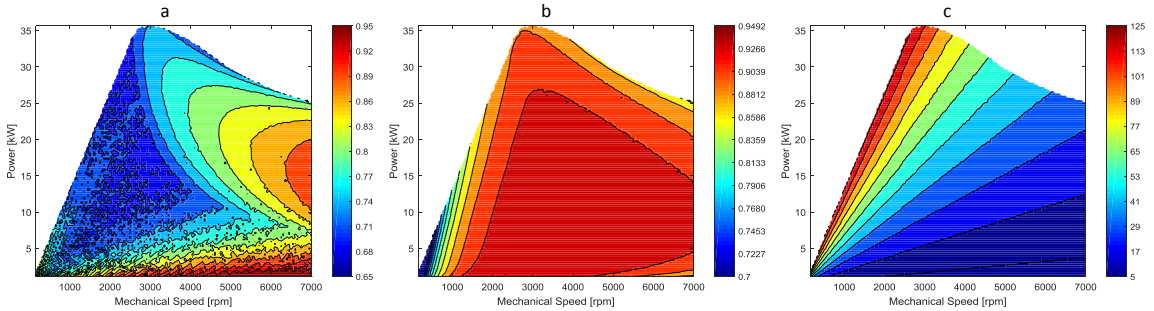


Figure 92. Behavior maps represented in the power-speed plane. a) Power factor [p.u.]. b) Efficiency [p.u.]. c) Torque [Nm]

Finally, yet importantly, the torque representation in *dq*-current plane can be used to obtain the MTPA trajectories. The iso-torque curves can be observed in Figure 93. Note that, the results are obtained considering iron losses, magnetic saturation, and phase resistance.

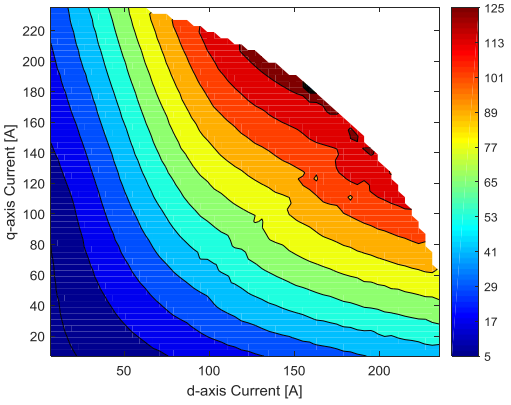


Figure 93. Torque representation in *dq*-current plane.

## 6.6 Conclusions

The presented chapter deals with the contributions on behavior maps calculation. An analytical model to calculate the different behavior maps are presented. Some conclusions can be extracted,

- Behaviors maps can assist the design process since different motor performances such as efficiency, power factor, iron losses, voltage, among others can be calculated in a few seconds in the completely operating zone.
- Control based on lookup tables can be extracted in the presented procedure. The *dq*-currents components are calculated for each torque-speed coordinates. The currents components are extracted considering the iron losses, thermal variations, and magnetic saturation.
- The accuracy of the behavior maps is adaptable to the application, i.e. the points density required in the optimization process is lesser than the necessaries to build a LUT control. Note that, the computational time required is strongly related to the number of calculated points.
- Not only the torque-speed plane can be extracted in the presented procedure but also other planes can be analyzed. The power-speed plane can be used in the energy consumption estimation or the iso-torque curves can be represented in the *dq*-currents planes in order to obtain the real MTPA trajectories.

# 7.

# Analysis of sensibility

The proposed method allows considering the possibility to include or neglect some motor effects in the calculation of the behaviors maps. Increasing the level of accuracy makes it harder to solve the system proposed. A further analysis of the influence of the different accuracy levels dq-model in the efficiency and control parameters for PMa-SynRM.

*CONTENTS:*

# 7. Analysis of sensibility

## 7.1 Introduction

The previous section shows an analytical procedure to obtain the different behavior maps without the use of FEA. These behavior maps are calculated taking into account cross-coupling saturation, thermal effect and iron losses. However, the proposed procedure allows considering or neglecting these effects. A further analysis of the accuracy of the behavior maps when these parameters are neglected are carried out with the intention of showing the influence of them in PMaSynRM. Therefore, the variation on the solutions can be observed and the influence of the neglected parameters can be quantified. The differences between complete or simplify models not only can be quantify in the proposed behaviors maps but also in Blondel diagram can be observed in a qualitative approach.

Analyzing the error caused by neglecting some parameters is interesting since current methodologies try to reduce the use of FEA contribution by using analytical descriptions of the motor in order to speed up the design process. However, some motor effects are neglected, such as cross-coupling saturation, thermal variation and iron losses, due to the mathematical complexity involved in its formulation. For instance, in [28, 114, 141, 142] the cross-coupling effect is not considered in the model. In [100] temperature is not included, so the magnet properties are lower and the ratio torque per current measured is smaller than the calculated by FEA. In [143] the iron losses are neglected, so the calculated efficiency is not correct.

The section evaluates the error made in the estimation of efficiency, current, and current angle when these effects are neglected. In this context, these performances are represented in the torque-speed plane to visualize not only the difference in the boundaries but also the difference in the value. Motor efficiency is significant for many drive applications, for instance, in energy management for electric vehicles. The other two parameters are critical for defining the MTPA trajectories in motor control. Note that, in spite of the PMaSynRM the correct control is based on a lookup table (LUT) [134], some authors use the traditional equations and neglect the cross-coupling saturation [114, 144].

## 7.2 Complete model

In previous sections, the calculation of different parameters and performances, such as inductances, temperature, iron losses, and behaviors maps, are developed. The magnetic model allows calculating the inductances (considering cross-coupling), the magnet flux linkage, and the magnetic saturation to estimate the iron losses. The thermal model calculates the temperature of the machine, so the winding and magnets temperatures are kwon. Then, the final value of the phase resistance and magnetic properties of the ferrite are calculated. At last, the electric model combines the information obtained in the magnetic and thermal models to calculate the motor performances in different operation points. Then, the motor performances are calculated coupling the thermal, magnetic, and electric model as can be observed in Figure 94.

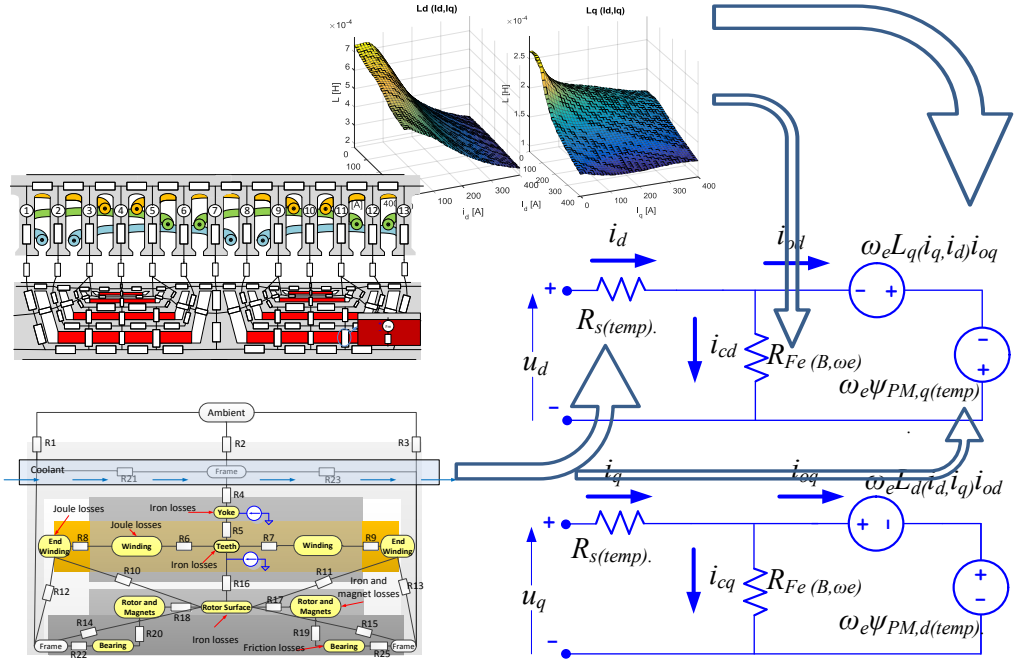


Figure 94. Thermal, magnetic and electric relations.

In this section, the motor performances are calculated considering different levels of accuracy. In the complete model, the phase resistance and the magnets are affected by the temperature, the inductances are calculated considering the cross-coupling saturation, and the iron losses are considered. The main characteristics of the analyzed motor are summarized in Table 7.

Table 7. Motor's characteristics

| Items [unit] | Value |
|---|---|
| Mechanical power [kW] | 27 |
| Corner speed [rpm] | 2800 |
| Phase voltage [Vrms] | 104 |
| Phase current [Arms] | 170 |
| Number of phases | 3 |
| Number of poles pairs | 8 |
| Number of slots | 96 |
| Iron lamination | M300-35A |
| Ferrite magnet | HF 26/24 |
| Outer stator diameter | 270 mm |
| Stack length | 70 mm |
| Insulation type | H |

As former mentioned, the behavior maps are represented in a torque-speed plane. Is important to mention that the number of calculated points on these three maps is the same, but the points represented on the torque-speed plane are different for efficiency map from for the other two maps. This effect can be observed in the flux-weakening region in Figure 95 and Figure 96, where the boundary line is more accurate in the current angle and current module maps. More accuracy is necessary because the efficiency map is compared against the extracted map from FEA whereas the other two maps are validated against experimental results, with fewer values to compare.

Moreover, the FEA software needs to realize one simulation per point, so the time required is strongly connected with the number of points in the behavior map. Therefore, the calculated working points for comparisons are reduced. On the other hand, the experimental validation requires a higher precision in measurements in order to obtain the correct value for the working point.

In the full model developed, the behavior maps are calculated using the proposed analytical method considering the real motor temperature, i.e. using the real value of phase resistance and magnetic properties of ferrites. The cross-coupling saturation and the iron losses are considered too. As mention before, the parameters chosen for comparisons are efficiency, current angle and current module. The first one focuses on design problems since the range optimization requires several points to evaluate the motor behavior during the design process. Figure 95 shows the efficiency in the torque-speed plane.

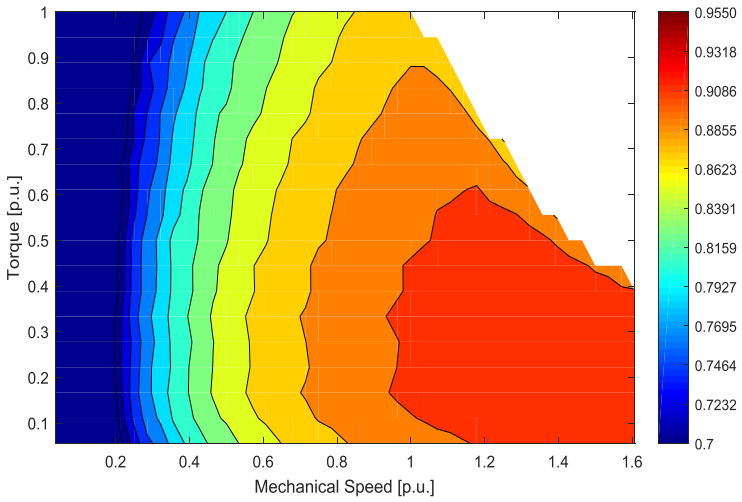


Figure 95. Analytical efficiency map considering cross-coupling saturation, temperature effects, and iron losses

Note that the axes (torque-speed) are represented at per unit with the aim to make easy the comparison between different maps. Furthermore, the color bar is according to all the shown behavior maps in the work to facilitate to visualize the similarities between all the maps.

The strongly variation of the current angle with the motor saturation makes impossible to develop a control based in the traditional equations. Therefore, the proposed work obtains the motor performances necessary to develop a control. The current angle and current module behavior maps are necessary to develop a MTPA control based on a lookup table. Therefore, these maps are here obtained and compared for its significance for the motor control. Figure 96 shows the evolution of the current angle in the torque-speed plane.

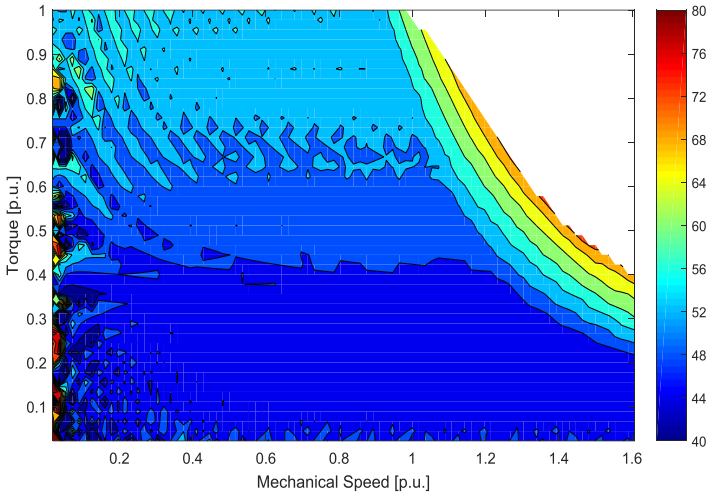


Figure 96. Analytical current angle map considering cross-coupling saturation, temperature effects, and iron losses

As mention before, in this motor topology the current angle of MTPA change with the saturation as can be observed. Note that, the current angle of the MTPA varies from 40º (low load) to 55º (high load) in the non-flux weakening region. The *q*-current component increases when the motor is more saturated to increase the saliency, so the resultant torque will be higher. In addition, the *q*-current also increase in the flux weakening region with the aim of reducing the voltage requirement due to the reduction of the machine magnetic saturation

Apart of current angle, the current module is necessary to implement the control based on LUTs. Figure 97 shows the current module distribution on the torque-speed map. The value of the current rises together of the torque in the MTPA region, as expected. Notice that the current module is in per unit too.

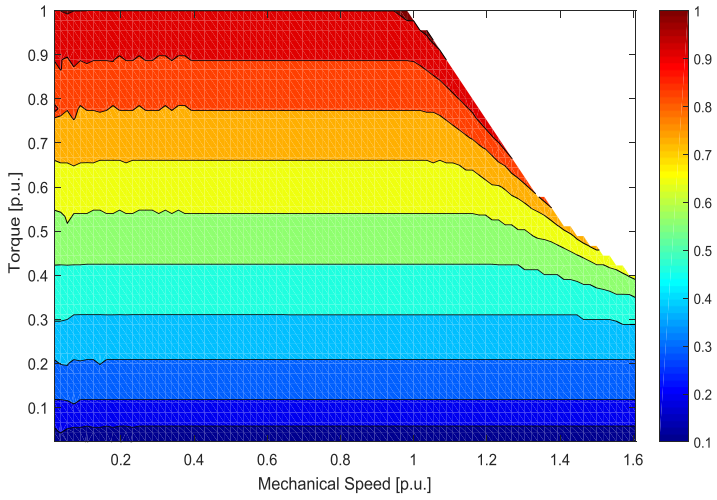


Figure 97. Analytical current module map considering cross-coupling saturation, temperature effects, and iron losses

For validation purposes, FEA is used to obtain the efficiency maps. The program used is Flux (Altair, v12.2). The configuration chosen in this case is a mesh grid of interval of 5Nm and 100 rpm. At the starting point, 810 simulations are required to obtain this map, and despite the number is reduced

in the flux weakening zone, this process needs a high computational time. Figure 98 shows the efficiency map obtained.

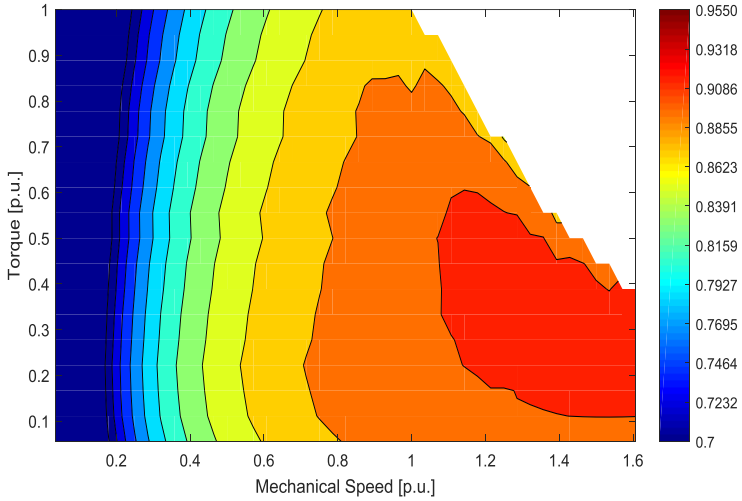


Figure 98. FEA efficiency map

The comparison of the whole map shows the great agreement between the analytical calculation considering all the effects and the FEA results. The average error is 1.98% and the standard deviation is 1.32%. The maximum error is located at 0.035 of the corner speed and 0.1 of the rated torque and is 9.32%.

Finally for model validation, experimental measurements are performed. The test consists of changing manually the current angle on several working points in order to find the *dq*-components of the currents with the lower current module in each case. Thus, the data measured corresponds with the real MTPA and can be compared with the calculated behavior maps.

The behavior maps can be used to develop a control based on lookup tables since the *dq*-currents can be calculated on each operational point [134]. The calculated *d*-current and *q*-current of several working points, which are obtained from Figure 96 and Figure 97, are summarized in Table 8. Therefore, these maps are calculated considering all the effects. Figure 99 shows the *dq*-currents maps.

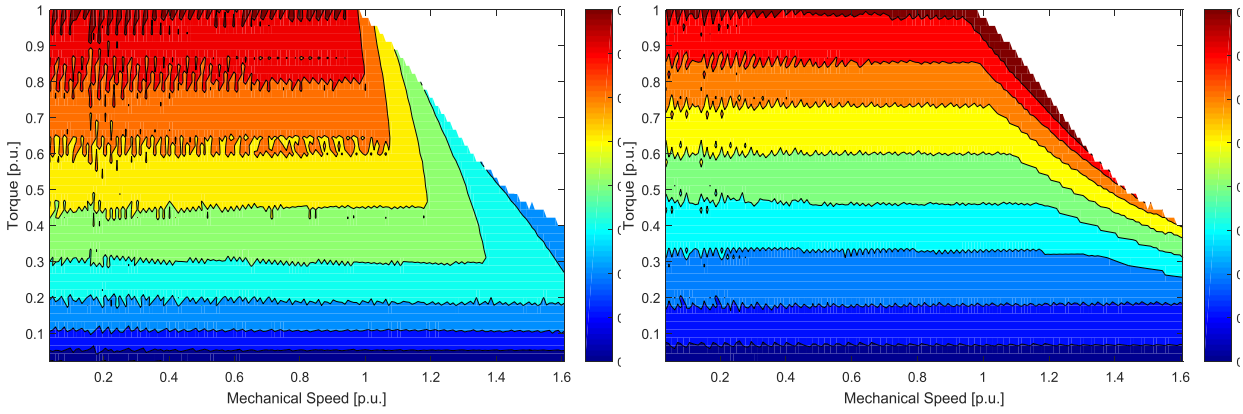


Figure 99. *dq*-currents map considering cross-coupling saturation, thermal effects, and iron losses. Left: d-current. Right: q-current.

A representative scheme of the experimental test bench is shown in Figure 100. The used materials in the data acquisition are a T22 torque sensor from HBM, a RI 76TD encoder from Hengstler, a 1FT6108-8SB71-1DK3 Surface Mounted PMSM from Siemens and a CompactRIO acquisition system.

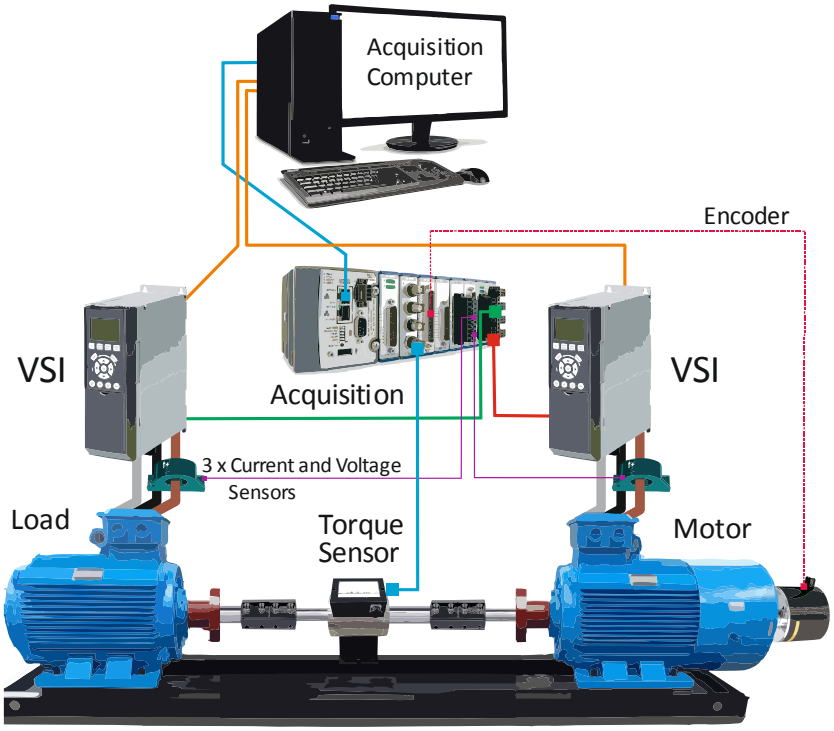


Figure 100. Representation of the experimental test bench

Table 8 compares the estimated *dq*-current components of several working points, which are described as a torque-speed combination, with the experimental data measured in the test bench. The results show a close agreement between the results provided by the proposed simulation tool and experimental data, thus validating the approach presented in this paper for the analytical model.

Table 8. Experimental test comparison

| Points (n,T) | | d-current [p.u.] | | Error [%] | q-current [p.u] | | Error [%] |
|---|---|---|---|---|---|---|---|
| [p.u.] | [p.u.] | Estimated | Experimental | | Estimated | Experimental | |
| 0.05 | 0.42 | 0.324 | 0.317 | 2.1 | 0.362 | 0.364 | 0.5 |
| 0.05 | 0.53 | 0.398 | 0.402 | 0.9 | 0.505 | 0.507 | 0.4 |
| 0.05 | 0.78 | 0.497 | 0.497 | 0.1 | 0.678 | 0.692 | 1.9 |
| 0.10 | 0.15 | 0.220 | 0.227 | 2.9 | 0.223 | 0.224 | 0.2 |
| 0.10 | 0.45 | 0.383 | 0.389 | 1.5 | 0.445 | 0.454 | 2.1 |
| 0.10 | 0.86 | 0.536 | 0.546 | 1.7 | 0.767 | 0.744 | 3.0 |
| 0.25 | 0.10 | 0.203 | 0.198 | 2.5 | 0.185 | 0.191 | 3.0 |
| 0.25 | 0.55 | 0.455 | 0.439 | 3.8 | 0.522 | 0.531 | 1.6 |
| 0.25 | 0.82 | 0.545 | 0.544 | 0.2 | 0.723 | 0.741 | 2.4 |
| 0.35 | 0.29 | 0.306 | 0.311 | 1.6 | 0.325 | 0.335 | 2.8 |
| 0.35 | 0.44 | 0.393 | 0.388 | 1.2 | 0.440 | 0.450 | 2.3 |
| 0.35 | 0.60 | 0.444 | 0.446 | 0.5 | 0.541 | 0.551 | 1.8 |
| 0.50 | 0.13 | 0.214 | 0.212 | 0.8 | 0.210 | 0.210 | 0.2 |
| 0.50 | 0.30 | 0.329 | 0.329 | 0.0 | 0.342 | 0.350 | 2.1 |
| 0.50 | 0.78 | 0.510 | 0.525 | 2.9 | 0.675 | 0.695 | 2.8 |
| 0.60 | 0.10 | 0.193 | 0.196 | 1.2 | 0.195 | 0.195 | 0.0 |
| 0.60 | 0.35 | 0.342 | 0.340 | 0.8 | 0.366 | 0.372 | 1.5 |
| 0.60 | 0.66 | 0.460 | 0.480 | 4.1 | 0.590 | 0.612 | 3.6 |
| 0.75 | 0.20 | 0.258 | 0.259 | 0.3 | 0.254 | 0.259 | 1.9 |
| 0.75 | 0.44 | 0.384 | 0.390 | 1.7 | 0.444 | 0.449 | 1.2 |
| 0.75 | 0.66 | 0.467 | 0.487 | 4.2 | 0.591 | 0.599 | 1.3 |
| **Average** | | - | - | **1.7** | - | - | **1.8** |

## 7.3 Accuracy levels

This section aims to quantify the influence of the cross-coupling saturation, thermal effect and iron losses on several motor's performances, which are represented in the mentioned behaviors maps.

Three different tests are realized for the comparison purposes. In test A the cross-coupling effect is neglected. In test B, the thermal variation (on phase resistance and magnet flux) is not considered. In test C, the iron losses are ignored. Then, results are compared to those obtained from the complete analytical model.

### 7.3.1 Test A: Effects of neglecting the cross-coupling saturation

In PMaSynRM machines, the magnetic saturation is closely related to the motor capabilities, so neglecting the cross-coupling saturation might increase the expected torque of the motor, which of course is erroneous. It can be observed in Figure 101 that shows a maximum torque of 11.11% higher than the real one depicted in Figure 95 or Figure 96.

Regarding the value, the maximum efficiency is now 0.931 that is similar to the real one, so the cross-coupling saturation is not strongly related to the efficiency values. Although, it affects the efficiency distribution regarding speed, as Figure 101 shows.

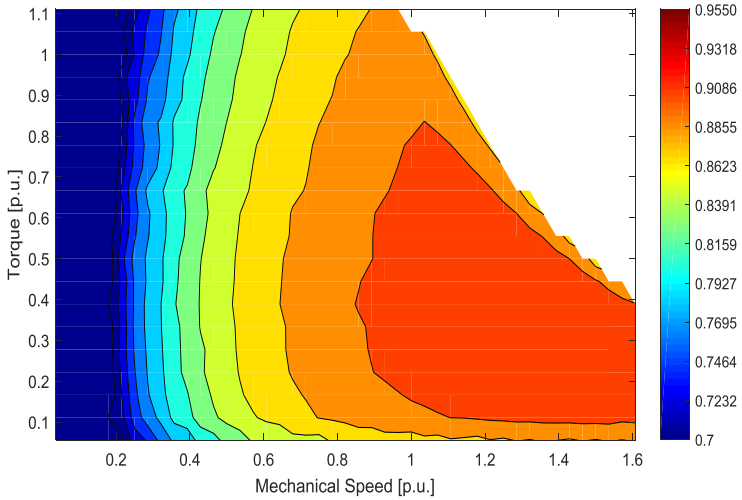


Figure 101. Analytical efficiency map neglecting the cross-coupling saturation

Instead, neglecting the cross-coupling saturation in the motor model affects significantly the current angle. Neglecting the cross-saturation means that the direct inductance is not affected by the q-current. Thus, increasing the current angle the saturation on the direct axis decreases, so the saliency of the motor increases. Figure 102 shows the current angle analytically obtained in this test.

The current angle results five degrees higher if the cross-coupling is not considered, so the use of this wrong map in a lookup table will introduce an important error in the maximum torque per ampere trajectory. Then, the obtained torque in the real motor using this value will not achieve the rated torque expected. In this example, the torque error generated to the control due to the use of this angle is 4.1%.

Finally, without cross saturation consideration the current module necessary to obtain the same torque is lower than the real one, as can be observed in Figure 103 when compared with Figure 97 (9% lower in this example).

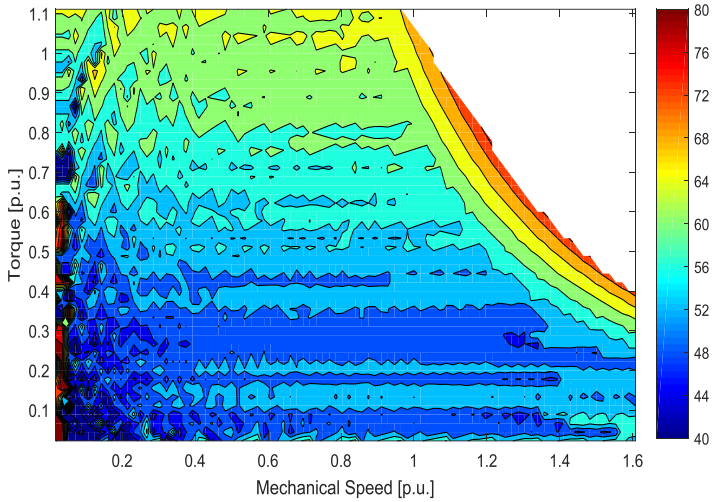


Figure 102. Analytical current angle map neglecting cross-coupling saturation

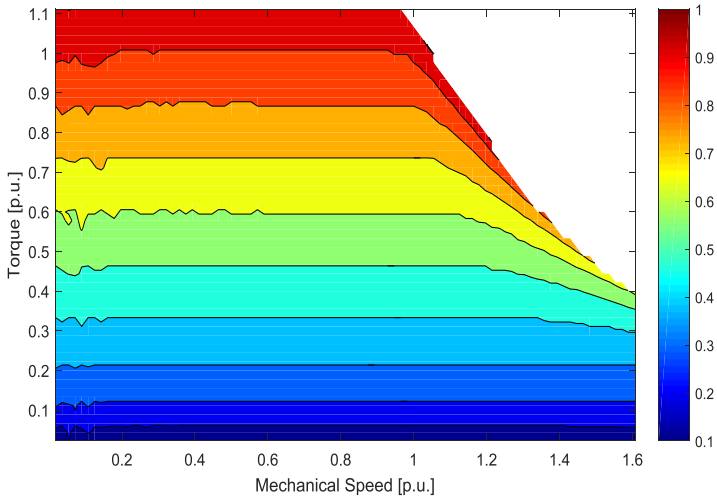


Figure 103. Analytical current module map neglecting cross-coupling saturation

Using this current module the torque obtained in the real motor is 11% less than the correct one. Furthermore, if the error on a current angle and current module are considered at the same time, the real torque obtained from the machine will be 17.5% lower than the calculated one, which strongly affects the motor drive design and application. Therefore, the cross-coupling saturation is fundamental to calculate the motor must be considered to calculate the motor control performances.

### 7.3.2 Test B: Effects of neglecting the thermal effects

The sizing of the machine based on analytical equations roughly estimates the end-winding hot point temperature, to prevent overheating [119]. However, the temperatures of the other parts of the machine are not calculated. Furthermore, in the optimization process the geometry of the slots can change, so the thermal behavior is affected. In this context, the real temperature of other critical parts, such as the permanent magnets, is totally unknown. Then, the motor performances are affected, i.e. the permanent magnet properties and the phase resistance depend on the temperature. For this reason, this test aims to evaluate the influence of the magnet and phase resistance temperatures in this motor.

It can be observed on the behaviors maps obtained in this test that the torque is higher than the real one as expected. In this case, the torque is 5.55% higher in the efficiency map and 4.44% higher in the other two maps. This divergence comes from the resolution of the maps because the intervals on the efficiency map are 0.05 and the intervals on the current angle and module maps are 0.02.

In this case, the efficiency is greatly affected as shown in Figure 104. The area with the maximum efficiency is almost the whole flux-weakening region zone. The maximum efficiency neglecting the thermal effects is 0.941.

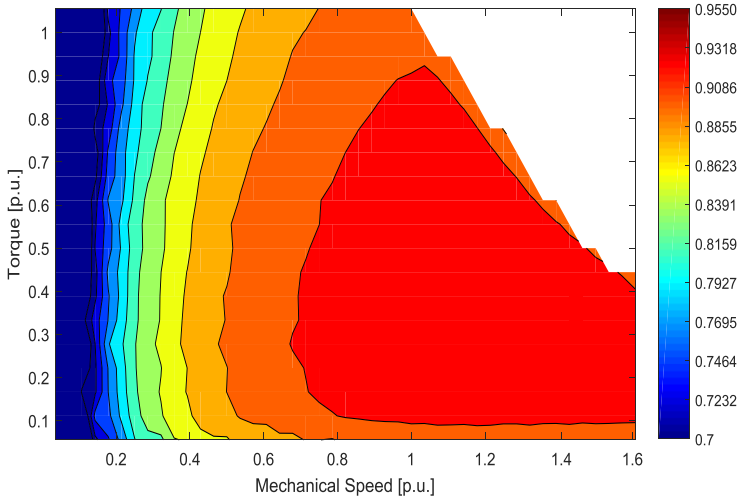


Figure 104. Analytical efficiency map neglecting thermal effects

Considering the motor properties, a higher magnetic flux linkage can increase the *d*-current component. Figure 105 shows the current angle map. It can be observed that the first angle level (around 45º) is over 0.5 of the total torque and the second level (around 52º) is over 0.75 of the total torque. The same levels of complete model are over 0.4 and 0.61 of the torque respectively. However, the error in the torque calculating by using these values of current angle is not important. For example, at rated torque using the current angle obtained in this test the torque error is 0.2%.

Finally, the current module is also affected, because less current is necessary to obtain the same torque since the magnet flux linkage is higher than before. However, the error is lower than obtained without considering the cross-coupling saturation, because the magnet torque in PMaSynRM is smaller than the reluctance torque. Figure 106 shows the current module in the torque-speed plane.

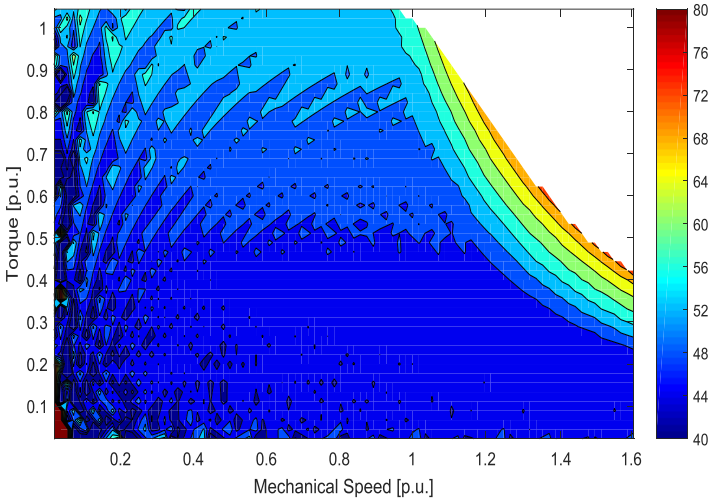


Figure 105. Analytical current angle map neglecting thermal effects

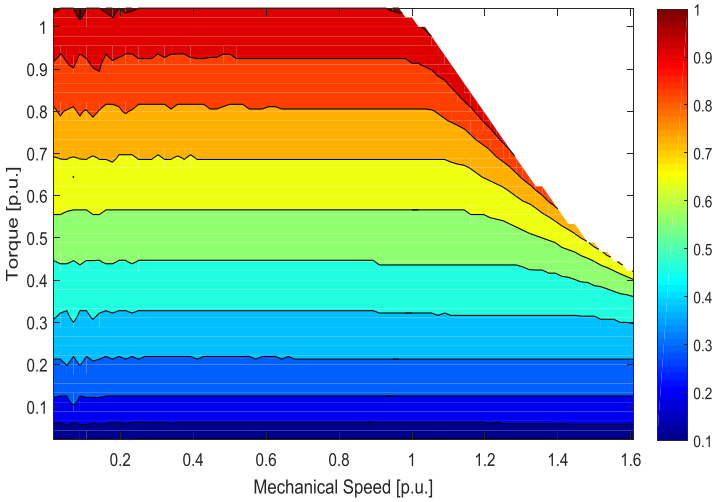


Figure 106. Analytical current module map neglecting thermal effects

The current at rated torque, in this case, is 3.33% less than the obtained in complete model. The torque with this current wrong value is 3.4% lower. Finally, the error considering the current angle and current module calculated without thermal consideration is 3.5%.

### 7.3.3 Test C: Effects of neglecting the iron losses

In this test the iron losses are neglecting, and as it can be observed in Figure 107 the maximum torque is the same than the torque in the complete (real) model. Although the torque-speed boundaries are not exactly the same, the iron losses have not a big effect on the torque calculation. However, the efficiency in this case is higher than in other tests. Figure 107 shows the efficiency contour. In this case, the maximum efficiency is 0.955.

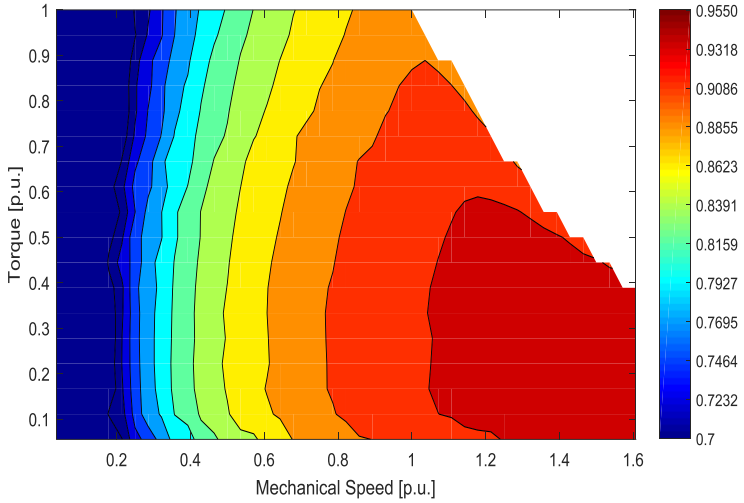


Figure 107. Analytical efficiency map neglecting iron losses

The current angle and current module are practically the same than those obtained from the complete model (Figure 96 and Figure 97), as it is shown in Figure 108 and Figure 109 respectively. Then, the iron losses are not essential to compute the control maps.

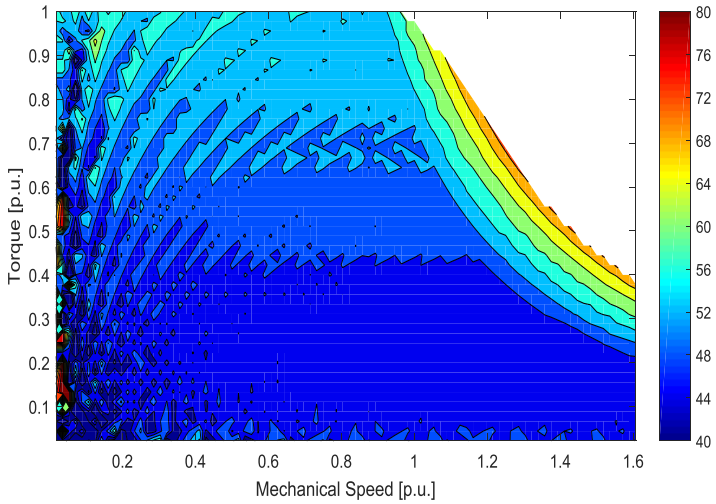


Figure 108. Analytical current angle map neglecting iron losses

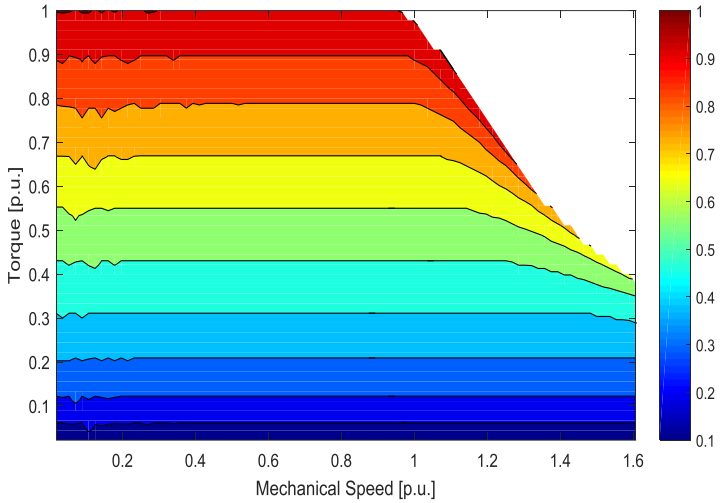


Figure 109. Analytical current module map neglecting iron losses

The error in the current module is 0.1% and the current angle error is less than 0.5 degrees. Then, the torque obtained with these maps has an error lower than 0.2%. Also, increasing the resolution of the mesh, the torque-speed boundaries are more similar to the complete model as shown in current angle and module maps.

### 7.3.4 Comparisons and discussion test

To summarize, there are several differences between the behavior maps obtained considering diverse grades of accuracy in the motor model. For instance, neglecting the cross-coupling saturation and thermal effects the torque-speed boundaries change. Besides, not only the boundaries vary but also the performances on the different working points as can be observed on the different behavior maps.

Table 9 shows a comparison between the results obtained in the different tests. In this comparison, the error at the rated point is shown (i.e., maximum torque at corner speed). Furthermore, the variation on current angle and module in rated point and the torque error obtained with these values are also shown.

Table 9. Comparison of different levels of accuracy

| Error in : | Test A | Test B | Test C |
|---|---|---|---|
| Maximum torque | 11.1% | 5.5% | 0.0% |
| Corner speed | 3.6% | 3.6% | 0.0% |
| Maximum efficiency | 0.4% | 1.1% | 2.6% |
| Current module at rated point | 9% | 3.4% | 0.1% |
| Current angle at rated point | 5.6º | 2.4º | 0.5º |
| Torque obtained with these values | 17.5% | 3.5% | 0.2% |

The study of these tests confirms the strong effect of the cross-coupling saturation in this kind of machines, especially when the design is very tight in terms of saturation conditions. If the calculation of maps focuses on control strategy, the cross-coupling saturation must be included since the final error is highly significant, as it is shown in Table III (17.5%).

## 7.4 Conclusions

This section presents an analysis of the influence of cross-coupling, temperature and iron losses effects on the calculation of several PMaSynRM's behaviors maps, specifically, efficiency, current module and current angle. The inductances considering cross-coupling effect are obtained using a reluctance network and the behavior maps are calculated by using the resulting an analytical model, which is validated against FEA and experimental measurements. Validations show that it is possible to obtain accurate behavior motor maps without the use of FEA, but considering cross-coupling saturation, thermal variations, and iron losses analytically modeled. Also, the data calculated with the model permits developing a MPTA control based on a lookup table since the current angle and module are determined on the whole torque-speed plane with high exactness.

Furthermore, an analysis of the accuracy of the motor models by considering or neglecting these effects are performed. Results confirm that cross-coupling and temperature cannot never be discarded in PMaSynRM motor models neither for design (motor efficiency) nor control (current module and current angle), because they extremely affects the motor behavior and operation.

# 8.

# Experimental validation

This chapter aims to show the experimental validation of the proposed methodology.

*CONTENTS:*

# 8. Experimental validation

During the thesis development several motors have been designed and some of them have been manufactured to validate the proposed methodology. A summarize of the obtained results and the validation with FEA or experimental data are discussed in this section.

## 8.1 Driving cycle optimization

This section applies the proposed optimization approach to obtain a motor with the performances calculated in *Section 2.2.2. Optimization*. For the sake of readability, methodology for motor design is again presented in

Two motor technologies are designed, the SynRM and PMaSynRM machines, to prove the suitability of including ferrites in the rotor of a SynRM. SynRMs have lower manufacture costs and can work at higher temperature, but have lower power density than PMaSynRMs. Three-phase SynRM and PMaSynRM are designed using the methodology proposed in this paper. Following the developed methodology, the process starts with the predesign stage, whose input values are summarized in Table 10.

Table 10. Motor specifications

| Items [unit] | Value |
|---|---|
| Rated mechanical power [kW] | 45 |
| Corner speed [rpm] | 4000 |
| Number of phases | 3 |
| Number of poles pairs | 4 |
| Number of slots | 48 |
| Iron laminations material | M330-35A |
| Ferrite permanent magnet | HF 30/26 |
| Flow rate of coolant [L/min] | 9 |
| Nominal temperature of coolant [ºC] | 90 |
| Specific heat capacity of EGW50/50 coolant [J/(kgK)] | 3364 |
| DC bus voltage [V] | 600 |
| Insulation class | H |

The solutions of the predesign for both machines are shown in Figure 110. The half pole located on the right side corresponds to the PMaSynRM, whereas the half pole located on the left side belongs to the SynRM. Next, both pre-designs are used as input values of the GA, in order to optimize the designs and achieve the performances desired. The variables to optimize are the stack length ($l$), inner rotor diameter ($D_{ir}$) and the variables shown in Figure 12.

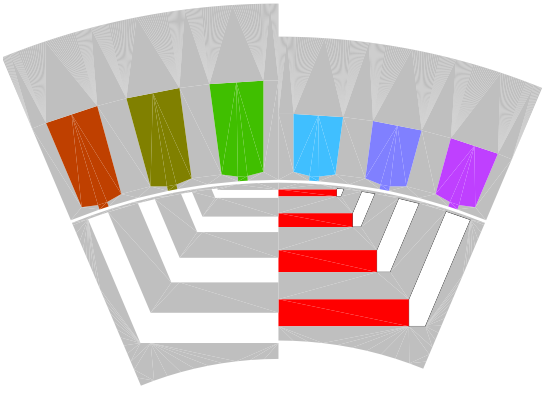

Figure 110. Pre-design comparison between SynRM (left) and PMa-SynRM (right)

The GA configuration chosen in this paper for both machines includes a population of 100 individuals, 80 generations, elite count of 20 individuals, stall generation limit of 25 generations or function tolerance of $10^{-10}$, among others. The optimization process was carried out using an Intel® Xeon® E5-1620 processor with 32 GB RAM. The time required to obtain the solutions was 24.35 hours for the SynRM and 39.45 hours for the PMaSynRM. This time difference is related to the magnetic models since the SynRM has less unknown values than the PMaSynRM.

The methodology proposed allows evaluating different parameters, including the power factor, output power or the amount of permanent magnet required, among others. In this example the cost function is calculated as the arithmetic mean of the average efficiency, power factor and specific power. The average efficiency and power factor are evaluated by averaging the efficiency and power factor of the 50% selected points of the WLTP driving cycle. Some torque restrictions are applied to ensure a correct match with the torque-speed plane shown in Figure 14. The cost function applied to the optimization process is given by,

$$\max\left\{\eta_{avg} + cos\varphi_{avg} + \frac{sp}{sp_{pre-design}}\right\}$$

subject to $T_{max} > 100\ Nm, T_{9.000\ rpm} > 50\ Nm$ and $T_{11.000\ rpm} > 40\ Nm$ .

It is noted that because of the inherent restrictions of traction applications, electric vehicles require motors with high specific power, efficiency and power factor, this latter being very important to reduce the input current and thus power losses and the size of the inverter. Therefore, a single-objective approach combining the three features has been proposed.

Table 11 summarizes the values of the PMaSynRM parameters obtained during the predesign stage, the range of these variables imposed during the GA optimization process, and the final solution attained.

Table 11. Parameters to optimize the PMa-SynRM

| Variables | Predesign | GA range | Solution |
|---|---|---|---|
| $l$ | 87.5 mm | 67.5 – 107.5 mm | 70.1 mm |
| $b_{tooth}$ | 6.3 mm | 5.3 – 7.3mm | 6.2 mm |
| $D_{ir}$ | 158.4 mm | 138.4 – 178.4 mm | 153.2 mm |
| $h_{tooth}$ | 14.4 mm | 12.4 – 16.4 mm | 13.8 mm |
| $h_{yoke}$ | 16.5 mm | 14.5 – 18.5 mm | 15.5 mm |
| $W_{q1}$ | 5.8 mm | 4.8 – 6.8 mm | 5.6 mm |
| $W_{q2}$ | 4.7 mm | 3.7 – 5.7 mm | 4.2 mm |
| $W_{q3}$ | 2.9 mm | 1.9 – 2.9 mm | 2.2 mm |
| $W_{q4}$ | 1.5 mm | 0.5 – 2.5 mm | 1.4 mm |
| $S_1$ | 3.1 mm | 2.1 – 4.1 mm | 2.5 mm |
| $S_2$ | 5.8 mm | 4.8 – 6.8 mm | 5.4 mm |
| $S_3$ | 4.9 mm | 3.9 – 5.9 mm | 4.3 mm |
| $S_4$ | 3.6 mm | 2.6 – 3.6 mm | 3.1 mm |
| $S_5$ | 1.5 mm | 0.5 – 2.5 mm | 1.1 mm |
| $W_{d1}$ | 5.4 mm | 4.4 – 6.4 mm | 6.3 mm |
| $W_{d2}$ | 4.4 mm | 3.4 – 5.4 mm | 4.9 mm |
| $W_{d3}$ | 2.8 mm | 1.8 – 3.8 mm | 2.3 mm |
| $W_{d4}$ | 1.4 mm | 0.4 – 2.4 mm | 1.8 mm |

The performances of the results obtained are represented in the torque-speed plane in order to compare the motor features with the driving cycle requirements. Figure 111 shows the efficiency map and the power factor of the optimized PMaSynRM.

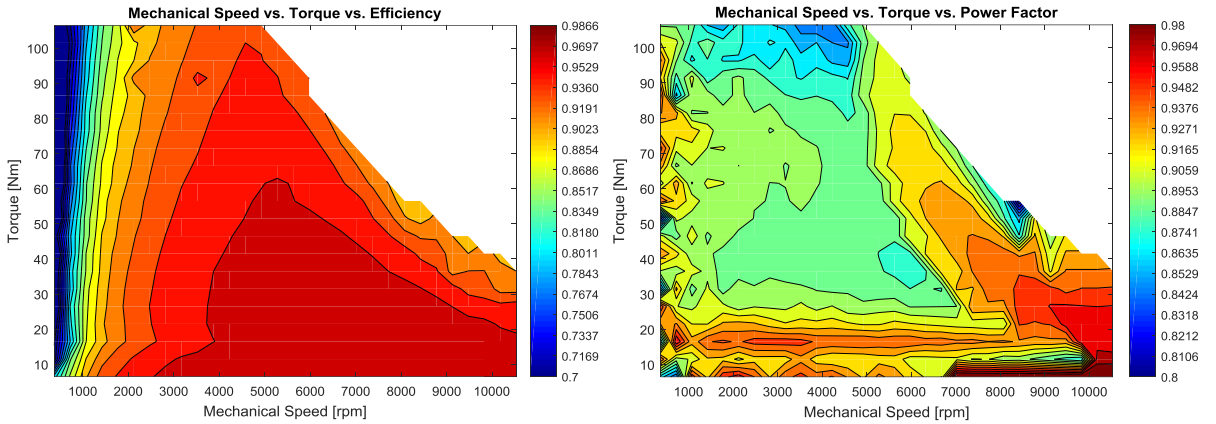


Figure 111. Efficiency (left) and Power factor (right) maps of the GA solution of the PMa-SynRM

The average efficiency at the desired zone, which is located between 2000 to 7500 rpm and 10 – 30 Nm, is 0.958 and the average power factor is 0.91. The total mass of the motor is 10.9 kg, so the specific power is 5.15 kW/kg. The average efficiency of the predesign was 0.939, the average power factor 0.87 and the total mass 16.7 kg, leading to a specific power of 2.8 kW/kg. Therefore, the optimization process allows a great improvement of the performances of the motor with respect to the predesign stage.

Table 12 summarizes the values of the SynRM parameters obtained during the predesign stage, the range of these variables imposed during the GA optimization process, and the final solution attained.

Table 12. Parameters to optimize the SynRM

| Variables | Pre-design | GA range | Solution |
|---|---|---|---|
| $l$ | 87.5 mm | 67.5 – 107.5 mm | 73.2 mm |
| $b_{tooth}$ | 6.3 mm | 5.3 – 7.3 mm | 5.3 mm |
| $D_{ir}$ | 150.5 mm | 130.5 – 170.5 mm | 131.5 mm |
| $h_{tooth}$ | 21.2 mm | 19.2 – 23.2 mm | 19.5 mm |
| $h_{yoke}$ | 16.5 mm | 14.5 – 18.5 mm | 18.1 mm |
| $W_{q1}$ | 6.5 mm | 5.5 – 7.5 mm | 5.7 mm |
| $W_{q2}$ | 5.2 mm | 4.2 – 6.2 mm | 4.4 mm |
| $W_{q3}$ | 3.3 mm | 2.3 – 4.3 mm | 2.6 mm |
| $W_{q4}$ | 1.7 mm | 0.7 – 2.7 mm | 1.9 mm |
| $S_1$ | 3.4 mm | 2.4 – 4.4 mm | 2.5 mm |
| $S_2$ | 6.5 mm | 5.5 – 7.5 mm | 7.2 mm |
| $S_3$ | 5.5 mm | 4.5 – 6.5 mm | 4.6 mm |
| $S_4$ | 4.0 mm | 3.0 – 5.0 mm | 4.9 mm |
| $S_5$ | 1.9 mm | 0.9 – 2.9 mm | 1.0 mm |
| $W_{d1}$ | 4.5 mm | 3.5 – 5.5 mm | 5.4 mm |
| $W_{d2}$ | 3.6 mm | 2.6 – 4.6 mm | 4.3 mm |
| $W_{d3}$ | 2.3 mm | 1.3 – 3.3 mm | 1.9 mm |
| $W_{d4}$ | 1.2 mm | 0.2 – 2.2 mm | 1.9 mm |

Figure 112 shows the efficiency map and the power factor of the optimized SynRM. They show that the average efficiency at the desired zone is 0.961 and the average power factor is 0.63. The total mass of the motor is 12.8 kg, so the specific power is 3.85 kW/kg. The average efficiency of the predesign was 0.964, the average power factor 0.58 and the total mass 19.6 kg, leading to a specific power of 2.29 kW/kg. Therefore, the optimization process allows a great improvement of the performances of the motor with respect to the predesign stage. However, the improvement is not good enough since some of the torque restrictions have not been achieved. The torque at maximum

speed is about 20 Nm, but the torque required at this speed is 37 Nm. This is because at high-speed operation, the torque-speed characteristic of the SynRM drops faster than that of the PMaSynRM due to the rotor saturation owing to the flux barriers, thus decreasing the available power and torque [23], so the SynRM solution must be discarded.

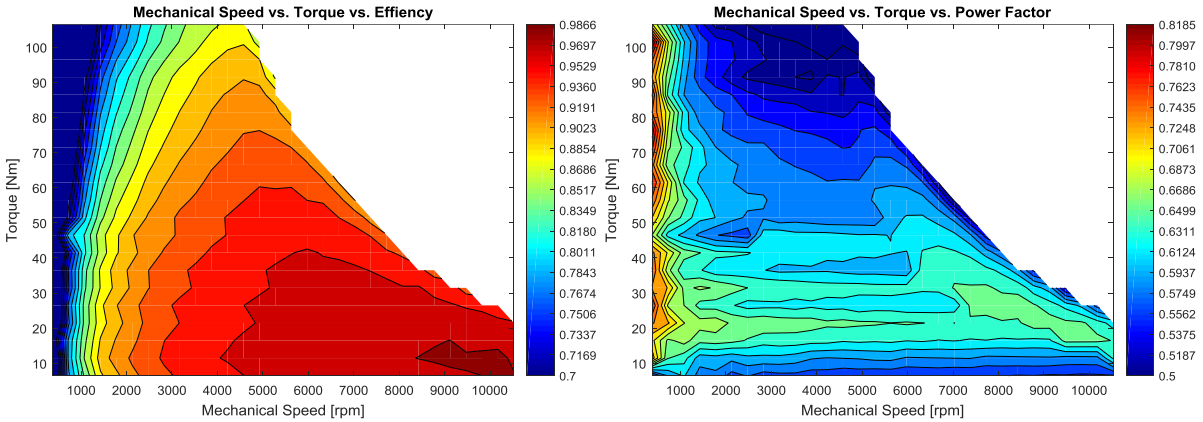


Figure 112. Efficiency (left) and Power factor (right) of the GA solution of the SynRM

By comparing, the importance of the magnets to increase the power factor is evident, since the minimum power factor of the PMa-SynRM solution is similar to the maximum one of the SynRM solution. Therefore, the PMa-SynRM is the selected in this case.

The validation is based on the PMaSynRM machine against commercial software For this purpose, the end-winding temperature obtained by the thermal network is compared with the temperature calculated by means of MotorCad® (MDL, v9.5.2), whereas the electromagnetic model is validated by means of FEM simulations carried out with Flux® (Altair, v12.1). Figure 113 shows the magnetic flux density of the PMa-SynRM in Flux.

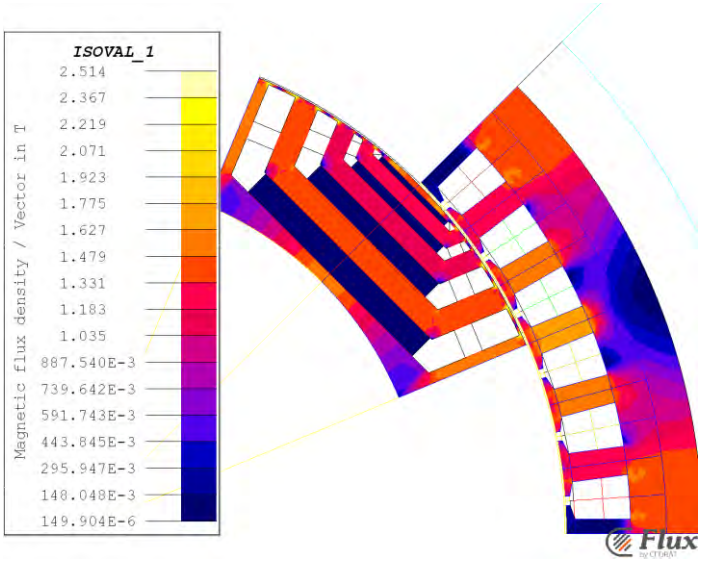


Figure 113. Magnetic flux density (T) of the PMa-SynRM calculated in Flux

Table 13 shows the comparison between the end-winding temperatures obtained with MotorCad® and the thermal model dealt with in this work, calculated at several values of current and mechanical speed.

Table 13. End-Winding temperature of the PMa-SynRM comparison between thermal model and MotorCad

| Current [A] | Speed [rpm] | Thermal model Temp.[ºC] | MotorCad Temp.[ºC] |
|---|---|---|---|
| 10 | 1000 | 90.5 | 90.3 |
| 10 | 3000 | 90.6 | 90.4 |
| 10 | 12000 | 92.4 | 92.7 |
| 50 | 2000 | 103.2 | 99.2 |
| 50 | 8000 | 106.3 | 103.9 |
| 142 | 1000 | 152.0 | 144.3 |
| 142 | 11000 | 163.1 | 170.3 |

The magnetic model has been validated by two ways. First, the *dq* inductance curves obtained by means of the magnetic model are compared with those obtained in Flux (2D-magnetostatic simulation). Next, different representative points, such as maximum speed or corner speed among others are calculated in Flux (2D-transient magnetic simulation) and the values are compared with those shown in Figure 112.

The validation of the values of the inductances is essential because these parameters have a deep impact on motor performances. Figure 114 compares the inductances obtained by means of the magnetic model and FEA.

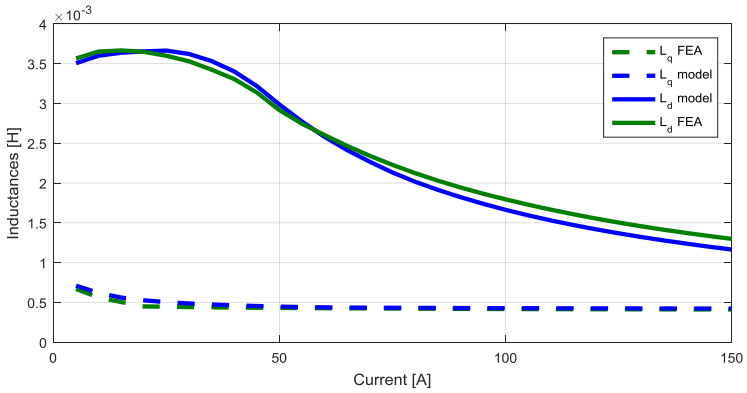


Figure 114. Inductances comparison between FEA and model for PMaSynRM GA solution

The average difference between both solutions is 5.1% and 4.5% for the *d* and *q* inductances, respectively. The low error attained in the calculation of the inductances is directly related to the accuracy of the model, because the different motor parameters, such as voltage or output torque can be calculated with high precision.

Then, solving the equation system developed in *Section 6. Behavior maps* the torque at different speeds is obtained according a given voltage limit. Table 14 shows a comparison between different working points calculated by means of the electric model and FEA.

Table 14. Working points comparison

| Speed [rpm] | Electric model Torque [Nm] | FEA Torque [Nm] |
|---|---|---|
| 4000 | 102.5 | 100.2 |
| 9125 | 51.5 | 54.7 |
| 11000 | 37.5 | 40.7 |

Results presented in Table 14 shows that the results obtained by means of the electric model differ by 5.3% in average with respect those attained by means of FEA.

## 8.2 Size constrained optimized motor

The methodology proposed is applied to optimize a rare-earth-free traction motor for a hybrid vehicle. The minimum steady state requirements are 32 kW at 2500 rpm, and by considering the driving cycle, the efficiency within the most frequent operating zone must be higher than 92%. Table 15 summarizes the specifications of the analyzed ferrite PMa-SynRM. Due to the volumetric constraints of this particular application, the inner rotor diameter, the outer stator diameter and the motor length, are fixed during the optimization process.

Table 15. Motor specifications

| Items [unit] | Value |
|---|---|
| Mechanical power [kW] | 32 |
| Corner speed [rpm] | 2500 |
| Number of phases | 3 |
| Number of poles pairs | 8 |
| Number of slots | 96 |
| Iron lamination | M330-35A |
| Ferrite magnet | HF 30/26 |
| Flow rate of coolant [L/min] | 10 |
| Nominal temperature of coolant [ºC] | 75 |
| DC Bus [V] | 400 |
| Insulation | Type H |

The variables to be calculated by the GA are related to the size of the flux barriers and segments (see Figure 12), outer rotor diameter, tooth width, tooth height and yoke width. Moreover, the possibility of including magnets in the lateral barriers to increase the motor capabilities is also considered during the optimization stage.

The optimization process is focused to maximize the power density**,** the average efficiency, and the average power factor within the most frequent working zone. To this end, the objective function is proposed, which is subjected to a torque ripple ± 5%. The most frequent zone is delimited within the [1200, 2000] rpm and [30, 80] Nm intervals.

$$\max\left\{\eta_{avg} + cos\varphi_{avg} + \frac{sp}{sp_{pre-design}}\right\}$$

The GA configuration chosen for this case consists of a population of 80 individuals, 100 generations, stall generation limit of 25 generations, 20 individuals as elite count and a function tolerance of $10^{-10}$. A E5-1620 Intel® Xeon® processor with 32 GB of RAM memory has been used to carry out the optimization process.

The motor obtained during the pre-design stage has a power-to-weight ratio of 2.02 kW/kg, an average efficiency of 90% and an average power factor of 0.73. Previous tests proved that the geometrical constraints together with the high performances required, make it necessary to include lateral magnets. The mechanical analysis also revealed the need to use two radial ribs in the innermost flux barriers (see *Wq1* and *Wq2* in Figure 12).

Table 16 summarizes the variables to optimize, their values during the pre-design and optimization stages, and the final solution.

Table 16. Parameters to Optimize

| Variables | Pre-design | GA range | Solution |
|---|---|---|---|
| Tooth width | 3.5 mm | 2.5 – 4.5 mm | 3.1 mm |
| Outer rotor diam. | 215.2 mm | 205.2 – 235.2 mm | 219.4 mm |
| Tooth height | 16.4 mm | 14.4 – 18.4 mm | 17.0 mm |
| Yoke width | 9.2 mm | 7.2 – 11.2 mm | 7.5 mm |
| Wq1 | 3.4 mm | 2.4 – 4.4 mm | 3.8 mm |
| Wq2 | 2.6 mm | 1.6 – 3.6 mm | 2.8 mm |
| Wq3 | 2.0 mm | 1.0 – 3.0 mm | 2.7 mm |
| S1 | 2.4 mm | 1.4 – 3.40 mm | 2.2 mm |
| S2 | 3.5 mm | 2.5 – 4.5 mm | 3.0 mm |
| S3 | 1.9 mm | 0.9 – 2.9 mm | 2.7 mm |
| S4 | 0.8 mm | 0.5 – 1.8 mm | 0.7 mm |
| Wd1 | 2.4 mm | 1.4 – 3.4 mm | 2.3 mm |
| Wd2 | 2.0 mm | 1.0 – 3.0 mm | 1.7 mm |
| Wd3 | 1.8 mm | 0.8 – 2.8 mm | 1.1 mm |

The solution motor has a power-to-weight ratio of 2.33 kW/kg, an average efficiency of 93%, and a power factor of 0.85. The power-to-weight ratio considers the maximum power in the whole operation area, which is achieved at 2600 rpm and 125 Nm.

Figure 115 (left) shows the efficiency map, and some working points to be compared with the corresponding ones of the FEA solution. Note that, the mesh grid of the map in the torque-speed plane is formed by steps of 10 Nm and 100 rpm. Then, some information in the torque-speed boundaries is lost. The size of the grid is selected to reduce the number of simulation in the validation. The validation is carried out using the Flux® (v12.2, Altair) FEA package. Figure 115 (right) shows the efficiency map obtained with FEA. The average difference between the results provided by the approach proposed in this work and FEA is less than 3%. It is noted that the efficiency map obtained through FEA simulations requires some days of computations. Therefore, including FEA to perform a range optimization can be unfeasible in terms of computational burden. However, by using the proposed methodology, the time required to obtain the different torque-speed maps for one motor is below 8 minutes, so it can be included to determine the objective function during the optimization process.

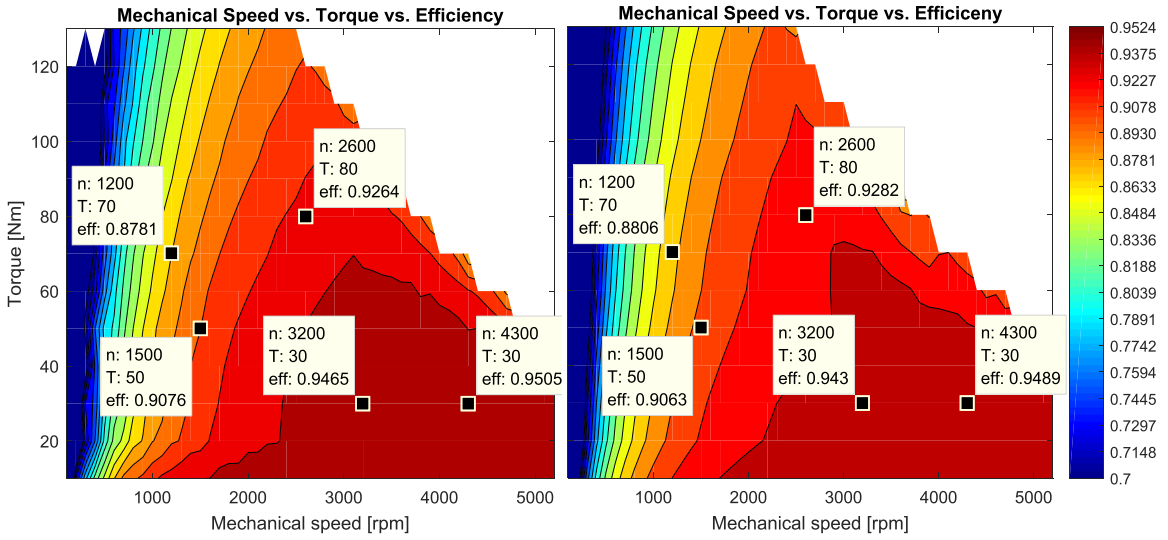


Figure 115. Efficiency map obtained by means of proposed tool (left) and FEA (right)

Then, the optimized motor is validated experimentally. Figure 116 shows the stator and rotor of the experimental machine, which were designed using the methodology proposed in this test.

Figure 116. The stator and rotor obtained with the proposed methodology

The motor was tested in our laboratory, as shown in Figure 117. Different tests were carried out to measure the motor capabilities and to validate the accuracy of the model.

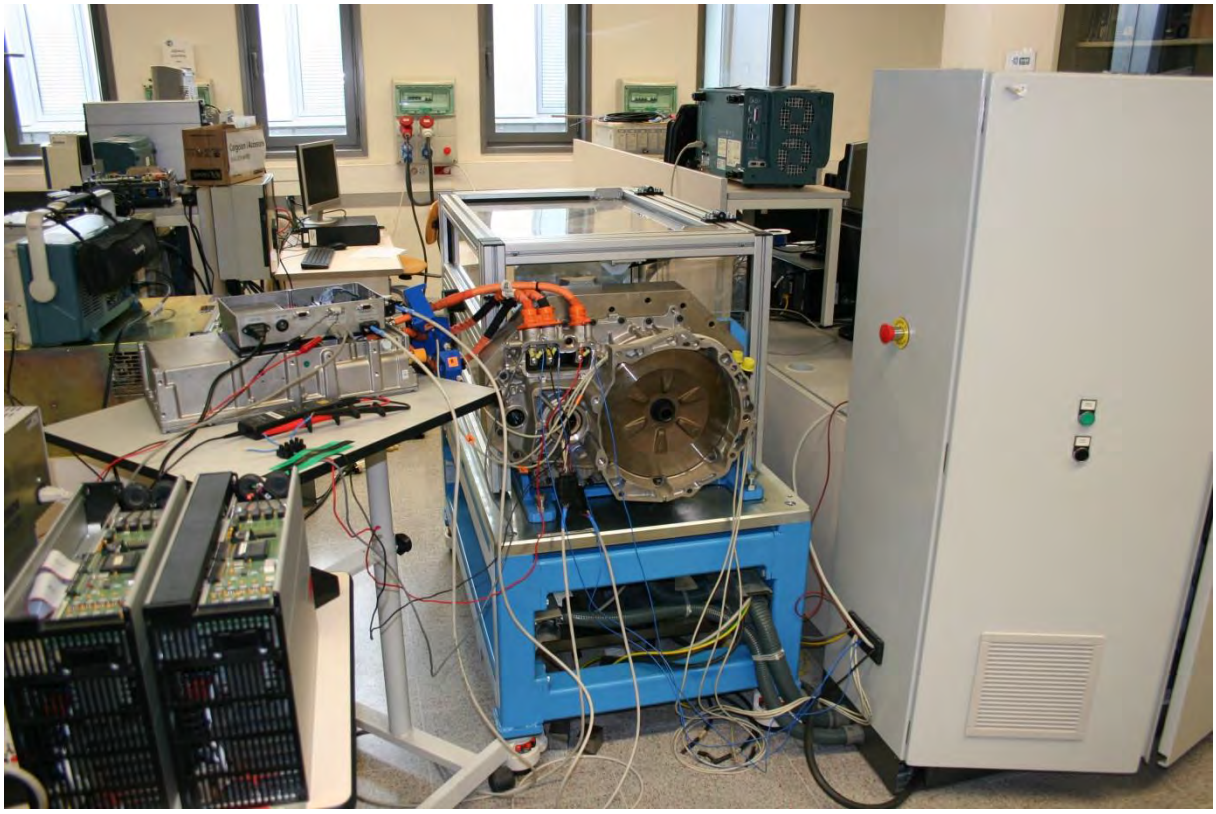

Figure 117. Motor, inverter and test bench

In a first test, the back-emf was analyzed at 2000 rpm to validate the correct calculation of the magnets. Figure 118 shows the line-to-line back-EMF waveforms at 2000 rpm obtained with FEA considering the rotor skew, with the proposed model, and the experimental values.

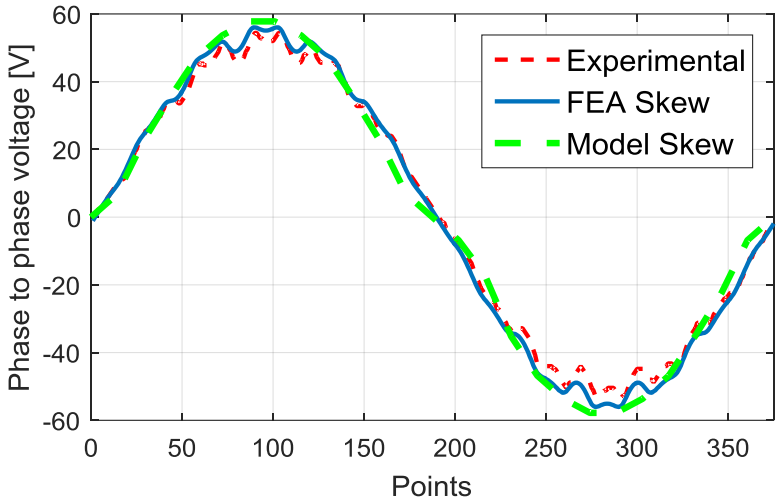


Figure 118. Comparison of the back EMF obtained experimentally, through FEA simulations, and by means of the proposed model

To validate experimentally the efficiency map shown in Figure 115 (left), some operating points were analyzed by means of the proposed tool and from experimental data. It was not possible to evaluate the total area of the motor because of the laboratory limitations in terms of power and test bench capabilities. The region examined was delimited within [0, 60 Nm] and [0, 2200 rpm].

Table 17 summarizes the efficiency of the evaluated operating points calculated from experimental measurements and by means of the proposed tool. Therefore, the methodology proposed is in agreement with the experimental results, since as shown in Table 17, the average error of the points evaluated in efficiency map is below 2%.

Table 17. Efficiency comparison

| Working point | | Experimental efficiency | Estimated efficiency | Error |
|---|---|---|---|---|
| 30 Nm | 250 rpm | 66.2% | 67.6% | 2.1% |
| 40 Nm | 250 rpm | 62.3% | 62.7% | 0.6% |
| 10 Nm | 500 rpm | 80.8% | 83.1% | 2.8% |
| 10 Nm | 750 rpm | 92.1% | 90.4% | 1.8% |
| 10 Nm | 1500 rpm | 95.4% | 94.3% | 1.1% |
| 30 Nm | 500 rpm | 75.0% | 78.2% | 4.2% |
| 40 Nm | 500 rpm | 75.7% | 76.8% | 1.4% |
| 40 Nm | 750 rpm | 83.7% | 84.2% | 0.6% |
| 60 Nm | 750 rpm | 81.3% | 82.6% | 1.6% |
| 20 Nm | 1000 rpm | 90.2% | 91.1% | 1.0% |
| | **Average** | - | - | **1.7%** |

## 8.3 Five phase optimized motor

The principal aim to this part of the project is the constructive model of five – phases PMa-SynRM. The major motor performance to be optimized in this case is the density power.

The density power required is 2.5 kW/kg and the definition of density power is the maximum motor power per motor mass without coolant system. The motor mass is the sum of stator iron, windings, rotor iron and magnets.

The motor design is carried out taking into account the silicon carbide technologies on the motor converter, so the DC voltage chosen is around 550 V. The maximum value of Bus DC allowed on electric vehicles is 600 V. In order to assess the technology, the motor is designed to achieve 5 kW @ 5000rpm with a phase voltage between 220 – 240 Vrms and phase current between 3.5 - 4.5 Arms. This value of current depends on the thermal behavior of the final motor geometry.

The reliability, i.e. fault tolerant, have to be considered on motor design, so the usual three phases motor are increase to five phase motor. Furthermore, the different phases will be physical separated on slots, so the winding will be single layer. Finally, the neutral point has to be accessible to implement a fault tolerant control.

The rotor and stator material used on this motor is the M330-35a. Taking into account the rare-earth less motor, ferrite is the magnet on this motor. The magnet chosen is HF 30/26 Sr. Finally, taking into the temperatures allowed on motor environment the insulator chosen is the Type R, so the maximum temperature is 180°C.

Table 18 summarizes the motor characteristics. It will be divided on performances and electric parameters. The motor size will be explained on design process.

Table 18. Motor characteristics to start the design process

| **Motor features (Desired)** | | **Electric parameters (Estimated)** | |
|---|---|---|---|
| Power density (peak) | 2.5 kW/kg | Phase voltage | 230 Vrms |
| Rated Power | 3 kW | Phase current | 4 Arms |
| Rated Torque | 7 Nm | Number of phases | 5 |
| Rated Speed | 4000 rpm | Peak current | 6.5 Arms |
| Maximum Power | 5 kW | Number of poles | - |

In this case, the pre-design is very important since the number of pole pairs is not fixed. In order to choose the correct number of poles, several pre-design are realized to compare the mass of the different results. As explained in *Section 3. Pre-design,* the seed value for the optimization process is the pre-design. Table 19 summarizes the obtained results of the pre-design using different pole pairs numbers.

Table 19. Relation of mass with pole pairs (pre-design)

| **Pole pairs** | **Mass** |
|---|---|
| 2 | 4.46 kg |
| 3 | 3.59 kg |
| 4 | 3.17 kg |
| 5 | 3.05 kg |
| **6** | **2.95 kg** |
| 7 | 2.95 kg |

According to the Table 19, the best pole pair number is 6 since the mass of this solution has the lower value than the other solution. Figure 119 shows the obtained solution of the pre-design depending on the pole pair number.

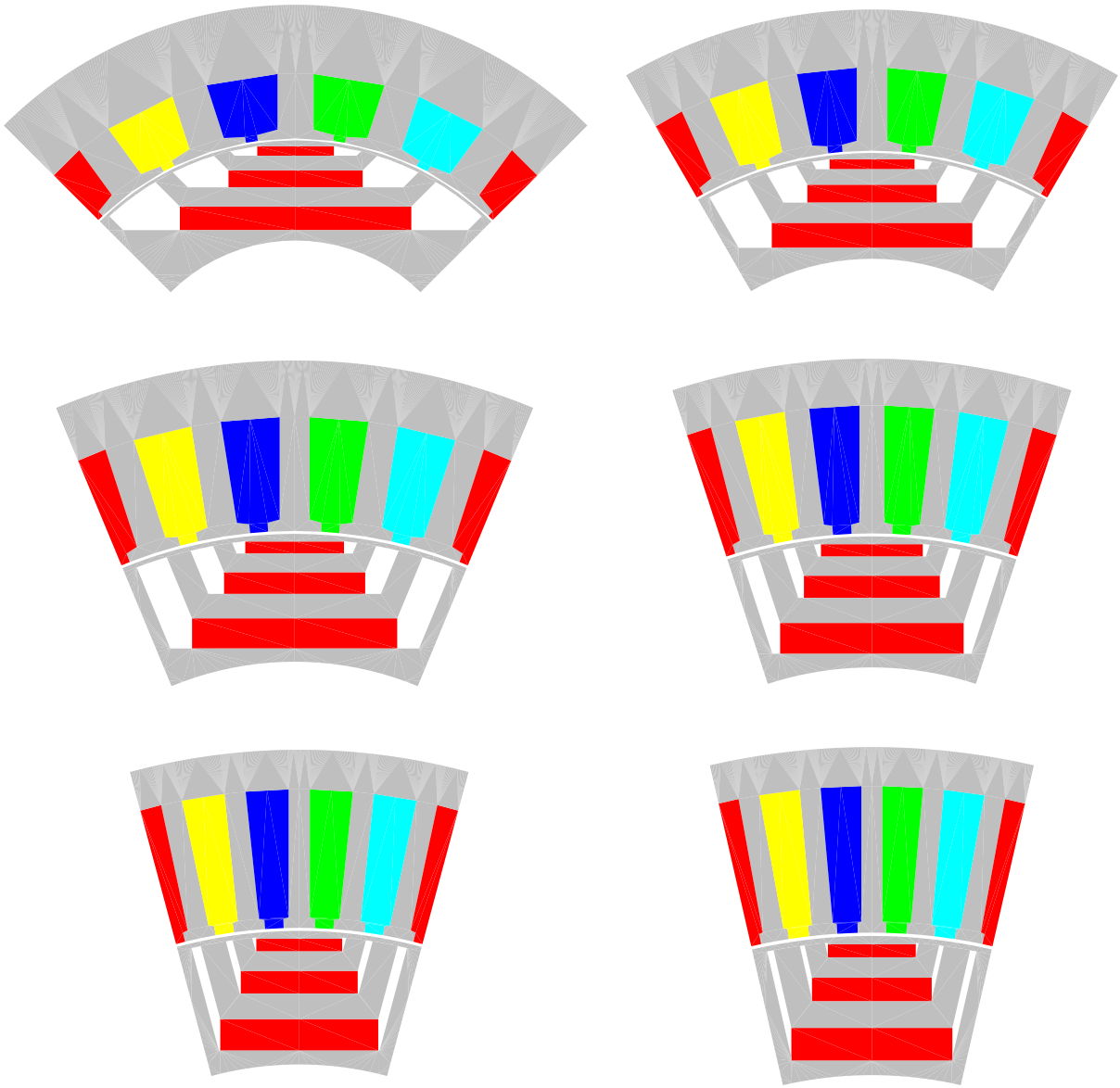

Figure 119. One magnetic pole of the pre-design solution from 2 pole pairs to 7 pole pairs.

Then, the GA is started considering the geometry of the pre-design with 6 pole pairs. Then, the chosen cost function is given by;

$$\max\{sp\}$$

Subject to maximum power below 5.5 kW, torque ripple below ± 5%, and temperature of hot spot below 175ºC.

Using the proposed optimization procedure in this thesis, the geometry of the pre-design (6 pole pair) is optimized. The torque ripple reduction is obtained by means of using skew. The final results are summarized in Table 20.

Table 20. Results of the GA

| | |
|---|---|
| **Main dimension** | |
| Stack length | 26.0 mm |
| Outer stator diameter | 148.0 mm |
| Inner stator diameter | 114.6 mm |
| Outer rotor diameter | 114.0 mm |
| Inner rotor diameter | 87.7 mm |
| Number of poles | 12 |
| Number of slots | 60 |
| Angle skew | 6º |
| **Stator dimension** | |
| Tooth height | 13.00 mm |
| Tooth weight | 1.73 mm |
| Slot opening | 1.20 mm |
| Radial tip | 1.00 mm |
| Angle (slot tip) | 15º |
| **Rotor dimension** | |
| $W_{q1}$ | 3.1 mm |
| $W_{d1}$ | 2.2 mm |
| $W_{q2}$ | 2.2 mm |
| $W_{d2}$ | 1.6 mm |
| $W_{q3}$ | 1.2 mm |
| $W_{d3}$ | 0.9 mm |
| S1 | 1.2 mm |
| S2 | 2.5 mm |
| S3 | 2.0 mm |
| S4 | 1.0 mm |

The optimal motor has a fault-tolerant winding, since each slot only accommodates a unique phase, as shown in Figure 120. In addition, the combination of the low current design and the large inductances (each slot includes 60 conductors) reduces the risk of high short-circuit currents.

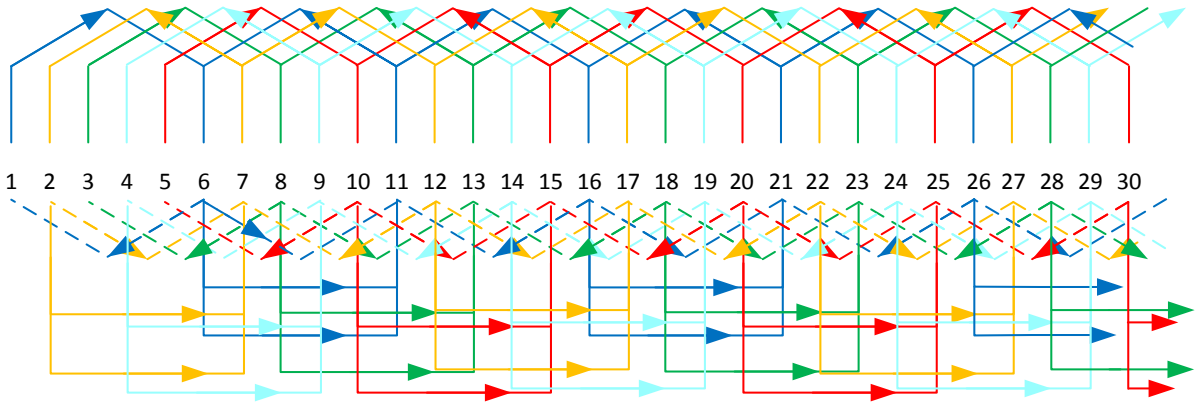


Figure 120. Half winding of the five-phase 60-slots machine with a double layer and constant pitch with q=1

Using the presented methodology, the torque-speed and power-speed planes are presented in transient conditions. Figure 121 shows the phase peak current [A] in the torque-speed map. Note that, the rated current is 4.5 Arms (peak 6.4 A), so the steady state map can be estimated disregarding the colors from orange to red.

| | Optimal design, |
|---|---|
| Torque@4700 rpm | 10 Nm |
| Power@4700 rpm | 4.9 kW |
| Maximum speed | 7000 rpm |

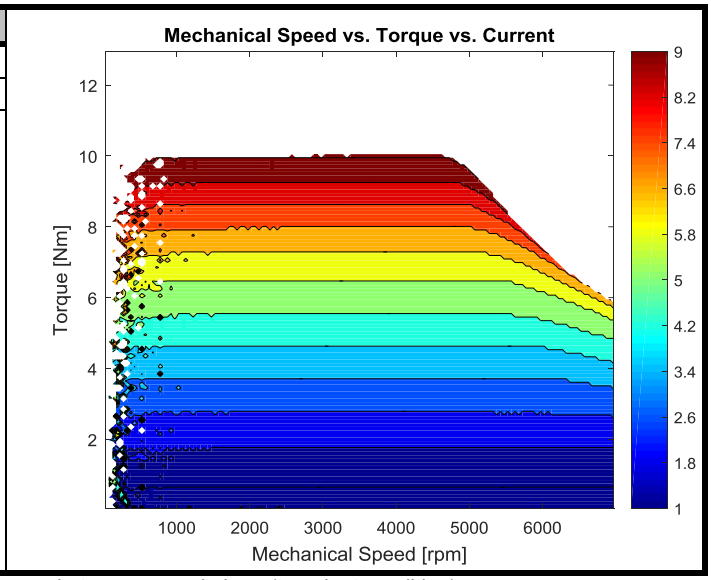


Figure 121. Current module map in torque-speed plane (transient condition)

On the other hand, Figure 122 shows the phase peak current [A] in the power-speed plane. It is worthy to mention that, the point of maximum power is not the same of the based speed. The final motor mass is 2.2 kg, so the final power density is 2.3 kW/kg. The final power density is close to the objective (2.5 kW/kg), but the skew and the lack of coolant system reduces the motor capabilities.

| | Optimal design, |
|---|---|
| Torque@5250 rpm | 9.3 Nm |
| Power@5250rpm | 5.1 kW |
| Maximum speed | 7000 rpm |

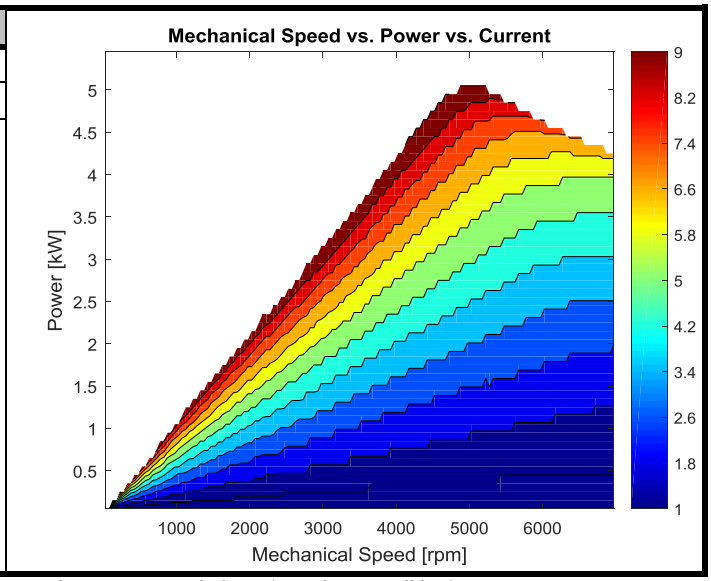


Figure 122. Current module map in power-speed plane (transient condition)

Before the motor manufacturing, the machine is validated against FEA, so the geometry is introduced in Flux to start the validation. Figure 123 depicts one magnetic pole of the motor in Flux. The skew angle can be observed.

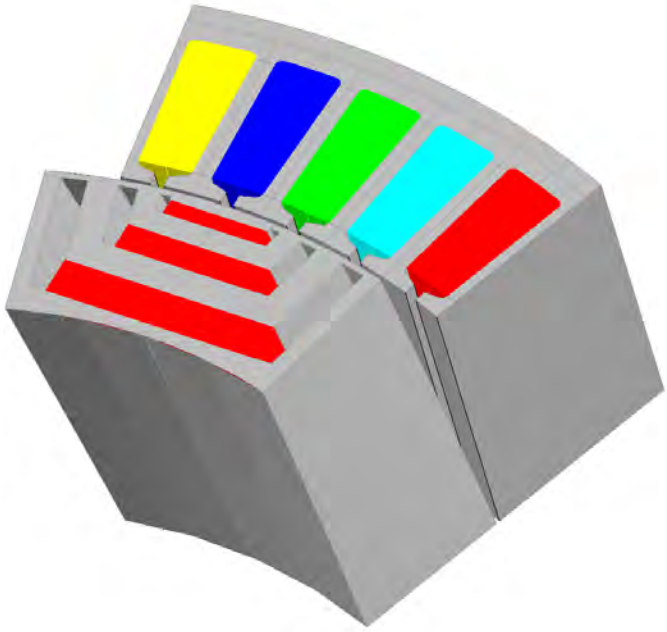

Figure 123. One magnetic pole of the optimal solution (Flux)

Several working points are calculated to validate the correct sizing of the machine. Table 21 summarizes some of the extracted working points. The calculated torque is considering the MTPA region.

Table 21. Working points comparison

| Current [A] | Electric model Torque [Nm] | FEA Torque [Nm] | Error [%] |
|---|---|---|---|
| 4.20 | 4.68 | 4.58 | 2.18 |
| 6.60 | 7.15 | 7.11 | 0.57 |
| 7.40 | 8.21 | 8.14 | 0.86 |
| 9.00 | 10.0 | 9.78 | 2.24 |

Then, the motor is manufactured according to the geometry obtained in the optimal design. Figure 124 shows the lamination of the manufactured motor.

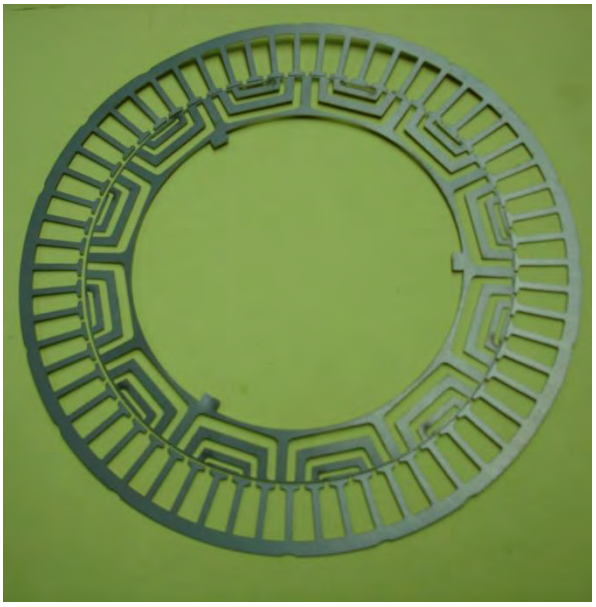

Figure 124. Rotor and stator lamination of the five-phase PMa-SynRM optimal design

Figure 125 shows the final structure of the motor considering the rotor, magnets, shaft, housing, stator, and windings.

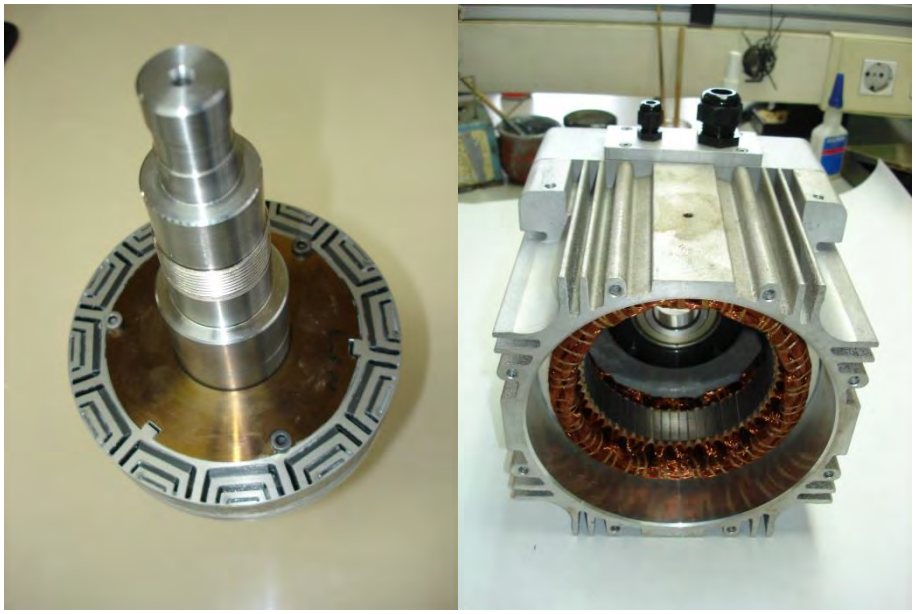

Figure 125. Left: Rotor, magnets, and shaft. Right: Stator, winding, and housing.

Then, the manufactured motor is tested in our laboratory to validate experimentally the expected results. Figure 126 shows the motor in the test bench and the acquisition system.

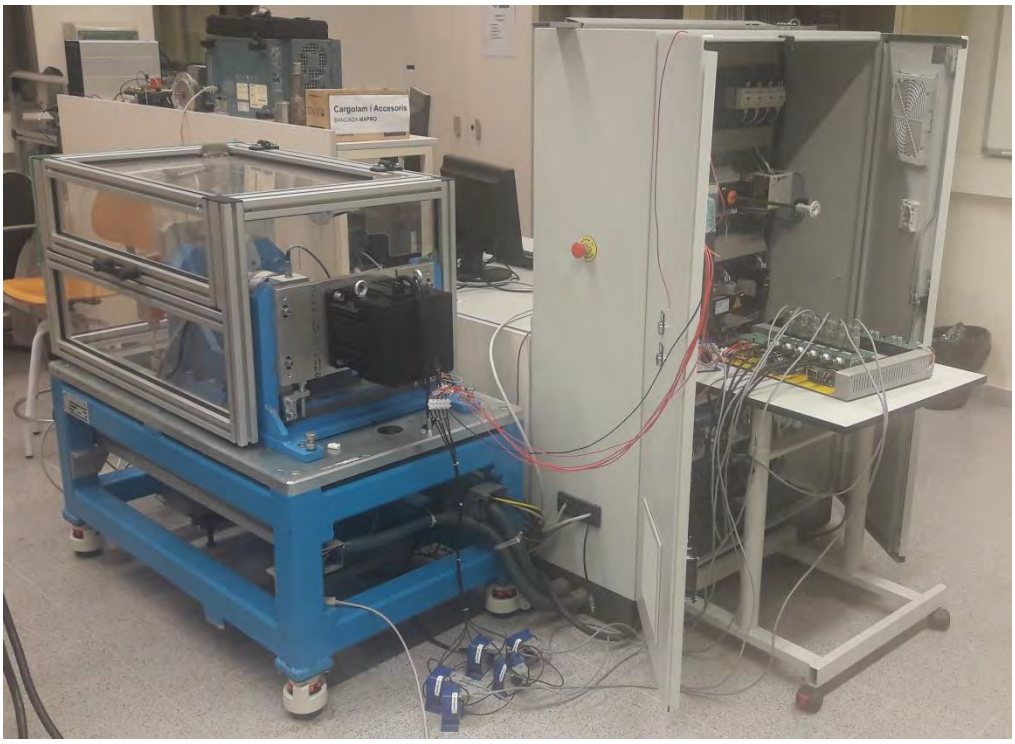


Figure 126. Test bench, five phase PMa-SynRM, and acquisition system

# 9.

# Thesis results dissemination

The direct contributions resulting from this Thesis work, in international journals as wells as in specialized conferences, are collected in this Chapter.

*CONTENTS:*

# 9. Thesis results dissemination

## 9.1 Publications: Thesis contributions

### Journals

J.-R.Riba, **C. López-Torres**, L. Romeral, and A. Garcia, “Rare-earth-free propulsion motors for electric vehicles: A technology review, “Renewable and Sustainable Energy Reviews, vol. 57, pp.367-379,2016.

**C. López-Torres**, A. Garcia, J. Riba, and L. Romeral, "Design and optimization for vehicle driving cycle of rare-earth-free SynRM based on coupled lumped thermal and magnetic networks," *IEEE Transactions on Vehicular Technology,* vol. PP, no. 99, pp. 1-1, 2017.

**C. López-Torres**, C. Colls, A. Garcia, J. Riba, and L. Romeral, " Development of a behavior maps tool to evaluate drive operational boundaries and optimization assessment of PMa-SynRMs," *IEEE Transactions on Vehicular Technology,* vol. PP, no. 99, pp. 1-1, 2018.

**C. López-Torres**, A. Garcia, G. Lux, J. Riba, and, L. Romeral " Computationally efficient design and optimization approach of PMa-SynRM in frequent operating torque-speed range," *IEEE Transactions on Energy Conversion,* vol. PP, no. 99, pp. 1-1, 2018. **Under minor revision**

**C. López-Torres**, A. Garcia, J. Riba, and L. Romeral, " Analysis of the effect of different accuracy levels on dq-model in the efficiency and control parameters for PMa-SynRM," *IEEE Transactions on Vehicular Technology,* vol. PP, no. 99, pp. 1-1, 2018. **Under revision**

**C. López-Torres**, J.-R. Riba, L. Romeral, and A. Garcia, “Detection of Eccentricity Faults in Five-Phase Ferrite-PM Assisted Synchronous Reluctance Machines”, Applied sciences, 31 May 2017

### Book chapter

**C. López-Torres**, A. Garcia, J. Riba. “Reliable design of PMaSynRM.” New Trends in Electrical Vehicles Powertrains – Reliability and Resilience. INTECH. 2018.

## Conferences

**C. López-Torres**, E. Sala, A. Espinosa, L. Romeral, "Constrained-Size Torque Maximization in SynRM Machines by means of Genetic Algorithms," Diagnostics for Electrical Machines, Power Electronics and Drives (SDEMPED), 2015 10th IEEE International Symposium

**C. López-Torres**, T. Michalski, A. Espinosa, L. Romeral, "Rotor of Synchronous Reluctance Motor optimización by means reluctance network and genetic algorithm," International Conference on Electrical Machines (ICEM), 2016 12th

**C. López-Torres**, T. Michalski, A. Espinosa, L. Romeral, "New SynRM design approach base-on behaviour maps analysis," International Conference on Electrical Machines (ICEM), 2016 12th

**C. López-Torres**, T. Michalski, A. Espinosa, L. Romeral, "Fast optimization of the Magnetic Model by means of Reluctance Network for PMa-SynRM," in IECON 2016-42th Annual Conference on IEEE Industrial Electronics Society

T. Michalski, **C. López-Torres**, A. Espinosa, L. Romeral, "Sensorless Control of Five Phase PMSM Bases on Extended Kalman Filter," in IECON 2016-42th Annual Conference on IEEE Industrial Electronics Society

T. Michalski, **C. López-Torres**, A. Espinosa, L. Romeral, "Dynamic Nonlinear Reluctance Network Analysis of Five Phase Outer Rotor BLDC Machine, "in IECON 2016-42th Annual Conference on IEEE Industrial Electronics Society

**C. López-Torres**, T. Michalski, A. Espinosa, L. Romeral, "Operational boundaries calculation of Permanent Magnet assisted Synchronous Reluctance Motor", IAS2017- 52ND Annual meeting on IEEE Industrial Application Sociecty, Cincinnati, OH.

**C. López-Torres**, G. Bacco, N. Bianchi, A. Garcia, L. Romeral, "A parallel analytical computation of synchronous reluctance machine", ICEM 2018, International Conference on Electrical Machines, September 3-6, Alexandroupoli – Greece. **Under review**

C. Babetto, **C. López-Torres**, N. Bianchi, A. Garcia, L. Romeral, "Synchronous Reluctance Motor Analysis and Design for High Speed Applications by means of Reluctance Network", PEMC 2018, International Conference on Power Electronics and Motion Control, August 26-30, Budapest – Hungary. **Under review**

# References

[1] M. Kamiya, "Development of Traction Drive Motors for the Toyota Hybrid System," ed. JAPAN: Toyota Motor Corporation, 2006.

[2] K. Akatsu and N. Matsui, "New trend of motor technology for automobiles - Introduction and overview," in *ECCE Asia Downunder (ECCE Asia), 2013 IEEE*, 2013, pp. 130-135.

[3] T. Kato, R. Mizutani, H. Matsumoto, and K. Yamamoto, "Advanced technologies of traction motor for automobile," in *ECCE Asia Downunder (ECCE Asia), 2013 IEEE*, 2013, pp. 147-152.

[4] J. O. Estima and A. J. Marques Cardoso, "Efficiency Analysis of Drive Train Topologies Applied to Electric/Hybrid Vehicles," *Vehicular Technology, IEEE Transactions on,* vol. 61, no. 3, pp. 1021-1031, 2012.

[5] Z. Xiang, X. Zhu, L. Quan, Y. Du, C. Zhang, and D. Fan, "Multilevel Design Optimization and Operation of a Brushless Double Mechanical Port Flux-Switching Permanent-Magnet Motor," *IEEE Transactions on Industrial Electronics,* vol. 63, no. 10, pp. 6042-6054, 2016.

[6] S. Ray and D. A. Lowther, "Multi-Objective Optimization Applied to the Matching of a Specified Torque-Speed Curve for an Internal Permanent Magnet Motor," *IEEE Transactions on Magnetics,* vol. 45, no. 3, pp. 1518-1521, 2009.

[7] L. Romeral, J. C. Urresty, J. R. R. Ruiz, and A. G. Espinosa, "Modeling of Surface-Mounted Permanent Magnet Synchronous Motors With Stator Winding Interturn Faults," *IEEE Transactions on Industrial Electronics,* vol. 58, no. 5, pp. 1576-1585, 2011.

[8] K. Ahn, A. E. Bayrak, and P. Y. Papalambros, "Electric Vehicle Design Optimization: Integration of a High-Fidelity Interior-Permanent-Magnet Motor Model," *IEEE Transactions on Vehicular Technology,* vol. 64, no. 9, pp. 3870-3877, 2015.

[9] J. Wang, X. Yuan, and K. Atallah, "Design Optimization of a Surface-Mounted Permanent-Magnet Motor With Concentrated Windings for Electric Vehicle Applications," *IEEE Transactions on Vehicular Technology,* vol. 62, no. 3, pp. 1053-1064, 2013.

[10] X. Liu, H. Chen, J. Zhao, and A. Belahcen, "Research on the Performances and Parameters of Interior PMSM Used for Electric Vehicles," *IEEE Transactions on Industrial Electronics,* vol. 63, no. 6, pp. 3533-3545, 2016.

[11] Y. S. Lin, K. W. Hu, T. H. Yeh, and C. M. Liaw, "An Electric-Vehicle IPMSM Drive With Interleaved Front-End DC/DC Converter," *IEEE Transactions on Vehicular Technology,* vol. 65, no. 6, pp. 4493-4504, 2016.

[12] T. A. Burress *et al.*, "Evaluation of the 2010 toyota prius hybrid synergy drive system," ed. Oak Ridge, Tennessee: OAK Ridge National Laboratory, March 2011.

[13] Y. Kano, Y. Inoue, and M. Sanada, "Current specifications of vehicle motors," in *ECCE Asia Downunder (ECCE Asia), 2013 IEEE*, 2013, pp. 136-140.

[14] C. Haiwei, G. Bo, and X. Longya, "Low-Cost Ferrite PM-Assisted Synchronous Reluctance Machine for Electric Vehicles," *Industrial Electronics, IEEE Transactions on,* vol. 61, no. 10, pp. 5741-5748, 2014.

[15] J.-R. Riba, C. López-Torres, L. Romeral, and A. Garcia, "Rare-earth-free propulsion motors for electric vehicles: A technology review," *Renewable and Sustainable Energy Reviews,* vol. 57, pp. 367-379, 2016.

[16] M. Kimiabeigi *et al.*, "High-Performance Low-Cost Electric Motor for Electric Vehicles Using Ferrite Magnets," *IEEE Transactions on Industrial Electronics,* vol. 63, no. 1, pp. 113-122, 2016.

[17] E. Carraro, M. Morandin, and N. Bianchi, "Traction PMASR Motor Optimization According to a Given Driving Cycle," *IEEE Transactions on Industry Applications,* vol. 52, no. 1, pp. 209-216, 2016.

[18] E. Oksuztepe, "In-Wheel Switched Reluctance Motor Design For Electric Vehicles By Using Pareto Based Multi Objective Differential Evolution Algorithm," *IEEE Transactions on Vehicular Technology,* vol. PP, no. 99, pp. 1-1, 2016.

[19] A. G. Sarigiannidis, M. E. Beniakar, and A. G. Kladas, "Fast Adaptive Evolutionary PM Traction motor Optimization based on Electric Vehicle Drive Cycle," *IEEE Transactions on Vehicular Technology,* vol. PP, no. 99, pp. 1-1, 2016.

[20] M. Morandin, M. Ferrari, and S. Bolognani, "Power-Train Design and Performance of a Hybrid Motorcycle Prototype," *IEEE Transactions on Industry Applications,* vol. 51, no. 3, pp. 2216-2226, 2015.

[21] V. Ruuskanen, J. Nerg, J. Pyrhönen, S. Ruotsalainen, and R. Kennel, "Drive Cycle Analysis of a Permanent-Magnet Traction Motor Based on Magnetostatic Finite-Element Analysis," *IEEE Transactions on Vehicular Technology,* vol. 64, no. 3, pp. 1249-1254, 2015.

[22] S. Taghavi and P. Pillay, "A Novel Grain-Oriented Lamination Rotor Core Assembly for a Synchronous Reluctance Traction Motor With a Reduced Torque Ripple Algorithm," *IEEE Transactions on Industry Applications,* vol. 52, no. 5, pp. 3729-3738, 2016.

[23] M. Ferrari, N. Bianchi, and E. Fornasiero, "Analysis of Rotor Saturation in Synchronous Reluctance and PM-Assisted Reluctance Motors," *IEEE Transactions on Industry Applications,* vol. 51, no. 1, pp. 169-177, 2015.

[24] S. Taghavi and P. Pillay, "A Sizing Methodology of the Synchronous Reluctance Motor for Traction Applications," *Emerging and Selected Topics in Power Electronics, IEEE Journal of,* vol. 2, no. 2, pp. 329-340, 2014.

[25] H. M. Hasanien, A. S. Abd-Rabou, and S. M. Sakr, "Design Optimization of Transverse Flux Linear Motor for Weight Reduction and Performance Improvement Using Response Surface Methodology and Genetic Algorithms," *Energy Conversion, IEEE Transactions on,* vol. 25, no. 3, pp. 598-605, 2010.

[26] S. Taghavi and P. Pillay, "A Sizing Methodology of the Synchronous Reluctance Motor for Traction Applications," *IEEE Journal of Emerging and Selected Topics in Power Electronics,* vol. 2, no. 2, pp. 329-340, 2014.

[27] S. Stipetic, D. Zarko, and M. Kovacic, "Optimised design of permanent magnet assisted synchronous reluctance motor series using combined analytical–finite element analysis based approach," *IET Electric Power Applications,* vol. 10, no. 5, pp. 330-338, 2016.

[28] J. Baek, S. S. R. Bonthu, and S. Choi, "Design of five-phase permanent magnet assisted synchronous reluctance motor for low output torque ripple applications," *IET Electric Power Applications,* vol. 10, no. 5, pp. 339-346, 2016.

[29] J. Hochang, K. Deokjin, L. Chun-Beom, A. Jihyun, and J. Sang-Yong, "Numerical and Experimental Design Validation for Adaptive Efficiency Distribution Compatible to Frequent Operating Range of IPMSM," *Magnetics, IEEE Transactions on,* vol. 50, no. 2, pp. 881-884, 2014.

[30] L. Xiaomin, K. L. V. Iyer, K. Mukherjee, K. Ramkumar, and N. C. Kar, "Investigation of Permanent-Magnet Motor Drives Incorporating Damper Bars for Electrified Vehicles," *Industrial Electronics, IEEE Transactions on,* vol. 62, no. 5, pp. 3234-3244, 2015.

[31] W. Aimeng, L. Heming, L. Weifu, and Z. Haisen, "Influence of skewed and segmented magnet rotor on IPM machine performance and ripple torque for electric traction," in *Electric Machines and Drives Conference, 2009. IEMDC '09. IEEE International*, 2009, pp. 305-310.

[32] S. Yoshioka, S. Morimoto, M. Sanada, and Y. Inoue, "The influence of magnetic properties of permanent magnet on the performance of IPMSM for automotive application," in *Power Electronics Conference (IPEC-Hiroshima 2014 - ECCE-ASIA), 2014 International*, 2014, pp. 246-251.

[33] J. Kim, Y.-H. Jeon, Y.-H. Jeong, and J.-Y. Park, "Development of a Switched Reluctance Motor-based Electric AC Compressor Drive for HEV/EV Applications," presented at the International Conference on Electrical Machines and Systems (ICEMS), October 2013.

[34] J.-R. Riba, A. Garcia, and L. Romeral, "A computer experiment to simulate the dynamic behavior of electric vehicles driven by switched reluctance motors," *International Journal of Electrical Engineering Eductaion,* vol. 51, pp. 368-82, 2014.

[35] T. Ishikawa and H. Dohmeki, "The fundamental design technique of switched reluctance motors, and comparison with PMSM," in *2012 XXth International Conference on Electrical Machines*, 2012, pp. 500-504.

[36] I. Boldea, L. N. Tutelea, L. Parsa, and D. Dorrell, "Automotive Electric Propulsion Systems With Reduced or No Permanent Magnets: An Overview," *IEEE Transactions on Industrial Electronics,* vol. 61, no. 10, pp. 5696-5711, 2014.

[37] X. D. Xue, K. W. E. Cheng, and N. C. Cheung, "Selection of eLECTRIC mOTOR dRIVES for electric vehicles," in *2008 Australasian Universities Power Engineering Conference*, 2008, pp. 1-6.

[38] D. G. Dorrell, A. M. Knight, M. Popescu, L. Evans, and D. A. Staton, "Comparison of different motor design drives for hybrid electric vehicles," in *2010 IEEE Energy Conversion Congress and Exposition*, 2010, pp. 3352-3359.

[39] L. Kumar and S. Jain, "Electric propulsion system for electric vehicular technology: A review," ed: Renewabel and Sustainable Energy Reviews, 2014, January, pp. 924-940.

[40] S. W. Moore, K. Rahman, and M. Ehsani, *Effect on Vehicle Performance of Extending the Constant Power Region of Electric Drive Motors*. 0002.

[41] A. Chiba, M. Takeno, N. Hoshi, M. Takemoto, S. Ogasawara, and M. A. Rahman, "Consideration of Number of Series Turns in Switched-Reluctance Traction Motor Competitive to HEV IPMSM," *IEEE Transactions on Industry Applications,* vol. 48, no. 6, pp. 2333-2340, 2012.

[42] S. Amjad, N. Subramanyan, and R. Rudramoorthy, *Review of design considerations and technological challenges for successful development and deployment of plug-in hybrid electric vehicles*. 2010, pp. 1104-1110.

[43] A. Chiba, K. Kiyota, N. Hoshi, M. Takemoto, and S. Ogasawara, "Development of a Rare-Earth-Free SR Motor With High Torque Density for Hybrid Vehicles," *IEEE Transactions on Energy Conversion,* vol. 30, no. 1, pp. 175-182, 2015.

[44] J. Zhang, X. Lu, J. Lu, Q. Kang, and X. Dong, "Study of the New Permanent Magnet switched reluctance motor," in *2011 International Conference on Advanced Power System Automation and Protection*, 2011, vol. 3, pp. 1684-1687.

[45] H. Hongsik, H. Jin, and L. Cheewoo, "Novel permanent-magnet-assisted switched reluctance motor (I): Concept, design, and analysis," in *2013 International Conference on Electrical Machines and Systems (ICEMS)*, 2013, pp. 602-608.

[46] A. Fasquelle *et al.*, "Coupled electromagnetic acoustic and thermal-flow modeling of an induction motor of railway traction," *Applied Thermal Engineering,* vol. 30, no. 17–18, pp. 2788-2795, 12// 2010.

[47] T. Haubert, "Optimal Control of Mathematical Model of the Electrovehicle," Czech Techical University, Prague, 2015.

[48] G. K. Singh, *Multi-phase induction machine drive research - A survey*. 2002, pp. 139-147.

[49] A. Boglietti, A. Cavagnino, L. Feraris, and M. Lazzari, "Energy-efficient motors," *IEEE Industrial Electronics Magazine,* vol. 2, no. 4, pp. 32-37, 2008.

[50] J. L. Kirtley, J. G. Cowie, E. F. Brush, D. T. Peters, and R. Kimmich, "Improving Induction Motor Efficiency with Die-cast Copper Rotor Cages," in *2007 IEEE Power Engineering Society General Meeting*, 2007, pp. 1-6.

[51] A. H. R. Cha, B. T. W. Jeong, C. D. Y. Im, D. K. J. Shin, and E. Y. J. Seo, "Design of outer rotor type induction motor having high power density for in-wheel system," in *2012 15th International Conference on Electrical Machines and Systems (ICEMS)*, 2012, pp. 1-4.

[52] P. Guglielmi, B. Boazzo, E. Armando, G. Pellegrino, and A. Vagati, "Permanent-Magnet Minimization in PM-Assisted Synchronous Reluctance Motors for Wide Speed Range," *Industry Applications, IEEE Transactions on,* vol. 49, no. 1, pp. 31-41, 2013.

[53] S. Rick, M. Felden, M. Hombitzer, and K. Hameyer, "Permanent magnet synchronous reluctance machine - bridge design for two-layer applications," in *Electric Machines & Drives Conference (IEMDC), 2013 IEEE International*, 2013, pp. 1376-1383.

[54] J. Haataja, "A comparative performance study of four-pole induction motors and synchronous reluctance motors in variable speed drives.," Lappeenranta University of Technology, 2003.

[55] N. Bianchi, S. Bolognani, D. Bon, and M. D. Pré, "Torque harmonic compensation in a synchronous reluctance motor," in *2006 37th IEEE Power Electronics Specialists Conference*, 2006, pp. 1-6.

[56] S. Morimoto, S. Ooi, Y. Inoue, and M. Sanada, "Experimental Evaluation of a Rare-Earth-Free PMASynRM With Ferrite Magnets for Automotive Applications," *IEEE Transactions on Industrial Electronics,* vol. 61, no. 10, pp. 5749-5756, 2014.

[57] E. Carraro, M. Degano, and N. Bianchi, "Permanent magnet volume minimization in permanent magnet assisted synchronous reluctance motors," in *Ecological Vehicles and Renewable Energies (EVER), 2013 8th International Conference and Exhibition on*, 2013, pp. 1-4.

[58] S. Ooi, S. Morimoto, M. Sanada, and Y. Inoue, "Performance evaluation of a high power density PMASynRM with ferrite magnets," in *Energy Conversion Congress and Exposition (ECCE), 2011 IEEE*, 2011, pp. 4195-4200.

[59] P. Niazi and H. A. Toliyat, Permanent magnet assisted synchronous reluctance motor, design and performance improvement, College Station, Tex.: Texas A&M University,, 2006. [Online]. Available: http://hdl.handle.net/1969.1/3178.

[60] J. Yun-Ho, K. Kwangdeok, K. Yong-Jae, P. Byung-Sup, and J. Sang-Yong, "Design characteristics of PMa-SynRM and performance comparison with IPMSM based on numerical analysis," in *Electrical Machines (ICEM), 2012 XXth International Conference on*, 2012, pp. 164-170.

[61] M. Obata, S. Morimoto, M. Sanada, and Y. Inoue, "Performance of PMASynRM With Ferrite Magnets for EV/HEV Applications Considering Productivity," *Industry Applications, IEEE Transactions on,* vol. 50, no. 4, pp. 2427-2435, 2014.

[62] K. Ki-Chan, A. Joon Seon, W. Sung Hong, and L. Ju, "A Study on the Calculation and Reduction Method of Torque Ripple for Permanent Magnet Assisted Synchronous Reluctance Motor by using the Load Angle Curves," in *Electromagnetic Field Computation, 2006 12th Biennial IEEE Conference on*, 2006, pp. 76-76.

[63] L. Jung Ho, Y. Tae Won, and J. Ah Ram, "Characteristic analysis & optimum design of Permanent Magnet Assisted Synchronous Reluctance Motor for premium efficiency performance," in *Electromagnetic Field Computation (CEFC), 2010 14th Biennial IEEE Conference on*, 2010, pp. 1-1.

[64] M. Paradkar and J. Boecker, "Design of a high performance ferrite magnet-assisted synchronous reluctance motor for an electric vehicle," in *IECON 2012 - 38th Annual Conference on IEEE Industrial Electronics Society*, 2012, pp. 4099-4103.

[65] A. J. Piña Ortega and L. Xu, "Investigation of Effects of Asymmetries on the Performance of Permanent Magnet Synchronous Machines," *IEEE Transactions on Energy Conversion,* vol. 32, no. 3, pp. 1002-1011, 2017.

[66] N. Bianchi and H. Mahmoud, "An Analytical Approach to Design the PM in PMAREL Motors Robust Toward the Demagnetization," *IEEE Transactions on Energy Conversion,* vol. 31, no. 2, pp. 800-809, 2016.

[67] C. M. Spargo, B. C. Mecrow, J. D. Widmer, C. Morton, and N. J. Baker, "Design and Validation of a Synchronous Reluctance Motor With Single Tooth Windings," *IEEE Transactions on Energy Conversion,* vol. 30, no. 2, pp. 795-805, 2015.

[68] C. L. Torres, A. Garcia, J. Riba, and L. Romeral, "Design and optimization for vehicle driving cycle of rare-earth-free SynRM based on coupled lumped thermal and magnetic networks," *IEEE Transactions on Vehicular Technology,* vol. PP, no. 99, pp. 1-1, 2017.

[69] C. Ma and L. Qu, "Multiobjective Optimization of Switched Reluctance Motors Based on Design of Experiments and Particle Swarm Optimization," *IEEE Transactions on Energy Conversion,* vol. 30, no. 3, pp. 1144-1153, 2015.

[70] G. Lei, C. Liu, J. Zhu, and Y. Guo, "Techniques for Multilevel Design Optimization of Permanent Magnet Motors," *IEEE Transactions on Energy Conversion,* vol. 30, no. 4, pp. 1574-1584, 2015.

[71] G. Zwe-Lee, L. Cin-Hsien, T. Ming-Hsiao, H. Min-Fu, and T. Mi-Ching, "Rigorous Design and Optimization of Brushless PM Motor Using Response Surface Methodology with Quantum-Behaved PSO Operator," *Magnetics, IEEE Transactions on,* vol. 50, no. 1, pp. 1-4, 2014.

[72] M. E. Beniakar, A. G. Sarigiannidis, P. E. Kakosimos, and A. G. Kladas, "Multiobjective Evolutionary Optimization of a Surface Mounted PM Actuator With Fractional Slot Winding for Aerospace Applications," *Magnetics, IEEE Transactions on,* vol. 50, no. 2, pp. 665-668, 2014.

[73] O. Yeniay, "A comparative study on optimization methods for the constrained nonlinear programming problems," *Mathematical Problems in Engineering,* vol. 2005, no. 2, pp. 165-173, 2005.

[74] E. Sala, K. Kampouropoulos, F. Giacometto, and L. Romeral, ""Smart Multi-Model Approach based on Adaptive Neuro-Fuzzy Inference Systems and Genetic Algorithms,"" presented at the in Industrial Electronics Society, IECON 2014 - 40th Annual Conference of the IEEE,, 2014.

[75] A. Ashoush, S. M. Gadoue, A. S. Abdel-Khalik, and A. L. Mohamadein, "Current optimization for an eleven-phase induction machine under fault conditions using Genetic Algorithm," in *Diagnostics for Electric Machines, Power Electronics & Drives (SDEMPED), 2011 IEEE International Symposium on*, 2011, pp. 529-534.

[76] M. Alamyal, S. M. Gadoue, and B. Zahawi, "Detection of induction machine winding faults using genetic algorithm," in *Diagnostics for Electric Machines, Power Electronics and Drives (SDEMPED), 2013 9th IEEE International Symposium on*, 2013, pp. 157-161.

[77] J. Pyrhönen, T. Jokinen, and V. Hrabovková, "Design of rotating electrical machines," second edition ed: Wiley, 2014.

[78] N. Bianchi, H. Mahmoud, and S. Bolognani, "Fast synthesis of permanent magnet assisted synchronous reluctance motors," *IET Electric Power Applications,* vol. 10, no. 5, pp. 312-318, 2016.

[79] M. Gamba, "Design of non conventional Synchronous Reluctance machine," Politecnico di Torino, 2017.

[80] C. Lu, S. Ferrari, and G. Pellegrino, "Two Design Procedures for PM Synchronous Machines for Electric Powertrains," *IEEE Transactions on Transportation Electrification,* vol. 3, no. 1, pp. 98-107, 2017.

[81] J. R. a. M. Hendershot, T.J.E., *Design of brushless permanent-magnet motors* (Monographs in electrical and electronic engineering). Hillsboro, OH : Oxford : Magna Physics Pub: Motor Design Books LLC, 1994.

[82] J. Huppunen, "High-speed solid-rotor induction machine - electromagnetic calculation and design," Lappeenranta University of Technology, Finland, 2004.

[83] I. Petrov and J. Pyrhonen, "Performance of Low-Cost Permanent Magnet Material in PM Synchronous Machines," *Industrial Electronics, IEEE Transactions on,* vol. 60, no. 6, pp. 2131-2138, 2013.

[84] E. E. Montalvo-Ortiz, S. N. Foster, J. G. Cintron-Rivera, and E. G. Strangas, "Comparison between a spoke-type PMSM and a PMASynRM using ferrite magnets," in *Electric Machines & Drives Conference (IEMDC), 2013 IEEE International*, 2013, pp. 1080-1087.

[85] K. Chiba, S. Chino, M. Takemoto, and S. Ogasawara, "Fundamental analysis for a ferrite permanent magnet axial gap motor with coreless rotor structure," in *Electrical Machines and Systems (ICEMS), 2012 15th International Conference on*, 2012, pp. 1-6.

[86] K. Sone, M. Takemoto, S. Ogasawara, K. Takezaki, and H. Akiyama, "A Ferrite PM In-Wheel Motor Without Rare Earth Materials for Electric City Commuters," *IEEE Transactions on Magnetics,* vol. 48, no. 11, pp. 2961-2964, 2012.

[87] T. Miura, S. Chino, M. Takemoto, S. Ogasawara, C. Akira, and H. Nobukazu, "A ferrite permanent magnet axial gap motor with segmented rotor structure for the next generation hybrid vehicle," in *Electrical Machines (ICEM), 2010 XIX International Conference on*, 2010, pp. 1-6.

[88] M. Obata, S. Morimoto, M. Sanada, and Y. Inoue, "Performance evaluation of high power and low torque ripple structure of rare-earth free PMASynRM with ferrite magnet," in *Power Electronics and Drive Systems (PEDS), 2013 IEEE 10th International Conference on*, 2013, pp. 714-719.

[89] G. Pellegrino, A. Vagati, B. Boazzo, and P. Guglielmi, "Comparison of Induction and PM Synchronous Motor Drives for EV Application Including Design Examples," *IEEE Transactions on Industry Applications,* vol. 48, no. 6, pp. 2322-2332, 2012.

[90] D. G. Dorrell, A. M. Knight, L. Evans, and M. Popescu, "Analysis and Design Techniques Applied to Hybrid Vehicle Drive Machines—Assessment of Alternative IPM and Induction Motor Topologies," *Industrial Electronics, IEEE Transactions on,* vol. 59, no. 10, pp. 3690-3699, 2012.

[91] P. Mishra and S. Saha, "Design modeling and simulation of low voltage squirrel cage induction motor for medium weight electric vehicle," in *Advances in Computing, Communications and Informatics (ICACCI), 2013 International Conference on*, 2013, pp. 1697-1704.

[92] S. Chino, S. Ogasawara, T. Miura, A. Chiba, M. Takemoto, and N. Hoshi, "Fundamental characteristics of a ferrite permanent magnet axial gap motor with segmented rotor structure for the hybrid electric vehicle," in *2011 IEEE Energy Conversion Congress and Exposition*, 2011, pp. 2805-2811.

[93] Y. Liu, J. Zhao, R. Wang, and C. Huang, "Performance Improvement of Induction Motor Current Controllers in Field-Weakening Region for Electric Vehicles," *IEEE Transactions on Power Electronics,* vol. 28, no. 5, pp. 2468-2482, 2013.

[94] K. Kiyota, T. Kakishima, and A. Chiba, "Comparison of Test Result and Design Stage Prediction of Switched Reluctance Motor Competitive With 60-kW Rare-Earth PM Motor," *Industrial Electronics, IEEE Transactions on,* vol. 61, no. 10, pp. 5712-5721, 2014.

[95] P. Niazi, H. A. Toliyat, C. Dal-Ho, and K. Jung-Chul, "A Low-Cost and Efficient Permanent-Magnet-Assisted Synchronous Reluctance Motor Drive," *Industry Applications, IEEE Transactions on,* vol. 43, no. 2, pp. 542-550, 2007.

[96] A. Vagati, M. Pastorelli, G. Francheschini, and S. C. Petrache, "Design of low-torque-ripple synchronous reluctance motors," *Industry Applications, IEEE Transactions on,* vol. 34, no. 4, pp. 758-765, 1998.

[97] R. R. Moghaddam and F. Gyllensten, "Novel High-Performance SynRM Design Method: An Easy Approach for A Complicated Rotor Topology," *IEEE Transactions on Industrial Electronics,* vol. 61, no. 9, pp. 5058-5065, 2014.

[98] G. Pellegrino, F. Cupertino, and C. Gerada, "Automatic Design of Synchronous Reluctance Motors Focusing on Barrier Shape Optimization," *Industry Applications, IEEE Transactions on,* vol. 51, no. 2, pp. 1465-1474, 2015.

[99] M. Ferrari, N. Bianchi, A. Doria, and E. Fornasiero, "Design of synchronous reluctance motor for hybrid electric vehicles," in *Electric Machines & Drives Conference (IEMDC), 2013 IEEE International*, 2013, pp. 1058-1065.

[100] M. Barcaro, T. Pradella, and I. Furlan, "Low-torque ripple design of a ferrite-assisted synchronous reluctance motor," *IET Electric Power Applications,* vol. 10, no. 5, pp. 319-329, 2016.

[101] K. S. Khan, "Design of a Permanent-Magnet Assisted Synchronous Reluctance Machine for a Plug-in Hybrid Electric Vehicle," Electrical Machines and Power Electronics, School of Electrical Engineering, KTH, Stockholm, Sweden, 2011.

[102] C. Carvajal Almendros, "Design and Analysis of a Fractional-Slot Concentrated-Wound Permanent-Magnet-Assisted Synchronous Reluctance Machine," Electronic Power Engineering, Electrical Engineering, KTH Royal Institute of Technolog, Stockholm, Sweeden, 2015.

[103] Y. Wang, G. Bacco, and N. Bianchi, "Geometry Analysis and Optimization of PM-Assisted Reluctance Motors," *IEEE Transactions on Industry Applications,* vol. 53, no. 5, pp. 4338-4347, 2017.

[104] N. Bianchi, E. Fornasiero, E. Carraro, S. Bolognani, and M. Castiello, "Electric vehicle traction based on a PM assisted synchronous reluctance motor," in *Electric Vehicle Conference (IEVC), 2014 IEEE International*, 2014, pp. 1-6.

[105] C. L. Torres, T. Michalski, A. G. Espinosa, and L. Romeral, "Fast optimization of the magnetic model by means of reluctance network for PMa-SynRM," in *IECON 2016 - 42nd Annual Conference of the IEEE Industrial Electronics Society*, 2016, pp. 1642-1647.

[106] C. Lopez Torres, T. Michalski, A. Garcia, and L. Romeral, "Rotor of Synchronous Reluctance Motor optimization by means reluctance network and genetic algorithm," ed. *Electrical Machines and Systems (ICEMS)*, 2016.

[107] M. Barcaro, G. Meneghetti, and N. Bianchi, "Structural Analysis of the Interior PM Rotor Considering Both Static and Fatigue Loading," *IEEE Transactions on Industry Applications,* vol. 50, no. 1, pp. 253-260, 2014.

[108] F. Cupertino, M. Palmieri, and G. Pellegrino, "Design of high-speed synchronous reluctance machines," in *2015 IEEE Energy Conversion Congress and Exposition (ECCE)*, 2015, pp. 4828-4834.

[109] C. Babetto, G. Bacco, and N. Bianchi, "Analytical approach to determine the power limit of high-speed synchronous reluctance machines," in *2017 IEEE International Electric Machines and Drives Conference (IEMDC)*, 2017, pp. 1-7.

[110] S. Taghavi and P. Pillay, "A core analysis of the synchronous reluctance motor for automotive applications," in *Electrical Machines (ICEM), 2014 International Conference on*, 2014, pp. 961-967.

[111] D. Prieto, B. Daguse, P. Dessante, P. Vidal, and J. Vannier, "Effect of magnets on average torque and power factor of Synchronous Reluctance Motors," in *Electrical Machines (ICEM), 2012 XXth International Conference on*, 2012, pp. 213-219.

[112] A. J. Pi, x00F, H. Cai, Y. Alsmadi, and L. Xu, "Analytical model for the minimization of torque ripple in permanent magnets assisted synchronous reluctance motors through asymmetric rotor poles," in *2015 IEEE Energy Conversion Congress and Exposition (ECCE)*, 2015, pp. 5609-5615.

[113] N. Bianchi, S. Bolognani, D. Bon, Pre, x, and M. D., "Rotor Flux-Barrier Design for Torque Ripple Reduction in Synchronous Reluctance and PM-Assisted Synchronous Reluctance Motors," *Industry Applications, IEEE Transactions on,* vol. 45, no. 3, pp. 921-928, 2009.

[114] W. H. Kim *et al.*, "Optimal PM Design of PMA-SynRM for Wide Constant-Power Operation and Torque Ripple Reduction," *IEEE Transactions on Magnetics,* vol. 45, no. 10, pp. 4660-4663, 2009.

[115] S. Yammine *et al.*, "Synchronous reluctance machine flux barrier design based on the flux line patterns in a solid rotor," in *Electrical Machines (ICEM), 2014 International Conference on*, 2014, pp. 297-302.

[116] R. R. Moghaddam, F. Magnussen, and C. Sadarangani, "Novel rotor design optimization of Synchronous Reluctance Machine for low torque ripple," in *Electrical Machines (ICEM), 2012 XXth International Conference on*, 2012, pp. 720-724.

[117] B. Jeihoon, S. S. R. Bonthu, K. Sangshin, and C. Seungdeog, "Optimal design of five-phase permanent magnet assisted synchronous reluctance motor for low output torque ripple," in *Energy Conversion Congress and Exposition (ECCE), 2014 IEEE*, 2014, pp. 2418-2424.

[118] G. B. Mariani, A. Besri, N. Voyer, C. Chillet, M. Fassenet, and L. Garbuio, "Synchronous reluctance motor multi-static MEC model," in *Industrial Electronics Society, IECON 2015 - 41st Annual Conference of the IEEE*, 2015, pp. 000843-000848.

[119] A. Boglietti, A. Cavagnino, D. Staton, M. Shanel, M. Mueller, and C. Mejuto, "Evolution and Modern Approaches for Thermal Analysis of Electrical Machines," *IEEE Transactions on Industrial Electronics,* vol. 56, no. 3, pp. 871-882, 2009.

[120] G. Kylander, "Thermal modelling of small cage induction motors," ed. Göteborg, 1995.

[121] M. Mahmoudi, "Thermal modelling of the Synchronous Reluctance Machine," Electrical Engineering, Royal Institute of Technology, 2012.

[122] D. A. Staton and A. Cavagnino, "Convection Heat Transfer and Flow Calculations Suitable for Electric Machines Thermal Models," *Industrial Electronics, IEEE Transactions on,* vol. 55, no. 10, pp. 3509-3516, 2008.

[123] P. S. Ghahfarokhi, A. Kallaste, A. Belahcen, T. Vaimann, and A. Rassõlkin, "Review of thermal analysis of permanent magnet assisted synchronous reluctance machines," in *2016 Electric Power Quality and Supply Reliability (PQ)*, 2016, pp. 219-224.

[124] S. Nategh, O. Wallmark, M. Leksell, and Z. Shuang, "Thermal Analysis of a PMaSRM Using Partial FEA and Lumped Parameter Modeling," *Energy Conversion, IEEE Transactions on,* vol. 27, no. 2, pp. 477-488, 2012.

[125] A. M. El-Refaie, N. C. Harris, T. M. Jahns, and K. M. Rahman, "Thermal analysis of multibarrier interior PM synchronous Machine using lumped parameter model," *Energy Conversion, IEEE Transactions on,* vol. 19, no. 2, pp. 303-309, 2004.

[126] N. Zhao and W. Liu, "Loss Calculation and Thermal Analysis of Surface-Mounted PM Motor and Interior PM Motor," *IEEE Transactions on Magnetics,* vol. 51, no. 11, pp. 1-4, 2015.

[127] Cogent. *Electrical Steel Non Oriented Fully Processed*. Available: https://perso.uclouvain.be/ernest.matagne/ELEC2311/T2006/NOFP.pdf

[128] SKF. *model for calculating the frictional moment*. Available: http://www.skf.com/binary/30-299767/The%20SKF%20model%20for%20calculating%20the%20frictional%20moment_tcm_12-299767.pdf

[129] A. Boglietti, A. Cavagnino, M. Pastorelli, D. Staton, and A. Vagati, "Thermal analysis of induction and synchronous reluctance motors," in *Electric Machines and Drives, 2005 IEEE International Conference on*, 2005, pp. 1592-1597.

[130] K. Kyu-Seob, L. Byeong-Hwa, K. Hae-Joong, H. Jung-Pyo, and J. Jang-Hyun, "Thermal analysis of outer rotor type IPMSM using thermal equivalent circuit," in *Electrical Machines and Systems (ICEMS), 2012 15th International Conference on*, 2012, pp. 1-4.

[131] R. Antonello, M. Carraro, A. Costabeber, F. Tinazzi, and M. Zigliotto, "Energy-Efficient Autonomous Solar Water-Pumping System for Permanent-Magnet Synchronous Motors," *IEEE Transactions on Industrial Electronics,* vol. 64, no. 1, pp. 43-51, 2017.

[132] K. Emmrich, A. Brune, and B. Ponick, "Evaluation of an analytical, efficiency-optimized torque-speed characteristic of induction machines coupled with a thermal-electromagnetic energy consumption calculation," in *Electrical Machines (ICEM), 2014 International Conference on*, 2014, pp. 762-767.

[133] G. Pellegrino, B. Boazzo, and T. M. Jahns, "Magnetic Model Self-Identification for PM Synchronous Machine Drives," *IEEE Transactions on Industry Applications,* vol. 51, no. 3, pp. 2246-2254, 2015.

[134] B. Cheng and T. R. Tesch, "Torque Feedforward Control Technique for Permanent-Magnet Synchronous Motors," *IEEE Transactions on Industrial Electronics,* vol. 57, no. 3, pp. 969-974, 2010.

[135] S. A. Odhano, R. Bojoi, A. Boglietti, Ş. G. Roşu, and G. Griva, "Maximum Efficiency per Torque Direct Flux Vector Control of Induction Motor Drives," *IEEE Transactions on Industry Applications,* vol. 51, no. 6, pp. 4415-4424, 2015.

[136] D. Q. Dang, M. S. Rafaq, H. H. Choi, and J. W. Jung, "Online Parameter Estimation Technique for Adaptive Control Applications of Interior PM Synchronous Motor Drives," *IEEE Transactions on Industrial Electronics,* vol. 63, no. 3, pp. 1438-1449, 2016.

[137] R. Monajemy and R. Krishnan, "Control and dynamics of constant-power-loss-based operation of permanent-magnet synchronous motor drive system," *IEEE Transactions on Industrial Electronics,* vol. 48, no. 4, pp. 839-844, 2001.

[138] G. Luo, R. Zhang, Z. Chen, W. Tu, S. Zhang, and R. Kennel, "A Novel Nonlinear Modeling Method for Permanent-Magnet Synchronous Motors," *IEEE Transactions on Industrial Electronics,* vol. 63, no. 10, pp. 6490-6498, 2016.

[139] R. H. Moncada, J. A. Tapia, and T. M. Jahns, "Saliency analysis of PM machines with flux weakening capability," in *Electrical Machines, 2008. ICEM 2008. 18th International Conference on*, 2008, pp. 1-6.

[140] E. Schmidt, "Synchronous reluctance machines with high-anisotropy rotors — Comparison of their operational characteristics," in *2014 Australasian Universities Power Engineering Conference (AUPEC)*, 2014, pp. 1-6.

[141] W. Wu, X. Zhu, L. Quan, Y. Du, and Z. Xiang, "Design and Analysis of a Hybrid Permanent Magnet Assisted Synchronous Reluctance Motor Considering Magnetic Saliency and PM Usage," *IEEE Transactions on Applied Superconductivity,* vol. 28, no. 3, pp. 1-6, 2018.

[142] S. S. R. Bonthu, A. Arafat, and S. Choi, "Comparisons of Rare-Earth and Rare-Earth-Free External Rotor Permanent Magnet Assisted Synchronous Reluctance Motors," *IEEE Transactions on Industrial Electronics,* vol. 64, no. 12, pp. 9729-9738, 2017.

[143] C. T. Liu *et al.*, "On the Design and Construction Assessments of a Permanent-Magnet-Assisted Synchronous Reluctance Motor," *IEEE Transactions on Magnetics,* vol. 53, no. 11, pp. 1-4, 2017.

[144] Y. Wang, D. M. Ionel, and D. Staton, "Ultrafast Steady-State Multiphysics Model for PM and Synchronous Reluctance Machines," *IEEE Transactions on Industry Applications,* vol. 51, no. 5, pp. 3639-3646, 2015.